A MÖSSBAUER STUDY OF THE SPIN-FLOP PHASE TRANSITION IN SOME ANTIFERROMAGNETIC MATERIALS

by

QUENTIN ANDREW PANKHURST

A thesis submitted in accordance with the requirements of the University of Liverpool for the degree of Doctor of Philosophy.

Oliver Lodge Laboratory,
University of Liverpool.

May 1986.

Thesis User's Declaration

DATE	NAME (IN BLOCK LETTERS)	SIGNATURE	ADDRESS
2/11/95	JOHN HUTCHINGS	John Hutchings	PHYSICS DEPT.
13/2/96	M J LONGFIELD		"
3/10/08	D M DAWSON		CHEM DEPT

ACKNOWLEDGEMENTS

It has been a great pleasure for me to have spent the last three years in Liverpool, and I am grateful to the Commonwealth Scholarship Commission U.K. for making it possible.

I am greatly indebted to Professor C.E. Johnson and to my supervisor Dr M.F. Thomas for their continual guidance, interest and inspiration throughout this work. I am very grateful to Dr D.H. Jones for his insight and help with many of the theoretical and computational aspects of my research. The technical expertise and assistance provided by Mr R.L. Bilsborrow was likewise essential to the completion of the experimental part of my research. Thanks are also due to Drs D.P.E. Dickson and I. Hall for the many suggestions and comments that they have offered during the course of my work.

Thanks to all my friends in the Liverpool Mössbauer group (past and present) for all the good times, especially Tim, John, Huub, Sue, Jackie, Clay, Adrian, Xavier, Don and Judy. Heartfelt thanks also to LFC for the double, to LFB and RSC for the poetry, and to Chan and Devi for the home. Finally, thanks to my mother (may she rest in peace) and to my father for all the love and support that they have given me over the years.

ABSTRACT

The spin-flop phase transition has long been of interest to both theoretical and experimental physicists, ever since it was first predicted by Louis Néel in 1936. In this work spin-flop transitions in the antiferromagnetic materials K_2FeF_5, Rb_2FeF_5 and α-Fe_2O_3 have been studied by means of ^{57}Fe Mössbauer spectroscopy.

Spectra of K_2FeF_5 and Rb_2FeF_5 single crystals were recorded at 4.2K with external magnetic fields of up to 14T applied in different modes, providing information on the effect of misalignment on the sharpness or 'order' of the observed transition. Directing the applied field parallel to the easy anisotropy axis resulted in a sharp 'first-order' transition, while misaligning the field by ~30° produced a broadened 'second-order' transition.

Field-induced spin-flop transitions in α-Fe_2O_3 single crystal samples were studied at low temperatures by applying fields of up to 10T either parallel to or perpendicular to the easy anisotropy axis. The observed transitions were found to be of first-order in the 'parallel' case, and second-order in the 'perpendicular' case. The Morin transition, a temperature driven spin-flop which occurs naturally in α-Fe_2O_3 at ~260K, was also studied and was found to be of first-order.

Comparison of the character of the observed transitions with the predictions of several theoretical models of the spin-flop led to the conclusion that the conventional mean-field theory of the transition provides a good qualitative description of the phenomenon.

CONTENTS

CHAPTER ONE : INTRODUCTION

Phase transitions in magnetic systems have long been of interest to both theoretical and experimental physicists. One such transition is the 'spin-flop' phase transition that was initially predicted by Louis Néel in 1936 and was subsequently observed experimentally in $CuCl_2.2H_2O$ by C.J. Gorter in 1953. This transition has since been found to occur in a number of antiferromagnetic materials.

In simple terms the spin-flop transition may be described as follows. The free energy of an antiferromagnet subject to an applied magnetic field B is reduced by an amount $-(1/2\mu_o)\chi B^2$, where μ_o is the permeability of free space. The magnetic susceptibility χ is generally smaller in the direction of the antiferromagnetic axis of the spins than in the perpendicular direction ($\chi_\parallel<\chi_\perp$), and therefore the spins will tend to align perpendicular to the applied field. However this effect is hampered if the antiferromagnet is slightly anisotropic and has a preferred orientation ('easy axis') for the spins in the crystalline lattice. In such a case an applied field directed along the easy axis will induce a transition when the anisotropy energy $-\kappa$ is balanced by the field energy term $-(1/2\mu_o)(\chi_\perp-\chi_\parallel)B^2$. At the critical field $B_{sf}=[2\kappa\mu_o/(\chi_\perp-\chi_\parallel)]^{\frac{1}{2}}$ the antiferromagnetic axis of the spins reorients to a direction perpendicular to the easy axis in what is known as a 'spin-flop' transition.

The spin-flop phenomenon has found applications in many diverse fields. For example, the spin-flop has recently been used as a practical method of measuring the magnetocrystalline anisotropies present in randomly mixed antiferromagnets (Ito et al. 1986). In contrast, Rohrer and Gerber (1977) have utilised the effect to test some predictions of the renormalisation group theory of crossover phenomena.

However the majority of work to date has centered on obtaining a full understanding of the mechanism of the transition itself.

Many investigators have studied the sharpness or 'order' of the spin-flop transition. Néel (1936) predicted that the transition would be abrupt provided the applied field was perfectly aligned with the easy axis, but that any misalignment would result in a broadening of the transition. More recent work (Chepurnykh 1968, Rohrer and Thomas 1969) has shown that if the misalignment angle exceeds a critical angle $\psi_c(T)$ a gradual rotation of the antiferromagnetic axis away from the easy axis will take place. The critical angle ψ_c corresponds to the edge of a 'shelf' of first-order transitions in the magnetic phase diagram of the weakly anisotropic antiferromagnet. It has also been found (Rohrer and Gerber 1978) that the nature of the anisotropy in the system (e.g. uniaxial or orthorhombic) is of importance. In the latter case the first-order 'shelf' may be very wide, extending to the paramagnetic phase boundary.

In the present work the spin-flop transition in the orthorhombic antiferromagnets K_2FeF_5 and Rb_2FeF_5, and the 'Dzyaloshinsky' antiferromagnet α-Fe_2O_3 have been observed. The contrasting characteristics of these materials allows a comparative study to be made, both between the systems and with theoretical predictions.

K_2FeF_5 and Rb_2FeF_5 exhibit similar quasi one-dimensional properties, but they have quite different ordered magnetic structures. In K_2FeF_5 the spins align collinearly along the crystal b-axis, while in Rb_2FeF_5 four magnetic sublattices are present, with distinct easy axes at ~30° to the b-axis. Therefore in K_2FeF_5 it is possible (in principle) to align the applied field with the easy axis, but in Rb_2FeF_5 a field directed along the b-axis is effectively misaligned by 30°. The effect of misalignment on the transition can thus be investigated.

Hematite (α-Fe_2O_3) is a three-dimensional antiferromagnet, noted for its temperature dependent spin-flop at $T_M \simeq 260K$ known as the 'Morin transition'. Below T_M the spins lie along the crystal <111> axis, and a magnetic field applied along that axis may induce a second spin-flop. It is of interest to compare the field-dependent spin-flop with the temperature-driven Morin transition.

The different dimensionalities of the systems studied also provides insight into aspects of the spin-flop phenomenon, such as the applied field dependence of the excitation of spin-waves (magnons) in the lattices. Recent theories relating the spin-flop effect in one-dimensional materials to non-linear spin waves or 'solitons' (de Jongh 1982) may also be tested.

The experimental technique utilised in this study was ^{57}Fe Mössbauer spectroscopy. The Mössbauer effect is a particularly useful tool for observing spin-flop transitions since the presence of unflopped, flopped or intermediate phases in the crystal may be directly observed in the positions, splittings and intensities of the spectral lines.

An outline of this thesis is as follows. In Chapter 2 a review of the theoretical basis of the spin-flop transition is given. The technique of Mössbauer spectroscopy is briefly discussed in Chapter 3, and in Chapter 4 the experimental details of the work are described. Chapter 5 deals with the results of the experiments performed on K_2FeF_5 and Rb_2FeF_5, and the work on α-Fe_2O_3 is reported in Chapter 6. Finally, the various results are summarised and discussed in Chapter 7.

CHAPTER TWO

THE SPIN-FLOP PHASE TRANSITION

2.1 INTRODUCTION

Theoretical analysis of the spin-flop phase transition was first performed by L. Néel in 1932 and 1936 on the basis of a classical mean-field model. This work was later extended by several authors, including Van Vleck (1941), Nagamiya (1951) and Gorter and Haantjes (1952). Chepurnykh (1969) and Rohrer and Thomas (1969) independently described the nature of the spin-flop at zero temperature for a field applied in an arbitrary direction with respect to the easy anisotropy axis of a uniaxial antiferromagnet. Later work by Rohrer, Thomas and co-workers has dealt with the temperature dependence of the critical field values and with the effect of non-uniaxial anisotropy.

Several assumptions are inherent in the classical spin-flop theory. All the spins in the lattice are regarded as moving independently, and the interaction of their average values is taken as sufficient. This approximation has serious limitations, particularly at low temperatures where it fails to allow for collective movement of the spins. A more realistic approach using spin-wave theory (Bloch 1930) has been applied to the spin-flop transition by Kanamori and Yosida (1955) and Jacobs and Silverstein (1964). This analysis indicates that in the course of the spin-flop the applied field influences the spin-waves in the system, a feature which may be observed as a field-dependent mean spin value for the magnetic atoms.

It has recently been proposed that in low-dimensional systems the spin-flop may be interpreted in terms of moving domain walls or 'solitons' (de Jongh 1982). In this model the transition corresponds to a softening of the energy required for the creation of a soliton. The width of the transition is found to be broader than that predicted by either the classical or spin-wave theories.

In this chapter the classical theory of the spin-flop transition is described in some detail. First the simplest example of a uniaxial antiferromagnet at zero temperature subject to a perfectly aligned field is considered. Thereafter the effects of field misalignment, non-zero temperature and non-uniaxial anisotropy are discussed. In sections 2.3 and 2.4 the spin-wave and soliton theories are briefly reviewed, with particular reference to those predicted effects that were likely to be observable in the present experiment.

2.2 MEAN-FIELD THEORY

The earliest quantitative treatment of a magnetic phase transition was made by P.Weiss in 1907, and is known as mean (or molecular) field theory. In this theory every spin in a ferromagnetic body is subject to a virtual magnetic field which is proportional to the local value of the average magnetisation. Heisenberg (1928) interpreted this virtual field to be a consequence of a quantum-mechanical exchange interaction between neighbouring atoms. Néel (1932,1936) introduced the concept of antiferromagnetism by assuming a negative exchange interaction between nearest neighbours in a lattice. He was able to show that below some critical temperature (now known as the Néel temperature) two magnetic sublattices would appear, with the atoms on one sublattice experiencing a mean field of magnitude proportional to (but of opposite direction to) the average magnetisation of the other sublattice. Néel also noticed that the directions of the two sublattice magnetisations would tend to align themselves perpendicularly to an applied field, but that this tendency would be opposed by a crystalline anisotropy favouring other directions. This observation forms the basis of the spin-flop phenomenon.

Some years ago Rohrer and Thomas (1969), Thomas (1969a,1969b) and Blazey et al. (1971a,1971b) studied the spin-flop transition in the mean-field approximation. The main steps in their analysis may be summarised as follows. The method is to minimise the free energy $F=E-T\Sigma$, where E is the energy and Σ is the entropy of the system. F is calculated as a function of the sublattice magnetisations $\langle S_i \rangle$ and $\langle S_j \rangle$, the equilibrium values of which are found by minimising F with respect to $\langle S_i \rangle$ and $\langle S_j \rangle$. The stability limits of a given phase (e.g. antiferromagnetic or spin-flopped) are then obtained from the second derivatives of the free energy with respect to the sublattice magnetisations.

In this section we illustrate the analysis of Rohrer, Thomas and Blazey by taking as a simple example the uniaxial antiferromagnet at zero temperature. The effect of finite temperature and other types of anisotropy are also discussed. But first we shall consider the form of the spin Hamiltonian which is used to describe the antiferromagnet:

2.2a The Spin Hamiltonian

The energy of an antiferromagnet may be given by the expectation value of a Hamiltonian of the form

$$H = H_{ex} + H_{anis} + H_{field} \,. \qquad (2.1)$$

The first term is the isotropic (Heisenberg) exchange energy:

$$H_{ex} = 2\Sigma_{ij} J_{ij} \underline{S}_i \cdot \underline{S}_j \,,$$

where $\underline{S}_i$ refers to the spins on one sublattice and $\underline{S}_j$ to those on the other sublattice, and the summation is restricted to pairs of neighbouring spins. The exchange constants J_{ij} are positive so that the antiparallel orientation of the neighbouring spins is preferred. We may note that J_{ij} may have different strengths along different directions in the lattice. In a quasi one-dimensional antiferromagnet the coupling J between neighbours in the chain is much stronger than

the coupling J' between chains. In a three-dimensional system J is isotropic.

Magnetic anisotropy may arise from the coupling between the spin and the orbital angular momentum of the ion : the orbital state is directly affected by the atomic arrangement and the spin can therefore 'see' the lattice through this coupling. The anisotropy energy may be written as a sum of anisotropic exchange and single-ion terms (Kanamori 1963) :

$$H_{anis} = -\Sigma_{ij} K_{ij} S_{zi} S_{zj} - L\Sigma_i [(S_{zi})^2 - S(S+1)/3] \ .$$

The anisotropic exchange is said to be of 'Ising' type if $K_{ij}>0$ and the spins prefer to lie along the crystal z axis, and of 'X-Y' type if $K_{ij}<0$ and the spins lie in the xy-plane. The anisotropy energy is often written in a simplified form. In the case of a uniaxial antiferromagnet

$$H_{anis} = -K\Sigma_i (S_{zi})^2 \ , \quad K>0 \ ,$$

designates the z axis as the magnetically 'easy' axis and the xy-plane as magnetically 'hard'. In the case of an orthorhombic antiferromagnet with

$$H_{anis} = -K\Sigma_i (S_{zi})^2 + K'\Sigma_i (S_{yi})^2 \ , \quad K,K'>0 \ ,$$

and with K>K', the z axis is described as 'easy', the y axis 'hard' and the x axis 'medium'.

The last term in equation (2.1) represents the energy associated with an applied field of flux density B :

$$H_{field} = -g\mu \underline{B} \cdot \Sigma_i \underline{S}_i \ ,$$

where g is the spectroscopic splitting factor and $\mu \equiv \mu_B$ is the Bohr magneton.

2.2b Uniaxial Antiferromagnet at Zero Temperature

As an illustration of the classical treatment of the spin-flop transition, let us consider the simplest of cases: the uniaxial antiferromagnet at zero temperature. We use the Hamiltonian :

$$H = 2J\Sigma_{ij}\underset{\sim}{S}_i \cdot \underset{\sim}{S}_j - K(\Sigma_i(S_{zi})^2+\Sigma_j(S_{zj})^2) - g\mu\underset{\sim}{B}\cdot(\Sigma_i\underset{\sim}{S}_i+\Sigma_j\underset{\sim}{S}_j) \quad , \quad (2.2)$$

where $J>0$ and $K>0$, and $2J$ is the exchange constant between each spin and its nearest neighbours. In general the applied field $\underset{\sim}{B}$ is directed at an angle ψ to the easy anisotropy axis (the z axis). We define the directions of a representative spin from each sublattice, $\underset{\sim}{S}_1$ and $\underset{\sim}{S}_2$, in terms of two angles : the 'canting angle' θ between the spins and their antiferromagnetic axis and the 'rotation angle' α between the ferromagnetic axis of the spins and the applied field. These angles, shown in Figure 2.1, are often directly measurable in a Mössbauer effect study of the spin-flop.

2.2b(i) Perfect Alignment

We first consider the situation for $\underset{\sim}{B}=(0,0,B)$: the applied field perfectly aligned with the easy axis ($\psi=0$). Assuming that $|\underset{\sim}{S}_1|=|\underset{\sim}{S}_2|=S$, the free energy of the system is

$$E = -NS[2JzS\cos 2\theta + KS(\sin^2(\alpha+\theta)+\sin^2(\alpha-\theta)) + 2g\mu B\cos\alpha\sin\theta] \quad ,$$

where N is the number of spins on each sublattice and z is the number of nearest neighbours each spin has. Writing the 'exchange field' $B_E=2JzS/g\mu$ and the 'anisotropy field' $B_A=2KS/g\mu$ gives :

$$E = -NSg\mu[B_E\cos 2\theta + \tfrac{1}{2}B_A(\sin^2(\alpha+\theta)+\sin^2(\alpha-\theta)) + 2B\cos\alpha\sin\theta] . \quad (2.3)$$

The equilibrium values of α and θ occur when E is a minimum and both $\partial E/\partial\alpha=0$ and $\partial E/\partial\theta=0$. These equilibrium conditions are immediately satisfied in the antiferromagnetic (AFM) phase where $\alpha=90°,\theta=0$, and in the paramagnetic (PM) phase where $\alpha=0,\theta=90°$. However, in the spin-flop (SF) phase where $\alpha=0$ and $\theta<90°$ the equilibrium equations impose the condition $B=(2B_E-B_A)\sin\theta$. Using these equations we obtain the following expressions of the ground state energies of each phase:

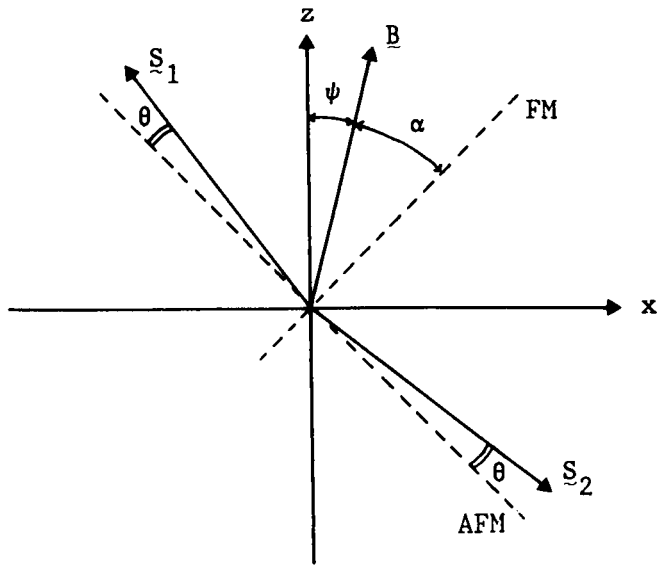

Figure 2.1 Definition of the sublattice spin directions in terms of the canting angle θ, the rotation angle α and the field misalignment angle ψ.

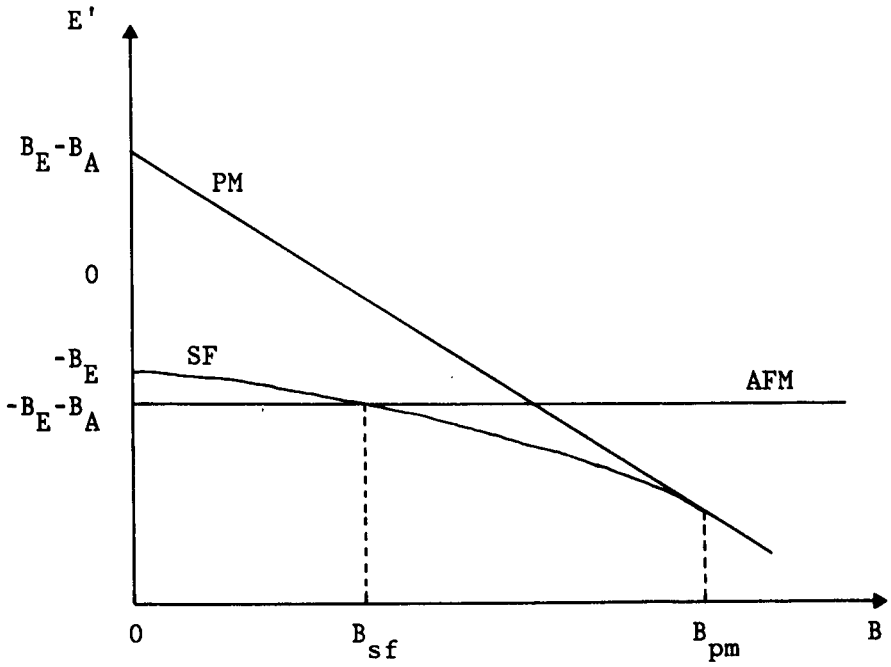

Figure 2.2 Dependence of the ground state energies (E=NSgμE') of the AFM, SF and PM phases of a uniaxial antiferromagnet on the magnitude of applied field directed along the easy anisotropy axis.

$$E_{afm} = -NSg\mu[B_E + B_A] \ ,$$

$$E_{sf} = -NSg\mu[B_E + B^2/(2B_E - B_A)] \ ,$$

and $$E_{pm} = -NSg\mu[-B_E + B_A + 2B] \ .$$

These are shown as a function of B in Figure 2.2, assuming that $B_A << B_E$. It is apparent that a first-order phase transition occurs when $E_{afm}=E_{sf}$, at a critical field :

$$B_{sf} = [B_A(2B_E - B_A)]^{\frac{1}{2}} \ ,$$

which is known as the 'thermodynamic spin-flop field'. A smooth second-order transition takes place between the SF and PM phases at the critical field $B_{pm}=2B_E-B_A$.

The stability limits of a given phase are determined by the condition that the eigenvalues of the 2×2 matrix

$$\nabla^2 E = \begin{bmatrix} \partial^2 E/\partial\alpha\partial\alpha & \partial^2 E/\partial\alpha\partial\theta \\ \partial^2 E/\partial\theta\partial\alpha & \partial^2 E/\partial\theta\partial\theta \end{bmatrix}$$

be positive or zero. This may be interpreted as the condition that the stationary point in the two-dimensional surface $E(\alpha,\theta)$ defined by $\nabla E=0$ should not be a maximum. From equation (2.3) we obtain :

$$\nabla^2 E = \begin{bmatrix} x + z & y \\ y & x \end{bmatrix}$$

with $x = B\cos\alpha\sin\theta - B_A\cos 2\alpha\cos 2\theta$, $y = B\sin\alpha\cos\theta + B_A\sin 2\alpha\sin 2\theta$, and $z = 2B_E\cos 2\theta$. The eigenvalues are given by $\lambda_{\pm} = \frac{1}{2}[(2x+z)\pm(z^2+4y^2)^{\frac{1}{2}})]$, and the stability criterion $\lambda_- \geq 0$ reduces to $x(x+z) \geq y^2$.

Thus the PM phase $(x=B+B_A, y=0, z=-2B_E)$ is stable provided $B \geq 2B_E - B_A$ and the AFM phase $(x=B_A, y=B, z=2B_E)$ may be stable up to the field $B_1=[B_A(2B_E+B_A)]^{\frac{1}{2}}$. The limits of stability of the SF phase $(x=B\sin\theta-B_A\cos 2\theta, y=0, z=2B_E\cos 2\theta)$ occur either when $x=0$ and $B=B_2=(2B_E-B_A)[B_A/(2B_E+B_A)]^{\frac{1}{2}}$ or when $(x+z)=0$ and $B=2B_E-B_A$. The inequality of the critical fields B_1 and B_2 is indicative of the phenomenon of hysteresis in the first-order spin-flop transition.

2.2b(ii) Imperfect Alignment

We now consider the nature of the spin-flop when $\underset{\sim}{B}=(B_x,0,B_z)=B(\sin\psi,0,\cos\psi)$ is applied at a non-zero angle ψ to the easy axis. The free energy of the system is then :

$$E = -NSg\mu[B_E\cos2\theta + \tfrac{1}{2}B_A(\sin^2(\psi+\alpha+\theta)+\sin^2(\psi+\alpha-\theta)) + 2B\cos\alpha\sin\theta] ,$$

and the equilibrium conditions $\nabla E=0$ lead to :

$$B\cos\alpha\cos\theta = (B_E - \tfrac{1}{2}B_A\cos(2\psi+2\alpha))\sin2\theta \qquad (2.4a)$$

and $$B\sin\alpha\sin\theta = \tfrac{1}{2}B_A\sin(2\psi+2\alpha)\cos2\theta . \qquad (2.4b)$$

The stability criterion is again in the form of an inequality $x(x+z)\geq y^2$, with :

$$x = B\cos\alpha\sin\theta - B_A\cos(2\psi+2\alpha)\cos2\theta ,$$

$$y = B\sin\alpha\cos\theta + B_A\sin(2\psi+2\alpha)\sin2\theta , \qquad (2.5)$$

and $$z = 2B_E\cos2\theta .$$

It is difficult to manipulate these equations into a recognisable form, so we proceed numerically. Equating $\sin\alpha\sin\theta\times$(2.4a) to $\cos\alpha\cos\theta\times$(2.4b) and dividing through by $\cos\theta$ we obtain an expression for θ as a function of α :

$$\sin^2\theta = B_A\cos\alpha\sin(2\psi+2\alpha)/(4B_E\sin\alpha + 2B_A\sin(2\psi+\alpha)) . \qquad (2.6)$$

An interesting feature of this relation, shown in Figure 2.3, occurs at the onset of the PM phase where $\theta=90°$. At that point the ferromagnetic component of the spins is not (in general) parallel to the applied field, but is tilted towards the easy anisotropy axis by a small angle α_{PM}. In the perfectly aligned cases of $\psi=0$ or $90°$ $\alpha_{PM}=0$, but in general it is non-zero. By means of some tedious algebra one can show that α_{PM} has a maximum value of $\sim B_A/4B_E$ near $\psi=45°$.

Equations (2.4a) and (2.6) allow us to express B as a function of the rotation angle α :

$$B^2 = [B_A\sin\psi_2(2B_E-B_A\cos\psi_2)^2]/[\cos\alpha(4B_E\sin\alpha+2B_A\sin\psi_1)] , \qquad (2.7)$$

where $\psi_1=2\psi+\alpha$ and $\psi_2=2\psi+2\alpha$. We are then able, with (2.6) and (2.7), to calculate the equilibrium values of B and θ (as a function of α)

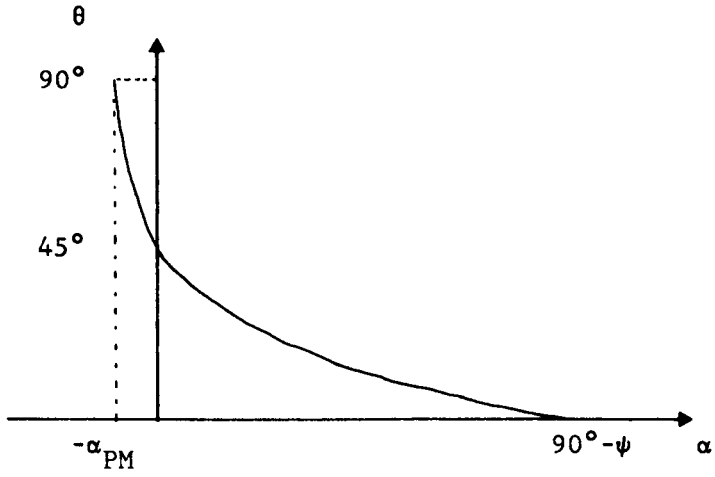

Figure 2.3 Schematic diagram of the equilibrium values of the canting angle θ as a function of the rotation angle α. (Not to scale.)

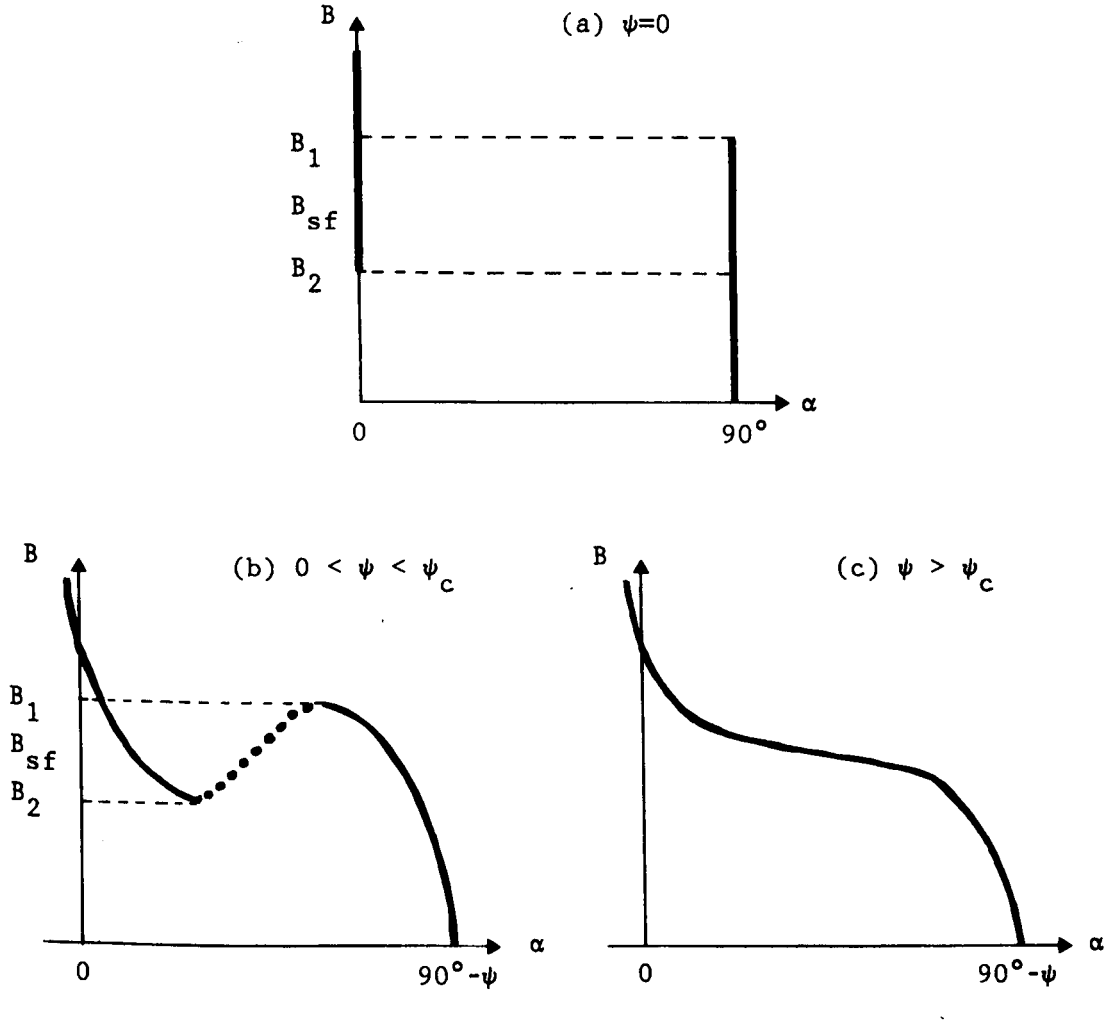

Figure 2.4 Equilibrium values of B(α) for different misalignment angles ψ. Bold (or dotted) lines represent stable (or unstable) solutions according to equations (2.5). B_1 and B_2 mark the stability limits of the AFM-like and SF-like states.

for any given magnetic system specified by B_E, B_A and ψ. The stability of that solution may then be tested using equations (2.5).

Applying this procedure we can distinguish three types of spin-flop transition, shown schematically in Figure 2.4 in terms of the dependence of B on α. The first case is that of perfect alignment ($\psi=0$), where hysteresis appears in the transition from the $\alpha=90°$ to $\alpha=0°$ states. If $\psi\neq0$ but is less than some critical angle ψ_c, the transition is still of first-order but connects states with $\alpha<90°-\psi$ to states with $\alpha>-\alpha_{PM}$ (see Figure 2.4b). Thus as B increases from zero the spins rotate slightly before discontinuously flopping to a position close to (but not exactly) perpendicular to the field. In the third case (Figure 2.4c) $\psi>\psi_c$ and the transition is entirely continuous. As B increases the spins rotate towards the field direction in a reversible transition, and no hysteresis is observed.

2.2b(iii) Phase Diagram

Continuing with this numerical analysis it is possible to map out the regions of stability of the AFM, SF and PM phases in the B_xB_z-plane. This has been done by Chepurnykh (1969) and Rohrer and Thomas (1969). Their results are shown in Figure 2.5.

The PM phase boundary may be derived analytically by making a suitable choice of coordinate angles. If we define γ and δ as the angles between the sublattice spins and the easy axis (corresponding to $\gamma=\psi+\alpha-\theta+90°$ and $\delta=\psi+\alpha+\theta+270°$ in the previous notation) and solve the equilibrium and stability equations for the PM phase in which $\gamma=\delta$, we obtain :

$$B_x = (2B_E + B_A\sin^2\gamma)\sin\gamma$$

and $$B_z = (2B_E - B_A\cos^2\gamma)\cos\gamma \ .$$

This is a parameter representation of an ellipse which intersects the B_x axis at $\pm(2B_E+B_A)$ and the B_z axis at $\pm(2B_E-B_A)$. When B lies outside this ellipse the spins are in a PM state.

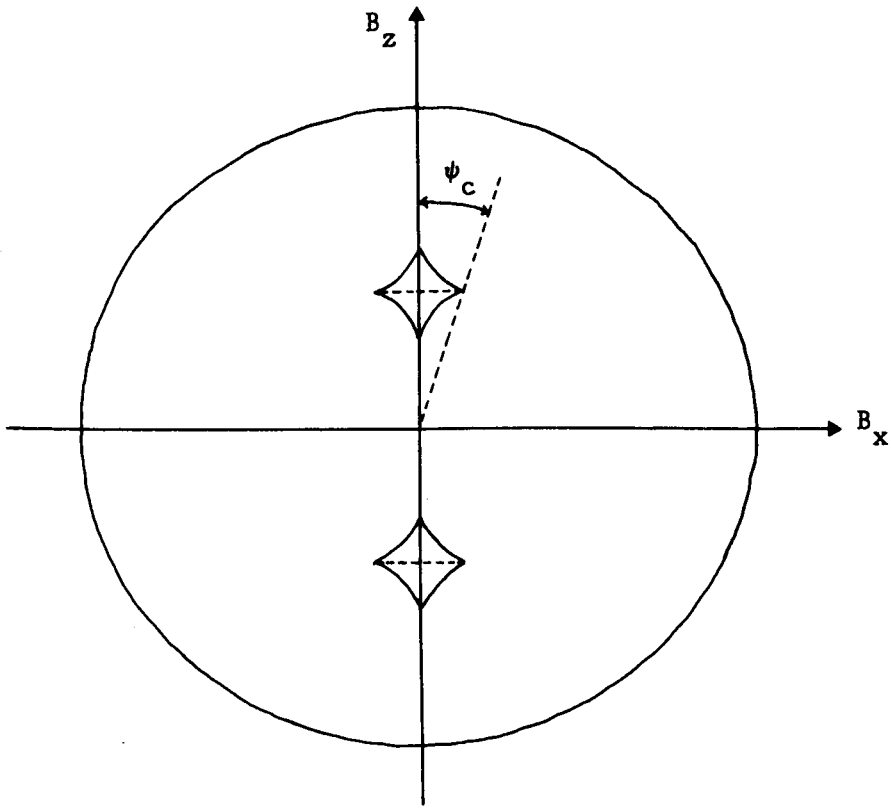

Figure 2.5 Schematic phase diagram of the uniaxial antiferromagnet at T=0. An ellipse marks the PM phase boundary and the 'star-shaped' regions contain two stable states (SF and AFM), as discussed in the text.

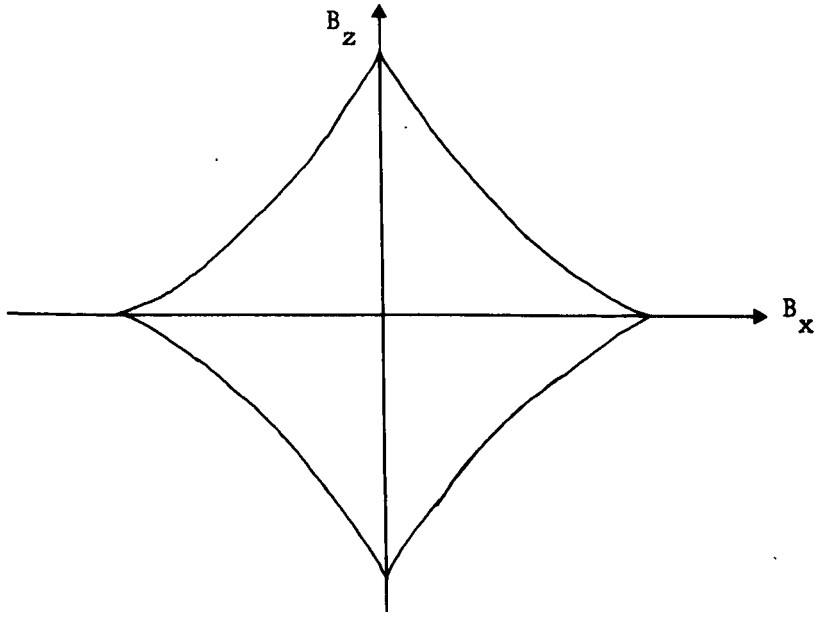

Figure 2.6 Schematic phase diagram of the uniaxial ferromagnet. Critical points on the B_x and B_z axes are at $\pm B_A$.

Within the PM phase boundary the spins are mostly in a non-symmetric rotated state. The exceptions are when B is parallel to the x axis giving a symmetric SF phase, or when B is parallel to the z axis giving the AFM and SF phases discussed in Section 2.2b(i). If B passes through the 'star-shaped' regions on the z-axis then a first-order transition takes place from an AFM-like state to a SF-like state. Within the star-shaped region there are two stable states for the spins to be in, while outside the star only one stable state is available.

The boundary curve of the star-shaped region is analogous to that found in the uniaxial ferromagnet (Landau and Lifshitz 1960), where

$$B_x^{2/3} + B_z^{2/3} = B_A^{2/3} .$$

This is shown in Figure 2.6. The situation in the uniaxial AFM is similar, with two star phases situated at $B_z = \pm B_{sf}$ where B_{sf} is the thermodynamic spin-flop field. The critical points B_1 and B_2 on the z axis are not exactly equidistant from B_{sf} (see Section 2.2b(i)), but to first order in B_A/B_E they lie at $B_{sf} \pm B_A B_{sf}/2B_E$. Similarly the critical points in the B_x direction are close to $\pm B_A B_{sf}/2B_E$ (Chepurnykh 1969).

We therefore may obtain an estimate of the critical angle of misalignment ψ_c from $\tan\psi_c \simeq B_A/2B_E$. Since $B_A \ll B_E$ this gives $\psi_c \simeq B_A/2B_E$ radians. For $\psi > \psi_c$ the applied field rotates the spins in a continuous manner until at $B \sim 2B_E$ a second-order transition occurs and the spins decouple from each other to become paramagnetic. For $\psi < \psi_c$ a first-order transition from an AFM-like phase to a SF-like phase takes place for $B \sim B_{sf}\cos\psi$.

2.2c Uniaxial Antiferromagnet at Finite Temperature

The temperature dependence of the critical magnetic fields of the uniaxial antiferromagnet have been studied by Thomas (1969a) and Blazey et al. (1971a,1971b), following an extensive study of the phase diagram of the uniaxial ferromagnet (Thomas 1969a, 1969b). The phase diagram at finite temperature was found to be qualitatively similar to that at zero temperature.

The analysis method employed was an extension of the method we have discussed in the previous sections, with the difference that the free energy $F=E-T\Sigma$ includes the entropy Σ of the system at temperature T. The energy E was again calculated from a Hamiltonian of the form of equation (2.2). Following the notation of Blazey et al. (1971b) we write the free energy of an antiferromagnet containing N spins of magnitude S per sublattice subject to an applied field B directed at an angle ψ to the easy axis as :

$$F = N\{S^2[2J\sigma_i\sigma_j\cos(\alpha-\beta) - K(\sigma_i^2\cos^2\alpha + \sigma_j^2\cos^2\beta) - g\mu SB[\sigma_i\cos(\alpha-\psi) + \sigma_j\cos(\beta-\psi)] - T[s(\sigma_i) + s(\sigma_j)]\} .$$

The angles α and β define the directions of the sublattice spins with respect to the easy axis, and are equivalent to the angles γ and δ used in section 2.2b(iii); J and K are the exchange and anisotropy constants; and σ_i and σ_j are the average values of the spins on each sublattice, normalised to one : $\sigma=\langle S\rangle/S$. (Note that here we regard the number of nearest neighbours, z, as implicitly defined in the value of J.) The terms $s(\sigma_i)$ and $s(\sigma_j)$ represent the entropy per spin on each sublattice, and are of the differential form :

$$ds(\sigma)/d\sigma = -B_s^{-1}(\sigma) ,$$

where $B_s^{-1}(\sigma)$ is the inverse Brillouin function for spin S. The Brillouin function is approximated by the Taylor series :

$$B_s(\sigma) \simeq [(S+1)/3S]\,\sigma - [(S+1)(2S^2+2S+1)/90S^3]\,\sigma^3 + \ldots ,$$

provided $\sigma \ll 1$.

As in the preceding sections, the equilibrium positions of the sublattice spins are found by putting the first derivatives of F with respect to the variables - in this case α, β, σ_i and σ_j - equal to zero. The stability conditions are then found using the second derivatives of F.

2.2c(i) Perfect Alignment

For the applied field perfectly aligned along the easy axis (ψ=0) the equilibrium equations yield the following results: In the AFM state (α=0, β=180°) the sublattice spins are :

$$\sigma_i = B_s\{(S^2/T)[2J\sigma_j + 2K\sigma_i + g\mu B/S]\} \qquad (2.8a)$$

and $$\sigma_j = B_s\{(S^2/T)[2J\sigma_i + 2K\sigma_j - g\mu B/S]\} \; ; \qquad (2.8b)$$

in the SF state ($\sigma_i=\sigma_j=\sigma$, $\alpha=-\beta=\phi$) :

$$\sigma = B_s\{2J\sigma S^2/T\} \qquad (2.9)$$

and $\cos\phi = g\mu B/[2S\sigma(2J-K)]$;

while in the PM state ($\sigma_i=\sigma_j=\sigma$, $\alpha=\beta=0$) :

$$\sigma = B_s\{(S^2/T)[-2J\sigma + 2K\sigma + g\mu B/S]\} \; .$$

The equilibrium state is stable as long as all the eigenvalues of the 4×4 matrix of the second derivatives of F with respect to α, β, σ_i and σ_j are positive. The eigenvector belonging to the first eigenvalue to become zero characterises the type of instability of that state. The uniaxial antiferromagnet becomes unstable with respect to the following deviations and restrictions (Blazey et al. 1971b) : Along the AFM-PM phase boundary $\delta\sigma_i=-\delta\sigma_j$, $\delta\alpha=\delta\beta=0$; along SF-PM $\delta\sigma_i=\delta\sigma_j=0$, $\delta\alpha=-\delta\beta$; along AFM-SF (moving from the AFM to SF phases) $\delta\sigma_i=\delta\sigma_j=0$, $|\delta\alpha\sigma_i|<|\delta\beta\sigma_j|$; and along SF-AFM (from SF to AFM) $\delta\sigma_i=-\delta\sigma_j$, $\delta\alpha=\delta\beta$.

The critical field at the SF-PM phase boundary is readily obtained from the stability criteria. The 4×4 ∇^2F matrix decomposes into two 2×2 matrices, and the first eigenvalue to become zero is given by $\lambda=\partial^2F/\partial\alpha^2-|\partial^2F/\partial\alpha\partial\beta|=0$. This yields for the critical field :

$$B_c(T) = [2B_E - B_A]\sigma(B_c,T) \ , \qquad (2.10)$$

where $B_E=2JS/g\mu$ and $B_A=2KS/g\mu$ are the exchange and anisotropy fields, and $\sigma(B_c,T)$ is the spin value for field B_c and temperature T as given by equation (2.9). It is therefore apparent that the SF-PM phase boundary is a Brillouin curve (see Figure 2.7). We may rewrite $\sigma(B_c,T)$ in (2.10) in terms of the zero-field spins $\sigma(0,T)$ obtained from (2.8) by utilising a reduced temperature T'. That is, $\sigma(B_c,T)=\sigma(0,T')$ for $T'=T_NT/T_3$, where $T_N=2S(S+1)(J+K)/3$ is defined as the 'Néel temperature' and $T_3=2S(S+1)J/3$ is the 'triple-point temperature' at which the AFM, SF and PM phases coexist.

The AFM-SF and AFM-PM phase boundaries are not simple functions of B and T and numerical calculations are therefore necessary. The results of such calculations (Blazey et al. 1971b) are shown in Figure 2.7. For B=0 the AFM state exists for $T<T_N$, above which the PM phase is stable. The thermodynamic spin-flop field $B_{sf}(T)$ increases as T increases, which may be qualitatively understood if one recalls that $B_{sf}=[2\mu_o\kappa/(\chi_\perp-\chi_\parallel)]^{\frac{1}{2}}$ as discussed in Chapter 1. $\chi_\perp$ is largely temperature independent but $\chi_\parallel$ increases as T increases, and therefore B_{sf} also increases. The hysteresis region between the SF→AFM and AFM→SF stability limits decreases as T increases, and is zero at $T=T_3$.

2.2c(ii) Imperfect Alignment

We saw in section 2.2b(iii) that at zero temperature there is a critical angle of misalignment ψ_c between the applied field and the easy axis such that a first-order spin-flop will occur only for $\psi\leq\psi_c$. Blazey et al. (1971b) studied the temperature dependence of ψ_c and found it to be approximately linear :

$$\psi_c(T) \simeq \psi_c(0).(T_3-T)/T_3 \ , \qquad (2.11)$$

with $\psi_c=0$ at the triple-point temperature T_3. Thus for small but finite misalignment $\psi<\psi_c(0)$ a first-order transition occurs only for temperatures $T<T_c$, where the critical temperature T_c is less than T_3.

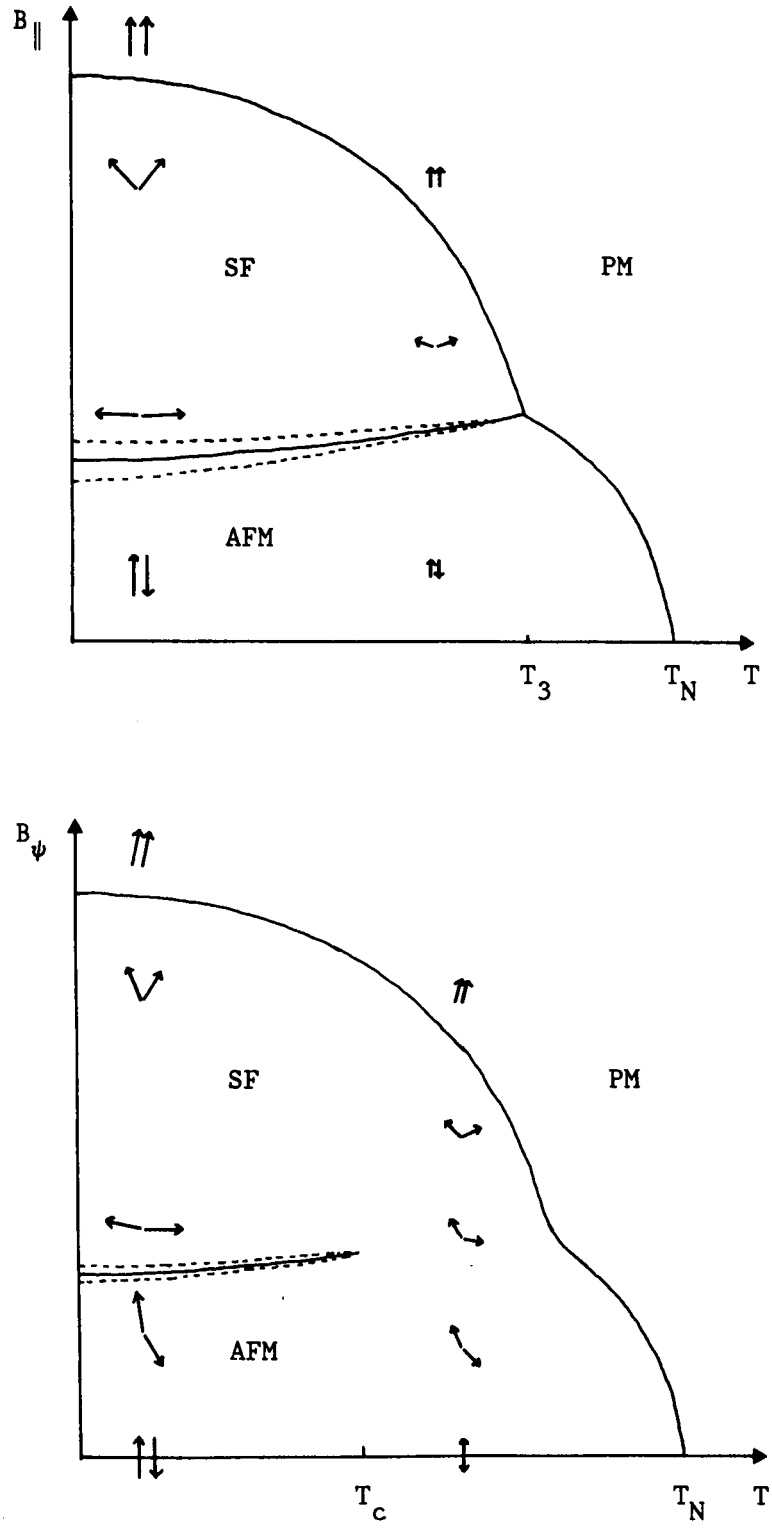

Figure 2.7 Schematic phase diagram of a uniaxial antiferromagnet subject to (a) a field $B_{\parallel}$ along the easy axis and (b) a field B_{ψ} at a small angle $\psi<\psi_c$ to the easy axis. Dotted lines denote the stability limits of the first-order SF→AFM and AFM→SF transitions. Pairs of arrows represent sublattice spin directions.

The corresponding phase diagram is shown in Figure 2.7b. At temperatures slightly exceeding T_c the transition from AFM-like to SF-like states is not first-order, but is a continuous spin rotation. However, the transition may take place over a narrow range of applied fields so that experimentally it is hard to distinguish from a first-order spin-flop. For large misalignment $\psi>\psi_c$ the first-order transition is avoided completely. When $\psi=90°$ the AFM state exists only when B=0, and the SF-PM phase boundary is the Brillouin curve :

$$B_c(T) = [2B_E + B_A]\ \sigma(0,T)\ , \qquad (2.12)$$

which is analogous to equation (2.10).

It is convenient to summarise the effects of misalignment and temperature on the phase diagram of the uniaxial antiferromagnet by drawing a three-dimensional 'contour map' of the phase boundaries (see Figure 2.8). In this diagram we treat $B_{\parallel}$, $B_{\perp}$ and T as the orthogonal coordinate axes, and for simplicity draw only one quadrant of the surface. The diagram is further simplified in the region of the AFM-SF boundary by drawing only the stability limits in the $B_{\perp}T$-plane. Figure 2.8 then allows us to regard equation (2.11) as defining a triangular 'shelf' of first-order transitions: i.e. if $B(\psi,T)$ passes through the shelf a first-order flop will occur. Equation (2.12) specifies the boundary curve in the $B_{\perp}T$-plane.

The phase diagram of Figure 2.8 has been well verified by experiment, such as the study of MnF_2 by King and Rohrer (1979). Figure 2.8 is known to also apply to the orthorhombic antiferromagnet provided $B_{\perp}$ lies in the direction of medium anisotropy (see later). Careful studies of the orthorhombic crystals $GdAlO_3$ (Blazey et al. 1971a,1971b, Rohrer 1975, and Rohrer and Gerber 1977) and $CsMnBr_3.2D_2O$ (Basten et al. 1980b) have compared favourably with the theoretical predictions.

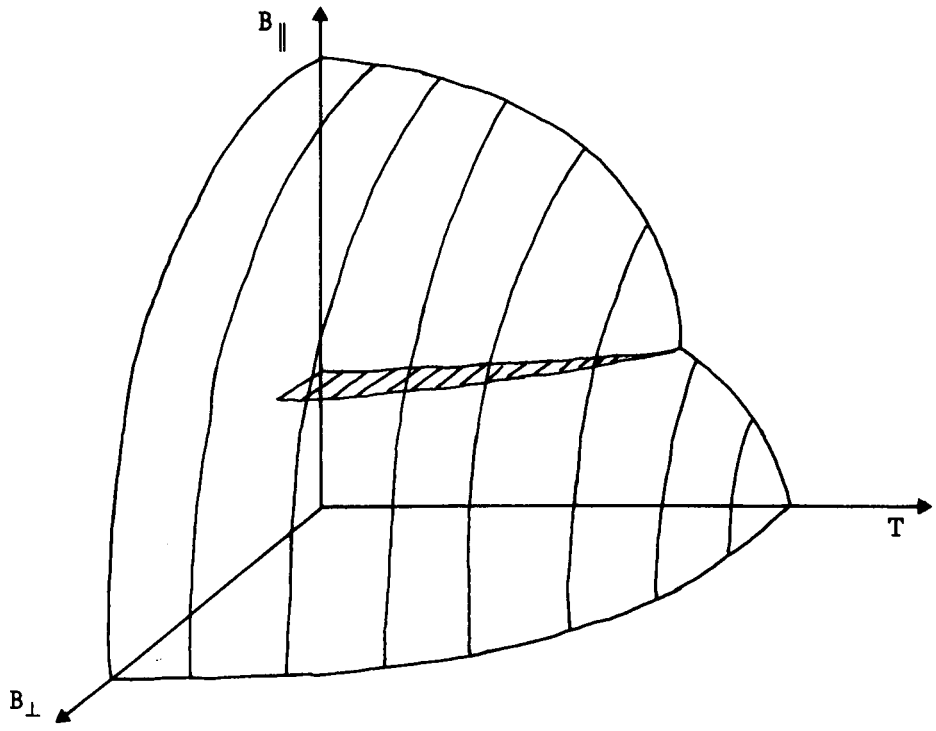

Figure 2.8 Schematic phase diagram of the uniaxial antiferromagnet, as discussed in the text.

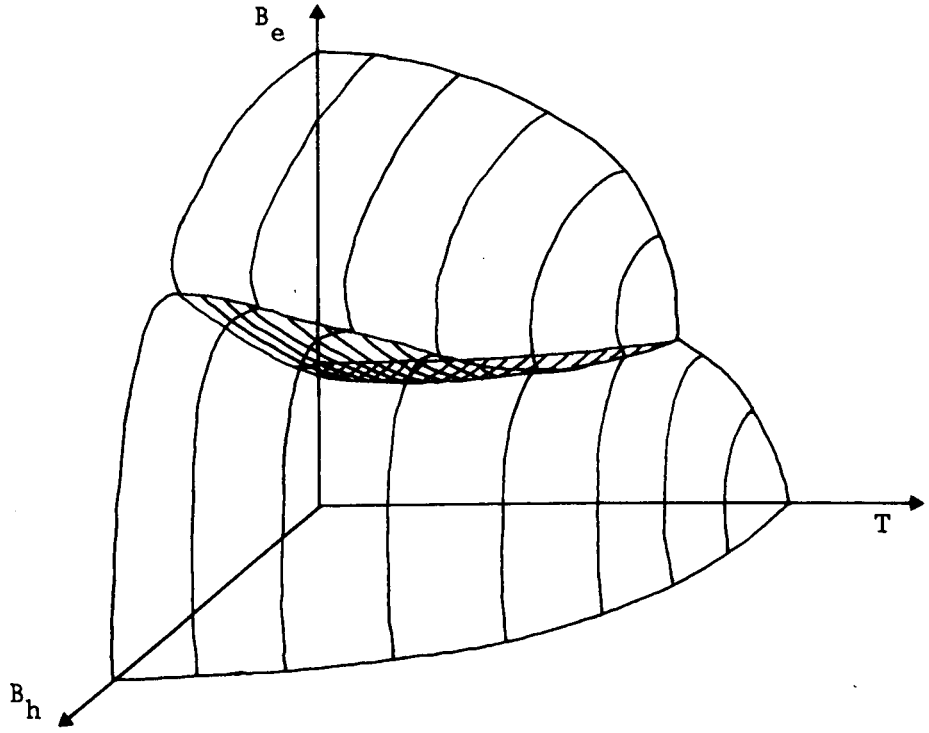

Figure 2.9 Schematic phase diagram of the orthorhombic antiferromagnet subject to an applied field in the easy-hard anisotropy plane, as discussed in the text.

2.2d Non-Uniaxial Anisotropy

Thus far we have considered the simplest form of anisotropic antiferromagnet, that with uniaxial anisotropy. However, departures from uniaxial anisotropy play an important role in determining the magnetic phase diagram of the system. We consider here two non-uniaxial types of anisotropy which are relevant to the present work : orthorhombic as in K_2FeF_5 and Rb_2FeF_5, and antisymmetric or 'Dzyaloshinsky' as in α-Fe_2O_3.

2.2d(i) Orthorhombic Anisotropy

Crystals with orthorhombic lattice symmetry often exhibit orthorhombic anisotropy. The anisotropy Hamiltonian may be written as:

$$H_{anis} = K_x\Sigma_i(S_{xi})^2 + K_y\Sigma_i(S_{yi})^2 + K_z\Sigma_i(S_{zi})^2 \ ,$$

where if for example $K_x>K_y>K_z>0$ the x axis is magnetically 'hard', the y axis 'medium' and the z axis 'easy'.

If the crystal is subject to an applied field in the easy-medium plane the spins remain in that plane and $S_{xi}=0$. The resultant phase diagram is then equivalent to that of the uniaxial antiferromagnet (Figure 2.8), with an effective anisotropy of K_z-K_y along the easy axis. The general case of an arbitrary applied field direction is more complicated. Although it is possible in principle to use the methods described in the preceding sections to compute the equilibrium spin directions, in practice the algebraic calculations rapidly become prohibitive. The preferred approach is therefore to make simplifying approximations about the system and to consider only the gross features of the phase diagram. Such methods have been employed by Gorter and Haantjes (1952), Nagamiya (1954) and Nagamiya et al. (1955).

One approximation is to assume that the sublattice spins remain antiparallel to each other as the field is applied (Nagamiya 1954).

The anisotropy energy (relative to K_z) is then given by:

$$E_{anis} = K_x[\Sigma_i(S_{xi})^2 + \Sigma_j(S_{xj})^2] + K_y[\Sigma_i(S_{yi})^2 + \Sigma_j(S_{yj})^2] ,$$
$$= \tfrac{1}{2}N\kappa_1(\alpha_i^2 + \alpha_j^2) + \tfrac{1}{2}N\kappa_2(\beta_i^2 + \beta_j^2) ,$$
$$\simeq N\kappa_1\alpha^2 + N\kappa_2\beta^2 ,$$

where $\kappa_{1,2} = 2S^2K_{x,y}$ and the spins on sublattices i and j are written in terms of direction cosines, e.g. $S_i = S(\alpha_i,\beta_i,\gamma_i)$. It is convenient to write the exchange and field energies in terms of the susceptibilities parallel to and perpendicular to the AFM axis of the spins. Taking N=1 for convenience, the total free energy is then:

$$F = -\tfrac{1}{2}(\chi_\parallel/\mu_o)B_\parallel^2 - \tfrac{1}{2}(\chi_\perp/\mu_o)B_\perp^2 + \kappa_1\alpha^2 + \kappa_2\beta^2 ,$$
$$= -\tfrac{1}{2}(\chi_\parallel/\mu_o)B^2(\alpha\alpha_B+\beta\beta_B+\gamma\gamma_B)^2 - \tfrac{1}{2}(\chi_\perp/\mu_o)B^2(1-(\alpha\alpha_B+\beta\beta_B+\gamma\gamma_B)^2)$$
$$+ \kappa_1\alpha^2 + \kappa_2\beta^2 ,$$

where $B = B(\alpha_B,\beta_B,\gamma_B)$ is the applied field and μ_o is the permeability of free space. To find the equilibrium spin directions we look at the first and second derivatives of F with respect to α, β and γ. The eigenvalues of the 3×3 ∇^2F matrix are given by the secular equation:

$$\lambda^3 - [1+k_1+k_2]\lambda^2 + [(k_1+k_2)\gamma_B^2+k_1\beta_B^2+k_2\alpha_B^2+k_1k_2]\lambda - k_1k_2\gamma_B^2 = 0$$

where $k_{1,2} = 2\mu_o\kappa_{1,2}/[(\chi_\perp-\chi_\parallel)B^2]$. The smallest eigenvalue corresponds to the stable state since it represents the smallest value of the free energy.

When $B_\perp$ lies in the direction of hard anisotropy ($\underline{B}$ in the xz-plane) $\beta_B=0$ and the secular equation yields:

$$\lambda_1 = k_2 , \quad \lambda_\pm = \tfrac{1}{2}\{(1+k_1) \pm [(1+k_1)^2-4k_1\gamma_B^2]^{\frac{1}{2}}\} .$$

A transition between two stable states occurs if $\lambda_-=\lambda_1$, for which $k_1\gamma_B^2=k_2(1+k_1-k_2)$. Writing $B_x=B\alpha_B$ and $B_z=B\gamma_B$ this implies that:

$$B_z^2/2\kappa_2 - B_x^2/[2(\kappa_2-\kappa_1)] = \mu_o/(\chi_\perp-\chi_\parallel) , \qquad (2.13)$$

which describes a hyperbola in the B_xB_z plane that cuts the B_z axis at:

$$B_z = [2\mu_o\kappa_2/(\chi_\perp-\chi_\parallel)]^{\frac{1}{2}} . \qquad (2.14)$$

The perpendicular susceptibility is given to a fair approximation by $\chi_\perp \simeq 2g\mu_o \mu S/(2B_E - B_A)$ where $B_E = 2JS/g\mu$ and $B_A = 2KS/g\mu$ (Morrish 1965), so that by taking $K = \kappa_2/2S^2$ equation (2.14) may be rewritten as:

$$B_{sf} = \{B_A(2B_E - B_A)/[1 - (\chi_\parallel/\chi_\perp)]\}^{\frac{1}{2}} , \qquad (2.15)$$

which is the thermodynamic spin-flop field (previously derived in section 2.2b(i) for zero temperature, $\chi_\parallel = 0$).

The region of the $B_x B_z$-plane which lies above the hyperbola (considering only the $B_z \geq 0$ half of the plane) corresponds to the $\lambda_1 = k_2$ eigenvalue. The corresponding eigenvector is $(\alpha,\beta,\gamma) = (0,1,0)$, indicating that the spins lie along the medium anisotropy y axis. Below the hyperbola the spins lie in the xz-plane. Thus (2.13) defines a critical line of first-order transitions between AFM-like and SF-like states.

The complete three-dimensional $(B_\parallel, B_\perp, T)$ phase diagram, as depicted by Rohrer et al. (1977), is shown in Figure 2.9. The spin-flop surface, which in the uniaxial case was a narrow triangular shelf, now extends to the PM phase boundary. The critical angle of misalignment ψ_c is much larger than in the uniaxial case, with $\tan\psi_c \simeq [(K_1 - K_2)/K_2]^{\frac{1}{2}}$.

It is important to note that Figure 2.9 is strictly only relevant when $B_\perp$ lies along the hard anisotropy axis. In the approximate analysis given above it appears that a first-order transition is possible only if B lies in the easy-hard plane. We might expect, on the basis of our more detailed analyses in sections 2.2b and 2.2c, that the requirement would be that B should lie within $\psi_c \simeq B_A/2B_E$ of the easy-hard plane. However, recent experimental results have cast some doubt on these predictions. Rohrer and Gerber (1978) studied the change in the phase diagram of $GdAlO_3$ as $B_\perp$ was rotated in the medium-hard plane, at temperatures very close to the triple point T_3. They observed appreciable broadening of the spin-flop shelf for $\psi' \sim 45°$ between $B_\perp$ and the hard axis, and at $\psi' \simeq 10°$ the shelf was about five times its initial

($\psi'=90°$) width. Although Rohrer and Thomas stated that the situation was by no means clear, their result may indicate that the effect of orthorhombic anisotropy on the nature of the spin-flop transition might be more pronounced than theoretically predicted.

2.2d(ii) Dzyaloshinsky Anisotropy

The second type of non-uniaxial anisotropy that we shall consider is that which occurs in hematite (α-Fe_2O_3) as a result of the so-called 'Dzyaloshinsky exchange' interaction. The magnetic properties of hematite have been studied extensively and have been reviewed by several authors, including Jacobs et al. (1971) and Creer et al. (1975). Hematite is essentially antiferromagnetic below its Neel temperature $T_N \simeq 960K$, but undergoes a temperature driven spin-flop transition known as the 'Morin transition' at $T_M \simeq 260K$. Below T_M the ferric spins are antiferromagnetically aligned along the crystallographic [111] (trigonal) axis. For $T>T_M$ the spins lie in the basal (111) plane but are not precisely antiparallel, being slightly canted to produce a weak ferromagnetic moment in the basal plane.

The microscopic origins of the weak ferromagnetism observed for $T_M<T<T_N$ were the subject of some controversy over many years, and will be discussed further in Chapter 6. At this point, however, it is sufficient to utilise the phenomenological description of Dzyaloshinsky (1958) and Moriya (1960). The exchange interaction between neighbouring spins is taken to include an anisotropic term :

$$H_{Dz} = - \underset{\sim}{D} \cdot \underset{\sim}{S}_1 \times \underset{\sim}{S}_2 \ , \qquad (2.16)$$

where $\underset{\sim}{D}$ is a constant vector parallel to the trigonal axis. It is clear that this coupling acts to cant the spins in the basal plane since the coupling energy is minimised when the two spins are perpendicular to each other. The exchange of (2.16) differs from the exchange

Hamiltonians discussed in section 2.2a in that it is 'antisymmetric', i.e. interchanging the two spins changes the sign of the term.

For temperatures below T_M a spin-flop transition takes place if a magnetic field B is applied along the trigonal axis. The Hamiltonian describing the system may be written as :

$$H = 2J\Sigma_{ij}\underset{\sim}{S}_i\cdot\underset{\sim}{S}_j - K[\Sigma_i(S_{zi})^2 + \Sigma_j(S_{zj})^2] - \Sigma_{ij}\underset{\sim}{D}\cdot\underset{\sim}{S}_i\times\underset{\sim}{S}_j$$
$$- g\mu\underset{\sim}{B}\cdot(\Sigma_i\underset{\sim}{S}_i+\Sigma_j\underset{\sim}{S}_j) \ , \qquad (2.17)$$

which is a combination of equations (2.2) and (2.16). We identify the z axis with the trigonal axis, so that $\underset{\sim}{D}=(0,0,D)$ and $\underset{\sim}{B}=(0,0,B)$. As in section 2.2b(ii) we obtain the thermodynamic spin-flop field $B_{\|c}$ by equating the ground state energies of the AFM and SF phases. The Dzyaloshinsky exchange energy is zero in the AFM state since $\underset{\sim}{S}_1\times\underset{\sim}{S}_2$ is then perpendicular to $\underset{\sim}{D}$, and $E_{afm}=-NSg\mu(B_E+B_A)$ as in the uniaxial case. However the SF state is affected by H_{Dz}, and might be more appropriately referred to as the weakly ferromagnetic (WFM) state. At zero temperature the energy of the WFM state is :

$$E = -NSg\mu[B_E(\sin^2\theta\cos2\phi-\cos^2\theta) + B_A\cos^2\theta$$
$$+ B_D\sin^2\theta\sin2\phi + 2B\cos\theta] \ , \qquad (2.18)$$

where $B_E=2JS/g\mu$, $B_A=2KS/g\mu$ and $B_D=DS/g\mu$ are the isotropic exchange, uniaxial anisotropy and Dzyaloshinsky anisotropy fields, and θ and ϕ are the polar angles of the spins as shown in Figure 2.10. The equilibrium conditions $\partial E/\partial\theta=\partial E/\partial\phi=0$ give the ground state energy :

$$E_{wfm} = -NSg\mu[B_E' + B^2/(B_E+B_E'-B_A)] \ , \qquad (2.19)$$

where $B_E'=[B_E^2+B_D^2]^{\frac{1}{2}}$. The spin-flop field is then found by putting $E_{afm}=E_{wfm}$, giving :

$$B_{\|c} = [B_A(2B_E'-B_A)-B_D^2]^{\frac{1}{2}} \ ,$$

which in the approximation $B_E>>B_D>>B_A$ reduces to :

$$B_{\|c} \simeq [2B_EB_A-B_D^2]^{\frac{1}{2}} \ . \qquad (2.20)$$

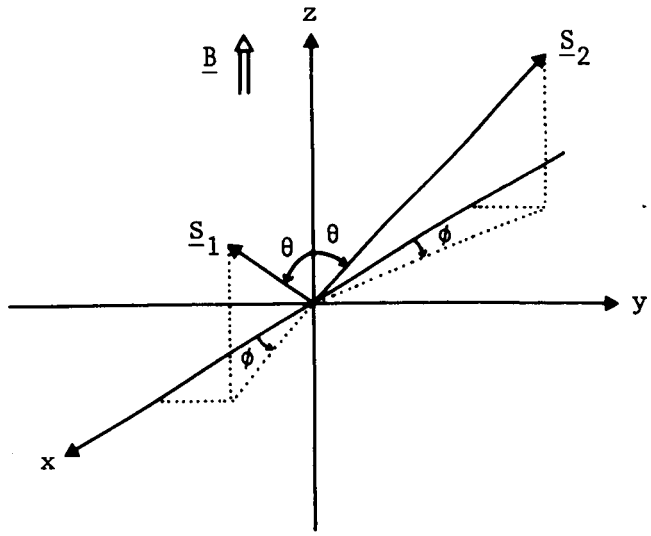

Figure 2.10 Sublattice spin directions in the WFM phase of α-Fe_2O_3 subject to an applied field parallel to the easy axis.

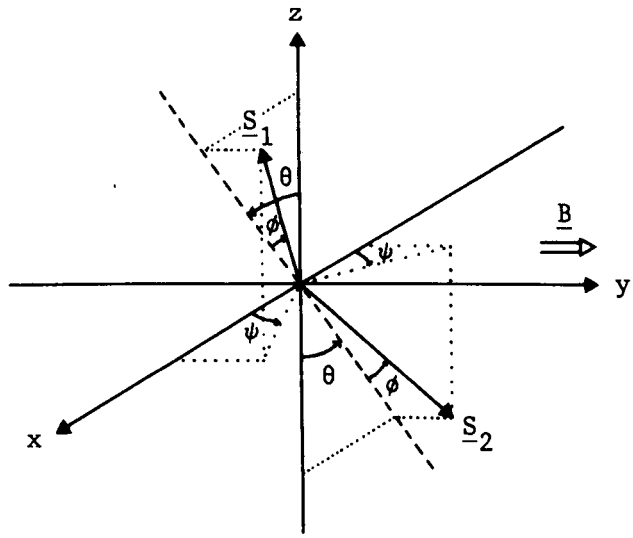

Figure 2.11 Sublattice spin directions in α-Fe_2O_3 subject to an applied field perpendicular to the easy axis.

Ozhogin and Shapiro (1968) calculated that in hematite (at T=77K) $B_E \simeq 450T$, $B_D \simeq 3T$ and $B_A \simeq 0.05T$, so the approximation of (2.20) looks likely to be valid.

If a field B is applied in a direction perpendicular to the easy axis the spins move towards the field direction. A 90° 'screw' rotation accompanies this motion since the Dzyaloshinsky interaction favours a WFM spin arrangement to be in the basal plane. Using a definition of the sublattice spin directions in terms of a rotation angle θ and a canting angle ϕ as shown in Figure 2.11, the free energy of the system is given by :

$$E = -NSg\mu[B_E\cos 2\phi + B_A\cos^2\theta\cos^2\phi + B_D\sin\theta\sin 2\phi + 2B\sin\phi] \ ,$$

where B is directed along the y axis. For applied fields $B \ll B_E$ the equilibrium equations yield :

$$\phi \simeq B_A B/(2B_E B_A - B_D^2) \quad \text{and} \quad \sin\theta \simeq B_D B/(2B_E B_A - B_D^2) \quad \text{for} \quad B \leq B_{\perp c} \ ,$$

and $\phi \simeq (B+B_D)/2B_E$ and $\sin\theta \simeq 1$ for $B \geq B_{\perp c}$.

The critical field $B_{\perp c}$ marks the second-order phase transition between the AFM-like and the WFM-like state (the WFM-like state is best defined as that in which the AFM axis of the spins lies in the basal plane and $\theta = 90°$), and is given by :

$$B_{\perp c} = (2B_E B_A - B_D^2)/B_D \ , \qquad (2.21a)$$

$$= B_{\parallel c}^2/B_D \ . \qquad (2.21b)$$

In the course of the 'screw' rotation the spins move in planes which intercept the basal plane at a constant angle $\psi \simeq B_A/B_D$ to the x axis. These results are in accord with those derived by Cinader and Shtrikman (1966), Cinader (1967) and Ozhogin and Shapiro (1968).

The case of arbitrary alignment of the applied field was considered by Ozhogin and Shapiro (1968). They found that the phase boundary between the AFM-like and WFM-like sates could be described by :

$$B_z^2 + [B_y - (B_A B_E - B_D^2)/B_D]^2 = (B_A B_E/B_D)^2 \ . \qquad (2.22)$$

This curve is a circle which cuts the z axis at $\pm B_{\parallel c}$ and the y axis at $+B_{\perp c}$ and $-B_D$. By symmetry the phase diagram in the B_yB_z-plane has the form shown in Figure 2.12, with the mirror image of (2.22) in the z axis included. The elliptical PM phase boundary (of radius $B \simeq 2B_E$) is also shown in Figure 2.12.

The temperature dependence of the phase diagram has also been considered by Ozhogin and Shapiro (1968). They identified the anisotropy field B_A as having a larger temperature variation than B_E or B_D, and deduced the phase diagram that is depicted in Figure 2.13 in the three dimensions $B_\parallel$, $B_\perp$ and T. The spin-flop transition fields between the AFM-like and WFM-like (AFM axis in basal plane) phases go to zero at the Morin temperature, and above the Neel temperature only the PM phase is present.

On the basis of the theory outlined above the spin-flop transition in a Dzyaloshinsky antiferromagnet is of first-order only if B is parallel to the easy axis. For any other orientation of B a second-order transition takes place. However, Kaczer and Shalnikova (1965) and Flanders (1969) observed the spin-flop at temperatures just below T_M and with B perpendicular to the easy axis, and found it to be abrupt. Several other authors found direct contradictions with the theoretical predictions. Voskanyan et al. (1968) and Foner and Shapira (1969) saw an anomaly in the perpendicular susceptibility near $B_{\perp c}$, and both Ozhogin and Shapiro (1967,1968) and Jacobs et al. (1971) noted that the value of $B_\perp$ at 77K predicted by $B_{\parallel c}{}^2/B_D$ was almost 30% higher than was observed. These discrepancies led to the development of an improved theory in which higher order anisotropy terms were included by Levitin and Shchurov (1968) and Ozhogin and Shapiro (1969). In the earlier theory described above the anisotropy energy was taken to be :

$$E_{anis} = -K[\Sigma_i(S_{zi})^2+\Sigma_j(S_{zj})^2] = -NS^2K(\cos^2\alpha_1+\cos^2\alpha_2) \ ,$$

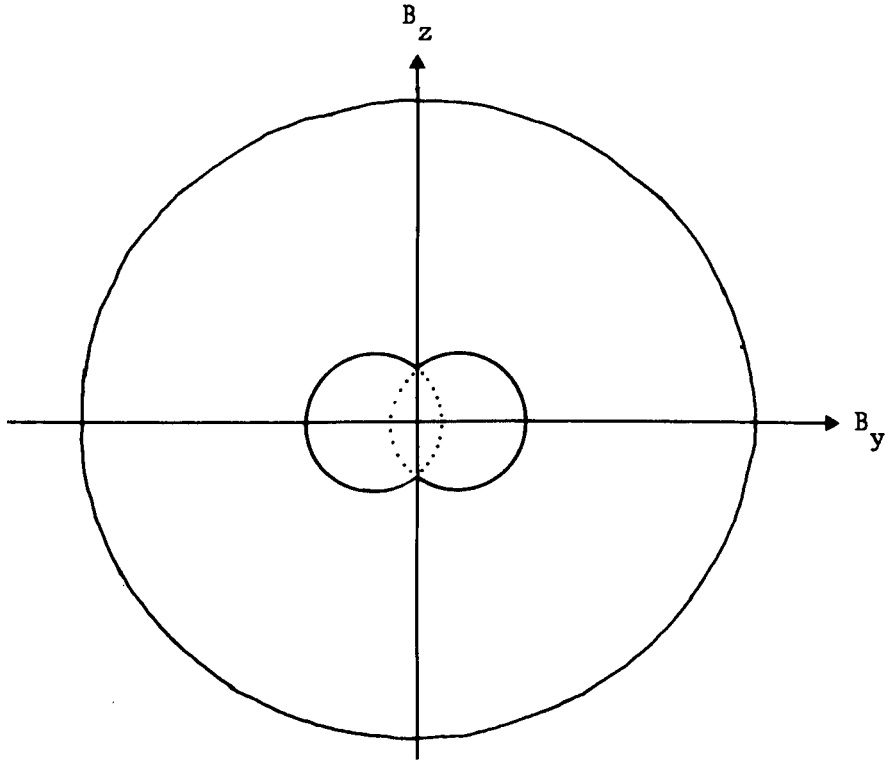

Figure 2.12 Schematic phase diagram of a 'Dzyaloshinsky' antiferromagnet at T=0, as discussed in the text. The dotted curve is an unphysical continuation of equation (2.22).

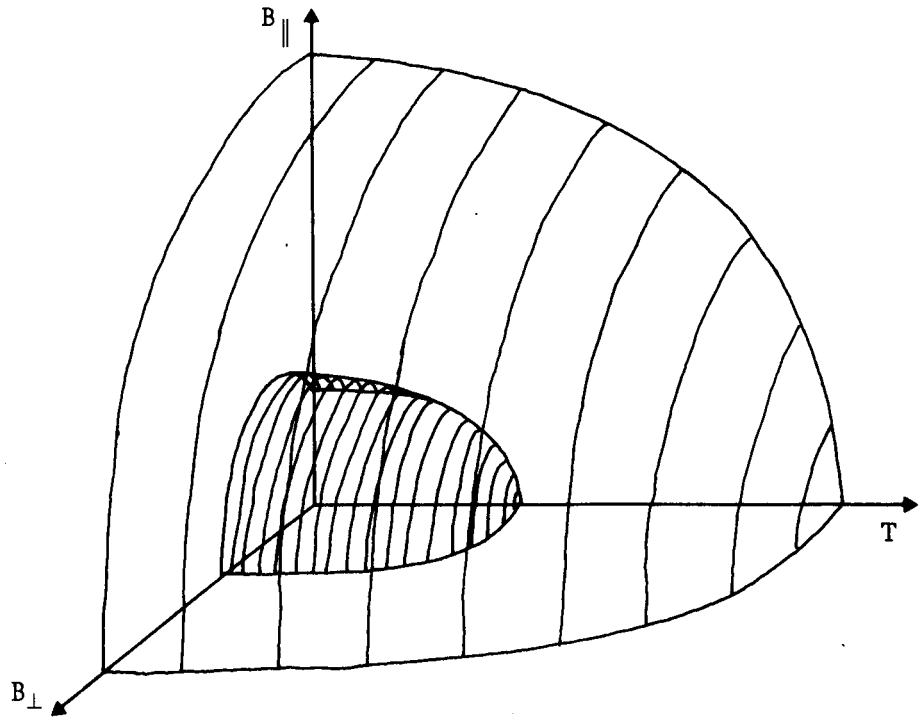

Figure 2.13 Schematic phase diagram of a 'Dzyaloshinsky' antiferromagnet (such as α-Fe_2O_3), as discussed in the text.

where α_1 and α_2 are the angles between the sublattice spins and the easy axis. In the improved theory the next term in the series expansion of the anisotropy is included :

$$E_{anis} = NS^2[-K(\cos^2\alpha_1+\cos^2\alpha_2) - K'(\cos^4\alpha_1+\cos^4\alpha_2)] ,$$

where $K' \leq K$. The addition of this term to the free energy of equation (2.17) provides the desired modifications to the predicted magnitude and character of the spin-flop transitions.

For a field applied parallel to the easy axis the second anisotropy field $B_A'=2K'S/g\mu$ is added to B_A in the ground state energy of both the AFM phase ($\alpha_1=0,\alpha_2=180°$) and the WFM phase ($\alpha_1=\alpha_2\approx 90°$). Thus B_A+B_A' replaces B_A in E_{afm} and E_{wfm}, and the critical field of equation (2.20) becomes :

$$B_{\|c}' = [2B_E(B_A+B_A')-B_D^2]^{\frac{1}{2}} .$$

When the applied field is perpendicular to the easy axis the equilibrium equations yield :

$$-4B_EB_A'\sin^3\theta + [2B_EB_A+4B_EB_A'-B_D^2]\sin\theta - B_DB = 0$$

and $$\phi \approx (B_A-2B_A'\cos^2\theta)\sin\theta/B_D$$

for $B \leq B_{\perp c}'$, where θ and ϕ are the angles defined previously in Figure 2.11. When $\theta=90°$ the critical field $B_{\perp c}'$ is the same as given in (2.21a), but now the parallel and perpendicular critical fields are related by :

$$B_{\perp c}' = [(B_{\|c}')^2-2B_EB_A']/B_D .$$

This reduction in the value of $B_{\perp c}$ predicted from a measurement of $B_{\|c}$ accounts for the overestimation that (2.21b) had given (Jacobs et al. 1971). It can also be shown (Ozhogin and Shapiro 1969, Jacobs et al. 1971) that the magnitude of B_A' in hematite is sufficient to change the character of the $B_{\perp c}$ transition to one of first-order. A discontinuous transition is then predicted for all $T<T_M$, although at temperatures below about 150K the transition is said to be 'nearly' of second-order. This result is in accord with the experimental observa-

tions of Kaczer and Shalnikova (1965) and Flanders (1969). It therefore appears that in α-Fe_2O_3 the spin-flop phase transition is of first order for any direction of applied field, for all $T<T_M$.

2.2e Demagnetisation Effects

To conclude this review of the mean-field theory of the spin-flop phase transition, let us note that some of the results derived above may depend on the morphology of the specimen being studied. To understand this 'demagnetisation effect' it is useful to first recall the distinction between the magnetic field quantities $\underset{\sim}{B}$ and $\underset{\sim}{H}$.

Thus far we have described magnetic field in terms of the 'flux density' (or 'induction') $\underset{\sim}{B}$. We may however define a second field quantity $\underset{\sim}{H}=\underset{\sim}{B}/\mu$ where μ is the 'permeability' of the medium in which the field occurs. (Note that the symbol μ was defined differently in previous sections, where it was the symbol for the Bohr magneton.) $\underset{\sim}{H}$ is called the magnetic 'intensity' or 'force', and does not depend on the medium. That is, $\underset{\sim}{H}$ may be regarded as the cause or 'force' which gives rise to a field of flux density $\underset{\sim}{B}=\mu\underset{\sim}{H}$ in the material. The permeability of the material may be written :

$$\mu = \mu_o(1 + \chi) ,$$

where $\mu_o=4\pi\times10^{-7}$ $WbA^{-1}m^{-1}$ is the permeability of free space and χ is the magnetic susceptibility. Furthermore, χ defines the relation between magnetic field and the magnetisation $\underset{\sim}{M}$ (magnetic moment per unit volume) :

$$\underset{\sim}{M} = \chi \underset{\sim}{H} = (\chi/\mu) \underset{\sim}{B} .$$

Bringing these definitions together yields :

$$\underset{\sim}{B} = \mu_o(\underset{\sim}{H} + \underset{\sim}{M}) , \qquad (2.23)$$

which is a well known result that is independent of the specimen morphology.

2.2e(i) The Demagnetising Field

The phenomenon of 'demagnetisation' arises when a material medium of finite size is placed in a magnetic field of intensity $\underset{\sim}{H}_o$ due to external sources. The field intensity $\underset{\sim}{H}$ within the medium is found to differ from the applied field $\underset{\sim}{H}_o$, with :

$$\underset{\sim}{H} = \underset{\sim}{H}_o + \underset{\sim}{H}_{dm} \ . \qquad (2.24)$$

$\underset{\sim}{H}_{dm}$ is due to the magnetisation present in the sample (both induced and/or inherent) and is called the 'demagnetising field' because it tends to oppose $\underset{\sim}{H}_o$. This effect has been discussed in numerous texts, including Morrish (1965) and Reitz and Milford (1969), while Kittel (1976) describes the analogous electrical effect of depolarisation. If the sample morphology is that of an ellipsoid of revolution (e.g. a sphere, cylinder or disc) $\underset{\sim}{H}_{dm}$ is proportional to the (uniform) magnetisation in the material. It is then commonly written :

$$\underset{\sim}{H}_{dm} = - N \underset{\sim}{M} \ ,$$

where N is the 'demagnetisation factor', although it is possibly more appropriate to define :

$$H_{dmx} = -N_x M_x \ , \quad H_{dmy} = -N_y M_y \ , \quad H_{dmz} = -N_z M_z \ ,$$

where x,y,z are the principal axes of the ellipsoid. The demagnetisation factors are positive and satisfy $N_x+N_y+N_z=1$ (in S.I. units). The values of N depend on the ratios of the ellipsoid principal axes. In the limiting cases of a sphere, cylinder or disc the factors have the values shown in Table 2.1.

Table 2.1 Demagnetisation factors of some ellipsoids of revolution.

Shape	Axis	N
Sphere	any	1/3
Thin slab (disc)	normal	1
	in plane	0
Long circular cylinder	longitudinal	0
	transverse	1/2

In the spin-flop transition we are concerned with the value of the 'local' magnetic field acting on the spin. This local field is significantly different from the macroscopic internal field H of equation (2.23), and may be written :

$$\underset{\sim}{H}_{local} = \underset{\sim}{H} + \underset{\sim}{H}_2 + \underset{\sim}{H}_3 \ ,$$

where $\underset{\sim}{H}_2+\underset{\sim}{H}_3$ is the field due to all the magnetic dipoles (with the exception of the dipole at the site being considered) in the material. The standard method of summing these dipole fields (Kittel 1976) is to first sum individually over a moderate number of neighbouring atoms inside an imagined sphere concentric with the reference atom. This defines the field :

$$\underset{\sim}{H}_3 = \Sigma_i[3(\underset{\sim}{m}_i \cdot \underset{\sim}{r}_i)\underset{\sim}{r}_i/r_i^5 - \underset{\sim}{m}_i/r_i^3] \ ,$$

where r_i is the distance of the i^{th} dipole (of moment m_i) from the reference point. In crystal lattices with cubic symmetry $H_3=0$, while in non-cubic lattices it is usually small and often neglected. The field $\underset{\sim}{H}_2$ arises from the density of magnetic 'poles' on the surface of the imagined spherical cavity, and is known as the 'Lorentz cavity field'. It is in effect a demagnetisation field whose direction is opposite to that which would accompany a solid sphere in an applied field. That is, $\underset{\sim}{H}_2 = + \underset{\sim}{M}/3$, where the factor 1/3 is the demagnetisation factor of a sphere. Combining these results we see that the local field intensity at a lattice site in a cubic crystal is :

$$\underset{\sim}{H}_{local} = \underset{\sim}{H}_o - N\underset{\sim}{M} + \underset{\sim}{M}/3 \ . \qquad (2.25)$$

This equation may also be written in terms of the local magnetic flux density $\underset{\sim}{B}_{local}$ by recalling that the distinction between $\underset{\sim}{B}$ and $\underset{\sim}{H}$ as defined by (2.23) is in essence a macroscopic formulation. From the microscopic viewpoint we treat a magnetic medium as a system of magnetic dipoles in vacuum, so that $\underset{\sim}{B}_{local} = \mu_o \underset{\sim}{H}_{local}$ and the distinction between $\underset{\sim}{B}$ and $\underset{\sim}{H}$ largely disappears. Thus (2.25) is equivalent to :

$$\underset{\sim}{B}_{local} = \underset{\sim}{B}_o - \mu_o N \underset{\sim}{M} + \mu_o \underset{\sim}{M}/3 \ , \qquad (2.26)$$

where $\underset{\sim}{B}_o = \mu_o \underset{\sim}{H}_o$ since the applied field is defined in the free space outside the sample.

2.2e(ii) Influence on the Spin-Flop

Let us now consider the effect of the specimen morphology on the spin-flop transition. Blazey et al. (1971b) pointed out that demagnetisation could affect the critical misalignment angle ψ_c in the uniaxial antiferromagnet. Their argument is illustrated as follows. Consider a long cylindrical sample whose easy anisotropy axis is parallel to the cylinder's longitudinal axis, and which is subject to an applied field that is slightly misaligned ($\psi<\psi_c$) with the easy axis. At first sight demagnetising effects might be thought negligible since in both the AFM and SF states the magnetisation direction is close to the cylinder axis, and since along that axis the demagnetisation factor is zero. However, in the course of the transition from the AFM to SF states the sublattice spins tilt away from the easy axis (see Figure 2.4b) and produce a component of magnetisation perpendicular to the cylinder axis. This results in a demagnetising field directed towards the cylinder axis which exerts a torque on the spins and inhibits their motion away from the easy axis. The instability field (B_1 in Figure 2.4b) is therefore pushed to a higher value. Similarly, the instability field for the SF → AFM transition (B_2 in Figure 2.4b) is reduced by the demagnetisation. Thus the hysteresis region B_1-B_2 of the transition is larger than expected, although the thermodynamic spin-flop field B_{sf} is unchanged. Another consequence of the demagnetisation in this case is that the critical angle ψ_c is increased so that first-order transitions will occur for larger misalignment angles than otherwise predicted. Experimentally verified calculations by Blazey et al. (1971b) for $GdAlO_3$ have shown that ψ_c is nearly tripled in the case of a cylinder as outlined above. The effect is not so pronounced

for other specimen morphologies, and is practically absent in a disc with easy axis and applied field normal to its plane.

Another possible demagnetisation effect, proposed by King and Paquette (1973), is the existence of an intermediate state between the AFM and SF states. This state consists of domains of AFM and SF material, and if present has a lower free energy than either of the 'pure' AFM or SF states. The method of King and Paquette is to consider a specimen of ellipsoidal shape which is placed in an external field of intensity H_o parallel to the easy anisotropy axis. A domain state is envisaged in which a fraction f of the sample is contained in narrow 'slabs' of SF material. Assuming that the domains are uniformly distributed, the macroscopic internal field H within the sample will be uniform and given by $\underset{\sim}{H} = \underset{\sim}{H}_o - N_z\underset{\sim}{M}$, where N_z is the overall demagnetisation factor of the sample in the direction of the applied field. In a low temperature approximation we regard the magnetic susceptibility along the AFM axis of the spins as being negligible so that $\chi_{\parallel} \simeq 0$, and the susceptibility of the sample is taken to be $\chi \simeq \chi_{\perp}$. Hence the magnetisation present in the sample arises only in the SF domains and $M = f\chi_{\perp}H$. The internal field may therefore be written as :

$$\underset{\sim}{H} = \underset{\sim}{H}_o/(1 + fN_z\chi_{\perp}) \quad : \qquad (2.27)$$

It is seen in this equation that the first SF domain appears when $H=H_o=H_{sf}$ and $f=0$. As H_o is increased the value of H within the sample is screened to the value H_{sf} by the formation of domains. When $f=1$ the last AFM region disappears and since $H=H_{sf}$ the applied field is $H_o=H_{sf}(1+N_z\chi_{\perp})$. Thus it is apparent that the extent of the domain region is :

$$\Delta H_o = N_z\chi_{\perp}H_{sf} \quad , \qquad (2.28)$$

and that the intermediate state is most easily observed in disc-shaped samples ($N_z=1$), while being completely absent in cylindrical specimens. King and Paquette (1973) report very good agreement between

(2.28) and the observed width of the spin-flop transition in MnF_2. However, in both $CoBr_2.6H_2O$ (Basten et al. 1980a) and K_2MnF_4 (de Jongh et al. 1982) domain states were observed over a larger range of applied fields than (2.28) predicted, and additional effects (such as solitons) were called upon to explain the results. It therefore appears that although experimental studies to date have not been conclusive, demagnetisation effects may in some cases be readily apparent in the mechanism of the spin-flop phase transition.

2.3 SPIN-WAVE THEORY

The spin-wave theory of the spin-flop transition has been treated by a number of authors, including Kanamori and Yosida (1955), Kittel (1963), Jacobs and Silverstein (1964), Keffer (1966) and Gupta et al. (1978a,1978b). One of the results of these analyses is the prediction of a significant applied field dependence of the spin reduction present in antiferromagnets with low Néel temperatures. This feature is of relevance in the present work as both K_2FeF_5 and Rb_2FeF_5 have $T_N<10K$, and is observed as a sharp minimum in the hyperfine field (corresponding to a maximum in the magnon-induced spin fluctuations) for applied fields near B_{sf}. In this section we will briefly sketch the theoretical description of this phenomenon, leading to quantitative expressions of the spin reduction as a function of applied field. It is useful, however, to begin by discussing the related phenomenon of zero point spin reduction.

2.3a Zero Point Spin Reduction

Following the standard theory for an antiferromagnetic system in the absence of an applied field (Kittel 1963, Keffer 1966), the

sublattice spin reduction $\Delta S = S - \langle S \rangle$ due to spin-waves may be given by :

$$\Delta S = N^{-1}\Sigma_k[(n_k+\tfrac{1}{2})\cosh 2\chi_k - \tfrac{1}{2}] \ . \qquad (2.29)$$

Here k is the wavevector, N is the number of spins on each sublattice, and χ_k is defined by :

$$\tanh 2\chi_k = -\omega_E\gamma_k/(\omega_E+\omega_A) \ ,$$

where $\omega_E = 2JzS/\hbar$ is the exchange frequency and $\omega_A = g\mu_B B_A/\hbar$ is the anisotropy frequency. In a system of loosely coupled linear chains the structure factor γ_k is :

$$\gamma_k = [\cos k_x a + (J'/J)(\cos k_y b + \cos k_z c)]/(1 + 2J'/J)$$

(Ishikawa and Oguchi 1975), where a is the lattice constant along the chains, b and c are the lattice constants perpendicular to the chains, and J and J' are the intrachain and interchain exchange constants. The number of spin waves excited at temperature T is given by :

$$n_k = [\exp(\hbar\omega_k/k_B T) - 1]^{-1} \ ,$$

since spin-waves obey Bose-Einstein statistics, where :

$$\omega_k = [(\omega_E+\omega_A)^2 - \gamma_k{}^2\omega_E{}^2]^{\frac{1}{2}}$$

is the frequency of the magnon of wavevector k.

It is interesting to note that the spin reduction described by equation (2.29) has a temperature-independent part :

$$\Delta S(0) = N^{-1}\Sigma_k \tfrac{1}{2}(\cosh 2\chi_k - 1) \ , \qquad (2.30)$$

which is known as the 'zero point spin reduction' (ZPSR). It is further instructive to note that the ZPSR is a direct consequence of the fully aligned Néel state $|\psi_N\rangle = |+-+-+-\ldots\rangle$ (where '+' denotes 'spin up' etc.) not being an eigenstate of the Heisenberg exchange Hamiltonian and therefore not being a ground state of the spin system. This may be seen by writing the exchange Hamiltonian (discussed in section 2.2a) in terms of raising and lowering spin operators :

$$H_{ex} = \Sigma_{ij} 2J_{ij}[S_{zi}S_{zj} + \tfrac{1}{2}(S_{+i}S_{-j}+S_{-i}S_{+j})] \ ,$$

and considering (for simplicity) a spin 1/2 system. When H_{ex} acts on $|\psi_N\rangle$ the $S_{+i}S_{-j}$ terms convert pairs of spins -+ to +-, so that states such as $|-++-+-...\rangle$, $|++--+-...\rangle$, etc. are produced. The true ground state of H_{ex} is therefore a mixture of $|\psi_N\rangle$ and all the other states in which one spin on each sublattice is reversed. The average spin $\langle S\rangle$ on each sublattice is thus less than that of the fully aligned state (S), giving rise to the ZPSR that is approximated by equation (2.30).

The ZPSR may be numerically calculated (Anderson 1952) by writing $\cosh 2\chi_k = (1-\alpha\gamma_k^2)^{-\frac{1}{2}}$ where $\alpha=(1+\omega_A/\omega_E)^{-2}$, and transforming the summation of (2.30) into a triple integral :

$$\Delta S(0) = \pi^{-3}\iiint \tfrac{1}{2}[(1-\alpha\gamma_k^2)^{-\frac{1}{2}}-1]d\kappa_x d\kappa_y d\kappa_z \ .$$

Here $\kappa_x=k_x a$, $\kappa_y=k_y b$ and $\kappa_z=k_z c$, and the integration limits ($0\rightarrow\pi$) are chosen to be those appropriate for the periodicity of the function. When $\alpha=1$ the ZPSR predicted for a three-dimensional material is found from this integral to be $\Delta S(0)=0.07836$, which for a spin S=5/2 system represents a spin reduction of ~3.1%, while in a two-dimensional system $\Delta S(0)=0.19660$, a ~7.9% reduction. In the case of a one-dimensional system with $\alpha=1$ $\Delta S(0)$ diverges, indicating that a pure isotropic one-dimensional system cannot sustain long range order, even at absolute zero. Experimental observation of ZPSR is often difficult in three-dimensional crystals, but it has been found to be >30% in some quasi one-dimensional materials, including K_2FeF_5 and Rb_2FeF_5.

2.3b Field-Dependent Spin Reduction

The origin of the field-dependence of the spin reduction in antiferromagnets lies in a modification of the normal mode frequencies ω_k by the external field. This effect is different for spins lying parallel to or perpendicular to the applied field direction, and is particularly noticeable during the spin-flop transition in quasi one-dimensional antiferromagnets.

In the presence of an external field $B<B_{sf}$ applied parallel to the AFM axis of the spins the magnon dispersion curve splits into two parts, with $\omega_{k\pm}=\omega_k\pm\omega_B$, where $\omega_B=g\mu_B B/\hbar$. The expression for the spin reduction at temperature T and field B is then :

$$\Delta S_{afm} \simeq N^{-1}\Sigma_k\{[\tfrac{1}{2}(n_{k+}+n_{k-})+\tfrac{1}{2}]\cosh 2\chi_k - \tfrac{1}{2}\} , \qquad (2.31)$$

where $n_{k\pm}$ are the numbers of magnons corresponding to $\omega_{k\pm}$. It may be noted that this equation is essentially the same as (2.29) except that n_k is replaced by the average of n_{k+} and n_{k-}. Another notable feature of (2.31) is that although the frequencies $\omega_{k\pm}$ split symmetrically about ω_k as B is increased, n_{k-} increases much faster than n_{k+} decreases and therefore the average of the two increases. This leads to an increase in spin reduction with increasing applied field.

In the spin-flopped phase ($B>B_{sf}$) the magnon frequency has been derived by Wang and Callen (1964) and Keffer (1966) to be :

$$\omega_{k\pm} = \omega_E\{[-(\omega_A/\omega_E)+1+\gamma_k]\cos 2\phi + (\omega_B/\omega_E)\sin\phi\}^{\frac{1}{2}}[(\omega_A'/\omega_E)+1\pm\gamma_k]^{\frac{1}{2}} ,$$

where ω_A' allows for anisotropy within the plane perpendicular to the applied field. ϕ is the angle by which the spins are canted out of the perpendicular plane by the applied field, and is given by :

$$\sin\phi = \omega_B/(2\omega_E-\omega_A) . \qquad (2.32)$$

(This equation may be derived by balancing the torques acting on a given spin, $g\mu_B\underset{\sim}{S}_1\times(\underset{\sim}{B}+\underset{\sim}{B}_E+\underset{\sim}{B}_A)=0$, where $\underset{\sim}{B}_E\|\underset{\sim}{S}_2$ and $\underset{\sim}{B}_A=|\underset{\sim}{B}_A|\sin\phi$ is directed along the easy anisotropy axis.) The spin reduction is then :

$$\Delta S_{sf} \simeq N^{-1}\Sigma_k\tfrac{1}{2}[a_{k+} + a_{k-} - 1] , \qquad (2.33)$$

with $a_{k\pm} = (\omega_E/\omega_{k\pm})(n_{k\pm}+\tfrac{1}{2})[1\pm\gamma_k\sin^2\phi-(\omega_A/2\omega_E)\cos^2\phi+(\omega_A'/2\omega_E)]$

(Wang and Callen 1964). Numerical calculations by Gupta et al. (1978a) have shown that the predicted spin reduction is greatest for $B\simeq B_{sf}$, and decreases as B is increased. When $B=2B_E-B_A$ the spins enter the paramagnetic phase with $\phi=90°$ given by (2.32), and ΔS_{sf} reduces to zero.

It should be noted that in its essence the standard spin-wave treatment of the spin-flop transition is a first-order model. That is, it is usually assumed that the applied field is perfectly aligned with the easy anisotropy axis of the antiferromagnet. The transition takes place when $\omega_B \simeq (2\omega_E\omega_A)^{\frac{1}{2}}$ and the long wavelength (k=0) magnon frequency ω_{k-} goes to zero, producing an instability in the spin-wave modes which then initiates the spin reorientation. In the case of imperfect alignment of the applied field with the easy axis the spin reduction calculation is greatly complicated by the non-diagonal nature of the spin Hamiltonian. Gupta et al. (1978b) obtained an approximate solution to this problem by assuming that any rotation of the antiferromagnetic axis of the spins away from the easy axis was negligible. According to the mean-field theory outlined in the previous section this assumption implies that the misalignment is slight, and within the critical angle $\psi_c \simeq B_A/2B_E$. A comprehensive treatment of the problem with $\psi > \psi_c$ has yet to appear in the literature.

2.4 SOLITON THEORY

We conclude this chapter by considering a third theoretical model of the spin-flop phase transition, one which is based on the concept of travelling domain walls or 'solitons'. This theory has been brought into prominence over the last few years by L.J. de Jongh and co-workers at the University of Leiden. Several review articles have been published by this group, including de Jongh (1982), de Jongh and de Groot (1985) and de Groot and de Jongh (1986). One of the predictions of this soliton theory is that in low-dimensional systems the spin-flop transition will be considerably broadened by the motion of domain walls, and its first-order character lost. This feature is of interest in the present work since both K_2FeF_5 and Rb_2FeF_5 are quasi

one-dimensional antiferromagnets of the type that may support soliton waveforms. In this section we shall sketch the soliton description of the spin-flop, but begin by reviewing the concept of the non-linear waveforms that are known as 'solitons'.

2.4a Solitons as Moving Domain Walls

Mathematically a soliton is defined as a solution $\phi(z,t)$ of the Sine-Gordon equation :

$$c_o^2\phi_{zz} - \phi_{tt} = \omega_o^2\sin\phi \ , \qquad (2.34)$$

where $\phi_z=\partial\phi/\partial z$ etc., and c_o and ω_o are the characteristic wave velocity and frequency. In the small amplitude limit $\sin\phi\simeq\phi$ and the equation reduces to the Klein-Gordon equation, which has the linear travelling wave solutions $\phi(z,t)\propto\cos(kz-\omega t)$ that are known as 'spin-waves' or 'magnons'. However, large amplitude solutions of (2.34) may occur, including the wave :

$$\phi(z,t) = 4\tan^{-1}\{\exp[\pm(\gamma\omega_o/c_o)(z-vt)]\} \ , \qquad (2.35)$$

where $\gamma=(1-v^2/c_o^2)^{-\frac{1}{2}}$ and v is the wave velocity. These are the 'soliton' solutions which describe localised waveforms in which ϕ changes by 2π over a finite width $d_s=c_o/\omega_o$. Usually the low density limit is considered in which the solitons may be treated as a dilute gas of non-interacting quasi-particles. In this approximation the soliton mass is given by $m_s=\omega_o/c_o$, the thermal velocity $v\propto c_o(k_BT/E_s)^{\frac{1}{2}}$, and the particle density $n_s\propto m_s(E_s/k_BT)^{\frac{1}{2}}\exp(-E_s/k_BT)$, where E_s is the soliton energy.

The importance of solitons in low-dimensional magnetism was first pointed out by Enz (1964), and may be illustrated by considering the spin Hamiltonian of a one-dimensional antiferromagnetic chain :

$$H = \Sigma_i[2J\underset{\sim}{S}_i\cdot\underset{\sim}{S}_{i+1} - K(S_{xi})^2 + K'(S_{zi})^2] \ .$$

Here $J>0$ is the exchange constant, $K'>0$ is an anisotropy constant which establishes a planar (xy-plane) preference for the spins, and $K>K'$ is

an Ising-type anisotropy constant which singles out the x axis as the easy axis for the spins. In the 'continuum approximation' (Enz 1964, Mikeska 1980,1981) this Hamiltonian may be rewritten in terms of the sum of exchange, kinetic and anisotropy energy terms :

$$H \approx 4E_o J \tfrac{1}{2}[(\theta_z)^2 - c_o^{-2}(\theta_t)^2 + \tfrac{1}{2}m^2\cos 2\theta]dz \ ,$$

where $E_o=\frac{1}{2}JS^2$, $m^2=K/J$, $c_o=4JS$ and the integration limits are $\pm\infty$. $\theta(z,t)$ is the angle that the spins make to the easy axis, and z is position along the chain measured in units of the lattice spacing. The Hamilton equation of motion $dp/dt=-\partial H/\partial q$ may now be applied by noting that the momentum $p=mv$ is constant as the soliton velocity v is invariant, and the position variable q is equivalent to z. Thus $\partial H/\partial z=0$, which leads to an equation of the form :

$$2\theta_{zz} - 2c_o^{-2}\theta_{tt} = m^2\sin 2\theta \ . \qquad (2.36)$$

This is a Sine-Gordon equation of the form of (2.34), with ϕ replaced by 2θ, so that c_o may be recognised as the maximum (cutoff) velocity of a soliton of mass m in the magnetic chain.

A physical picture of a soliton excitation in a one-dimensional AFM chain thus emerges. Since θ in (2.36) corresponds to $\frac{1}{2}\phi$ in (2.34) the soliton represents a π rotation of the spins. This π-soliton separates the two (degenerate) ordered configurations of the chain, and as such may be regarded as a domain wall of the 'Bloch' type. The passage of a soliton will be observed at a given spin site as a π rotation of the spin direction from e.g. +x to -x, with the spin moving in the xy-plane while the soliton propagates in the z direction.

2.4b Soliton Model of the Spin-Flop

In recent years it has been suggested that solitons may mediate the spin-flop transition in low-dimensional magnetic systems, and may also account for the broadening of the transition sometimes observed in such materials. de Jongh (1982) considered the effect of an external field

applied parallel to the easy axis of the spins by adding the term $-g\mu_B \Sigma_i \underset{\sim}{B} \cdot \underset{\sim}{S}_i$ to the spin Hamiltonian discussed above. In small fields ($B<B_{sf}$) the energy of a single domain wall (soliton) that is N spins wide may be estimated as the sum of exchange, anisotropy and applied field energy terms :

$$E_{wall} = \pi^2 JS^2/N + NKS^2 - (N/2\mu_o)(\chi_\perp - \chi_\parallel)B^2 \ .$$

Minimising this expression with respect to N and making the low temperature approximation that $\chi_\parallel \simeq 0$, the wall energy (or soliton creation energy) is given by :

$$E_s \simeq g\mu_B SB_{sf}(1-B^2/B_{sf}^2)^{\frac{1}{2}} \ . \qquad (2.37)$$

A rigorous derivation of this result has been given by Leung et al. (1980). Above the spin-flop ($B>B_{sf}$), the spins lie along the y axis and rotate from +y to -y during the passage of a soliton. The creation energy of a soliton in this flopped phase is :

$$E_s \simeq g\mu_B SB_{sf}(B^2/B_{sf}^2-1)^{\frac{1}{2}} \ . \qquad (2.38)$$

Equations (2.37) and (2.38) form the basis of a soliton description of the spin-flop. As B approaches B_{sf} the soliton creation energy E_s approaches zero so that both the width and the density of soliton excitations in the chains become very large. Since over the width of a soliton the spins have components perpendicular to the easy axis, one may view these excitations as creating admixtures of small segments of the SF phase in the AFM phase (for $B<B_{sf}$) and vice-versa. The mean angle $\langle\theta\rangle$ of the spins to the z axis will therefore vary continuously from $\langle\theta\rangle=0$ for $B<<B_{sf}$ to $\langle\theta\rangle=90^\circ$ for $B>>B_{sf}$. Such a transition is clearly reversible and continuous, so that in terms of the soliton theory the spin-flop may be regarded as of second-order.

We should note here that these solitons will occur in pairs because of the influence of interchain interactions. The excitation of a single π domain wall (below T_N) would imply that about half the spins in a chain would be overturned, and would move against the interchain cou-

pling J'. Although J' is small in quasi one-dimensional systems, the cost in energy would be large because of the large number of spins involved. Thus it is more likely that 'pair-states' consisting of a soliton and an anti-soliton would be created (for energy $2E_s$), with only the spins inside and between the two walls contributing to the interchain interaction energy.

The average angle $\langle\theta\rangle$ may be predicted from the soliton model. Assuming that the density n_s of solitons is small so that the excitations do not interact, the mean free space available to each pair-state is n_s^{-1}. It can then be shown (de Jongh and de Groot 1985) that the mean angle is approximated by :

$$\langle\theta\rangle \simeq 2n_s d_s \int(\theta/\sin\theta)d\theta \ ,$$

where the integration range is $0 \rightarrow \pi/2$. The integral may be evaluated numerically, giving $\langle\theta\rangle \simeq 3.66 n_s d_s$. It has also been shown (Leung et al. 1980) that in the low-density limit the soliton density is given by :

$$n_s \simeq 2d_s^{-1}(2/\pi)^{\frac{1}{2}}(E_s/k_BT)^{\frac{1}{2}}\exp(-E_s/k_BT) \ .$$

Thus the mean angle of rotation may be estimated as :

$$\langle\theta\rangle \simeq 5.85\ (2E_s/k_BT)\ \exp(-2E_s/k_BT) \ , \qquad (2.39)$$

where we recall that the excitation energy of the pair-state is $2E_s$. Using (2.37) and (2.38) for E_s the field dependence of $\langle\theta\rangle$ may therefore be calculated, although in the neighbourhood of B_{sf} the exponential diverges and unphysical behaviour is predicted, corresponding to the breakdown of the low-density non-interacting particle approximation.

In conclusion it is perhaps useful to reiterate that the soliton approach to the spin-flop transition is only valid in low-dimensional systems. In a three-dimensional material a soliton excitation might be envisaged as a 'droplet' or 'micro-domain' region of space in which the antiferromagnetic sublattices are interchanged. However the

excitation energy of such a micro-domain will typically be of the order of 10^3K (de Groot and de Jongh 1986), compared to 1-10K in a quasi one-dimensional material. Thus the contribution of solitons to the low temperature free energy of an antiferromagnet (and the subsequent broadening of the spin-flop transition) will only be significant in low-dimensional systems.

CHAPTER THREE

MÖSSBAUER SPECTROSCOPY

3.1 INTRODUCTION

In the 1920's it was noted that it should be possible to observe a nuclear analogue of the phenomenon of atomic resonant fluorescence (Kuhn 1929). A γ-ray emitted during a nuclear transition from an excited state to the ground state should be capable of exciting a second ground state nucleus of the same isotope. However, the high energy and momentum of the photon causes the nucleus to have a large recoil energy and reduces the probability of detecting the resonant absorption to negligible proportions.

A solution to the problem was found by R.L. Mössbauer in 1957-58 during his graduate work on the nuclear resonance scattering of 129 keV γ-rays from ^{191}Ir. He found that in the solid state it was possible to produce recoilless emission and absorption events (Mössbauer 1958a,1958b) and that resonant absorption could then be easily detected. His experiments formed the basis of a completely new branch of solid state spectroscopy which is now referred to as 'Mössbauer spectroscopy'.

Over the last thirty years Mössbauer spectroscopy has developed into an important and versatile tool for the study of solid state properties. Since the γ-rays emitted in recoilless events are very nearly monochromatic it is possible to observe the hyperfine interactions between a nucleus and its environment. This high resolution, coupled with the relative simplicity of the necessary instrumentation, has promoted the use of Mössbauer spectroscopy in many diverse fields and particularly in physics, chemistry, biology, geology and engineering.

Numerous books and review articles have been written on the Mössbauer effect, including Wertheim (1964), Greenwood and Gibb (1971)

and May (1971). Frauenfelder (1962) provides a collection of the most significant early papers, including translations of Mössbauer's work.

Although the Mössbauer effect has been observed in almost fifty elements, the majority of work to date has been restricted to about a dozen particularly convenient isotopes. Most notable are iron, tin and antimony. In the present work Mössbauer experiments were performed with a stable isotope of iron, ^{57}Fe, and therefore much of the discussion which follows will relate to this isotope.

3.2 THE MÖSSBAUER EFFECT

3.2a Recoilless Emission and Absorption

To better understand the Mössbauer effect, let us consider the energetics of γ-ray emission and absorption. Most modes of radioactive decay produce a daughter nucleus in a highly excited state, which then decays to the ground state by emitting a series of γ-ray photons. Consider an isolated free atom which has a nuclear excited state at an energy E above the ground state. If a single γ-ray of energy E_γ is emitted during de-excitation there is some energy loss to the recoiling nucleus so that

$$E_\gamma = E - E_R - E_D \qquad (3.1)$$

is the photon energy. Here E_R is the recoil energy, which by conservation of energy and momentum can be shown to be

$$E_R = E_\gamma^2/2Mc^2 \ ,$$

where c is the speed of light and M is the atomic mass. E_D is a term which is proportional to the initial velocity of the atom, and is called a 'Doppler-effect' or 'thermal-motion' energy. It has a mean value

$$\langle E_D \rangle \approx E_\gamma (kT/Mc^2)^{\frac{1}{2}} \ ,$$

where k is Boltzmann's constant and T is absolute temperature. The Doppler energy leads to a broadening of the statistical distribution of the emitted γ-ray energies into a Gaussian curve of half-width $\langle E_D \rangle$, centered at $E-E_R$.

In the reverse process of absorption the γ-ray distribution is similar but displaced by $+E_R$ to give :

$$E_\gamma = E + E_R - E_D \ . \qquad (3.2)$$

Nuclear resonant absorption will only have a significant probability if the emission and absorption profiles defined by equations (3.1) and (3.2) overlap strongly. Typical γ-ray events in free atoms have $E \sim 10^4$ eV and both E_R and $\langle E_D \rangle$ of order 10^{-2} eV, so that as shown in Figure 3.1 the overlap may be quite small and the resonant absorption difficult to detect.

The significance of the Mössbauer effect may now be seen in that for a nucleus imbedded in a solid the recoil and Doppler energies may be entirely eliminated. In a crystal lattice, if the recoil energy is less than the chemical binding energy, the only way that E_R can be dispersed is by the creation of phonons. However, if E_R is less than the energy required to create a single phonon there is a finite possibility that the γ-ray emission or absorption takes place without any phonons being created. To conserve energy the crystal mass as a whole must then move, so that the mass M in the equation for E_R becomes that of a crystal containing perhaps 10^{15} atoms, and E_R is very small. Similarly, the Doppler energy is associated with phonons and $\langle E_D \rangle$ is very small in a zero-phonon transition. With E_R and E_D thus eliminated in the solid state, nuclear resonant absorption becomes a strong possibility.

In the absence of recoil or thermal broadening the width of the γ-ray energy distribution is defined by the Heisenberg uncertainty principle, $\Delta E \Delta t \geq \hbar$, in which the uncertainties in energy and time

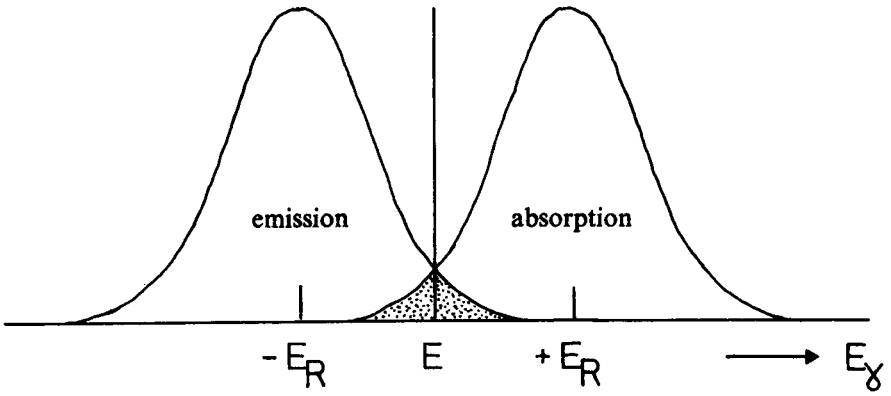

Figure 3.1 Statistical distributions of the γ-ray energy for emission and absorption, with the resonance overlap region shaded.

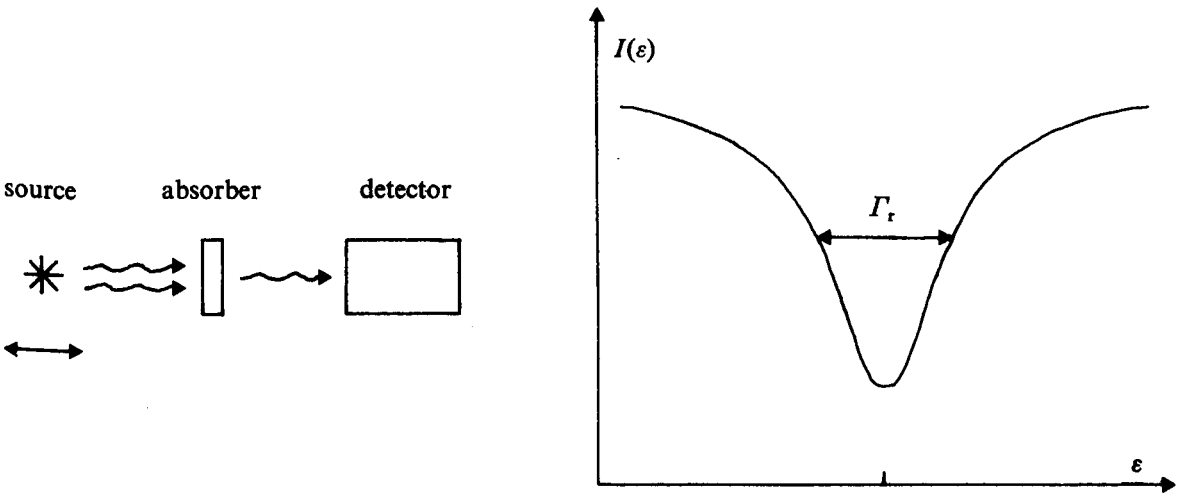

Figure 3.2 Schematic illustration of a Mössbauer effect experiment and a corresponding Mössbauer absorption spectrum.

are related to Planck's constant h (=2π ħ). Thus the width of the γ-ray distribution at half-height, Γ_o , is given by $\Gamma_o \tau = \hbar$, where τ is the mean lifetime of the excited state. For the first excited state of ^{57}Fe at 14.4 keV, τ=99ns and $\Gamma_o = 4.7 \times 10^{-9}$ eV, a monochromaticity of $\Gamma_o / E_\gamma \simeq 1$ part in 10^{12}.

The probability of zero-phonon γ-emission from a nucleus embedded in a solid can be quantitatively related to the vibrational properties of the lattice through dispersion theory (Frauenfelder 1962). This probability, known as the 'recoil-free fraction' or 'f-factor' is given by :

$$f = \exp (-E^2 \langle x^2 \rangle / \hbar^2 c^2) ,$$

where $\langle x^2 \rangle$ is the mean-square vibrational amplitude of the nucleus in the direction of the γ-ray. The f-factor is thus enhanced for low-energy γ-rays (small E) in a strong lattice (small $\langle x^2 \rangle$).

3.2b The Mössbauer Spectrum

Experiments on the Mössbauer effect usually utilise the recoilless emission of γ-rays from a solid matrix containing the excited nuclei of a given isotope (the 'source'), followed by their resonant absorption by a second matrix containing the same isotope in the ground state (the 'absorber'). Movement of the source relative to the absorber by a velocity v alters the effective value of E_γ 'seen' by the absorber by a small Doppler shift energy $\varepsilon = (v/c) E_\gamma$. A Mössbauer spectrum is obtained by recording the rate of transmission of the source γ-rays through the absorber, as a function of the Doppler velocity v (i.e. transmission as a function of energy). This is illustrated in Figure 3.2.

The line-shape of the absorption is derived from the source and absorber energy distributions. In the limit of a very thin source and absorber it is of Lorentzian form with a width $\Gamma_r = 2\Gamma_s$ where Γ_s is

the natural linewidth of the source. Thus the decrease in transmission with respect to the γ-ray energy ε is given by :

$$I(\varepsilon) = (\Gamma_r/2\pi)\times[(\varepsilon-E_\gamma)^2 + (\Gamma_r/2)^2]^{-1} .$$

A small increase in the absorber thickness causes an increase in Γ_r but only small distortion of the Lorentzian line-shape.

3.3 HYPERFINE INTERACTIONS

The great usefulness of the Mössbauer effect lies in the high definition of the resonance (about 1 part in 10^{12}) which is similar in magnitude to the slight influences on the energy of a nucleus due to its chemical environment.

The Hamiltonian describing the energy of the nucleus may be written in the form :

$$H = H_o + E_o + M_1 + E_2 ,$$

where H_o represents all terms other than the hyperfine interactions with the environment. The dominant term in H_o is due to intranuclear forces which give rise to quantised energy levels which have the nuclear spin quantum number I. The E_o term refers to electric monopole (Coulomb) interactions between the nucleus and its surrounding electrons. M_1 refers to the magnetic dipole interactions of the nuclear spin with a magnetic field. E_2 describes electric quadrupole interactions of the nuclear quadrupole moment with the local electric field gradient.

The three interactions E_o, M_1 and E_2 have characteristic influences on the Mössbauer spectrum, known respectively as the 'isomer shift', 'magnetic hyperfine splitting' and 'quadrupole splitting'. It is convenient to discuss them individually.

3.3a Isomer Shift

In a nuclear γ-transition it is usual for the effective nuclear radii of the excited and ground states to differ. The Coulomb interaction energy between the electronic charge at the nucleus and the nuclear charge is therefore different for the two states. The electronic charge at the nucleus is in turn dependent on the chemical environment of the atom.

If in a Mössbauer experiment the chemical structures of the source and absorber are different, the resonance line recorded by velocity scanning may be measurably displaced from zero velocity by an amount δ, known as the 'isomer shift'. This is illustrated in Figure 3.3a for ^{57}Fe as differing shifts in the I=3/2 and I=1/2 energy levels. For convenience δ is usually quoted in mm/s rather than in direct energy units. Although δ is not an absolute quantity it is possible to compare values using a suitable reference, such as the γ-ray source used or another absorber (which in the case of ^{57}Fe spectroscopy is usually a natural iron foil at room temperature).

A mathematical expression of the above concepts has been derived by DeBendetti et al. (1961) and Walker et al. (1961), assuming that the nucleus is a uniformly charged sphere and that the electronic charge density is uniform over nuclear dimensions. These approximations give :

$$\delta = (Ze^2/5\varepsilon_o).(\langle R_e^2\rangle - \langle R_g^2\rangle).(|\Psi_a(0)|^2 - |\Psi_s(0)|^2) \quad , \qquad (3.3)$$

where Z is the atomic number of the nucleus, ε_o is the permittivity of a vacuum and -e is the electronic charge. $\langle R_e^2\rangle$ and $\langle R_g^2\rangle$ are the root mean square radii of the excited and ground states, and $|\Psi_a(0)|^2$ and $|\Psi_s(0)|^2$ represent the s-electron densities at the absorber and source nuclei.

Equation (3.3) contains the product of a nuclear term which is a constant for a given transition, and a chemical term

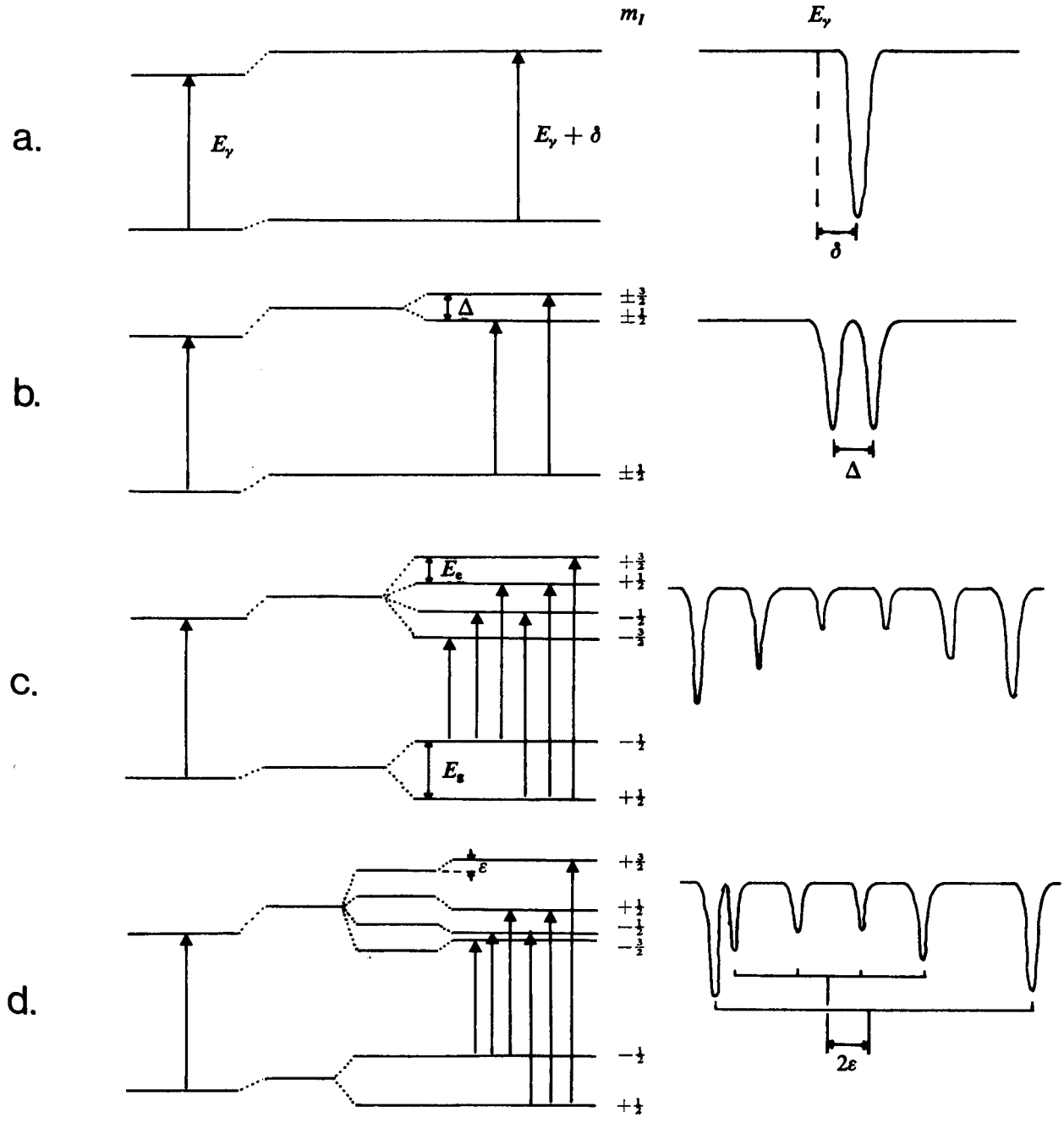

Figure 3.3 Energy level diagrams and corresponding Mössbauer spectra for ^{57}Fe in the presence of (a) isomer shift, (b) isomer shift and quadrupole splitting, (c) isomer shift and magnetic hyperfine splitting, and (d) isomer shift and combined magnetic and quadrupole splitting.

$(|\Psi_a(0)|^2-|\Psi_s(0)|^2)$ which describes the difference in s-electron density at the nucleus. Sometimes the two terms are referred to separately as the 'isomer shift' and the 'chemical shift', but it is conventional in Mossbauer spectroscopy to refer to their product as the 'isomer shift'.

Another effect contributing to the measured isomer shift is the second-order Doppler shift due to the thermal vibration of an atom on its lattice site. The relativistic equation for the Doppler effect on the emitted γ-ray predicts a frequency shift relative to a stationary atom of :

$$\nu = \nu_o(1 + \langle v^2\rangle/2c^2) \ ,$$

where $\langle v^2\rangle$ is the mean-square velocity of the atom in the direction of emission. There is a corresponding change in the γ-ray energy of :

$$\Delta E_\gamma/E_\gamma = -\langle v^2\rangle/2c^2 \ .$$

Since vibrations are temperature dependent, $\langle v^2\rangle$ will increase as temperature is raised, and the Mössbauer resonance will move to lower velocity. For ^{57}Fe this shift is typically ~0.07 mm/s per 100K. There is also a significant zero-point motion contribution at absolute zero.

3.3b Quadrupole Splitting

In a chemically bonded atom the electronic charge distribution is usually not spherically symmetric and an electric field gradient (EFG) tensor at the nucleus may be defined as :

$$E_{ij} = -V_{ij} = -\partial^2 V/\partial x_i \partial x_j \ ,$$

where $x_i, x_j = x,y,z$ and V is the electrostatic potential.

By a suitable choice of coordinate axes the EFG may be reduced to diagonal form. The Laplace equation then demands that :

$$\nabla^2 V = V_{xx} + V_{yy} + V_{zz} = 0 \ ,$$

so it is only necessary to specify two parameters to define the tensor completely. (Although the s-electron charge density at the nucleus is

non-zero the charge distribution is spherically symmetric and does not contribute to the EFG.) It is customary to define the axis system of the atom so the $V_{zz}=eq$ is an extremal value of the field gradient, and an 'asymmetry parameter' :

$$\eta = (V_{xx} - V_{yy})/V_{zz} ,$$

where $|V_{zz}|>|V_{yy}|\geq|V_{xx}|$ so that $0 \leq \eta \leq 1$. The EFG is then defined by V_{zz} and η.

The EFG at the nucleus has two sources : the incompletely filled electron shells in the atom itself (the 'valence' contribution), and the charges on distant ions in the crystal (the 'lattice' contribution). Numerical evaluation of the EFG is complicated by large shielding and antishielding effects (Sternheimer 1957), but many of the properties of the EFG may be deduced from the symmetry properties of the crystal. For example, if the crystal has a fourfold rotational symmetry axis then V_{zz} lies along that axis, and since a 90° rotation produces no change in the crystal and therefore no change in the EFG, $V_{xx}=V_{yy}$ and $\eta=0$.

A nucleus with a spin quantum number $I>1/2$ has a non-spherical charge distribution and hence a nuclear quadrupole moment eQ. This moment interacts with the EFG according to the Hamiltonian :

$$H = (eQ/2I(2I-1)).(V_{zz}I_z^2 + V_{yy}I_y^2 + V_{xx}I_x^2) ,$$

where I_x,I_y and I_z are conventional spin operators. In the case of $I=3/2$ this equation may be solved exactly to give the eigenvalues

$$E_Q = (eQV_{zz}/4I(2I-1)).(3M_I^2-I(I+1)).(1+\eta^2/3)^{\frac{1}{2}} , \qquad (3.4)$$

where $M_I=\pm3/2,\pm1/2$ are the spin projection quantum numbers ($M_I=I,I-1,\ldots,-I$). Thus the $I=3/2$ energy level is split into two levels with $M_I=\pm3/2$ and $\pm1/2$ respectively. If the sign of V_{zz} is positive the $M_I=\pm3/2$ states will be highest, as illustrated in Figure 3.3b. The corresponding Mössbauer spectrum (for an $I_e=3/2 \rightarrow I_g=1/2$ transition) comprises two lines with a separation :

$$\Delta = \tfrac{1}{2}eQ|V_{zz}|.(1+\eta^2/3)^{\frac{1}{2}} \ ,$$

which is referred to as the 'quadrupole splitting'. The line intensities are equal for a randomly oriented absorber (see Section 3.4).

3.3c Magnetic Hyperfine Splitting

If there is a magnetic field of flux density B at the nucleus it will interact with the nuclear magnetic moment μ to split the nuclear energy levels. The Hamiltonian describing the interaction is :

$$H = -\underset{\sim}{\mu}\cdot\underset{\sim}{B} = -g\mu_N\underset{\sim}{I}\cdot\underset{\sim}{B} \ ,$$

where μ_N is the nuclear magneton ($=e\hbar/2m_p$) and g is the nuclear g-factor ($=\mu/I\mu_N$). The solution of this Hamiltonian gives :

$$E_m = -g\mu_N BM_I \ ,$$

and the nuclear level is split into 2I+1 non-degenerate equally spaced sub-levels.

The magnetic hyperfine spectrum of ^{57}Fe is shown in Figure 2.2c. (The relative inversion of the I_e=3/2 and I_g=1/2 multiplets is due to the difference in sign of the excited and ground state nuclear magnetic moments). The selection rules for magnetic dipole transitions are that ΔM_I=0,±1 so that there are only six allowed transitions (see Section 3.4). The absorption lines have relative intensities 3:2:1:1:2:3 for a randomly oriented absorber.

The magnetic field at the nucleus may be considered to be due to two contributions :

$$\underset{\sim}{B} = \underset{\sim}{B}_{loc} + \underset{\sim}{B}_{hf} \ .$$

Here $\underset{\sim}{B}_{loc}$ is the value that the macroscopic internal field in the specimen takes at the nucleus, and $\underset{\sim}{B}_{hf}$ is the hyperfine field resulting from the immediate environment of the nucleus.

3.3c(i) The Local Field

The local field at a given atom site in a magnetic material is the sum of the applied field $\underset{\sim}{B}_{app}$ from external sources and the fields arising from the magnetic dipoles within the specimen :

$$\underset{\sim}{B}_{loc} = \underset{\sim}{B}_{app} + \underset{\sim}{B}_1 + \underset{\sim}{B}_2 + \underset{\sim}{B}_3 \ .$$

The standard method of summing the dipole fields was discussed in Chapter 2, section 2.2e. $\underset{\sim}{B}_1 = -\mu_o N \underset{\sim}{M}$ is the 'demagnetising field' associated with the outer boundary of the specimen, where N is the demagnetisation factor and $\underset{\sim}{M}$ is the sample magnetisation. $\underset{\sim}{B}_2 = \mu_o \underset{\sim}{M}/3$ is the 'Lorentz cavity field' corresponding to the magnetic poles on the surface of an imagined spherical cavity concentric with the reference atom. The third contribution, $\underset{\sim}{B}_3$, is the field due to the magnetic dipoles within the imaginary sphere. This field is generally small, and is zero for a lattice site with cubic symmetry.

In general the contributions of B_1, B_2 and B_3 to the total local field are small for dia-, para- and antiferro-magnets, but they can be quite large for ferro- and ferri-magnets.

3.3c(ii) The Hyperfine Field

In the hyperfine field at the nucleus three contributions may be distinguished :

$$\underset{\sim}{B}_{hf} = \underset{\sim}{B}_L + \underset{\sim}{B}_D + \underset{\sim}{B}_{FC}$$

(Marshall and Johnson 1962). The first term is the field produced by the orbital magnetic moment of the parent atom ,

$$\underset{\sim}{B}_L = -(\mu_o \mu_B / 2\pi) \langle r^{-3} \rangle \langle \underset{\sim}{L} \rangle \ , \qquad (3.5)$$

where μ_0 is the permeability of free space and μ_B is the Bohr magneton ($=e\hbar/2m_e$). The expectation values refer to the radial coordinate r and the orbital angular momentum $\underset{\sim}{L}$ of the contributing electrons, which in the case of ^{57}Fe are the 3d electrons.

The second term in $\underset{\sim}{B}_{hf}$ is the field produced by the dipolar interaction of the nucleus with the spin moment of the atom :

$$\underset{\sim}{B}_D = -(\mu_o\mu_B/2\pi) \langle 3\underset{\sim}{r}(\underset{\sim}{S}\cdot\underset{\sim}{r})r^{-5} - \underset{\sim}{S}r^{-3}\rangle ,$$

where S is the spin angular momentum operator. In a crystal with axial symmetry

$$\underset{\sim}{B}_D = -(\mu_o\mu_B/2\pi) \langle \underset{\sim}{S}\rangle \langle r^{-3}\rangle \langle 3\cos^2\theta - 1\rangle , \qquad (3.6)$$

where θ is the angle between the spin direction and the principal axis.

The Fermi contact field $\underset{\sim}{B}_{FC}$ arises from an imbalance in the s-electron density at the nucleus :

$$\underset{\sim}{B}_{FC} = -(4\mu_o\mu_B/3\varepsilon_o) \langle \Sigma_i s_{zi}\delta(r_i)\rangle , \qquad (3.7)$$

where the expectation value is of the spin density at the nucleus, r_i being the radial coordinate of the i^{th} electron and $\delta(r_i)$ being a Delta function. A spin imbalance may result from intrinsic impairing of the s-electrons, or indirectly from polarisation of filled s-orbitals by exchange interactions with unfilled shells. Since the field from a single unpaired 1s electron is very large ($\sim 10^4$T in iron), small differences in the s-electron orbitals can account for the occurrence of large fields at the nucleus.

In the case of iron, the Fermi contact interaction leads to a contact field directed antiparallel to the magnetic moment of the atom. The magnetic moment of an unpaired electron is antiparallel to its spin, therefore in a free atom subject to an applied field directed upwards the 3d shell electrons will be polarised spin-down, with $s_z = -\frac{1}{2}$. The quantum mechanical exchange interaction then leads to an attraction of the spin-down s-electrons (and a repulsion of the spin-up s-electrons) to (from) the 3d electrons. This is shown schematically in Figure 3.4. Thus the spin-up s-electrons have a greater density at the nucleus and $\underset{\sim}{B}_{FC}$ is negative, i.e. directed antiparallel to the atomic moment and to $\underset{\sim}{B}_{app}$.

If we consider the various contributions to the hyperfine field in a Fe^{3+} ion, we see from equation (3.5) that since in a weak crystal field the five 3d electrons have parallel spins and a total orbital

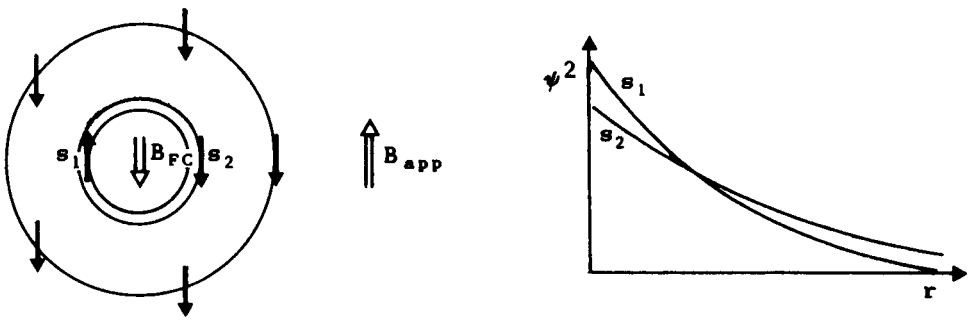

Figure 3.4 Schematic illustration of the Fermi contact interaction in Fe^{3+}. The solid arrows represent the 3d and 1s shell electron spins, and $\psi^2(r)$ represents the radial distributions of the 1s spin densities.

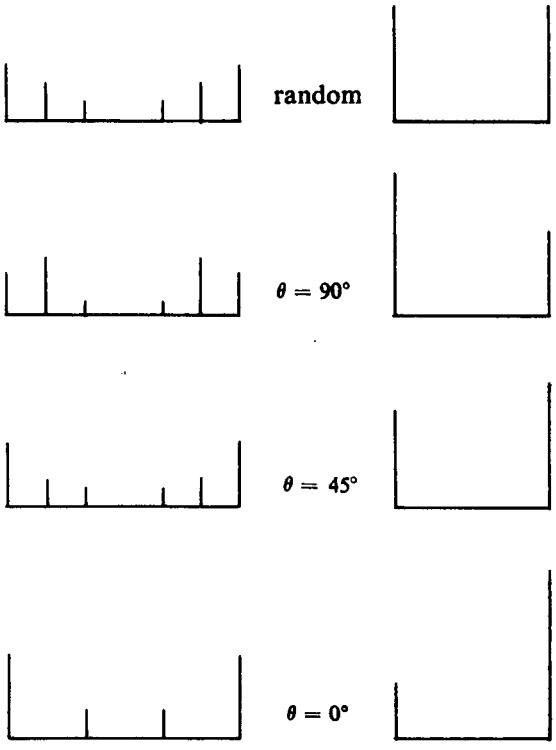

Figure 3.5 The effect of orientation on the line intensities of the magnetic and quadrupole split spectra for an I_1=3/2 to I_2=1/2 transition.

angular momentum L=0, the orbital field B_L=0. Similarly, since Fe^{3+} is a spherically symmetric ion the term $\langle 3\cos^2\theta - 1\rangle$ in (3.6) vanishes and the dipolar field B_D=0. (However there may be small contributions to B_D from the other magnetic dipoles in the specimen). Thus the major contribution to B_{hf} in ferric iron is due to the Fermi contact field.

The situation in Fe^{2+} is quite different. The sign of the spin-orbit coupling (which is negative for six 3d electrons) causes the orbital and spin angular momenta to be aligned parallel. $\underset{\sim}{B}_{FC}$ is parallel to $\underset{\sim}{S}$ whereas $\underset{\sim}{B}_L$ (which may be large since L=2) is antiparallel to $\underset{\sim}{L}$, so that depending on their relative strength (and to a lesser extent on the sign and value of $\underset{\sim}{B}_D$) the total field $\underset{\sim}{B}_{hf}$ may be either positive or negative, or zero.

3.3d Combined Magnetic and Quadrupole Splitting

In simple cases the electric quadrupole and magnetic hyperfine interactions are of very different size and one can be treated as a perturbation on the other. However, generally they must be treated together by diagonalising a combined Hamiltonian which is greatly complicated by the angles between the axis systems of the two interactions. Solutions cannot in general be found analytically and in practice are obtained by a full mathematical analysis using a digital computer.

One of the simple cases mentioned is when the quadrupole interaction acts as a first-order perturbation on the magnetic interaction. If the EFG is axially symmetric with its principal axis at an angle θ to the magnetic axis, and if $eQ|V_{zz}| \ll \mu B$, then the eigenvalues of the combined Hamiltonian are :

$$E = -g\mu_N B M_I + (-1)^{M_I+\frac{1}{2}} \cdot \tfrac{1}{4} eQ|V_{zz}| \cdot \tfrac{1}{2}(3\cos^2\theta - 1) \ .$$

This level splitting is shown in Figure 3.3d for ^{57}Fe, where the I=3/2 sub-levels are shifted away from their 'pure magnetic' positions by an amount :

$$\varepsilon = \tfrac{1}{4}eQ|V_{zz}|.\tfrac{1}{2}(3\cos^2\theta - 1) ,$$

sometimes known as the 'apparent quadrupole splitting' or the 'quadrupole shift'.

3.4 RELATIVE INTENSITIES OF THE ABSORPTION LINES

We have seen that from the shifts and splittings observed in a Mössbauer spectrum one can extract information relating to the electric and magnetic hyperfine interactions acting in the nucleus. However, more information on the directions of these interactions may be obtained by considering the relative intensities of the Mössbauer absorption lines.

In general, in a γ-ray transition between two nuclear levels of spin I_1 and I_2 (and furthermore between the two substates with I_z values m_1 and m_2) the probability of a γ-emission in a given direction is :

$$P \propto < I_1\ J\ -m_1\ m \mid I_2\ m_2 >^2 \Theta(J,m)$$

(Condon and Shortley 1935, Greenwood and Gibb 1971). This expression contains the square of the appropriate Clebsch-Gordan coefficient (where $J=I_1+I_2$ and $m=m_1+m_2$) and an angular dependent term $\Theta(J,m)$. J is known as the 'multipolarity' of the transition : J=1 is a dipole transition, J=2 is a quadrupole transition, etc. The smaller values of J give the larger intensities. If there is no change in parity during the decay it is classified as magnetic dipole (M1) or electric quadrupole (E2).

The 14.4keV level in ^{57}Fe decays primarily by a magnetic dipole transition. This restricts the values that $\Delta m = m_2 - m_1$ can adopt : all values other than $\Delta m=0,\pm1$ cause the coefficient to be zero. Thus

in ^{57}Fe where $I_1=3/2$, $I_2=1/2$ and $J=1$ there are only six allowed transitions, with the $\Delta m=\pm 2$ transitions forbidden. The relative probabilities of the allowed transitions are given in Table 3.1, including the angular dependence where θ is the polar angle of the γ-radiation in the principal axis system. (For simplicity the EFG asymmetry parameter η is assumed to be zero here.) The $\Delta m=0$ transitions have a classical dipole radiation pattern given by $\sin^2\theta$, while the $\Delta m=\pm 1$ transitions have a $(1+\cos^2\theta)$ pattern.

Table 3.1 Relative radiation probabilities for a magnetic dipole $I_1=3/2$ to $I_2=1/2$ transition.

Transitions	Δm	Probability
$+3/2 \rightarrow +1/2$	-1	$3(1 + \cos^2\theta)$
$-3/2 \rightarrow -1/2$	$+1$	
$+1/2 \rightarrow +1/2$	0	$4\sin^2\theta$
$-1/2 \rightarrow -1/2$	0	
$-1/2 \rightarrow +1/2$	$+1$	$1 + \cos^2\theta$
$+1/2 \rightarrow -1/2$	-1	

In a magnetically split ^{57}Fe spectrum the relative intensities of the outermost:middle:innermost pairs of lines are therefore given by

$$3 : 4\sin^2\theta/(1 + \cos^2\theta) : 1 ,$$

where θ is the angle between the incident γ-ray and the magnetic field axis. (The probability distribution of γ-absorption is the same as that of γ-emission). The limiting intensity ratios are 3:0:1 for $\theta=0°$ and 3:4:1 for $\theta=90°$. A polycrystalline absorber in which the magnetic field axis is randomly oriented gives a 3:2:1 ratio, since the average of $\cos^2\theta$ over a sphere is 1/3 and the average of $\sin^2\theta$ is 2/3. These cases are illustrated in Figure 3.5.

Similarly, in a quadrupole split ^{57}Fe spectrum the relative intensities of the two lines (which correspond respectively to the four $|M_I| = 1/2 \rightarrow 1/2$ transitions and the two $3/2 \rightarrow 1/2$ transitions) are given by :

$$P(1/2,1/2) : P(3/2,1/2) = 2+3\sin^2\theta : 3(1+\cos^2\theta) ,$$

where θ is now the angle between the incident γ-rays and the EFG principal axis. The limiting ratios are 1:3 for $\theta=0°$ and 5:3 for $\theta=90°$, and a polycrystalline absorber gives a 1:1 ratio (see Figure 3.5). Thus an angular dependence study of the quadrupole split spectrum of a single crystal absorber will define which of the two lines is the $3/2 \rightarrow 1/2$ transition, therefore determining the sign of the EFG principal component.

It is important to note that the intensity ratios given above are strictly only applicable in the limit of a very thin absorber and source, and that in reality the ratios are dependent on the finite thickness of a real absorber and source. Margulies and Ehrman (1961) have discussed this problem in detail. An effective absorber thickness may be defined as :

$$\tau = f\, n\, a\, \sigma_o\, t ,$$

where f is the recoil-free fraction, n is the density of the element concerned (e.g. iron), a is the fractional abundance of the resonant isotope (e.g. ^{57}Fe) and σ_o its absorption cross-section, and t is the absorber thickness (i.e. physical dimension). For $\tau<<1$ and assuming a thin source, the resonance Mössbauer line is Lorentzian with linewidth $\Gamma_r=2\Gamma_o$, where Γ_o is the source natural linewidth. For $0 < \tau \leq 5$ the lineshape is still basically Lorentzian, but is broadened to a width given approximately (Frauenfelder 1962) by :

$$\Gamma_r \simeq (2.00 + 0.27\tau)\, \Gamma_o .$$

In a magnetic or quadrupole split spectrum the effective absorber thickness corresponding to the j^{th} absorption line is not τ but $W_j\tau$,

where W_j is the relative intensity of the line. Thus the components will show a difference in saturation behaviour with the larger intensity lines being broadened more, causing an apparent accentuation of the weaker lines with increasing absorber thickness.

3.5 TIME CONSIDERATIONS

To conclude this chapter let us note some of the time-scales of relevance to the observation of a Mössbauer absorption spectrum.

The Heisenberg uncertainty principle states that if a system has two possible energy states, E_n and E_m, then any measurements to determine whether the system is in state n or in state m requires at least a time τ given by :

$$\tau \simeq \hbar / (E_n - E_m) .$$

Thus in a magnetic or quadrupole split spectrum the time required to distinguish between the energies $E_n = \hbar\omega_n$ and $E_m = \hbar\omega_m$ of two nuclear transitions is :

$$\tau_L \simeq (\omega_n - \omega_m)^{-1} ,$$

which is often referred to as the 'Larmor precession time'.

In order to resolve hyperfine structure in a Mössbauer spectrum at least one complete Larmor precession must take place before the nucleus decays. In other words, we require that $\tau_N \geq \tau_L$, where τ_N is the mean lifetime of the Mössbauer isotope. For the 14.4keV state of ^{57}Fe $\tau_N \simeq 10^{-7}$sec, so that the basic criterion for observing hyperfine structure in an ^{57}Fe Mössbauer spectrum is that $\tau_L \leq 10^{-7}$sec.

A third relevant timescale, τ_R , characterises any relaxation processes in the nuclear environment. For example, electronic spin-spin interactions with neighbouring ions or spin-lattice interactions may cause the spin directions of unpaired electrons to alter or 'flip' over a period of time τ_R. Since the magnetic hyperfine field

is often predominantly generated by the unpaired electron spins (via the Fermi contact interaction), it will fluctuate as well. If the relaxation is 'fast' with $\tau_R \ll \tau_L$ the nucleus will sense a time-averaged field which is less than the instantaneous value of B_{hf}, and may even be zero (as in a paramagnet). If the relaxation is 'slow' with $\tau_R \gg \tau_L$ the nucleus senses a static B_{hf} and yields a fully split spectrum. In the intermediate regime $\tau_R \sim \tau_L$ the nucleus will sense a range of hyperfine fields and the spectrum will exhibit broadened lines. In this way Mössbauer spectroscopy may sometimes be used to investigate dynamic processes in the solid state.

CHAPTER FOUR

EXPERIMENTAL

In this chapter the experimental techniques utilised for the work presented in this thesis are discussed. Reference is made to the experimental apparatus used, the method of sample preparation and the subsequent computer analysis of the spectral data.

4.1 EXPERIMENTAL APPARATUS

4.1a Mössbauer Spectrometer

Experimental methods in Mössbauer spectroscopy are well established (Cohen and Wertheim 1974) although the details of the instrumentation used may vary considerably from one laboratory to another. The transmission Mossbauer spectrometers in use in Liverpool (Figure 4.1) are based on those first used at AERE in Harwell (Cranshaw 1964). Each spectrometer consists of a γ-ray source, a mechanism for modulating the γ-ray energies (by vibrating the source), an absorber and a system to detect the transmitted γ-rays.

4.1a(i) γ-Ray Source

The most commonly used γ-ray source in this laboratory consists of radioactive ^{57}Co diffused into a foil of rhodium metal. These sources are commercially produced (Amersham International Ltd.) and have an initial activity of ~100mCi and a half-life of ~270 days. During the decay of ^{57}Co to ^{57}Fe a low energy 14.41 keV γ-ray is emitted (see Figure 4.2) which is ideally suited to Mössbauer effect experiments. Rhodium is chosen as the host matrix for the ^{57}Co because the emitted γ-rays make up a single-line source, and the source linewidth $\Gamma_s \simeq 0.11$mm/s is close to the theoretical minimum linewidth $\Gamma_o \simeq 0.097$mm/s as well as being largely temperature independent.

A second type of source used in Liverpool is ^{57}Co doped into iron metal. This is a six-line source since there is a hyperfine field acting on the ^{57}Co nuclei which splits the I=3/2 and I=1/2 levels of

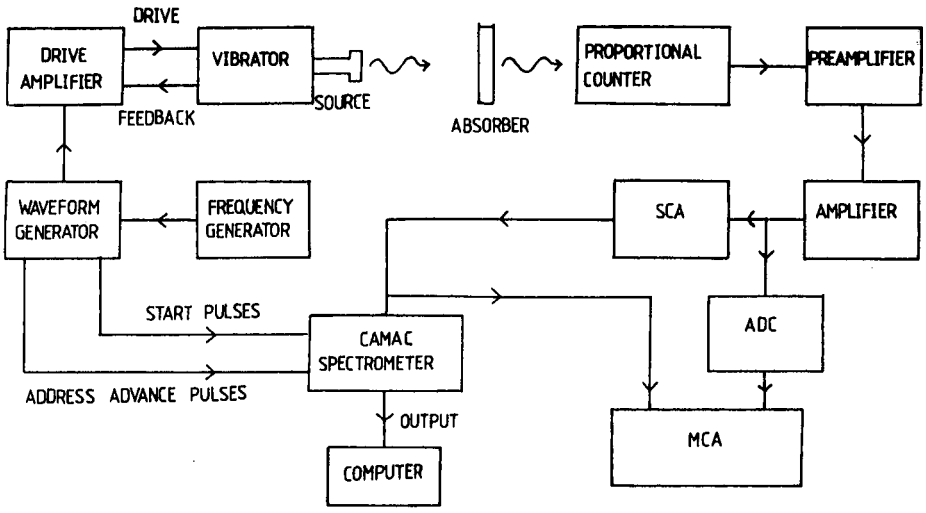

Figure 4.1 Schematic diagram of a Mössbauer spectrometer of the type used in Liverpool.

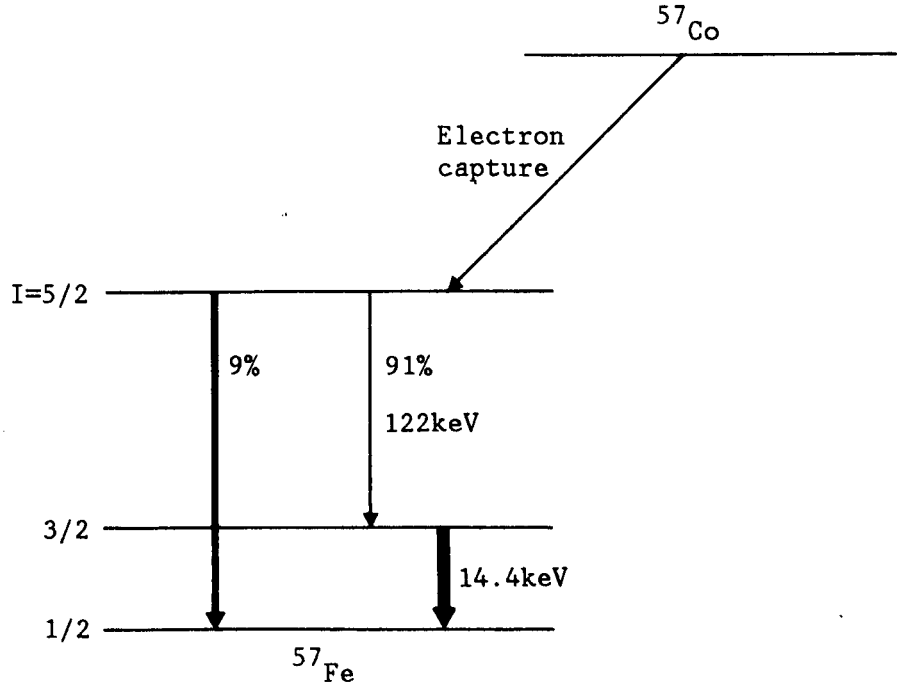

Figure 4.2 Decay scheme of ^{57}Co.

the ^{57}Fe decay product. This source had a lower activity than the others (initially ~25mCi) and is primarily used as a calibration source (see later).

4.1a(ii) Drive System

The energy modulation of the γ-rays is obtained by moving the source relative to the absorber. This motion is provided by the 'drive system' depicted in the upper left part of Figure 4.1. A waveform generator produces an asymmetric triangular waveform which, when integrated by the drive amplifier, generates a drive signal that determines the source displacement. The source is mounted on the drive-shaft of a 'vibrator', which is an electromechanical device similar to a loud-speaker.

The drive signal is parabolic for about 80% of each cycle and the corresponding source motion undergoes a constant acceleration. During this time the source moves away from the absorber, reaches a stationary point and then returns towards the absorber. In the remaining 20% of each cycle the source executes a rapid flyback. The quality or 'linearity' of the source motion is monitored by a voltage signal obtained from a pick-up coil around a part of the vibrator's drive-shaft which carries a small permanent magnet. Comparison of this 'feedback' signal with the drive signal enables corrections to be applied by the drive amplifier.

4.1a(iii) γ-Ray Detection

The components of the spectrometer that comprise the γ-ray detection system are shown in the right half of Figure 4.1. A gas proportional counter containing about 90% argon and 10% methane registers voltage pulses whose magnitude (or 'pulse-height') is proportional to the energy of the incident γ-ray. The pulses are shaped and amplified by a pre-amplifier and a spectroscopic amplifier, and may be displayed as a 'pulse-height spectrum' on a multi-channel analyser (MCA) after

being fed through an analogue-to-digital converter (ADC). The 14.4 keV γ-ray pulses are selected by a single-channel analyser (SCA), the setting of which is aided by reference to the MCA pulse-height spectrum.

4.1a(iv) CAMAC System

The overall operation of the spectrometer is controlled by a 'computer automated measurement and control' (CAMAC) data acquisition system that was developed by the Liverpool physics department's electronics group. At the beginning of a parabolic cycle of motion of the source the waveform generator sends a 'start pulse' to the CAMAC which sets it to the first channel and opens it to receive pulses from the SCA. After a fixed length of time, corresponding to a specific change in the source velocity, the CAMAC is sent an 'address advance pulse' by the waveform generator. The CAMAC then adds the number of γ-ray pulses or 'counts' received in that time to the number already in that channel before moving on to the next channel. This sequence continues for 255 address advance pulses (256 channels) while the vibrator scans through its full velocity range. There is then a period of 'dead-time' during which no counts are recorded and the source undergoes its flyback motion, before the entire process starts again.

In this way the CAMAC spectrometer accumulates a Mossbauer spectrum of γ-ray counts versus channel number. The spectrum may then be displayed on a terminal screen or sent via a data-line directly to a main-frame computer for storage and analysis.

4.1b Control of the Absorber Environment

In the Liverpool laboratory there are eight spectrometers of the form described above, each associated with a particular set of experimental apparatus. The different experimental sets offer different experimental conditions for the absorber, with a selection of

cryostats and a furnace allowing sample temperatures of between 1.3K and 1000K to be obtained, and with magnetic fields of up to 14T available at 4.2K. In the present work experiments were for the most part carried out on three different spectrometer sets : a variable temperature cryostat and two superconducting magnets.

4.1b(i) Variable Temperature Cryostat

For experiments requiring a variable sample temperature an Oxford Instruments CF500 'continuous flow' cryostat was used. This cryostat (Figure 4.3) operates by controlling the transfer of a coolant (such as liquid helium or liquid nitrogen) from a storage dewar to the sample space, and has been described in some detail by Bell (1983).

The cryostat is constructed from aluminium alloy, copper and stainless steel, and has sample space windows of aluminised mylar and radiation shields of aluminium foil. The sample is cooled by thermal contact with a 'heat exchanger' (a copper block) which is connected by a capillary tube to the coolant. The thermal contact is provided by the close proximity of the sample to the heat exchanger, and is enhanced via a small amount of helium exchange gas (or any other extraneous gases) in the sample space vacuum. The sample temperature is maintained by an Oxford Instruments DTC2 digital temperature controller which senses the sample temperature through a nickel-manganin grid resistance thermometer mounted on the sample holder. A suitable rate of coolant flow is selected manually by adjusting a needle valve on the rotary suction pump and the controller then stabilises the sample temperature by dissipating power into an electrical heater attached to the heat exchanger. In this way temperature control of better than about ±0.2K may be obtained. A calibrated resistance thermometer (carbon-glass) is also mounted on the sample holder. This thermometer provides more accurate sample temperature measurements than the Ni-Mn thermometer, but is not connected to the temperature controller.

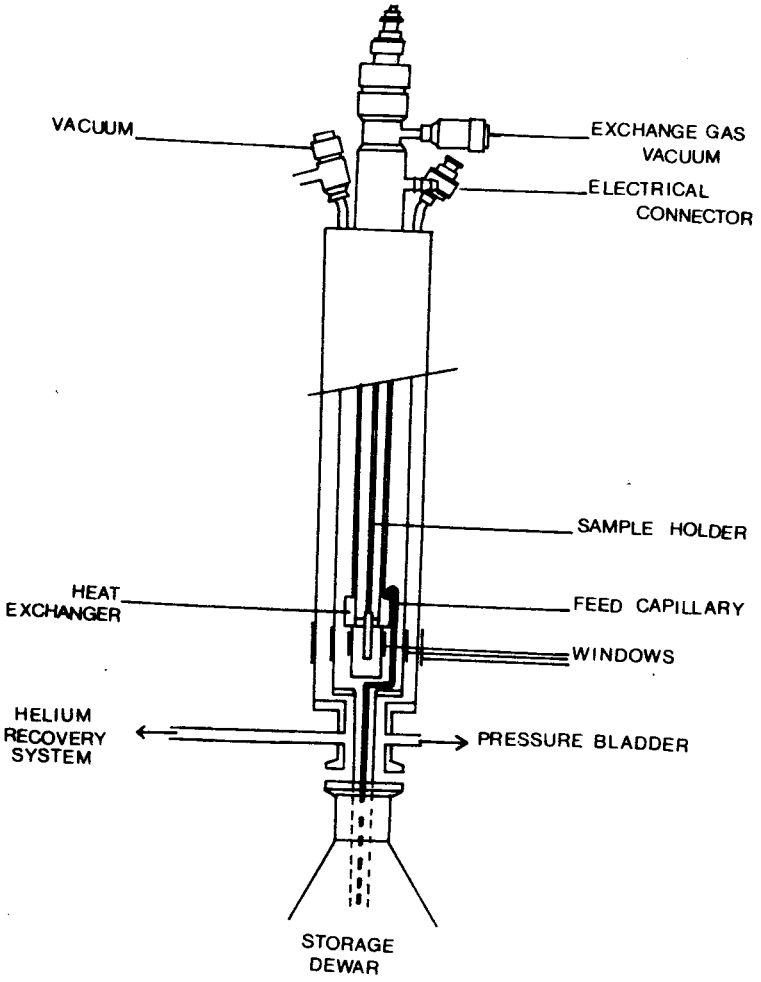

Figure 4.3 Diagram of the variable temperature cryostat.

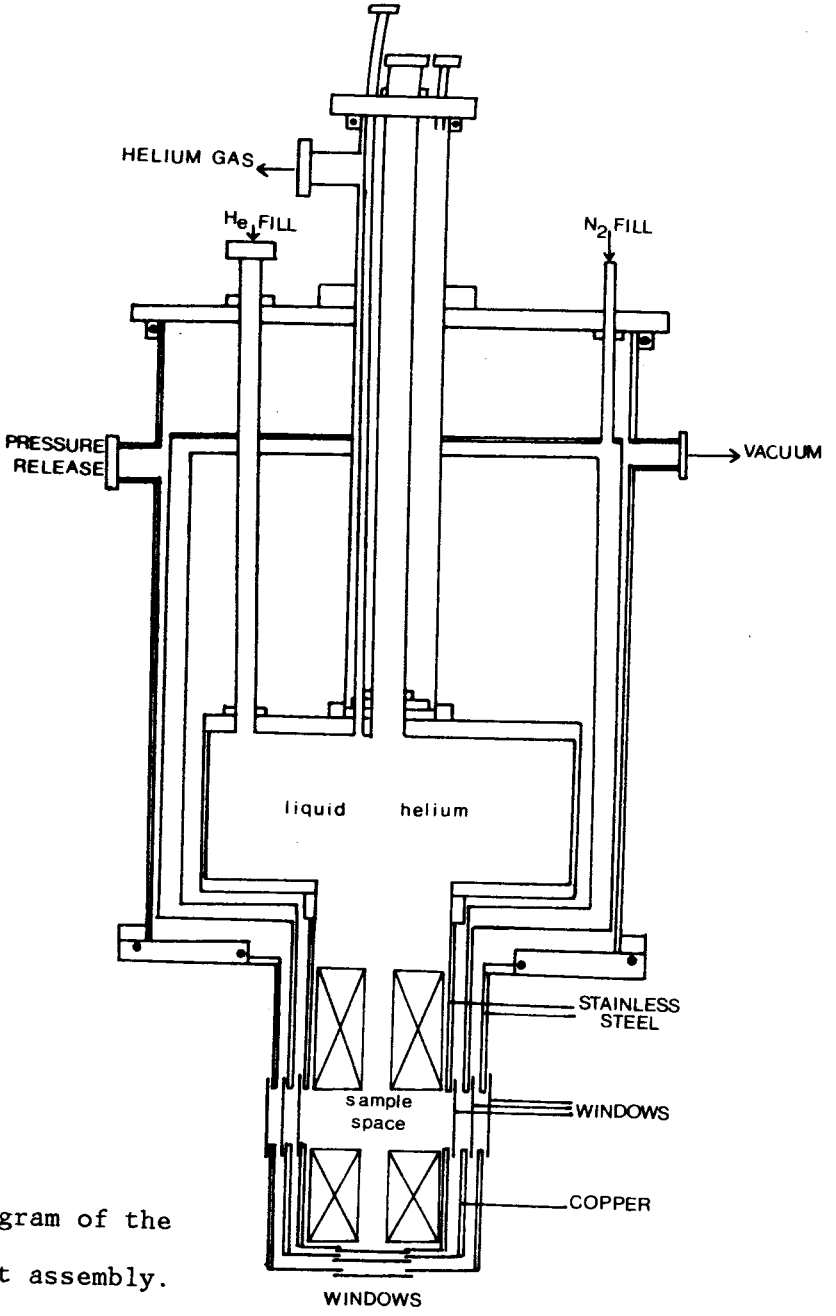

Figure 4.4 Diagram of the 10T magnet assembly.

4.1b(ii) Ten Tesla Superconducting Magnet

In the majority of the spectra presented in this thesis the absorber was subjected to an external magnetic field. For applied fields of up to 10T a Thor Cryogenics Ltd. superconducting magnet was used. This magnet consists of a split-pair of coils wound from NbTi wire, and is approximately 21.6cm in height, 14cm in diameter and has a 25mm bore. The solenoid is capable of carrying ~57.7A of current and producing a field of ~10T at the mid-point of the coils. Operation of the magnet requires that it be immersed in liquid helium and it is therefore housed in a low temperature cryostat (Figure 4.4) which was constructed in the departmental workshops. The uniformity of the field produced by the solenoid is very good (~±1%) within a vertical displacement of about ±7mm from the mid-point of the coil pair, and radially over the bore.

The Mössbauer spectrometer on the 10T magnet may be set up so that the applied field is either perpendicular to or parallel to the direction of the γ-ray beam. In the perpendicular mode the sample is suspended from the top of the cryostat and the γ-rays are directed horizontally through it and through the gap between the two magnet coils. To obtain the parallel mode a 'vertical drive' system is used, which allows the γ-ray beam to be directed vertically through the magnet bore. This system, shown in Figure 4.5, consists of a vibrator which drives a long drive-shaft (a thin-walled stainless steel tube) to which the source is attached. The sample is clamped at the bottom end of a second stainless steel tube which surrounds the drive-shaft. The distance between the source and the sample is fixed at ~11cm, and is such that when the sample is positioned in the centre of the solenoid the source is in a region of zero applied field. The null field region results from a small reverse-wound coil in the magnet at

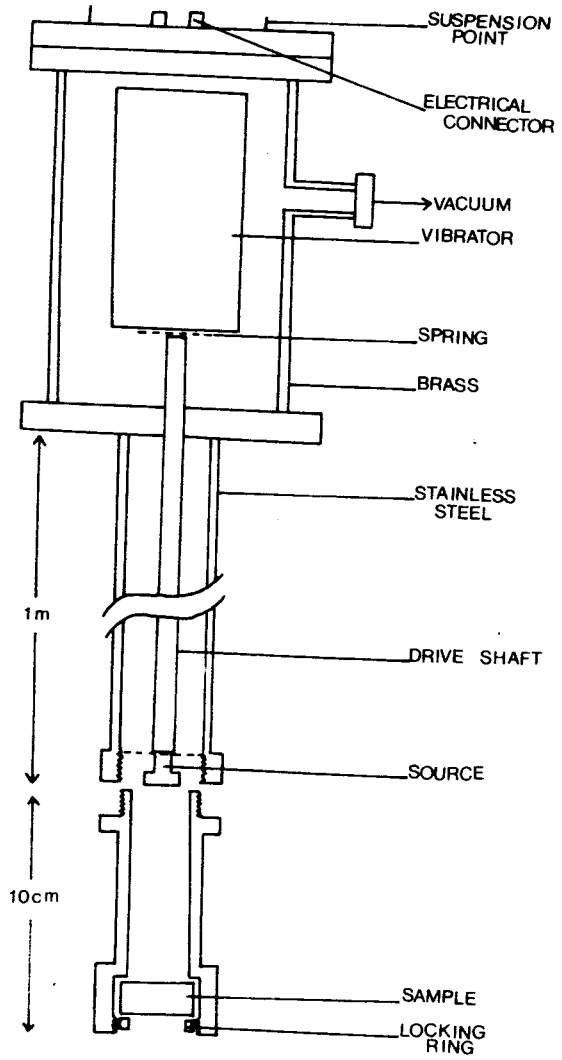

Figure 4.5 Diagram of the 'vertical drive' assembly.

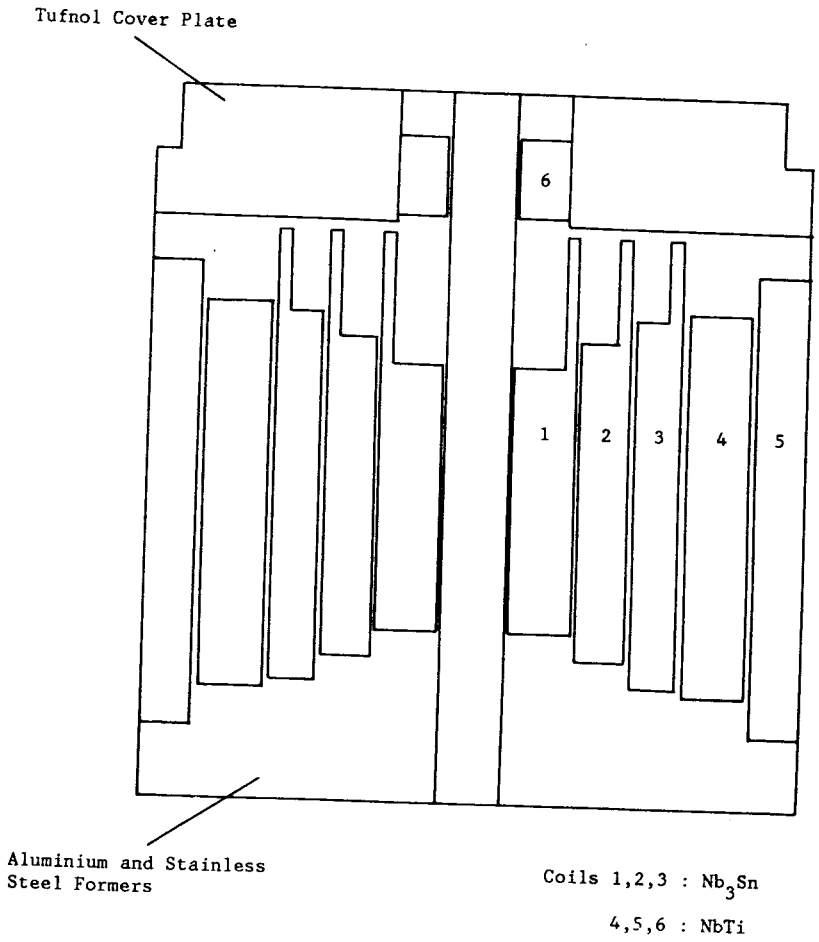

Figure 4.6 Cross-section of the 14T magnet solenoid.

that point. Thus the potential problem of a broadening of the source linewidth by the presence of a large magnetic field is avoided.

4.1b(iii) Fourteen Tesla Superconducting Magnet

Applied fields of greater than 10T were obtained using a Cryogenic Consultants Ltd. superconducting magnet that was recently commissioned in this laboratory. This magnet is a single solenoid wound from sections of NbTi and Nb_3Sn wire and is capable of carrying ~93.3A of current at 4.2K to give a field of ~14T at its centre point. A diagram of the magnet (which is about 27cm in height, 25cm in diameter and has a 25mm bore) is shown in Figure 4.6. The uniformity of the field is comparable to that of the 10T magnet, with a design specification of less than ±0.4% deviation within a central cylinder 5mm long and 15mm in diameter. The liquid helium cryostat in which the magnet operates is very similar to that of the 10T magnet (Figure 4.4). The design of the magnet dictates that spectra may only be taken in the 'parallel mode', with the γ-rays parallel to the field. The vertical drive of Figure 4.5 is therefore used, although since the distance between the null field point and the centre of the 14T magnet is larger than the corresponding distance in the 10T magnet an elongated sample-holding section is used.

One problem that was encountered whilst setting up the 14T magnet apparatus was that the observed Mössbauer spectra had very broad lines, of width ~0.4mm/s. This was attributed to mechanical vibrations in the cryostat. In an attempt to reduce these vibrations the cryostat was suspended from a 2cm aluminium alloy plate supported on two sides by massive concrete blocks. The linewidth was then better but still not good, so inflated rubber tyre inner-tubes were placed between thee steel plate and the concrete blocks. The cryostat was thus supported on a 'cushion of air' and mechanical vibrations were expected to be nearly absent. However the Mössbauer lines were still somewhat broad.

The source of this remanent broadening was eventually traced to electrical effects known as 'earth loops' which produce random fluctuations in the velocity drive signal. These effects were eliminated by insulating the cryostat from all its attendant electrical devices (pressure gauges, level sensors, etc.). A Mössbauer linewidth of ~0.28mm/s was then obtained which is quite good in light of the inherent non-linearity and susceptibility to vibration of the vertical drive system itself.

4.2 SAMPLE PREPARATION

4.2a Chemical Synthesis

Single crystals of K_2FeF_5 and Rb_2FeF_5 were prepared by Mrs B.M. Wanklyn at the Clarendon Laboratory, Oxford, using the 'flux growth' method (Wanklyn 1975, Wanklyn et al. 1979). The component fluorides AF (A=K,Rb) and FeF_3 were combined in stoichiometric ratio and placed in a platinum crucible along with some $PbCl_2$ flux. The purpose of the flux was to lower the melting point of FeF_3 (normally more than 1000°C) to near that of $PbCl_2$ (550°C). In this way the chemical reaction $2AF + FeF_3 = A_2FeF_5$ could be achieved by heating the crucible to ~650°C in a muffle furnace, avoiding the possibility of decomposing the constituent fluorides. On slow cooling of the solution (~1.5°C per hour) transparent crystals formed within the flux, the largest of which were about 3×2×1mm in size. The powder X-ray diffraction patterns of these crystals were then compared with those reported by Tressaud et al. (1970), and the crystals thereby identified as the desired compounds K_2FeF_5 and Rb_2FeF_5.

Single crystals of α-Fe_2O_3 were prepared in the same way (at the Clarendon Laboratory) by Mrs B.M. Wanklyn and Mr B.E. Watts. A variety of different flux compounds were tried, with PbO/PbF_2 and $Na_2B_4O_7$

providing the best results in the form of basal-plane platelets of area up to ~4mm×3mm. The fluxes Bi_2O_3/V_2O_5 and $NaVO_3$ were also tried but the resulting hematite crystallites were too small to be of use for single-crystal Mössbauer experiments.

4.2b Absorber Preparation and Mounting

In order that the single crystal K_2FeF_5, Rb_2FeF_5 and α-Fe_2O_3 samples be made suitable for Mössbauer experiments, they needed to be abrasively thinned. This was achieved by the following procedure. First the crystal is set in a tablet of epoxy resin (Oxford Instruments 'M5 Epoxy Resin Adhesive') with a chosen planar face of the crystal parallel to the tablet base. That crystal face is then exposed and polished by manually 'rubbing down' the base surface of the tablet with a fine grade of silicon-carbide abrasive paper, before being covered over again by a thin layer of epoxy resin. The top face of the tablet is then rubbed down until the remaining slice of sample is of a thickness that makes it suitable for transmission Mössbauer spectroscopy. The top face of the crystal is then covered with a protecting layer of epoxy resin and a lead mask attached to prevent γ-rays from missing the sample and adding to the background counts of the Mössbauer spectrum.

The optimum thickness of the sample is best determined by observing the percentage absorption of the Mössbauer spectral lines several times during the rubbing down process. In the beginning the sample is thick and the absorption lines are broadened and have distorted relative intensities. As the sample is rubbed down both the observed absorption and the count rate (the number of γ-rays passing through the sample in unit time) increases. When the sample is 'thin', continued thinning gives rise to a decrease in the percentage absorption as there are then less absorbing nuclei present. Thus the optimum thickness

corresponds to the point where the observed percentage absorption has just passed through its maximum and is beginning to decrease.

A less well-defined (but faster) method of determining optimal thickness is to observe the pulse-height spectrum of the γ-ray beam passing through the sample and rub down the crystal until the 14.4 keV γ-ray peak is well defined. This method is less time-consuming than the previous one, but requires a practiced eye to know what constitutes a 'good' pulse-height spectrum.

4.3 DATA ANALYSIS

In the previous sections we have seen how a single crystal absorber may be prepared, placed in a controlled environment and have its Mössbauer spectrum recorded. We now consider the way in which this spectrum may be analysed.

4.3a Velocity Calibration

4.3a(i) Calibration Spectrum

A Mössbauer spectrum is recorded as a series of γ-ray counts versus channel number. Before analysing the spectrum the energy scale must be established by finding the calibration relationship between channel number and source velocity. The usual method of velocity calibration is to measure the spectrum of a material with a well known hyperfine splitting. In ^{57}Fe Mössbauer spectroscopy the standard material is usually iron metal (α-Fe) at room temperature. The ideal line positions of α-Fe are calculated from the spectroscopic splitting factors E_e=-2.2363±0.0007mm/s and E_g=3.9156±0.0017mm/s (depicted in Figure 2.2c of Chapter 2) that were reported by Stevens and Preston (1972). Since the quadrupole splitting in α-Fe is thought to be identically zero these values of E_e and E_g imply that in the six-line spectrum

obtained using a ^{57}Co/Rh source the line positions are ±5.312, ±3.076 and ±0.840 mm/s relative to the centroid. These positions compare very favourably with those measured by the United States National Bureau of Standards (NBS 1971). A typical calibration spectrum taken in this laboratory is shown in Figure 4.7a. Comparison of the experimental line positions with the ideal values enables the velocity-to-channel calibration to be made.

The Mössbauer spectrum of α-Fe also offers a calibration relationship between magnetic hyperfine field and velocity. Since the spectroscopic splittings E_e and E_g are related to the hyperfine field B by $E=g\mu_N B$ (where $g=\mu/I\mu_N$ is the nuclear g-factor), we may calculate B from $E_e=2\mu_e B/3$ and $E_g=2\mu_g B$. Stevens and Stevens (1975) report that the ground state magnetic moment $\mu_g=(0.090604\pm0.000009)\mu_N$ and the ratio $\mu_e/\mu_g=-1.7142\pm0.0004$, which yields B=32.95±0.01T at room temperature. Comparing this field with the outer line splitting in α-Fe of 10.624mm/s thus provides a direct conversion factor between velocity and field.

A second type of calibration spectrum, obtained with the six-line ^{57}Co/Fe source, is shown in Figure 4.7b. The spectrum of α-Fe with such a source consists of 36 lines, some of which overlap to yield 13 distinct lines. Since the ideal velocity of each of the 13 lines is known, this spectrum offers a more complete velocity calibration than the 6 line type. However the 13 line spectrum requires a greater counting time and necessitates a change of source (which may alter the character of the spectrometer), and therefore it is not used as frequently as the 6 line spectrum.

4.3a(ii) Computer Fitting with Fit-A

The experimental line positions are obtained by computer fitting the calibration spectra using a program known as 'Fit-A'. This is a simple curve-fitting program which was brought to this laboratory by

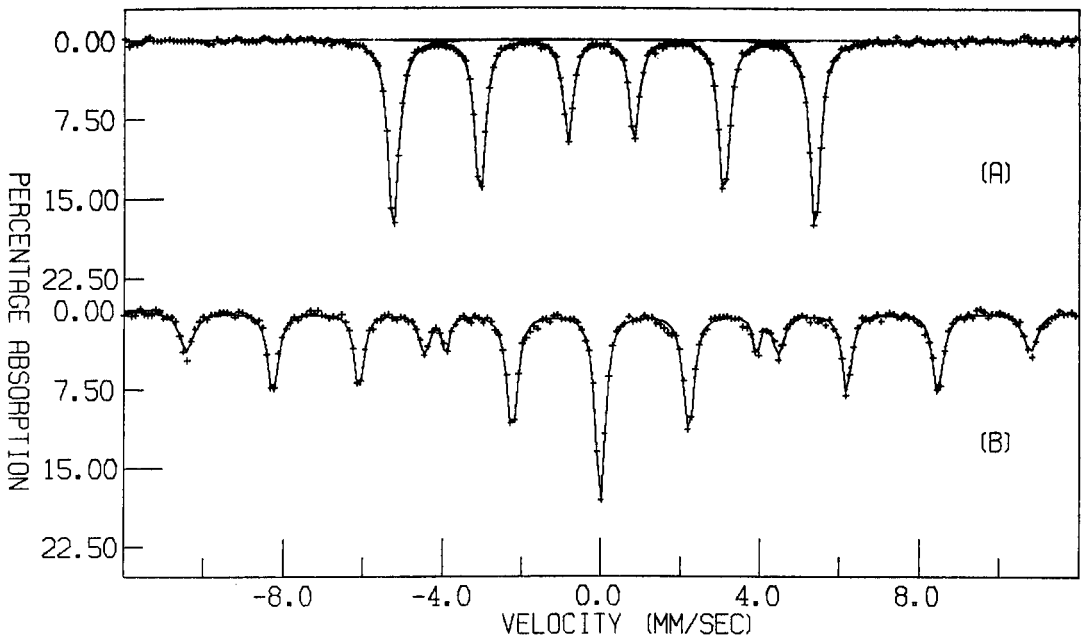

Figure 4.7 Calibration spectra of α-Fe at room temperature using (a) a single line ^{57}Co/Rh source and (b) a six line ^{57}Co/Fe source.

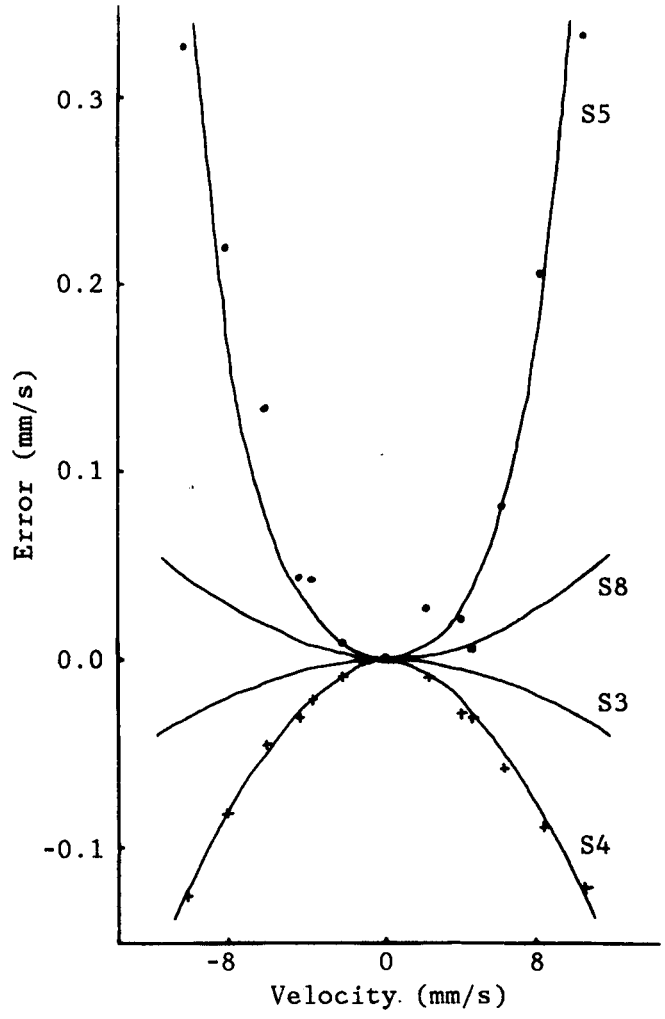

Figure 4.8 Observed error (experimental-ideal line positions) versus ideal velocity for four spectrometers. Solid curves are parabolic fits to the data. For clarity the data points for S4 and S5 only are shown.

G.J. Long and installed on the departmental IBM 4331 computer by I.G. Rumford in 1983. In general Fit-A generates a theoretical spectrum consisting of Lorentzian-line singlets, doublets and sextets which are governed by a set of 'spectrum parameters' such as isomer shift, quadrupole splitting, internal field, linewidth and percentage absorption. This calculated spectrum is then compared to the experimental spectrum and the 'goodness-of-fit' parameter :

$$\chi^2 = \Sigma_k [E(k)-C(k)]^2/E(k)$$

determined. Here E(k) and C(k) are the experimental and calculated γ-ray counts in channel k of the spectrum. The program then manipulates the spectrum parameters (in a procedure known as 'least-squares fitting') until a minimum in χ^2 is found. In an ideal spectrum the minimum in χ^2 is equal to the number of channels minus the number of fitted parameters, but in practice it is usually somewhat larger than that.

Having computed the experimental line positions the velocity calibration may now be obtained. This is normally assumed to be linear and of the form :

$$v(k) = SCALE \times [k-CENTRE] \ , \qquad (4.1)$$

where SCALE is the velocity increment per channel and CENTRE is the channel at which the centroid of the α-Fe sextet lies. We should note that (4.1) gives the velocity relative to the α-Fe centroid (as is standard practice), and is not the absolute velocity. The channel which corresponds to the stationary point of the source is called CENBOW in Fit-A and differs from CENTRE by the equivalent of ~0.11mm/s. CENBOW also corresponds to the lowest point in the parabolic baseline of the spectrum since at that point the source is at its largest distance from the γ-ray detector.

In practice the velocity parameters of a given calibration spectrum are found by assuming values of SCALE and CENTRE and fitting the spectrum with Fit-A to compute the line positions. These positions are

then compared with the ideal values in a small program named 'CAL' (written by D.H. Jones in 1985) which runs on the department's GEC 4085 computer, and the interpolated values of SCALE and CENTRE found. These are then taken as input parameters and the spectrum re-fitted, to confirm their applicability.

4.3a(iii) Linearity Tests

If the velocity calibration was strictly linear and of the form of (4.1) the error on the observed line positions would show no correlations. However, plots of the observed error versus ideal velocity for four different spectrometers used in this laboratory (Figure 4.8) show distinct trends. These trends appear to be roughly parabolic, implying that a correction should be made to the velocity of (4.1), to give :

$$v'(k) = v(k) - QCORR \times [v(k)]^2 \ , \qquad (4.2)$$

where QCORR is a constant. A small program called 'QCAL' has been written by the author to computer fit the observed errors and thereby determine QCORR.

The non-linearity is greatest in the vertical-drive system (S5), for which QCORR≈0.0033, but is also significant in the horizontal-drive systems S3,S4 and S8. Further, it is notable that the two spectrometers with the most non-linearity (S4 and S5) both operate with J&P Engineering Ltd. vibrators, while the more linear spectrometers (S3 and S8) use Harwell Mössbauer Group Ltd. vibrators. This implies that drive non-linearity may depend on the quality of the commercial components used, as well as the particular characteristics of the individual spectrometer.

4.3b Computer Fitting with Fit-Q

The majority of the spectra presented in this thesis were analysed using a least squares fitting program called 'Fit-Q'. This program is

more sophisticated than Fit-A and allows the interpretation of a Mössbauer spectrum in terms of the spin Hamiltonian parameters of the absorber.

Fit-Q is based on 'LANG6' which in turn is a modified version of 'LANG', a program written by Lang and Dale (1973,1974). In essence the program consists of two parts - one which calculates a theoretical spectrum for given parameters (via subroutines MGFITA, HINTER and SPFN), and one which varies the parameters in such a way as to minimise the mean square difference between the theoretical and experimental spectra (subroutines VA05A, CALFUN and LINFIT). The original program (LANG) was written to accommodate I=3/2 to I=1/2 nuclear transitions in paramagnetic and diamagnetic materials subject to applied fields. Fit-Q is somewhat simpler than LANG and is intended for use with the spectra of magnetically ordered powder or single-crystal absorbers in applied fields.

The theoretical spectra in LANG are derived from a spin Hamiltonian of the form $H=H_Q+H_M$ where :

$$H_Q = [eQV_{zz}/4I(2I-1)].[3I_z^2-I(I+1)+\eta(I_x^2-I_y^2)] \qquad (4.3)$$

is the nuclear quadrupole interaction (as discussed in Chapter 3.3b), and :

$$H_M = \mu_B \underset{\sim}{B} \cdot \underset{\approx}{g} \cdot \underset{\sim}{S} + \underset{\sim}{I} \cdot \underset{\approx}{A} \cdot \underset{\sim}{S} - g_N \mu_N \underset{\sim}{I} \cdot \underset{\sim}{B} \qquad (4.4)$$

is the magnetic interaction. Here $\underset{\sim}{I}$ is the nuclear spin, $\underset{\sim}{S}$ the atomic spin, $\underset{\sim}{B}$ the applied field, g_N and μ_N the nuclear g-factor and magneton, and $\underset{\approx}{g}$ and $\underset{\approx}{A}$ second-rank tensors representing the atomic g-factor and the hyperfine interaction between the electronic spin and the nucleus. All the terms are defined in the electric field gradient principal axis coordinate system. The spin Hamiltonian used in Fit-Q is similar to this, except that the electronic Zeeman term in (4.4) is removed and the remaining two terms treated as an effective magnetic field acting on the nucleus. Thus the magnetic interaction is taken as :

$$H_M' = -g_N \mu_N \underset{\sim}{B}_{eff} \cdot \underset{\sim}{I} \ , \qquad (4.5)$$

where $\underset{\sim}{B}_{eff} = \underset{\sim}{B} + \underset{\sim}{B}_{hf}$ is the vector sum of the applied and hyperfine fields.

It is interesting to note that the theoretical Mössbauer spectra generated in Fit-Q may contain up to eight lines. This feature appears when the electric quadrupole and magnetic interactions are of a comparable size and the usual first-order perturbative methods (as discussed in Chapter 3.3d) are not applicable. In Fit-Q the spectral line energies and intensities are computed in the subroutine SPFN, using a method that is similar to that described by Kundig (1967). The Hamiltonian matrices of the I=3/2 excited state and the I=1/2 ground state are first constructed in the $|Im\rangle$ basis by expressing $H=H_Q+H_M'$ in terms of the projection operator I_z and the ladder operators $I_\pm=I_x\pm I_y$. (We recall that $I_\pm|Im\rangle=[I(I+1)-m(m\pm1)]^{\frac{1}{2}}|Im\pm1\rangle$ and that $I_z|Im\rangle=m|Im\rangle$.) These matrices are then diagonalised and the transition energies obtained directly from the differences between the eigenvalues of the excited and ground states. The transition probabilities are calculated from the eigenvectors and the vector operator representing the incident photon. Since the eigenvectors are linear combinations of the $|Im\rangle$ basis vectors the photon may induce eight distinct transitions while retaining the selection rule (discussed previously in Chapter 3.4) that $\Delta m=\pm2$ transitions be forbidden.

The input dataset that is used by Fit-Q contains a set of hyperfine parameters, a 'constraint matrix' and the experimental spectrum. The hyperfine parameters include those which specify the experimental conditions under which the spectrum was recorded, such as the velocity calibration parameters, the γ-ray direction and the applied field magnitude and direction. The remaining parameters describe the Mössbauer spectra associated with up to four distinct sites in the absorber, and consist of the isomer shift SH, quadrupole splitting

SPL=$\frac{1}{2}eQV_{zz}(1+\eta^2/3)^{\frac{1}{2}}$, asymmetry ETA, linewidth FW and hyperfine field A. The 'constraint matrix' is a list of integers which determines which of the parameters are to be varied. If two or more parameters are given the same non-zero integer value in this list they are varied in such a way that the ratio between them is kept constant.

It may also be noted that in Fit-Q all the lines in a given sub-spectrum are assumed to have identical linewidth. The program may therefore be regarded as operating in the 'thin absorber approximation' where the effect of line broadening due to finite sample thickness (as discussed in Chapter 3.4) is taken to be negligible. Line intensity ratios are similarly calculated on the basis of zero absorber thickness. Both of these assumptions greatly simplify the theoretical problem of constructing a Mössbauer spectrum but will not be precisely realised in experimental spectra, and consequently the mis-fit parameter χ^2 will often be rather higher in practice than its theoretical minimum value.

CHAPTER FIVE

K_2FeF_5 AND Rb_2FeF_5

5.1 INTRODUCTION

Initial interest in K_2FeF_5 and Rb_2FeF_5 came as part of a wider study of the structural and magnetic properties of the fluorides of transition metals by the Solid State Chemistry group at Bordeaux University. Portier et al. (1968), Tressaud (1969) and Tressaud et al. (1970) studied the fluorides $A_xFe_yF_z$ where the monovalent cation A was one of Li, Na, K, Rb or Tl. These compounds were found to consist of networks of $(FeF_6)^{3-}$ octahedra, ranging from three-dimensional lattices in the phases $AFeF_3$, to layer structures as in $A_3Fe_2F_7$, $AFeF_4$, A_2FeF_4 and $A_5Fe_3F_{14}$, and the chain systems A_2FeF_5. It was expected that there would be some correspondence between the magnetic and structural properties of these compounds, since earlier work by Anderson (1963) and Goodenough (1963) had indicated that the magnetic coupling between the ferric ions was primarily by superexchange via the fluorine ions.

In Liverpool the magnetic properties of K_2FeF_5 and Rb_2FeF_5 were subsequently studied, and both systems were found to exhibit quasi one-dimensional characteristics. These observed properties included low Néel temperatures, zero point spin reduction, applied field dependent Néel temperatures and magnetisation curves, and the possible presence of soliton spin excitations. Publications related to these magnetic properties include Gupta et al. (1977, 1978a and 1979), Cooper et al. (1982), Boersma et al. (1982) and Pankhurst et al. (1985 and 1986) on K_2FeF_5 and Gupta et al. (1978b) and Pankhurst et al. (1986) on Rb_2FeF_5.

In the present work K_2FeF_5 and Rb_2FeF_5 were chosen to be the subject of a study of the spin-flop transition because of a number of advantageous features. Single crystal samples were available and after the considerable amount of previous work on the compounds in this laboratory their properties were well known. The exchange and anisotropy

fields in both K_2FeF_5 and Rb_2FeF_5 were known to be of such an order that the spin-flop field $B_{sf} \simeq (2B_E B_A)^{\frac{1}{2}}$ was experimentally obtainable (B_{sf}~3.7T in K_2FeF_5, ~7T in Rb_2FeF_5 at 4.2K). In fact the spin-flop itself had already been observed in K_2FeF_5 (Gupta et al. 1978a), although deficiencies in the experimental apparatus available at that time made a more detailed study worthwhile. It was also recognised that the anticipated critical fields were sufficiently large that readily discernible changes would occur in the observed Mössbauer spectra on passing through the transition. K_2FeF_5 and Rb_2FeF_5 were therefore considered well suited to a Mossbauer study of the spin-flop transition.

In the remainder of this introductory section we will review the crystallographic, electric and magnetic structures of K_2FeF_5 and Rb_2FeF_5. Subsequent sections of this chapter will then deal with the experimental results obtained, and their interpretation.

5.1a Crystal Structures

In 1970 Tressaud et al. analysed the X-ray diffraction patterns of K_2FeF_5 and Rb_2FeF_5 and found that both crystals possess orthorhombic symmetry. The unit cell dimensions that were determined at that time were only slightly revised in later work by Vlasse et al. (1977) on K_2FeF_5 and Dance et al. (1980) on Rb_2FeF_5. These dimensions are shown in Tables 5.1 and 5.2, which also illustrate the confusion that exists in the literature over the assignment of the lattice parameters to the crystallographic axes a, b and c. The present author (Pankhurst et al. 1986) has adopted the convention that b>c with a in extremum as a way of emphasising the similarities between the two crystal structures.

Table 5.1 Lattice parameters (in Ångstroms) of K_2FeF_5 as quoted in the literature.

a	b	c	References
7.35	12.76	19.66	Tressaud et al. (1970)
20.39	7.40	12.84	Vlasse et al. (1977), Hanzel et al. (1977), Gupta et al. (1977,1979)
20.39	12.84	7.40	Sabatier et al. (1979), Dance et al. (1980), Cooper et al. (1982), Johnson (1985), Pankhurst et al. (1985,1986)

Table 5.2 Lattice parameters (in Ångstroms) of Rb_2FeF_5 as quoted in the literature.

a	b	c	References
9.83	16.76	14.70	Tressaud (1969), Gupta et al. (1978b)
7.53	11.99	5.78	Tressaud et al. (1970)
7.54	5.79	11.98	Dance et al. (1980), Tressaud et al. (1981)
5.79	11.98	7.54	Pankhurst et al. (1986)

Both K_2FeF_5 and Rb_2FeF_5 are characterised by infinite chains of $(FeF_6)^{3-}$ octahedra running along the a axis. The major difference between the two crystals is that in Rb_2FeF_5 these chains are linear, while in K_2FeF_5 they form a zig-zag pattern in the ab-plane. This difference is illustrated in Figure 5.1, which is a simplified diagram of the projection of the two structures onto the ab-plane.

A study of the crystal structure of Rb_2FeF_5 by Dance et al. (1980) showed it to be isomorphous to that of Rb_2CrF_5 (Jacoboni et al. 1974). The crystal consists of FeF_6 octahedra sharing two adjacent ('cis') vertices which form linear chains along the a axis that are isolated from each other by the Rb atoms. The projection of the structure onto the bc-plane is given in Figure 5.2. The lattice parameter along the a axis, 5.79 Å, corresponds to a repeating unit of two octahedra which differ by a 'screw' symmetry operation about the chain axis. That is,

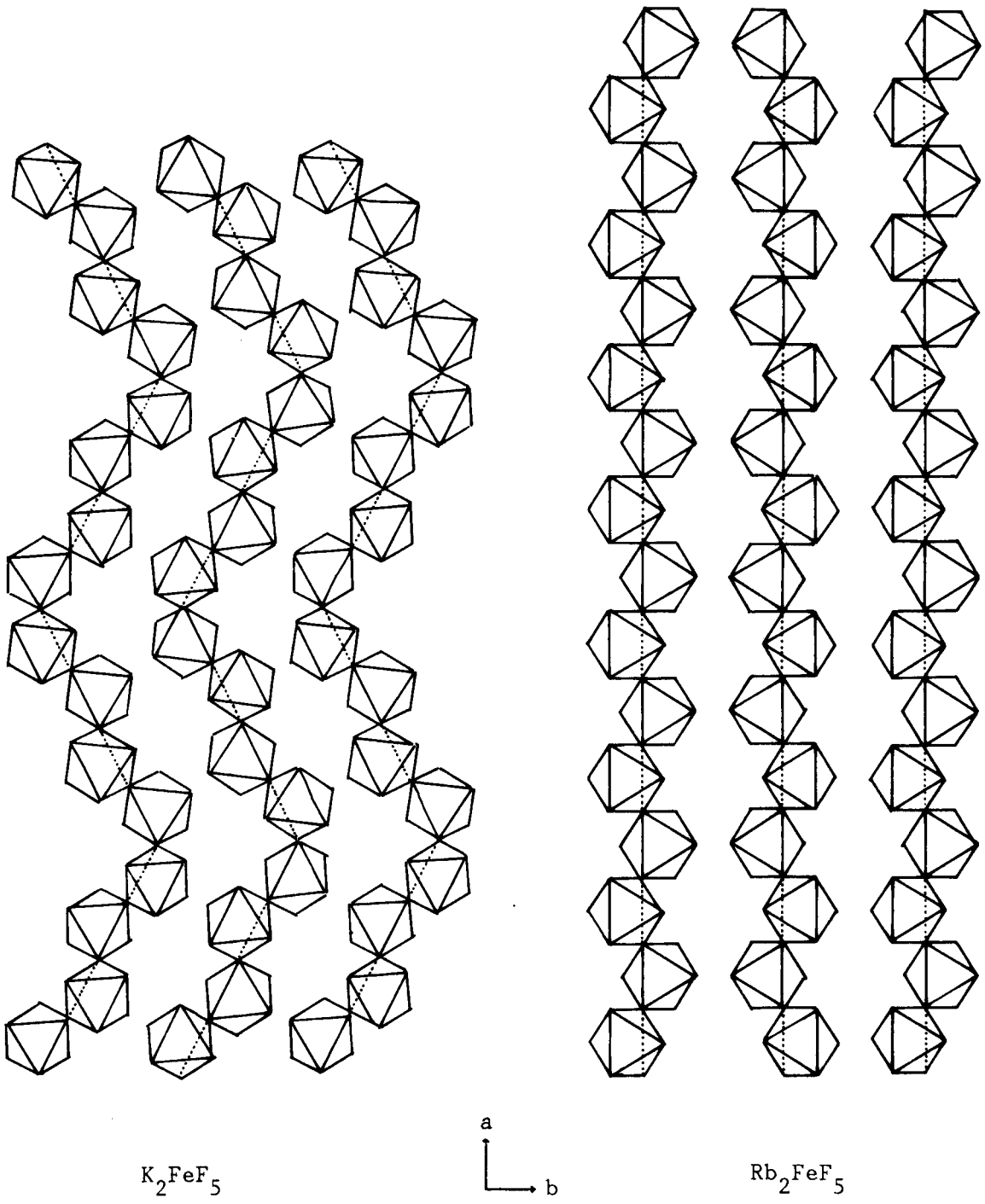

Figure 5.1 Schematic diagram of the chains of $(FeF_6)^{3-}$ octahedra which characterise the crystal structures of K_2FeF_5 and Rb_2FeF_5.

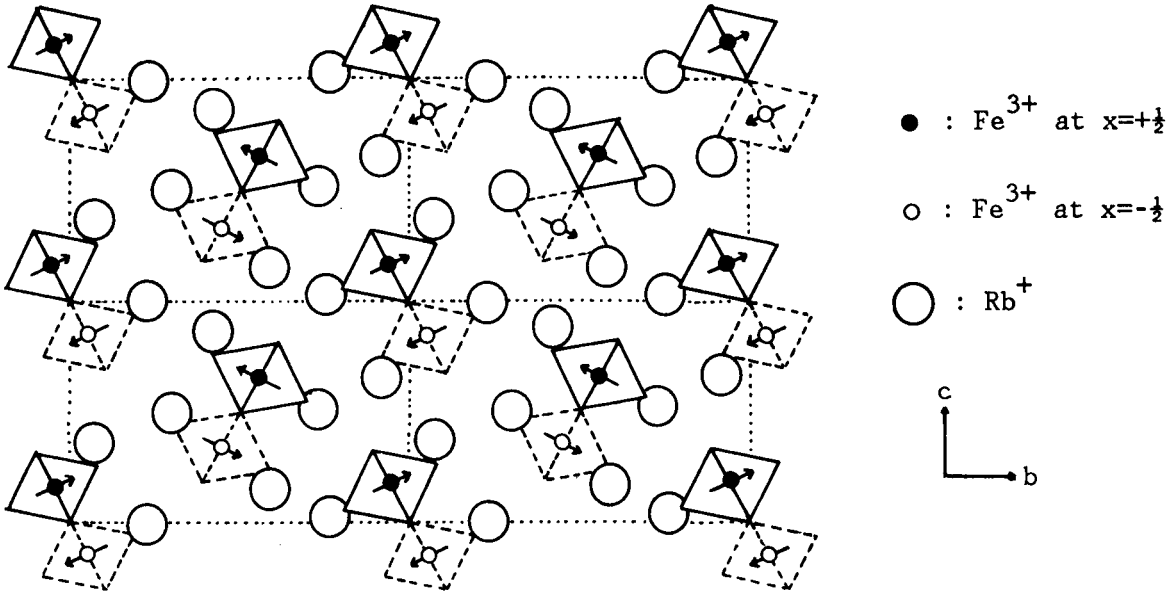

Figure 5.2 Projection onto the bc-plane of the crystal structure of Rb_2FeF_5. Arrows represent atomic spin directions.

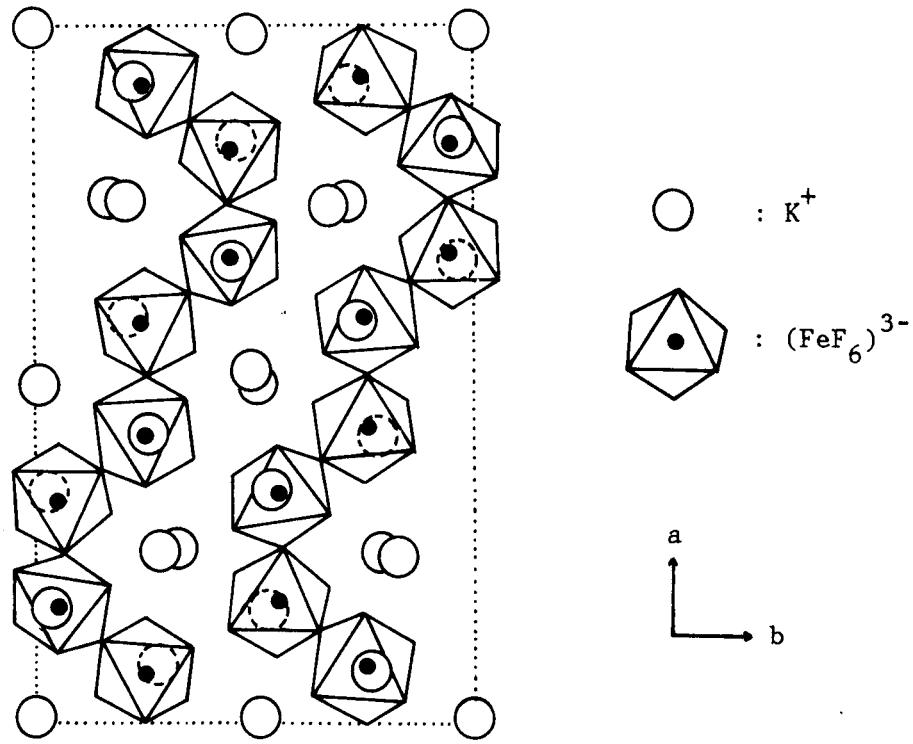

Figure 5.3 Projection onto the ab-plane of the crystal structure of K_2FeF_5.

rotating any given octahedron by 180° about the chain axis (the line connecting the shared fluorine ions) and translating it up or down the chain by ½a will bring it into coincidence with its neighbouring octahedron. Figure 5.2 also illustrates that neighbouring chains are not identical but differ by a reflection symmetry operation in the ac-plane.

The structure of K_2FeF_5 may be regarded as a similar but 'compressed' form of the Rb_2FeF_5 structure (Vlasse et al. 1977). In this case the chain axis (connecting shared fluorine ions) follows a zig-zag path in the ab-plane, as shown in Figure 5.1. Neighbouring chains are interspersed with K ions, as shown in a more complete unit cell diagram in the ab-plane in Figure 5.3. The lattice parameter along the a axis is 20.39 Å, and represents a repeating unit of eight octahedra. Comparison of this distance with the corresponding distance in Rb_2FeF_5 (eight octahedra in 4×5.79=23.16 Å) indicates the amount of compression that the zig-zag structure has achieved compared to the linear form.

5.1b Electric Field Gradient

Since the iron in K_2FeF_5 and Rb_2FeF_5 is in the high spin (S=5/2) Fe^{3+} state, the electric field gradient (EFG) at the ferric nuclei is dominated by the 'lattice' contribution while the 'valence' contribution of incompletely filled electron shells is effectively absent. Thus many of the characteristics of the EFG which may be observed by Mossbauer spectroscopy can be related to the lattice structure of the compounds, and in particular to the symmetry properties of the environment of the ferric ions.

Vlasse et al. (1977) noted that the FeF_6 octahedra in K_2FeF_5 are asymmetrically distorted. The average distance between a given Fe^{3+} ion and either of the two F^- ions that lie on the chain axis was de-

termined to be ~2.02Å, while the Fe-F distance to any of the other four 'terminal' F^- ions is ~1.88Å. A similar distortion was observed in Rb_2FeF_5 by Tressaud et al. (1981), with Fe-F ≃ 2.00Å for the 'chain' fluorines and Fe-F ≃ 1.86Å for the 'terminal' fluorines. These distortions lead one to anticipate a corresponding asymmetry in the EFG at the Fe^{3+} nuclei in both crystals.

Room temperature Mössbauer spectra of ac-plane single crystals of K_2FeF_5 and Rb_2FeF_5 are shown in Figure 5.4. (The crystal specimens used will be described in greater detail in following sections.) The spectra display a marked similarity. Computer fitting yields an isomer shift of $\delta \simeq 0.43$mm/s and a quadrupole splitting of $\Delta \simeq 0.72$mm/s in both spectra. We recall from Chapter 3 that Δ is defined as $\Delta = \frac{1}{2}eQ|V_{zz}|(1+\eta^2/3)^{\frac{1}{2}}$, where $|V_{zz}|$ is the magnitude of the EFG principal axis and $\eta=(V_{xx}-V_{yy})/V_{zz}$ is the asymmetry parameter. It is therefore evident that the room temperature evaluation of Δ provides limited information on the EFG, and does not define either the sign of V_{zz} or the degree of asymmetry. A more complex experiment is required to enable the determination of these quantities. Gupta et al. (1977,1978b) applied magnetic fields of 6T to polycrystalline samples of K_2FeF_5 and Rb_2FeF_5 at temperatures (~140K) at which the compounds were in their paramagnetic states. The resultant Mössbauer spectra could be unambiguously fitted to show that V_{zz} is negative in sign in both crystals and that the expected large asymmetry is present, with $\eta \simeq 0.57 \pm 0.05$ in K_2FeF_5 and $\eta \simeq 0.5 \pm 0.1$ in Rb_2FeF_5.

A second feature apparent in the room temperature spectra of Figure 5.4 is that in both cases the left-hand line is more intense than the right-hand line, with LH : RH ratios of about 1.2:1 in K_2FeF_5 and 1.4:1 in Rb_2FeF_5. As discussed in Chapter 3 the LH : RH intensity ratio is indicative of the angle θ between the incident γ-rays and the EFG principal axis direction. For negative V_{zz} the ratio is theoretically

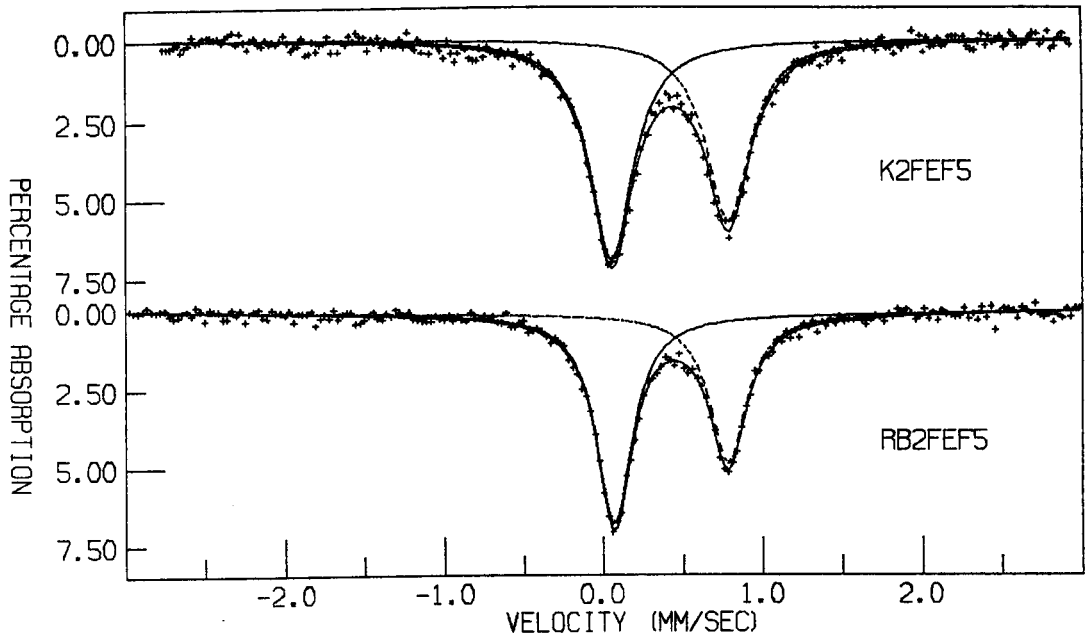

Figure 5.4 Room temperature Mossbauer spectra of ac-plane single crystals of K_2FeF_5 and Rb_2FeF_5.

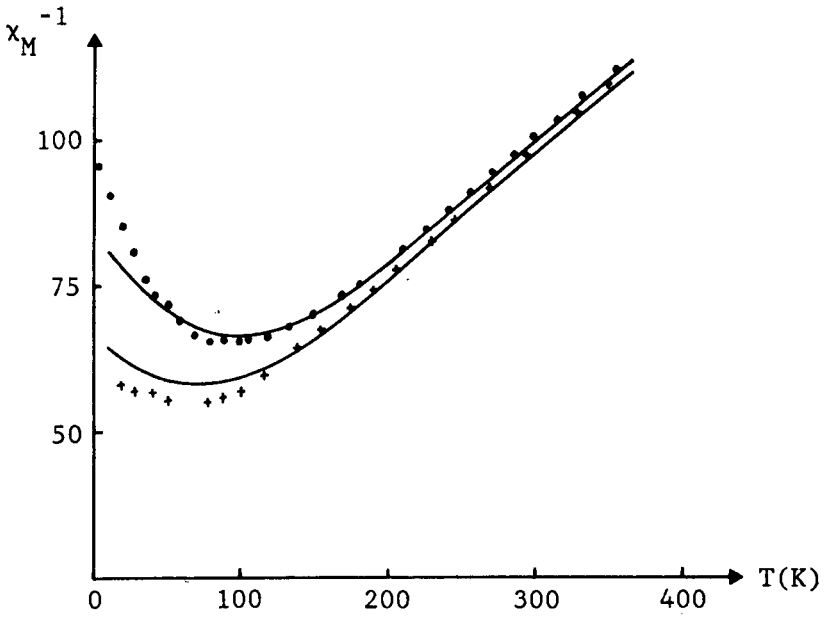

Figure 5.5 Temperature dependence of the inverse molar susceptibility (in CGS units) of K_2FeF_5 (•) and Rb_2FeF_5 (+) powders, as reported by Dance et al. (1980). Full curves were calculated using the method of Weng (1968).

LH : RH = $3(1+\cos^2\theta)$: $2+3\sin^2\theta$ (neglecting the effect of the non-zero η values), which implies that $\theta\simeq47°$ in K_2FeF_5 and $\theta\simeq43°$ in Rb_2FeF_5. Since the γ-rays were directed within a few degrees of the b axis it follows that the V_{zz} axis lies in the region of ~45° to the b axis in both crystals. More conclusive experiments have been conducted by Gupta et al. (1978b,1979) in which external fields were applied to magnetically ordered single crystal samples (at T≃4.2K). It was thus found that in both crystals the V_{zz} axis lies in (or close to) the bc-plane, at an angle ϕ to the b axis, with $\phi\simeq42°\pm5°$ in K_2FeF_5 (Gupta et al. 1979*) and $\phi\simeq40°\pm7°$ in Rb_2FeF_5 (Gupta et al. 1978b). V_{xx} lies along the a axis in both cases.

It may be seen that the EFG principal axis directions discussed above are in some accord with the known structures of the crystals. In Rb_2FeF_5 the environment of each Fe^{3+} ion has mirror symmetry in the bc-plane, and as a consequence V_{zz} lies in that plane. However, the measured angle $\phi\simeq40°$ between V_{zz} and the b axis does not appear to coincide with any particular plane of symmetry in the lattice. Another point is that by referring to the bc-plane cross-section of the Rb_2FeF_5 structure (Figure 5.2) it seems likely that there are in effect two V_{zz} directions in the crystal, each being associated with one of the two chain sublattices. That is, if the V_{zz} direction at a given ferric site lies at 40° to the b axis, the V_{zz} direction at a ferric ion on a neighbouring chain will lie at 180°-40°=140° to the b axis. This distinction between two sublattices with differing EFG principal axis directions will often be experimentally insignificant, as was the case in the spectrum of Figure 5.4 where the γ-rays were incident along the b axis.

---

* The lattice characterisation system a>c>b quoted in the second paragraph of Gupta et al. (1979) is misleading since the axes mentioned in the remainder of that paper correspond to the convention a<b<c (D.P.E. Dickson, private communication).

Comparisons between the observed EFG axis directions and the crystal structure of K_2FeF_5 are not so well defined as in Rb_2FeF_5 since the environment of the ferric ions in K_2FeF_5 does not possess mirror symmetry in the bc-plane. The zig-zag chain axis intersects the bc-plane at an angle of ~28°, so the mirror symmetry plane of the FeF_6 octahedra may be regarded as alternating between +28° and -28° of the bc-plane. Thus the fact that V_{zz} at the Fe^{3+} sites is observed to lie in the bc-plane is presumably a result of a long range averaging effect on the EFG in the crystal which overcomes the local symmetry preferences of the ferric ions' immediate environment.

5.1c Magnetic Properties

The nature of the magnetic ordering in K_2FeF_5 and Rb_2FeF_5 has been studied by several authors using a number of experimental techniques, including neutron diffraction, magnetic susceptibility and Mössbauer effect measurements.

Neutron diffraction experiments on K_2FeF_5 by Sabatier et al. (1979) and Dance et al. (1980) showed that below ~10K the ferric spins become antiferromagnetically aligned along (or close to) the crystal b axis. At 4.2K the Fe^{3+} ion magnetic moment was found to be ~3.0μ_B, a value which is ~40% smaller than the nominal 5μ_B associated with a spin 5/2 ion. Since the reduction in the moment due to covalency and crystal field effects is not expected to exceed ~10% the observed moment may be taken to infer the presence of spin wave induced spin reduction.

The magnetic susceptibility χ of a powder sample of K_2FeF_5 was also studied by Sabatier et al. (1979) and Dance et al. (1980). The observed dependence of inverse susceptibility χ^{-1} on temperature T is shown in Figure 5.5. A broad minimum occurs at T≈100K and χ^{-1} approaches a finite value as T→0, features that are indicative of antiferromagnetic ordering in low dimensional magnetic systems. At high temperatures

(T>350K) the susceptibility follows a Curie-Weiss law with $\chi=C/(T+\theta)$ and a Curie-Weiss temperature of $\theta\simeq125$K. The intrachain exchange constant J may be estimated from θ via the mean-field expression $k_B\theta=2zJS(S+1)/3$ with z=2 nearest neighbours and spin S=5/2, giving $J/k_B\simeq10.7$K (where k_B is Boltzmann's constant). A more refined estimate of J was determined by Sabatier et al. (1979) by fitting the $\chi^{-1}(T)$ data for T≥100K with a series expansion theory (Weng 1968). The fitted curve, shown in Figure 5.5, yields $J/k_B\simeq9.45$K for the exchange constant. Furthermore, the value of the interchain exchange constant J' may be estimated from the observed values of J, θ and T_N. The onset of long-range three dimensional ordering at T_N is largely governed by the magnitude of J', in a similar manner to the way that short-range correlations within the chains below θ are governed by J. It is therefore possible to derive a relation between the ratios J'/J and T_N/θ (Oguchi 1964). In this way the value $J'/J\simeq3.8\times10^{-3}$ may be estimated from the neutron diffraction and magnetic susceptibility data.

Several Mössbauer effect measurements on K_2FeF_5 have confirmed its quasi one-dimensional magnetic character. At low temperatures a saturation hyperfine field of ~41T is approached (Gupta et al. 1977), a value which represents a reduction of about 30% from the field of a free Fe^{3+} ion and is indicative of substantial zero point spin reduction. The Néel temperature was carefully measured by Cooper et al. (1982) to be 6.95K ± 0.05K. Experiments on oriented single crystal samples (Gupta et al. 1979) confirmed that below T_N the spins align along the b axis. Gupta et al. (1978a, 1979) and Cooper et al. (1982) compared the observed dependence of the hyperfine field on temperature and applied field with the predictions of spin-wave theory (as discussed in Chapter 2) to obtain estimates for the exchange constant ratio J'/J and the exchange and anisotropy fields B_E and B_A. The most

recent of these calculations (Cooper et al. 1982) gave $J'/J \simeq 9\times10^{-4}$, $B_A/B_E \simeq 8.5\times10^{-4}$ and $B_E \simeq 83.0$T.

A similar series of experiments have been performed on Rb_2FeF_5. Neutron diffraction measurements by Dance et al. (1980) and Tressaud et al. (1981) showed that three dimensional magnetic ordering takes place below ~8.0K, but that in the ordered state the spins were not collinear. Tressaud et al. (1981) established that the spins form four magnetic sublattices and that all the spins lie in (or close to) the bc-plane, canted at an angle $\phi \simeq 22° \pm 4°$ to the b axis. This structure is illustrated in Figure 5.2. The spins within any given chain are antiferromagnetically coupled to each other, but the angle between the AFM axis and the b axis alternates between ϕ and $180°-\phi$ for neighbouring chains.

The temperature dependence of the magnetic susceptibility of Rb_2FeF_5 (Dance et al. 1980, Tressaud et al. 1981), shown in Figure 5.5, is very similar to that seen in K_2FeF_5. Curve fitting yields $\theta \simeq 125$K for the Curie-Weiss temperature and $J/k_B \simeq 8.78$K and $J'/J \simeq 2.5\times10^{-3}$ for the exchange constants.

Mössbauer spectra of Rb_2FeF_5 show that the saturation hyperfine field is ~43T (Gupta et al. 1978b), representing a zero-point spin reduction of ~28%. A Néel temperature of ~9.3K was reported by Gupta et al. (1978b), although there is some doubt about this value. (The same authors had earlier measured $T_N \simeq 11.2$K in K_2FeF_5 (Gupta et al. 1977), a value that was later found to be in error because of inadequate thermal contact between the sample and temperature sensor. A similar overestimate of T_N in Rb_2FeF_5 is possible.) Below T_N the spectra of single crystal samples confirm that four magnetic sublattices are present, with an angle $\phi = 25° \pm 5°$ between magnetic easy axes and the b axis at 4.2K. By comparing the observed variation of hyperfine field with applied field and temperature with spin-wave

theory Gupta et al. (1978b) estimated the ratio $J'/J \leq 10^{-3}$ for the exchange constants and $B_A/B_E \simeq 4\times10^{-3}$ and $B_E \simeq 74T$ for the exchange and anisotropy fields.

Table 5.3 Parameters of K_2FeF_5 and Rb_2FeF_5, as determined by magnetic susceptibility (θ, J/k_B) and Mössbauer effect (T_N, J'/J, B_E, B_A/B_E) experiments.

	T_N	θ	J/k_B	J'/J	B_E	B_A/B_E
K_2FeF_5	6.95K	125K	9.45K	9×10^{-4}	83T	8.5×10^{-4}
Rb_2FeF_5	≤9.3K	125K	8.78K	$\sim10^{-3}$	74T	3.9×10^{-3}

A summary of the various parameters of the magnetically ordered states of K_2FeF_5 and Rb_2FeF_5 is given in Table 5.3. In most respects it appears that the systems are quite similar, with an exception being the magnitude of the anisotropy field B_A which is about four times larger in Rb_2FeF_5 than in K_2FeF_5. This difference might explain the different magnetic structures of the two compounds, with the greater influence of the exchange field in K_2FeF_5 resulting in a collinear spin structure, and the larger anisotropy in Rb_2FeF_5 accounting for the four sublattice state present there.

5.2 K_2FeF_5 EXPERIMENTAL RESULTS

In this section the results of a Mössbauer study of the spin-flop transition in K_2FeF_5 are presented. Three distinct experiments were performed. In a preliminary study a magnetic field was applied along the easy axis (the b axis) of an ab-plane single crystal while the γ-ray beam was incident along the c axis. Subsequently a large ac-plane crystal was obtained and the spin-flop experiment repeated in the favourable geometry (see later) of both γ-rays and applied field di-

rected along the b axis. In the third experiment the effect of misalignment on the transition was investigated by directing the applied field and γ-ray beam at ~30° to the b axis of the ac-plane crystal.

5.2a Applied Field Parallel to the Easy Axis

5.2a(i) ab-Plane Crystal

The first of the K_2FeF_5 spin-flop experiments utilised an ab-plane single crystal whose axes had been identified via Laue X-ray diffraction by Dr F.R. Wondre of the Clarendon Laboratory, Oxford. Mössbauer spectra were recorded at 4.2K with the incident γ-rays parallel to the c axis and applied fields of up to 6T along the b axis. These spectra are shown in Figure 5.6.

In zero applied field a six line hyperfine spectrum was recorded in which an intensity ratio of 3:4:1 in the outer:middle:inner pairs of lines is evident. Such a pattern is indicative of a perpendicular orientation of the spins with respect to the γ-ray beam direction. In an applied field of B=3.0T the spectral lines split into pairs. This splitting implies that the applied field was being directed along the magnetically easy axis of the spins so that two different effective fields (corresponding to the vector addition of the applied field to the hyperfine field on each of the sublattices of the antiferromagnet) were present. At higher fields (B=3.7T and 4.0T) the spectra showed some evidence of structure, indicating that some kind of transition was occurring. This transition appears to be complete in the B=6.0T spectrum which is again a simple six line pattern of unsplit lines, but whose line intensity ratio (about 3:2.6:1) is clearly different to that seen in the zero field spectrum.

The spectra were computer analysed using the program (Fit-Q) that was discussed in Chapter 4.3b. In each case the quadrupole splitting and asymmetry parameters were taken to be Δ=-0.68mm/s and η=0.57, as

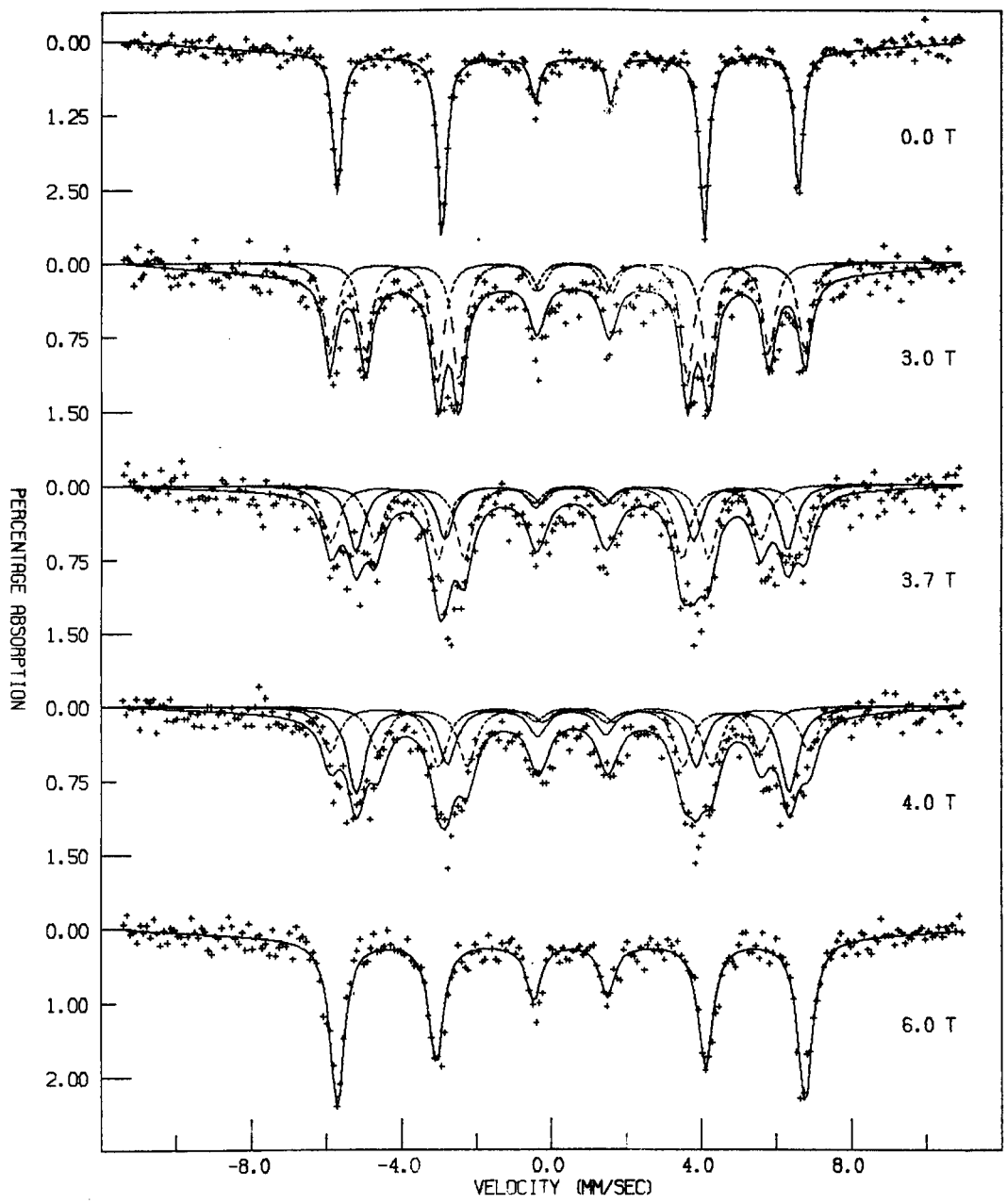

Figure 5.6 Spectra of an ab-plane single crystal of K_2FeF_5, with applied fields and γ-rays directed along the b and c axes respectively.

determined by Gupta et al. (1977). With reference to Gupta et al. (1979) the γ-ray direction (the c axis) was defined in the EFG coordinate system by the polar angles $\theta_g \simeq 132°$ and $\phi_g \simeq 90°$ (see Figure 5.7). The applied field direction (the b axis) was similarly defined by $\theta_H \simeq 42°$ and $\phi_H \simeq -90°$. (Note that here we have taken advantage of the symmetry properties of the crystal, as discussed in section 5.1b, to model the spectra via a single EFG coordinate system.) The parameters that were allowed to vary in the fitting process included the isomer shift δ, the linewidth Γ and the magnitude and direction of the hyperfine field. It was found to be most convenient to define the direction of $\underline{B}_{hf}$ in the lattice coordinate system with the polar angles θ_B and ϕ_B (see Figure 5.7) rather than in the EFG axis system. The optimal values of these fitted parameters are given in Table 5.4.

A note on errors is in order here. Unless otherwise stated, an estimate of the uncertainty of a fitted parameter such as those presented in Table 5.4 may be inferred from the number of significant figures to which the value is quoted. For example the isomer shift in the zero field spectrum might be read from Table 5.4 as $\delta = 0.53 \pm 0.01$mm/s. It should also be noted that such an error estimate refers to 'computational uncertainty' only and results from the spread of data points in the Mössbauer spectrum. Other sources of error, such as systematic errors due to uncompensated drive non-linearity and random errors due to spectrometer drift and inherent instabilities in the experimental apparatus, are acknowledged to be present but are not treated explicitly.

The zero field spectrum was fitted with $\phi_g = 90°$ assumed and gave $\theta_g = 130° \pm 1°$ which implies an angle of $40° \pm 1°$ between the V_{zz} and b axes. This value compares favourably with the $42° \pm 5°$ reported by Gupta et al. (1979) and the fit therefore confirms that the γ-rays were incident along the c axis. The B=3.0T spectrum was fitted under the assumption

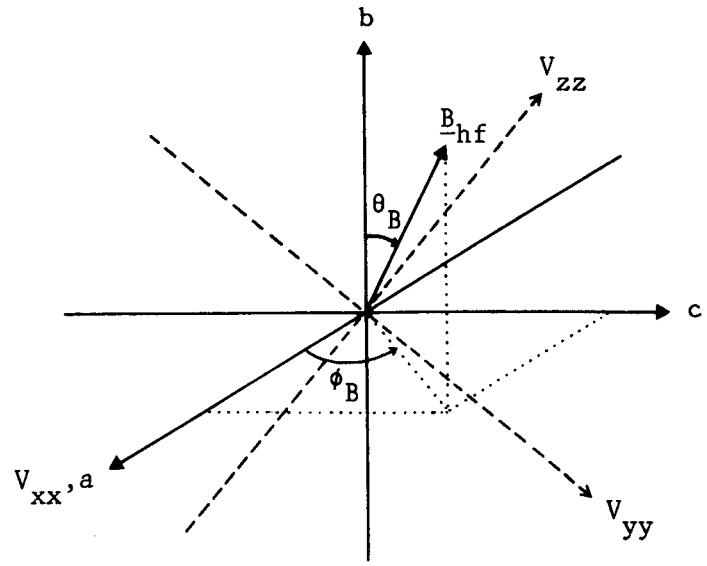

Figure 5.7 Definition of the hyperfine field direction in the lattice coordinate system. The EFG principal axes are indicated with dashed lines.

Table 5.4 Fitted hyperfine parameters of the spectra of an ab-plane K_2FeF_5 crystal subject to an applied field B along its b axis, as discussed in the text. δ and Γ measured in mm/s, B and B_{hf} in Tesla. * denotes parameters that were not allowed to vary.

B	δ	Γ	B_{hf}	θ_B	ϕ_B	Area
0.0	0.53	0.28	37.9	0*	0*	-
3.0	0.53	0.41	36.1	0*	0*	-
3.7	0.53	0.52	35.3	0*	0*	68%
				91.3°*	29°	32%
4.0	0.54	0.57	35.4	0*	0*	58%
				91.4°*	36°	42%
6.0	0.53	0.46	38.0	92.1°*	33°	-

that the applied and hyperfine fields were parallel (θ_B=0), corresponding to the 'unflopped' spin configuration. The polar angles of the applied field were found to be $\theta_H \simeq 40°$ and $\phi_H \simeq -90°$, a direction which coincides with the b axis as expected.

In the 6.0T spectrum it was assumed that all the spins had flopped into the $\theta_B \simeq 90°$ configuration. In fact θ_B was constrained to be 92.1°, a value which incorporates a 2.1° field-induced canting of the spins out of the ac-plane. (This canting was discussed in Chapter 2.3b.) An azimuthal angle of $\phi_B \simeq 33°$ was fitted, indicating that the medium anisotropy axis lies in the ac-plane at ~33° to the a axis. This result is in reasonable agreement with the ~38° measured by Gupta et al. (1979) from a bc-plane crystal, and the ~40° measured by Cooper (1981) in an ab-plane crystal. Cooper (1981) also established that there are two different medium anisotropy axes in the crystal (at $\phi = \pm 40°$) resulting from the different orientations of the $(FeF_6)^{3-}$ octahedra, but this feature is not observable in the current experiment.

The intermediate spectra (B=3.7T and 4.0T) were fitted as a superposition of components corresponding to unflopped (θ_B=0) and flopped ($\theta_B \simeq 90°$) phases in the crystal, the relative areas of which are given in Table 5.4. Unfortunately the poor statistical quality of the spectra makes it difficult to comment on the validity of the model. This problem led to the experiment being repeated using a large ac-plane crystal, with particular care being taken to obtain high quality spectra in the transition region. This experiment is discussed in the following section. Discussion of the observed dependence of hyperfine field and linewidth on applied field in the ab-plane crystal will also be deferred until later.

5.2a(ii) ac-Plane Crystal

In the second K_2FeF_5 spin-flop experiment an ac-plane single crystal of approximate dimensions 8×6×1 mm^3 was used. Again the crystal axes had been identified via Laue X-ray diffraction by Dr F.R. Wondre at the Clarendon Laboratory. Mössbauer spectra were recorded at 4.2K with both the incident γ-rays and applied fields of up to 14T along the b axis. These spectra are shown in Figure 5.8.

In zero applied field a four line spectrum was recorded. The complete absence of the $\Delta m=0$ lines (lines two and five of a magnetic sextet) implies that the γ-ray direction was within a few degrees of the magnetically easy axis. In small applied fields ($B\leq 3.0T$) the spectral lines split into pairs corresponding to the different effective fields on each of the two sublattices of the antiferromagnet. For $B\sim 3.7T$ additional lines appeared at the $\Delta m=0$ line positions and the outer lines showed evidence of structure. At higher fields ($B>3.8T$) a sextet with intensity ratios 3:4:1 in outer:middle:inner pairs of lines was observed, characterising a perpendicular orientation of the spins to the γ-ray beam.

The spectra were computer analysed using Fit-Q with $\Delta=-0.68$mm/s, $\eta=0.57$, $\theta_g=\theta_H\simeq 39°$ and $\phi_g=\phi_H=-90°$ assumed. The fitted parameters are shown in Table 5.5, with the exception of the isomer shift δ which did not vary greatly between the spectra. The optimum value of the mis-fit parameter χ^2 obtained from each fit is also given in Table 5.5. Note that to 'normalise' χ^2 one should divide through by the number of degrees of freedom, which was about 240 in all of the fits.

The low field ($B\leq 3.0T$) spectra could be well fitted with $\theta_B=\phi_B=0$, implying that the γ-ray and applied field direction was closely aligned with the b axis. The high field ($B\geq 3.8T$) spectra were fitted by assuming that the spins had flopped into the ac-plane and that $\theta_B=90°+\alpha$ where α is the canting angle given in Chapter 2.3b by

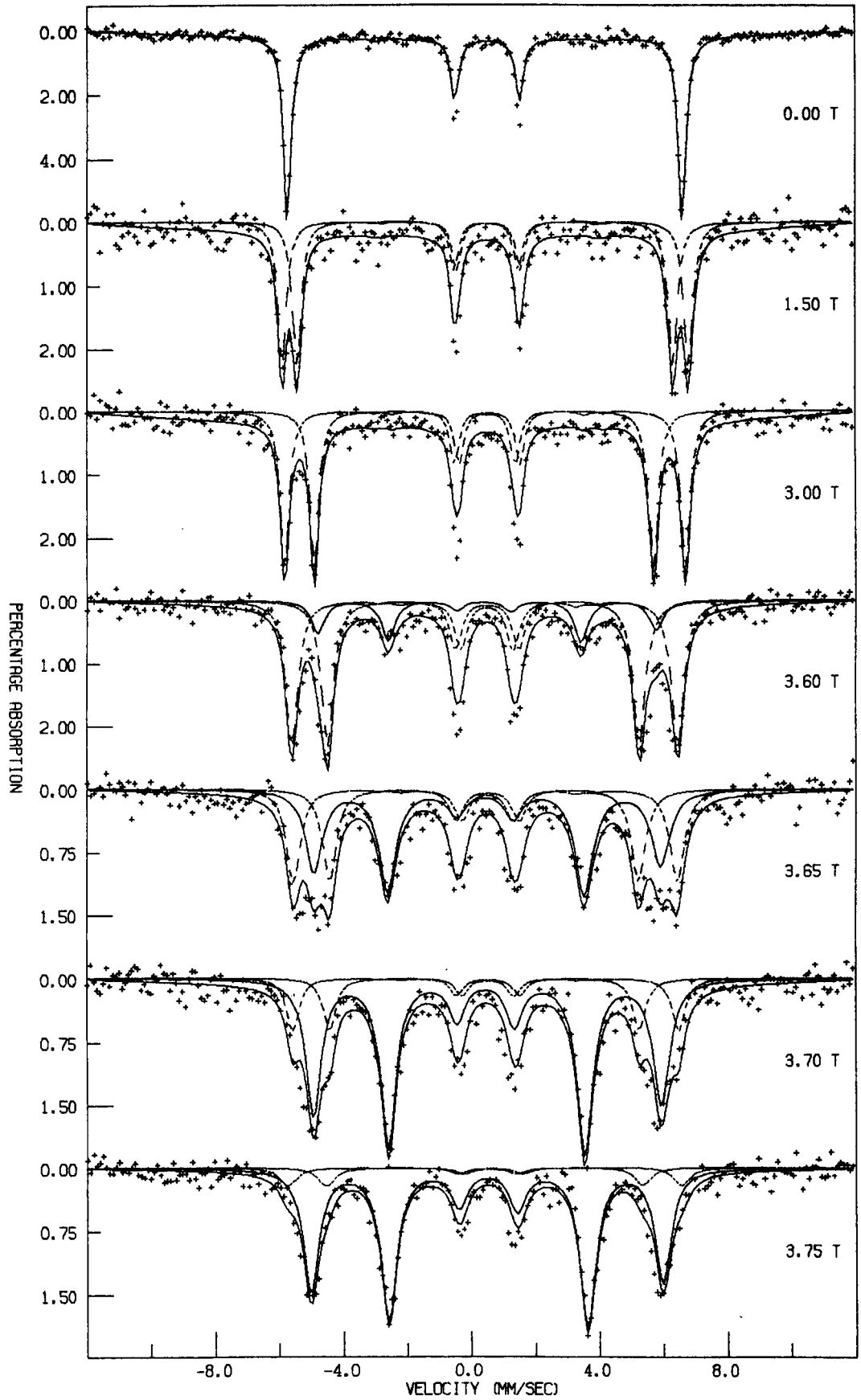

Figure 5.8 Spectra of an ac-plane crystal of K_2FeF_5, with applied fields and γ-rays directed along the b axis. Continued overleaf.

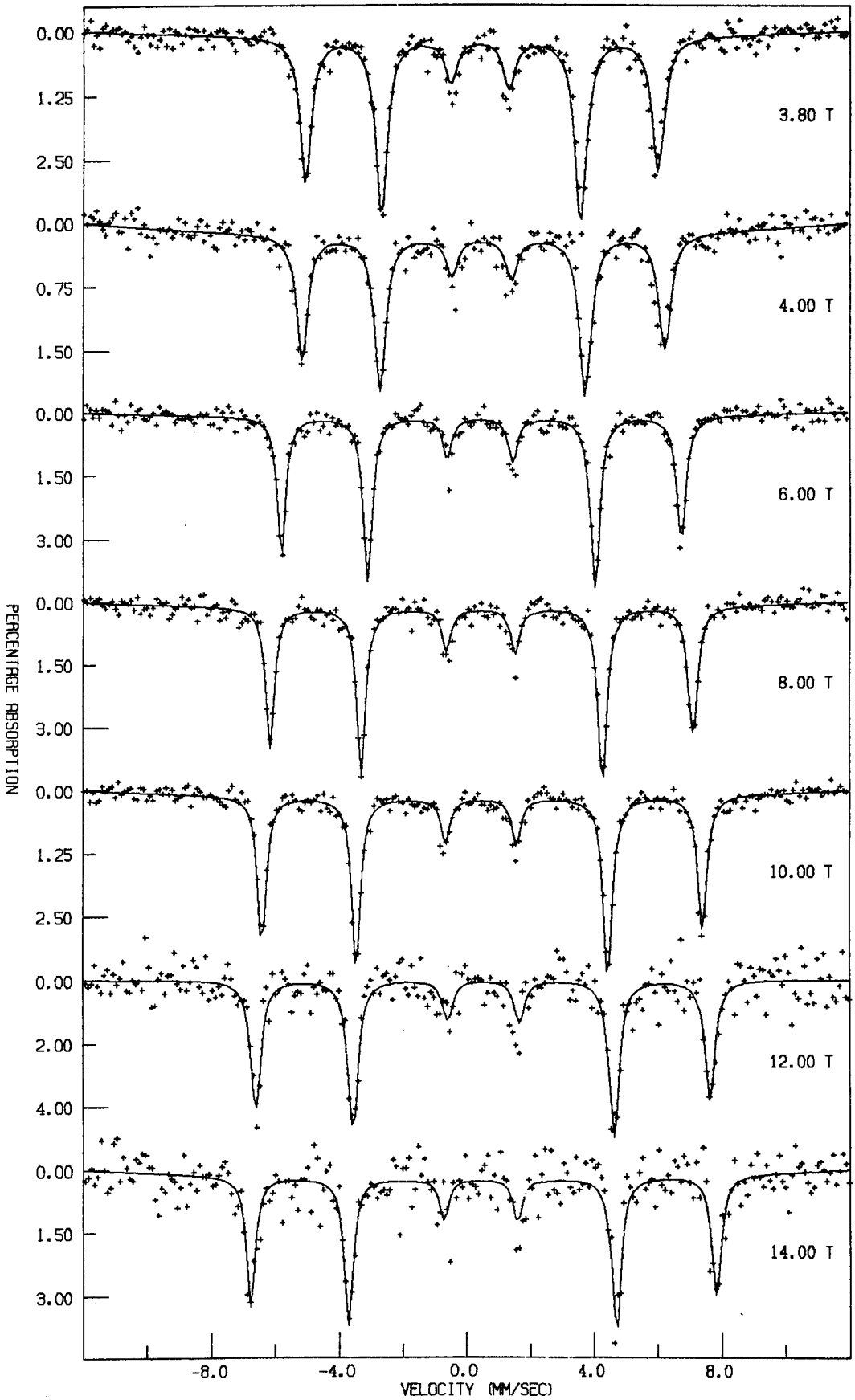

Figure 5.8 (continued) Spectra of an ac-plane crystal of K_2FeF_5, with applied fields and γ-rays directed along the b axis.

Table 5.5 Fitted hyperfine parameters of the spectra of an ac-plane K_2FeF_5 crystal subject to an applied field B along its b axis, as discussed in the text. Γ measured in mm/s, B and B_{hf} in Tesla. * denotes parameters that were not allowed to vary.

B	Γ	B_{hf}	θ_B	ϕ_B	Area	χ^2
0.00	0.30	38.0	0*	0*	-	395
1.50	0.34	37.7	0*	0*	-	338
3.00	0.34	35.6	0*	0*	-	371
3.60	0.47	33.5	0*	0*	81%	608
	0.51	32.4	91.2°*	50°	19%	
3.65	0.53	33.3	0*	0*	49%	401
	0.66	33.1	91.3°*	64°	51%	
3.70	0.47	33.4	0*	0*	25%	437
	0.59	33.3	91.3°*	79°	75%	
3.75	0.63	34.1	0*	0*	14%	430
	0.60	33.7	91.3°*	90°	86%	
3.80	0.44	33.8	91.3°*	89°	-	439
4.00	0.43	34.8	91.4°*	83°	-	263
6.00	0.34	38.3	92.1°*	86°	-	365
8.00	0.34	40.5	92.8°*	72°	-	273
10.00	0.34	42.0	93.5°*	58°	-	250
12.00	0.34	43.2	94.1°*	34°	-	245
14.00	0.34	44.0	94.8°*	38°	-	273

Table 5.6 Fitted hyperfine parameters of the transition spectra of the ac-plane crystal using a spin-rotation model, as discussed in the text. Symbols as in Table 5.5.

B	Γ	B_{hf}	θ_B	ϕ_B	χ^2
3.60	0.51	33.5	28°	9°	457
3.65	0.72	33.4	48°	13°	434
3.70	0.57	33.3	65°	28°	507
3.75	0.51	33.5	71°	31°	396

$\sin\alpha = B/(2B_E + B_A)$. Good fits were obtained, although the fitted ϕ_B values were quite variable. Since in these spectra ϕ_B was largely determined by the line positions, this variability may indicate that problems relating to the non-linearity of the velocity scale are still present.

The four spectra recorded in the transition region ($3.6T \leq B < 3.8T$) were analysed using two different models. In the first model the spectra were regarded as a superposition of components corresponding to unflopped (AFM) and flopped (SF) phases or 'domains' in the crystal. The unflopped spins contribute a subspectrum with split lines in 3:0:1 intensity ratio, and the flopped spins give an unsplit 3:4:1 sextet component. The fits to this 'coexistence' model are shown in Figure 5.8 and also in Figure 5.9, and the fitted parameters are given in Table 5.5.

The second model used to fit the transition spectra is a spin-rotation model. The spectra are taken to result from spins that are antiferromagnetically aligned along an axis which is rotated through some angle θ_B with respect to the applied field direction. The fits obtained using this model are shown in Figure 5.9 where they may be compared with the 'coexistence' fits, and the fitted parameters are given in Table 5.6.

It is not immediately apparent which of the two models provides the better fits to the data. Comparing the χ^2 values of the fits it seems that the 'coexistence' model is better for the B=3.65T and 3.70T spectra, but is worse for the B=3.60T and 3.75T spectra. However, by careful appraisal one may become convinced that the 'coexistence' model does at least attempt to reflect the features present in the spectra, while the 'rotation' model does not cope with the unsplit nature of some of the spectral lines. One may therefore conclude that the 'coexistence' model is more appropriate for fitting the data.

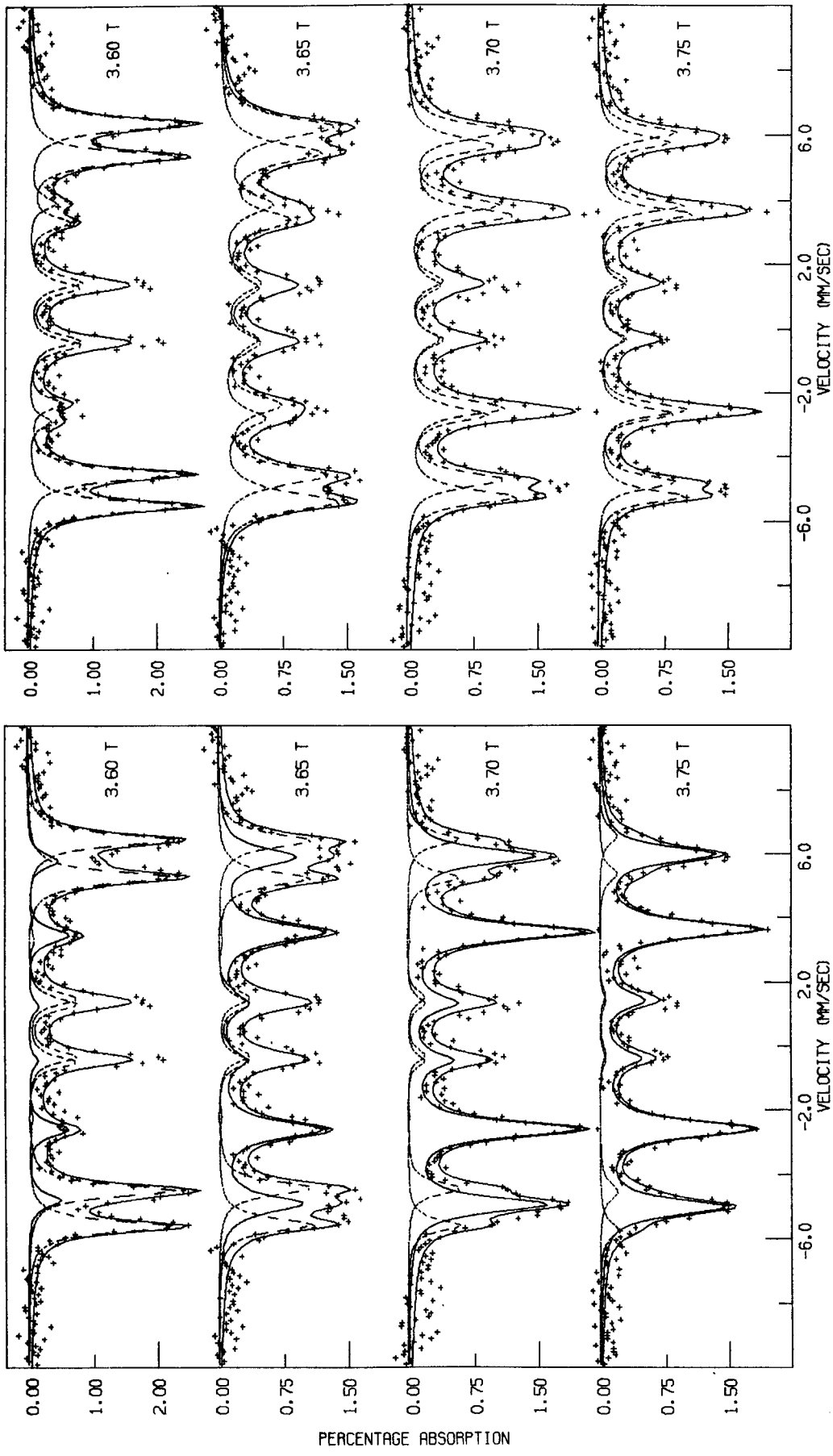

Figure 5.9 Comparison of the 'coexistence' and 'rotation' model fits of some of the spectra from Figure 5.8, as discussed in the text.

5.2a(iii) Width of the Spin-Flop

Some comments on the physical justification of the 'coexistence' model may be collated by considering the observed width of the spin-flop. Figure 5.10 shows the relative areas of the unflopped and flopped parts of the spectra, from which the width of the transition may be estimated as $\Delta B \simeq 0.4T$, centered at $B_{sf} \simeq 3.65T$. If the spin-flop transition is of first-order this coexistence of AFM and SF phases might be attributed to demagnetisation or hysteresis effects. Let us consider these possibilities in turn.

As discussed in Chapter 2.2e(ii), demagnetising fields give rise to a mixed-domain intermediate state over a range of fields $\Delta B = N_z \chi_\perp B_{sf}$ near the critical field. In the present experiment the applied field direction was perpendicular to the plane of a thin-slab crystal, so the demagnetisation factor $N_z = 1$. We may estimate the susceptibility (per unit volume) $\chi_\perp$ of K_2FeF_5 from the experiments of Sabatier et al. (1979) and Dance et al. (1980), who measured the inverse molar susceptibility of powder samples at 4.2K to be $\chi_M^{-1} \simeq 95$mole/emu (see Figure 5.5). Assuming that the crystal density is $\rho \simeq 2g/cm^3$ so that 1 mole of K_2FeF_5 occupies about $111cm^3$, and that $\chi_\parallel \simeq 0$ at 4.2K, the volume susceptibility is thus given by $\chi_\perp \simeq 1.0 \times 10^{-4}$emu/cm^3. It is convenient to carry out the rest of the calculation in CGS units, converting the field to units of Gauss and taking $N_z = 4\pi$ (the CGS equivalent of $N_z = 1$). The width of a demagnetisation broadened spin-flop in K_2FeF_5 is thus calculated to be $\Delta B_{dm} \simeq 46G$. This figure may be checked by estimating $\chi_\perp$ from M_o/B_E (in CGS units) where M_o is the saturation sublattice magnetisation. Since the mean magnetic moment $\langle\mu\rangle \simeq 3.5\mu_B$, $M_o \simeq 88G/cm^3$ and $\chi_\perp \simeq 1.1 \times 10^{-4}$emu/cm^3. The corresponding width is $\Delta B_{dm} \simeq 49G$, a value which compares very favourably with the previous result. We thus conclude that demagnetisation effects might produce a mixed AFM-SF state in

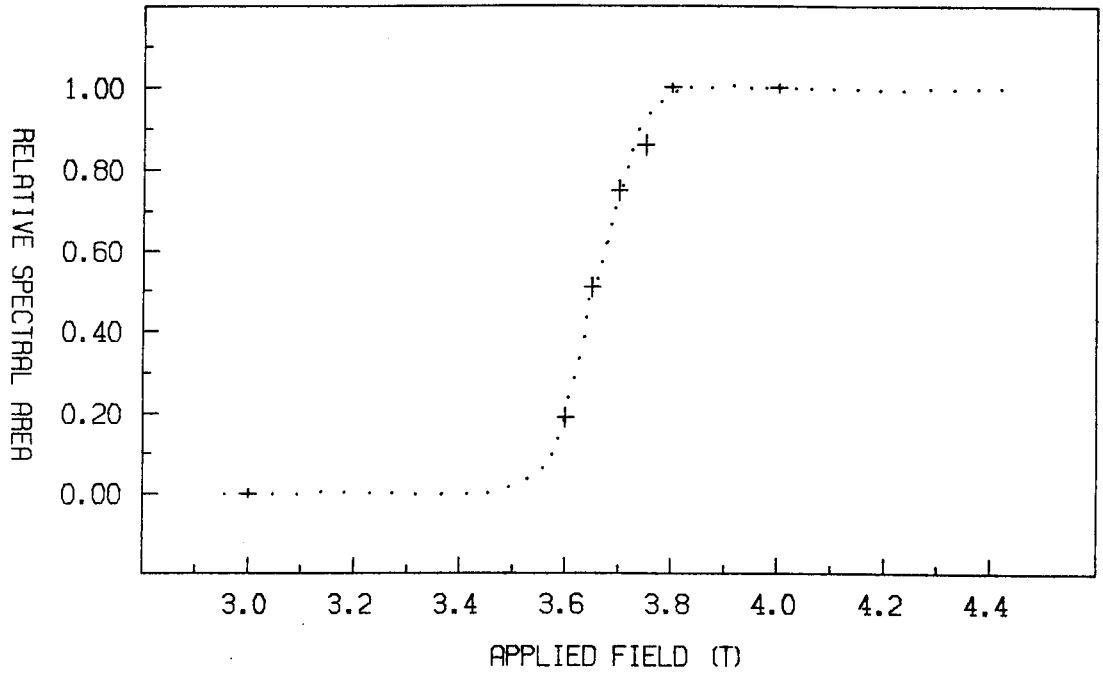

Figure 5.10 Observed field-dependence of the relative area of spin-flopped to unflopped spectral components, as fitted using the 'coexistence' model. The dotted curve is a guide to the eye.

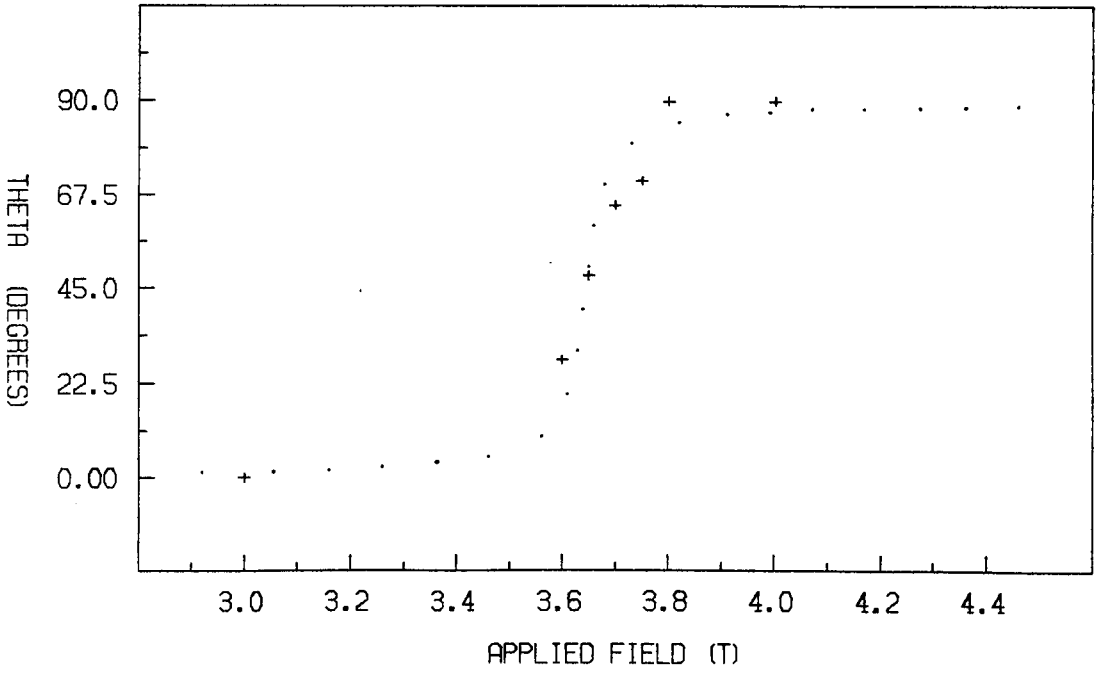

Figure 5.11 Comparison of the observed field-dependence of the rotation angle θ between the AFM axis of the spins and the applied field (as fitted with the 'rotation' model) with the curve predicted from mean-field theory for a misalignment angle ψ=0.5°.

K_2FeF_5 over a range of fields $\Delta B_{dm} \simeq 0.005T$ near B_{sf}. This is clearly much less than the observed ΔB of 0.4T.

A second mechanism for generating mixed-domain states near B_{sf} is the hysteresis associated with a first-order transition. As discussed in Chapter 2.2b(i), the spin-flop field $B_{sf}=[B_A(2B_E-B_A)]^{\frac{1}{2}}$ is in the centre of a region of instability bounded by the critical fields $B_1=[B_A(2B_E+B_A)]^{\frac{1}{2}}$ and $B_2=(2B_E-B_A)[B_A/(2B_E+B_A)]^{\frac{1}{2}}$. Assuming that $B_E=83.0T$ at 4.2K, the observed $B_{sf}=3.65T$ implies a value for B_A of about $8.0\times10^{-2}T$. This then gives $\Delta B_{hy}=B_1-B_2\simeq3.6\times10^{-3}T$, which again is much less than the observed ΔB.

To explain the large width of the observed coexistence region in this experiment we are therefore driven to speculation. It is certainly possible that there may be a distribution of 'local critical field' values within the crystal which results from the effect of random impurities, defects or distortions on the local environments of the ferric ions. The spin-flop in this case may be of first-order for each individual ion, but the summation of these transitions over the entire crystal would appear as a rather broadened transition in the Mossbauer experiment. Although this explanation is somewhat unsatisfactory in that it is neither quantitative nor predictable, it is clearly possible and may well be true.

At this point it is of use to compare the 'rotation' model with theoretical predictions. Although we have already concluded that the 'rotation' fits were inferior to the 'coexistence' fits there is some justification, on the basis of both mean-field and soliton theory, for anticipating a second-order transition to take place.

If for a moment we regard K_2FeF_5 as a uniaxial antiferromagnet then on the basis of the mean-field theory discussed in Chapter 2.2b a second-order spin-flop will take place if the applied field is misaligned from the easy axis by an angle exceeding $\psi_c \simeq \tan^{-1}(B_A/2B_E)$. In

K_2FeF_5 $B_E \simeq 83.0T$ and $B_A \simeq 0.08T$ at 4.2K, which gives $\psi_c \simeq 0.03°$. This critical angle is much smaller than the estimated uncertainty in alignment ($\pm 2°$), so that it would seem probable that a rotation transition would be observed. Referring to Chapter 2.2b(ii), the field-dependence of the rotation angle θ between the AFM axis of the spins and the applied field direction is given by :

$$B^2 = [B_A \sin\psi_2 (2B_E - B_A \cos\psi_2)^2] / [\cos\alpha (4B_E \sin\alpha + 2B_A \sin\psi_1)] \quad , \qquad (5.1)$$

where $\alpha = 90° - \theta$, $\psi_1 = 2\psi + \alpha$, $\psi_2 = 2\psi + 2\alpha$ and ψ is the misalignment angle. In the 'rotation' fits for $B \leq 3.75T$ the rotation angle θ was fitted as the polar angle θ_B, while in the SF phase ($B \geq 3.80T$) $\theta = 90°$. Thus the fitted field dependence of θ is as shown in Figure 5.11. Also shown in Figure 5.11 is the theoretical curve found from equation (5.1) for a misalignment of $\psi = 0.5°$. The agreement between theory and experiment appears to be quite good.

The soliton model of the spin-flop also predicts a second-order transition, even if the applied field is perfectly aligned with the easy axis. As discussed in Chapter 2.4b soliton theory predicts the field-dependence of the mean value of the rotation angle between the AFM and easy axes as :

$$\langle\theta\rangle \simeq 5.85 \, (2E_s/k_BT) \exp(-2E_s/k_BT) \quad , \qquad (5.2)$$

where $2E_s = 2g\mu_B S B_{sf} |1 - B^2/B_{sf}^2|^{\frac{1}{2}}$ is the creation energy of a soliton pair-state. This curve is compared with the experimental data in Figure 5.12. The divergence of the theoretical curve in the neighbourhood of B_{sf} arises from the breakdown of the low-density soliton approximation (de Jongh and de Groot 1985), and the behaviour in the intermediate region has been very roughly approximated by linear interpolation. In any event, it is clear from Figure 5.12 that the curve predicted by equation (5.2) is much broader than the observed transition. A much better fit to the data was obtained by arbitrarily changing the term $2E_s$ in (5.2) to $6E_s$ (see Figure 5.12). This corresponds to an increase

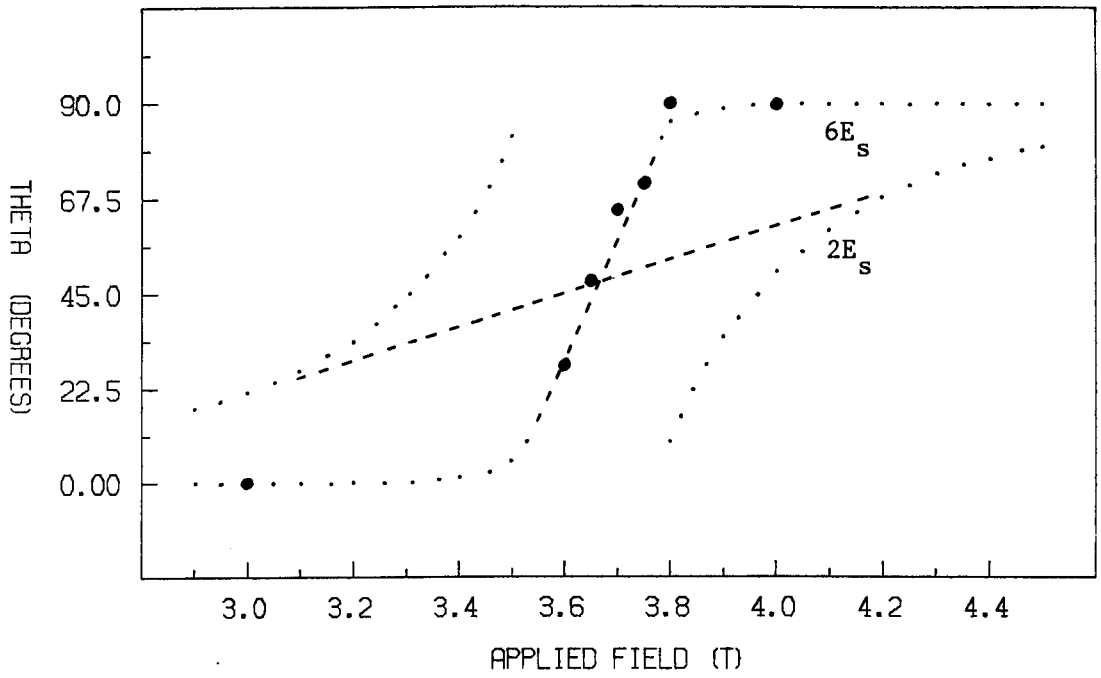

Figure 5.12 Comparison of the observed field-dependence of the rotation angle θ with the curves predicted from soliton theory, as discussed in the text.

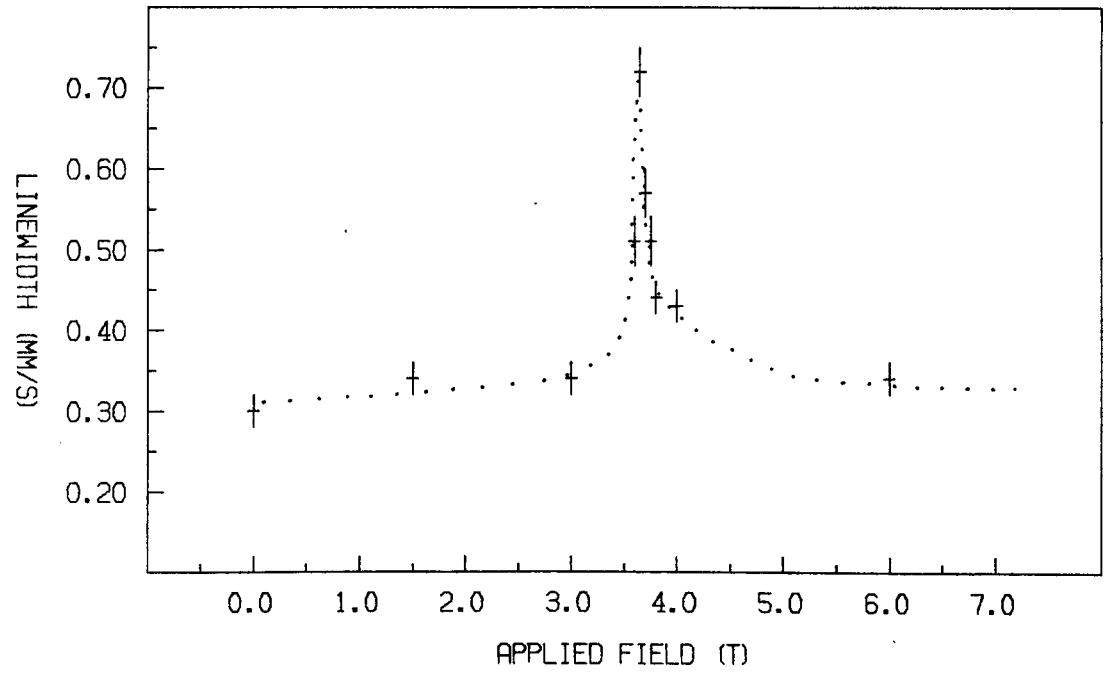

Figure 5.13 Observed field-dependence of the Mossbauer linewidth, as fitted using the 'rotation' model. The dotted curve is a guide to the eye.

in the zero-field soliton creation energy from $2E_s/k_B \simeq 24K$ to $2E_s'/k_B \simeq 72K$. Such a modification to the creation energy might possibly be justified by considering the effect of interchain interactions in hindering the formation of solitons (de Groot and de Jongh 1986). However in general it would seem that soliton theory (as it stands) does not provide close quantitative agreement with the observed transition width.

One aspect of the observed spin-flop does however support the notion of a soliton-mediated transition. In the neighbourhood of B_{sf} the width of the fitted Mössbauer spectral lines show a large maximum (see Figure 5.13). This peak is evident in both the 'coexistence' and 'rotation' fits, and was also apparent in the spectra taken on the ab-plane crystal. The presence of such a maximum in the linewidth might result from large numbers of finite-width domain walls in the crystal, as predicted by the soliton model of the spin-flop. The resultant distribution in the angle between the spin and EFG axis directions would then give a distribution in the line positions in the component Mossbauer subspectra, so that line-broadening would appear in the full spectrum. The 'coexistence' model of the transition might also support this behaviour if one envisages that for $B \sim B_{sf}$ a large number of AFM and SF domains are present, and that some fraction of the crystal could therefore be said to constitute the domain-wall regions. An alternative explanation is that some dynamic effects are present, such as spin-spin or spin-lattice relaxation, which cause the spins to 'flip' or change direction on such a timescale that the Mossbauer spectra are broadened.

5.2a(iv) Field-Dependent Spin Reduction

Another notable feature of the observed spin-flop is the marked variation in the hyperfine field B_{hf} as a function of the applied field (see Figure 5.14). Since in high-spin ferric ions such as those in

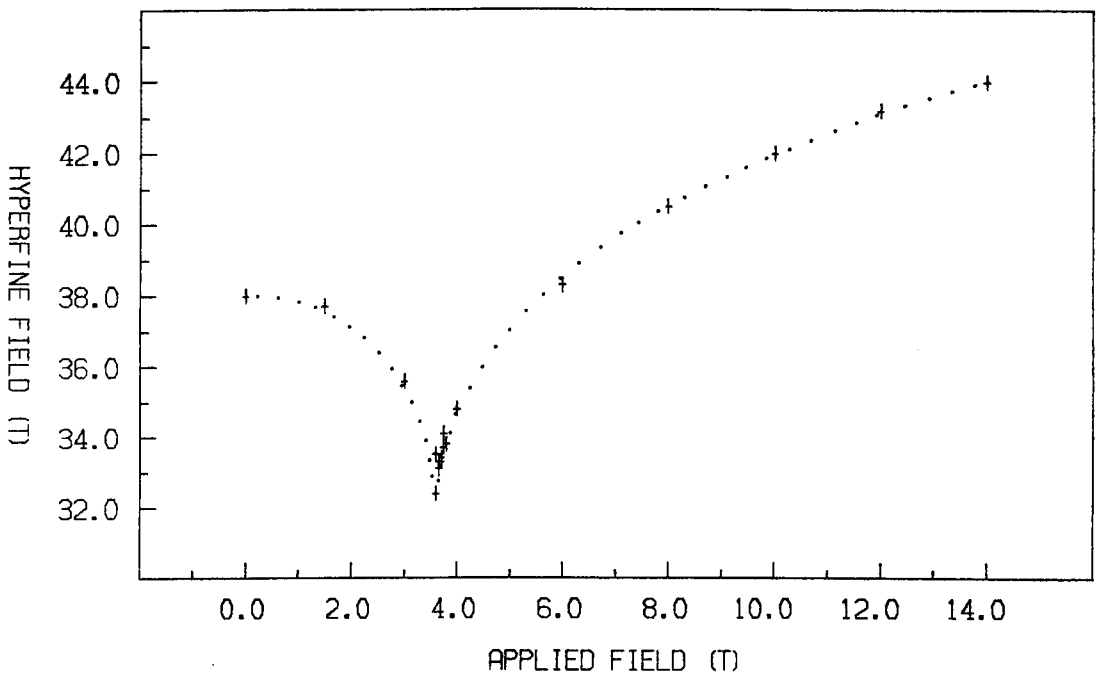

Figure 5.14 Observed field-dependence of the hyperfine field, as fitted using the 'coexistence' model. The dotted curve is a guide to the eye.

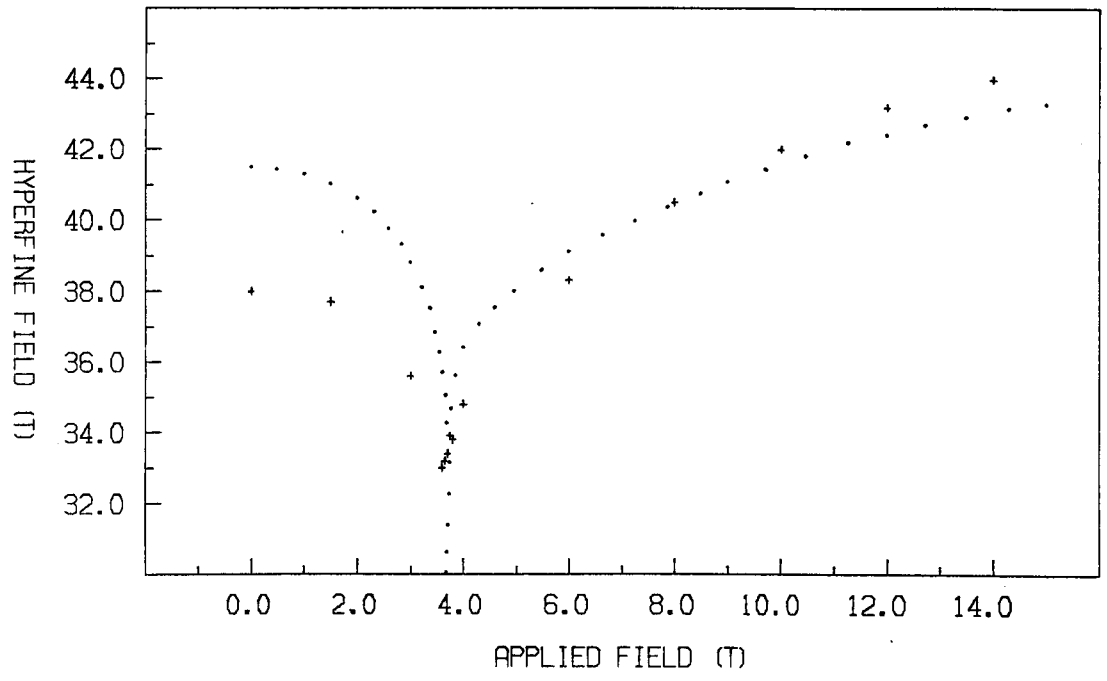

Figure 5.15 Comparison of the observed field-dependence of the hyperfine field with the curve predicted from spin-wave theory, as discussed in the text.

K_2FeF_5 the hyperfine field is (to a good approximation) proportional to the mean spin <S> on the ion, the variation of B_{hf} with B is indicative of field-dependent spin reduction. As discussed in Chapter 2.3, spin-wave theory predicts that an applied field $B<B_{sf}$ parallel to the easy anisotropy axis will promote the thermal excitation of spin-waves along the magnetic chains. This increased spin fluctuation is seen in Figure 5.14 as a drop in B_{hf} as B is increased. The fluctuations are maximal at $B=B_{sf}$ and B_{hf} is then a minimum. For $B>B_{sf}$ the spin axis is perpendicular to the applied field and the effect of B is to inhibit the spin-waves. Thus above the spin-flop B_{hf} increases as B increases, as is apparent in Figure 5.14.

Spin-wave theory provides quantitative predictions of the spin reduction ΔS due to spin-waves which results in an observed spin $<S>=S-\Delta S$ that is less than the full spin S (see Chapter 2.3). Since the hyperfine field associated with a free Fe^{3+} ion (with $S=<S>=5/2$) is known to be ~64.0T, this predicted <S> may then be converted to a hyperfine field. The solid curves in Figure 5.15 were determined in this way, using the parameters T=4.2K, B_A=0.08T, B_E=83.0T, $J'/J=9\times10^{-4}$ and $\omega_A'/\omega_A=10^{-3}$. It is evident from Figure 5.15 that although spin-wave theory gives a good qualitative description of the observed spin-flop, the quantitative description of the dependence of B_{hf} on B is not ideal.

5.2b Applied Field at ~30° to the Easy Axis

The object of the third K_2FeF_5 spin-flop experiment was to investigate the effect of misalignment by directing the applied field at a substantial angle ψ to the easy axis. To achieve this the ac-plane crystal was mounted in a special nylon sample holder which ensured that the crystal b axis was tilted at ~30° to vertical, in the approximate direction of the c axis. The sample and holder were then placed in

the vertical drive assembly in the 10T magnet, and a series of spectra recorded in which the γ-rays and applied field were directed at ~30° to the b axis, in the bc-plane. These spectra are shown in Figure 5.16.

The zero applied field spectrum contained six lines, with the non-zero intensity of the $\Delta m=0$ lines confirming that the γ-rays were incident at a non-zero angle to the easy axis. As the applied field was increased the spectral lines split and the intensity of the $\Delta m=0$ lines increased. This behaviour is in keeping with a gradual rotation (in unison) of the spins away from the field as it was increased. In this transition region ($3.0T \leq B < 5.0T$) the $\Delta m=0$ lines were also split, further implying that a 'rotation' transition was occurring (rather than a 'coexistence' of AFM and SF phases). At higher fields ($B \geq 5.0T$) a simple sextet pattern was recorded, indicating that the spin-flop was complete and the spins were lying in the plane perpendicular to the applied field direction.

Computer analysis of the spectra using Fit-Q proved to be very difficult. The major problem was that since the applied field was not directed along the b axis the two different EFG coordinate systems present in the crystal were no longer equivalent. Consequently it was found to be simpler to fit the spectra using the less sophisticated program Fit-A. Despite the resultant loss in information it was then at least possible to determine the hyperfine field B_{hf} and rotation angle θ from the fitted 'effective' fields B_{eff} (see below). The fitted values of these parameters are given in Table 5.7, along with the quadrupole shift ε and the linewidth Γ_{16} of the outer lines of the magnetic sextets.

A line intensity ratio of about 3:0.69:1 was fitted in the zero applied field spectrum, indicating that the γ-rays were incident at $\theta \approx 33°$ to the spins. This figure compares well with the intended misalignment of ~30°. In the magnetically split spectra ($3.0T \leq B \leq 4.5T$) two

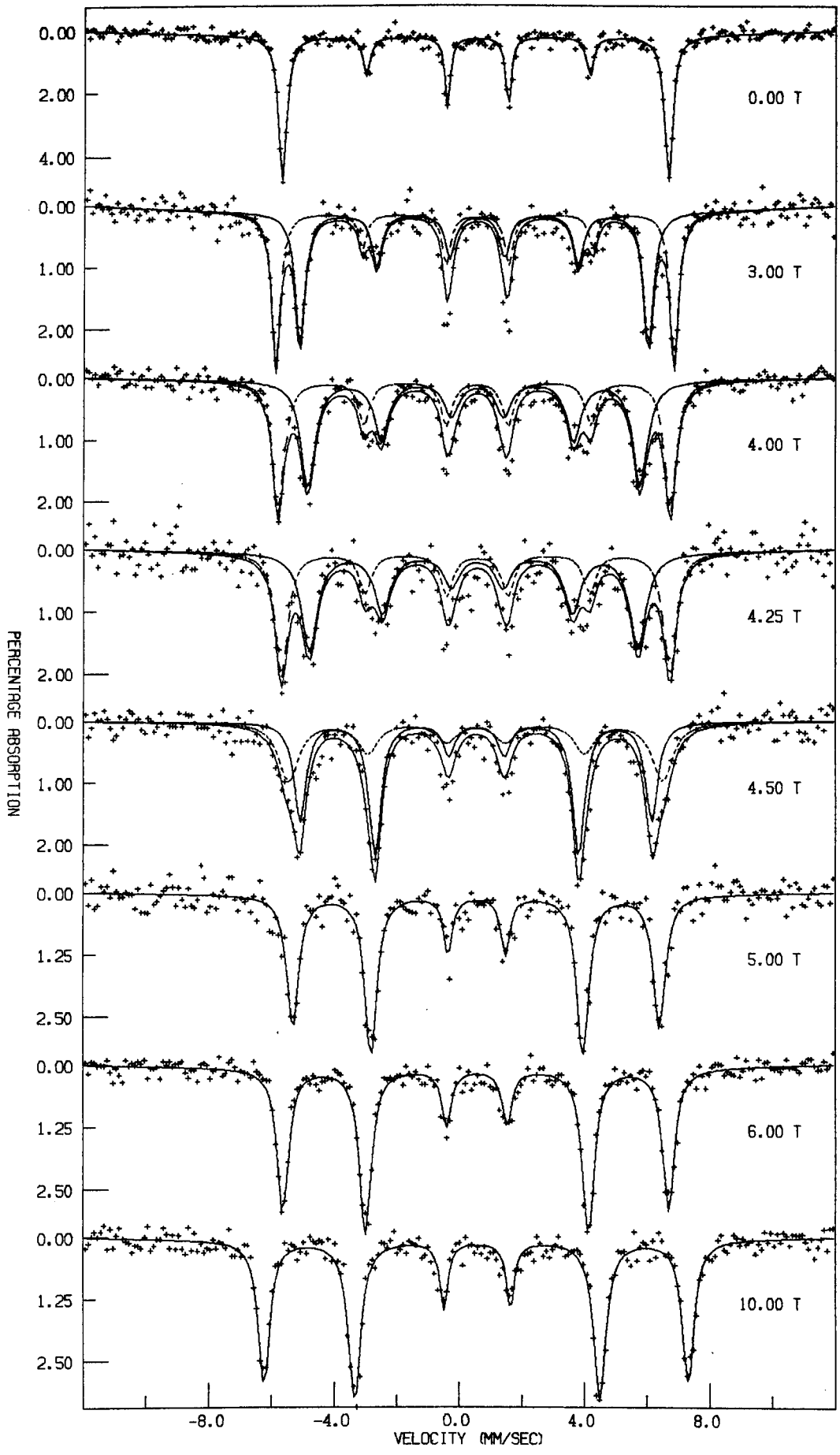

Figure 5.16 Spectra of an ac-plane crystal of K_2FeF_5, with applied fields and γ-rays directed at ~30° to the b axis, in the bc-plane.

'effective' hyperfine fields were fitted, corresponding to the vector addition of the applied and hyperfine fields. Assuming that the spins had rotated an angle θ away from the applied field but that the sublattice spins remained perfectly antiparallel, these effective fields are given by :

$$B_{eff\pm} = [B^2 + B_{hf}{}^2 \pm 2BB_{hf}\cos\theta]^{\frac{1}{2}} . \qquad (5.3)$$

The splitting between the two effective fields is $\Delta B_{eff}=2B\cos\theta$, so that θ could be directly estimated from the fitted data, and then (5.3) used to determine B_{hf}. This procedure was used to find the B_{hf} and θ values given in Table 5.7. The high field spectra, $B \geq 5.0T$, were presumed to result from spin-flopped spins for which the angle between the AFM and applied field axes was $\theta=90°$. The usual canting by $\alpha=\sin^{-1}[B/(2B_E+B_A)]$ was taken into account when determining the hyperfine fields in these spectra.

Table 5.7 Fitted hyperfine parameters of the spectra of an ac-plane K_2FeF_5 crystal subject to an applied field B at ~30° to its b axis, as discussed in the text. δ, ε and Γ_{16} measured in mm/s; B, B_{eff} and B_{hf} in Tesla. * denotes parameters that were not allowed to vary.

B	δ	2ε	Γ_{16}	B_{eff}	B_{hf}	θ
0.00	0.54	-0.10	0.31	38.2	38.2	33°
3.00	0.52	-0.11	0.39	34.5	36.9	35°
	0.54	-0.08	0.34	39.4		
4.00	0.53	-0.11	0.56	32.9	35.8	42°
	0.53	-0.10	0.45	38.8		
4.25	0.53	-0.12	0.61	32.5	35.4	46°
	0.56	-0.07	0.48	38.4		
4.50	0.55	-0.03	0.46	34.7	35.5	76°
	0.54	-0.04	0.69	36.9		
5.00	0.56	-0.03	0.45	36.2	36.0	90°*
6.00	0.55	-0.04	0.44	38.1	37.9	90°*
10.00	0.56	-0.05	0.45	41.9	41.3	90°*

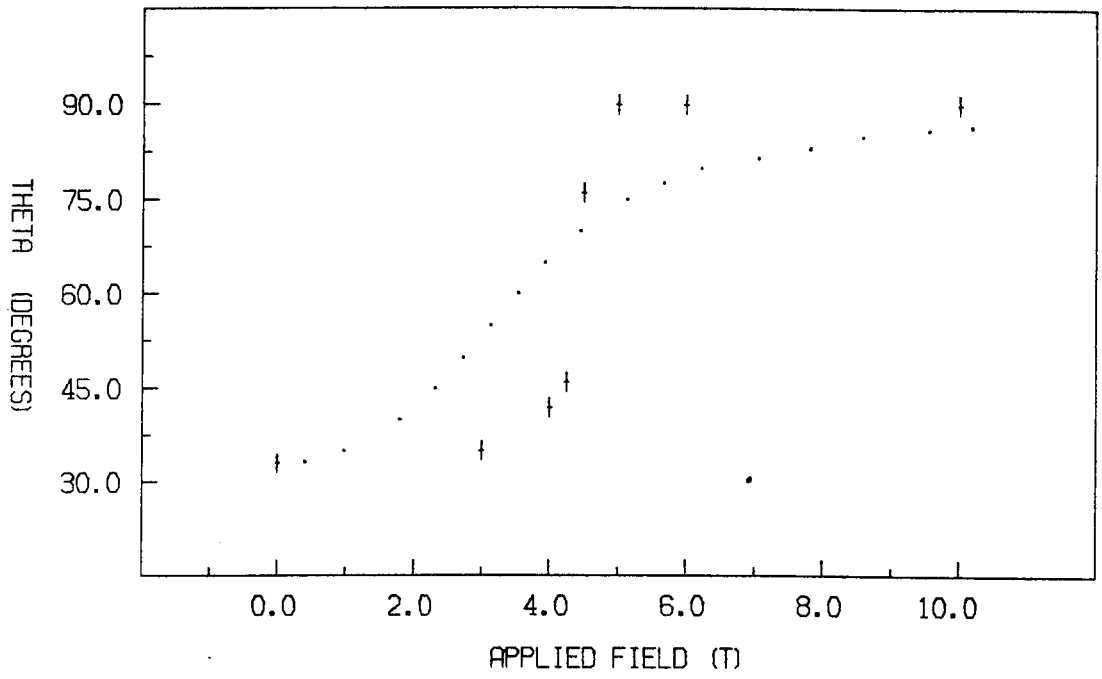

Figure 5.17 Comparison of the observed field-dependence of the rotation angle θ with the curve predicted from mean-field theory for a misalignment angle $\psi=33°$.

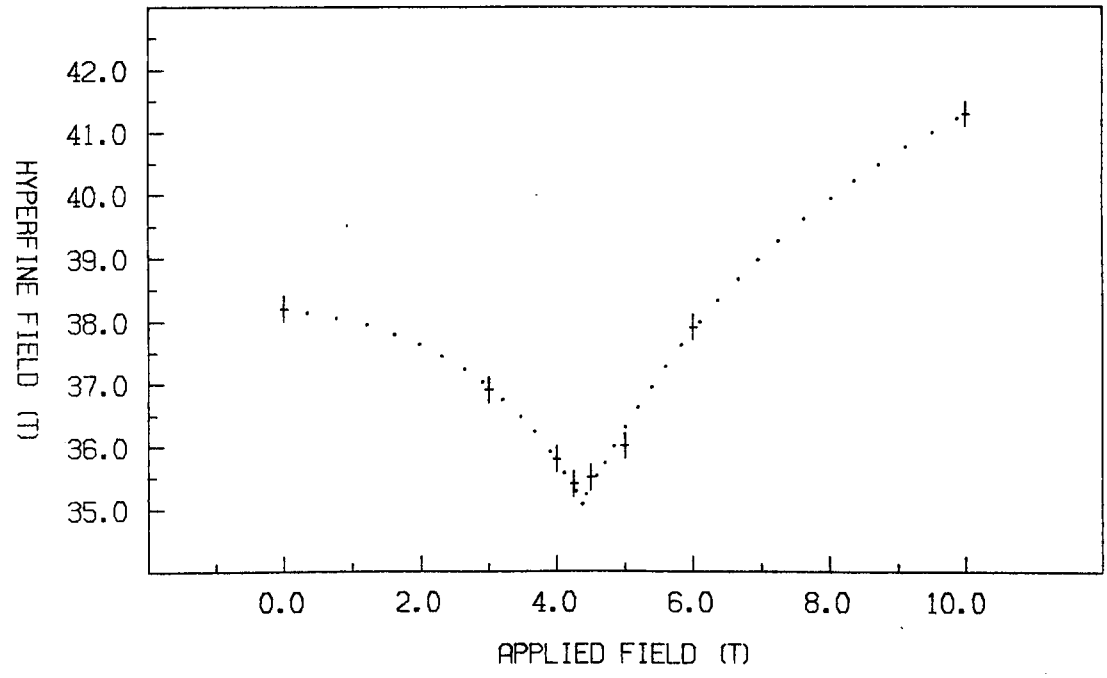

Figure 5.18 Observed field-dependence of the hyperfine field. The dotted curve is a guide to the eye.

Apart from the obvious observation that this spin-flop appears to be a second-order 'rotation' transition, there are two notable and rather surprising features to consider. Firstly the 'smoothness' of the transition is illustrated by the slow change in the rotation angle θ as B was increased (see Figure 5.17). However the mean-field theory prediction of the dependence of θ on B for a misalignment of $\psi \simeq 33°$, described by equation (5.1) and shown in Figure 5.17, is a good deal broader than the observed curve. The reason for such a large discrepancy is not clear. Secondly, the transition exhibits an unexpectedly 'sharp' character in the field-dependence of B_{hf}, as shown in Figure 5.18. A sharp minimum in B_{hf} occurs at a critical field $B_{sf} \simeq 4.3T$. The implication is that spin-waves continue to play an important role in the transition, despite the misalignment of the applied field and easy axes. However, it is still somewhat surprising to see such a sharp minimum in B_{hf} in what otherwise appears to be a smooth second-order transition.

5.3 Rb_2FeF_5 EXPERIMENTAL RESULTS

The Mössbauer study of the spin-flop transition in Rb_2FeF_5 discussed in this section utilised the same single crystal sample that had been the subject of earlier work in this laboratory (Gupta et al. 1978b). Comparison of the results of that earlier work with the neutron diffraction work of Tressaud et al. (1981) allowed the characterisation of the crystal axes in the sample, establishing that it was an ac-plane single crystal. Mössbauer spectra were recorded at 4.2K with both the incident γ-rays and applied fields of up to 14T directed along the b axis. These spectra are shown in Figure 5.19. We may note here that the modest size of the sample ($\sim 3 \times 1$ mm^2 in area) meant that long counting times (~3 days) were required to obtain

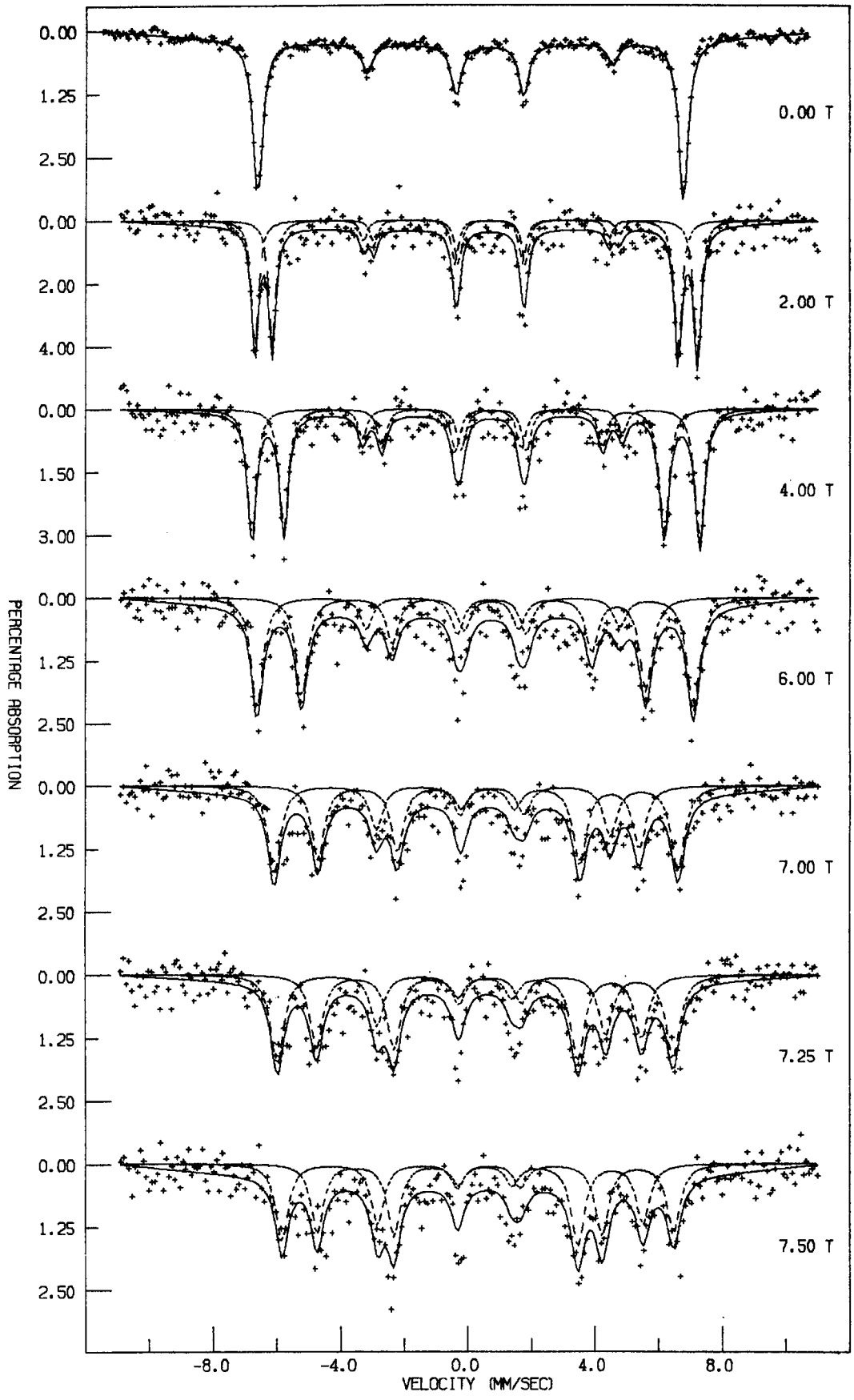

Figure 5.19 Spectra of an ac-plane crystal of Rb_2FeF_5, with applied fields and γ-rays directed along the b axis. Continued overleaf.

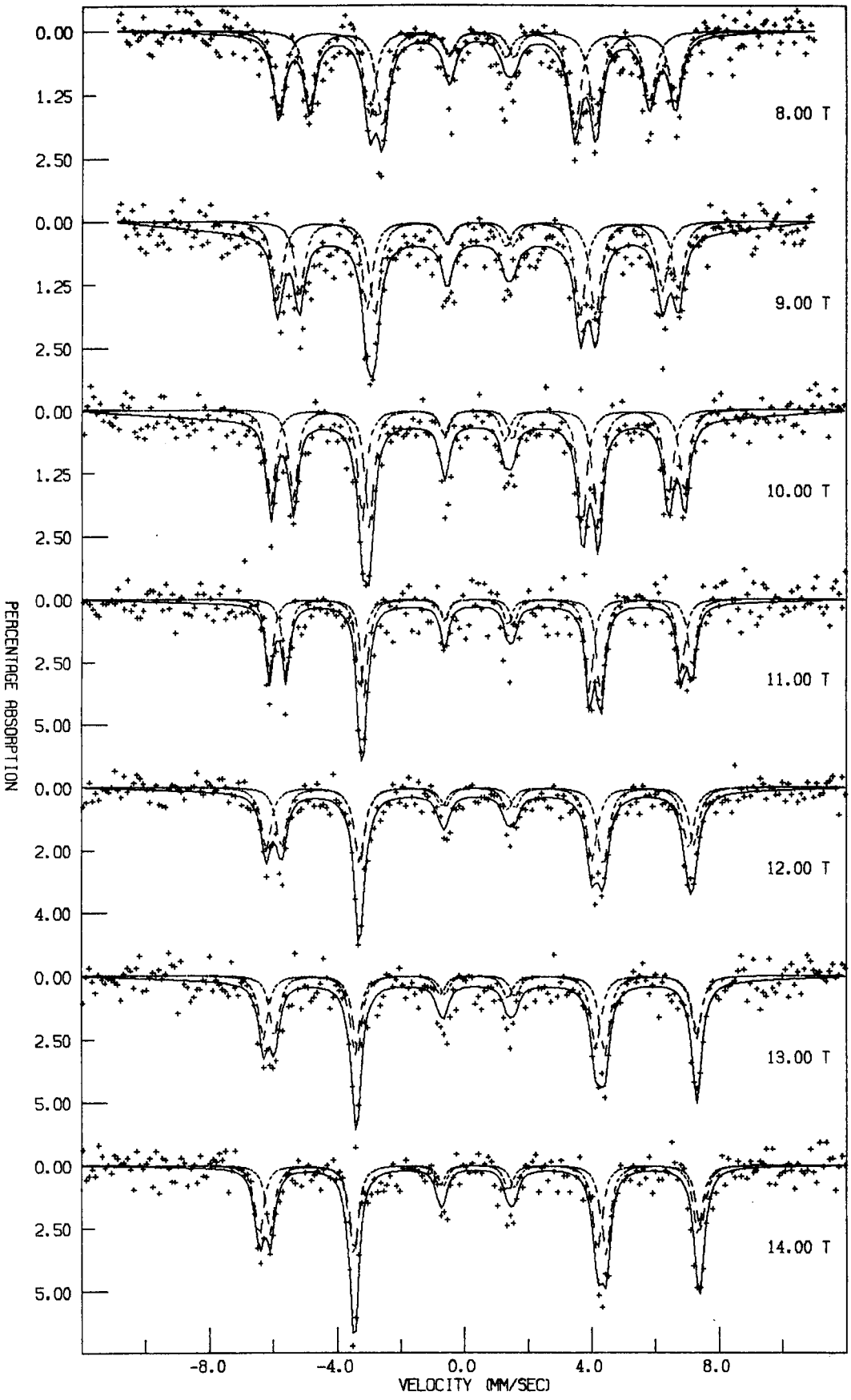

Figure 5.19 (continued) Spectra of an ac-plane crystal of Rb_2FeF_5, with applied fields and γ-rays directed along the b axis.

spectra of even moderate statistical quality, and consequently some of the spectra in Figure 5.19 are rather ill-defined.

The zero applied field spectrum contained six lines, with the non-zero $\Delta m=0$ lines implying that the spins and the γ-ray beam were not parallel. This is in keeping with the known magnetic structure of Rb_2FeF_5 (see Chapter 5.1c) in which the spins are antiferromagnetically ordered along two magnetically easy axes, both of which lie in the bc-plane at ~25° to the b axis. As the applied field was increased the spectral lines split and the intensity of the $\Delta m=0$ lines increased in a manner that is reminiscent of the 'rotation' transition that was observed in the 'misaligned' K_2FeF_5 experiment described in Chapter 5.2b. Thus the spectra imply that the spins were gradually rotating away from the field as it was increased. At higher fields (B>10.0T) the line splitting was smaller and the spectra approached a six line pattern, although even with B=14.0T applied some splitting was still apparent in the first and fifth lines of the spectrum. It therefore appears that even with the highest available field applied the spin-flop transition was not complete.

The spectra were computer analysed using Fit-Q with $\Delta=-0.68$mm/s, $\eta=0.50$, $\theta_g=\theta_H\simeq40°$ and $\phi_g=\phi_H=-90°$ assumed, following the results of Gupta et al. (1978b). Since the applied field was incident along the b axis it was once again possible to model the spectra via a single EFG coordinate system, using the same angle definitions as were given in Figure 5.7. The computer fit of the zero applied field spectrum gave $\theta_B=28°\pm1°$ with $\phi_B=90°$ assumed, which places the magnetic easy axes in the bc-plane at ~28° to the b axis. This result compares favourably with the 25°±5° reported by Gupta et al. (1978b) and the 22°±4° measured by Tressaud et al. (1981).

The non-zero applied field spectra were initially fitted by assuming a 'rotation' model in which the sublattice spins remained anti-

parallel while the AFM axis of the spins gradually rotated away from the applied field as it was increased. This model proved to be inadequate for the high field spectra (B≥8.0T). After a good deal of trial and error an alternative model incorporating 'canting' as well as 'rotation' was found to be suitable. In this 'canted rotation' model it is envisaged that in addition to a rotation of the AFM axis of the spins by an angle θ with respect to the applied field direction, the sublattice spins will also be canted away from the AFM axis by an angle α. This angle is expected to be of the order of $\alpha=\sin^{-1}[B_{\perp}/(2B_E+B_A)]$, where $B_{\perp}$ is the component of the applied field perpendicular to the AFM axis. It is also expected that the hyperfine fields associated with each of the magnetic sublattices will be different since (on the basis of spin-wave theory) the field-dependent spin reduction will depend on the the angle between the spins and the applied field. Thus in the 'canted rotation' fits two different hyperfine fields (each with an associated θ_B and ϕ_B) were allowed to vary. In this way quite good fits were obtained, and the intuitive supposition that the spins would remain in the bc-plane ($\phi_B=\pm 90°$) throughout the transition could be retained. The hyperfine parameters thus found are given in Table 5.8. Note that in order that both hyperfine field vectors might be defined with $\phi_B=+90°$ the magnitude of the second field, $\underline{B}_{hf2}$, was taken to be negative. The magnitude and polar angles of $\underline{B}_{hf2}$ are therefore given in Table 5.8 as $-|\underline{B}_{hf2}|$, θ_{B2} and $\phi_{B2}=+90°$, defining a vector which is equivalent to that described by $+|\underline{B}_{hf2}|$, $180°-\theta_{B2}$ and $\phi_{B2}=-90°$. Also shown in Table 5.8 are the fitted mean hyperfine fields $B_{av}=\frac{1}{2}(B_{hf1}+B_{hf2})$, rotation angles $\theta=\frac{1}{2}(\theta_{B1}+\theta_{B2})$ and canting angles $\alpha=\frac{1}{2}(\theta_{B1}-\theta_{B2})$ of each pair of sublattice spins.

Several comments on the validity of the 'canted rotation' model may be inferred from the fitted parameters. At first sight the field-dependence of the rotation angle θ (shown in Figure 5.20) is

Table 5.8 Fitted hyperfine parameters of the spectra of an ac-plane Rb_2FeF_5 crystal subject to an applied field B parallel to its b axis, as discussed in the text. Γ measured in mm/s; B, B_{hf} and B_{av} in Tesla. * denotes parameters that were not allowed to vary.

B	Γ	B_{hf}	θ_B	B_{av}	θ	α
0.00	0.37	41.4	28°	41.4	28°	0*
2.00	0.27	41.3	27°	41.3	27°	0*
4.00	0.35	40.3	34°	40.3	34°	0*
6.00	0.46	37.9	41°	37.9	41°	0*
7.00	0.49	35.1	58°	34.7	58°	0°
		-34.2	58°			
7.25	0.51	34.7	63°	34.3	63°	0°
		-34.0	63°			
7.50	0.50	35.4	75°	34.7	69°	5°
		-34.0	64°			
8.00	0.44	37.2	87°	35.7	80°	7°
		-34.2	74°			
9.00	0.40	38.1	92°	37.1	84°	8°
		-36.1	76°			
10.00	0.34	39.7	95°	38.4	86°	9°
		-37.0	78°			
11.00	0.29	41.4	100°	40.1	90°	10°
		-38.7	79°			
12.00	0.40	41.5	99°	40.3	91°	8°
		-39.1	82°			
13.00	0.37	42.3	100°	41.3	92°	9°
		-40.3	83°			
14.00	0.35	43.6	103°	42.6	91°	12°
		-41.6	79°			

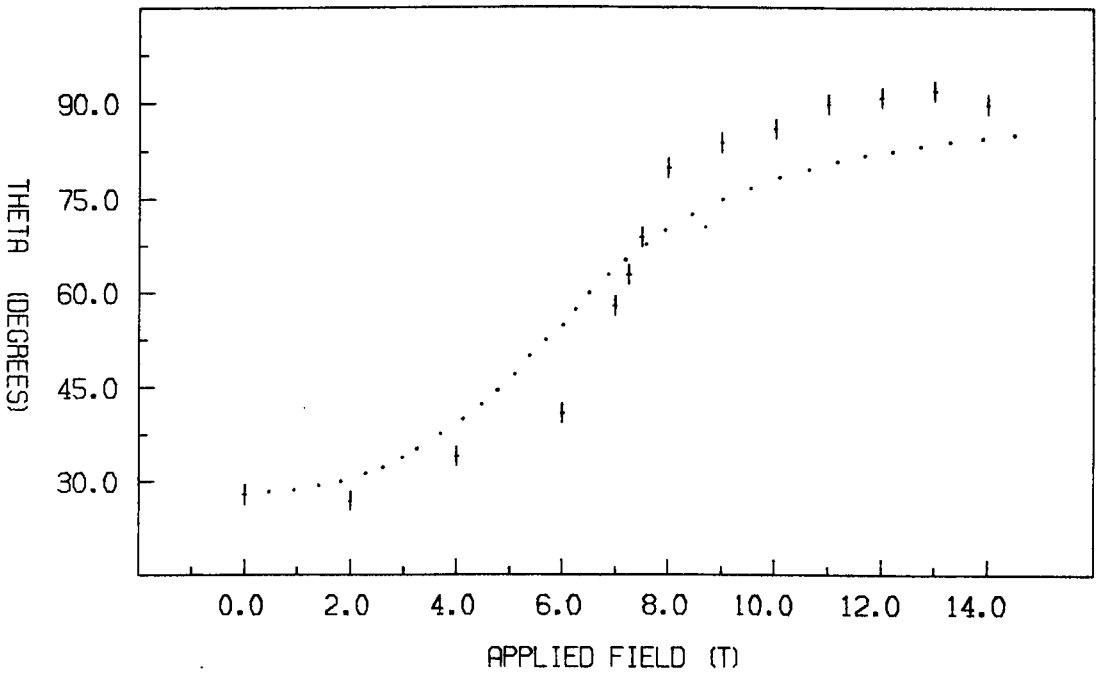

Figure 5.20 Comparison of the observed field-dependence of the rotation angle θ with the curve predicted from mean-field theory for a misalignment angle $\psi=28°$.

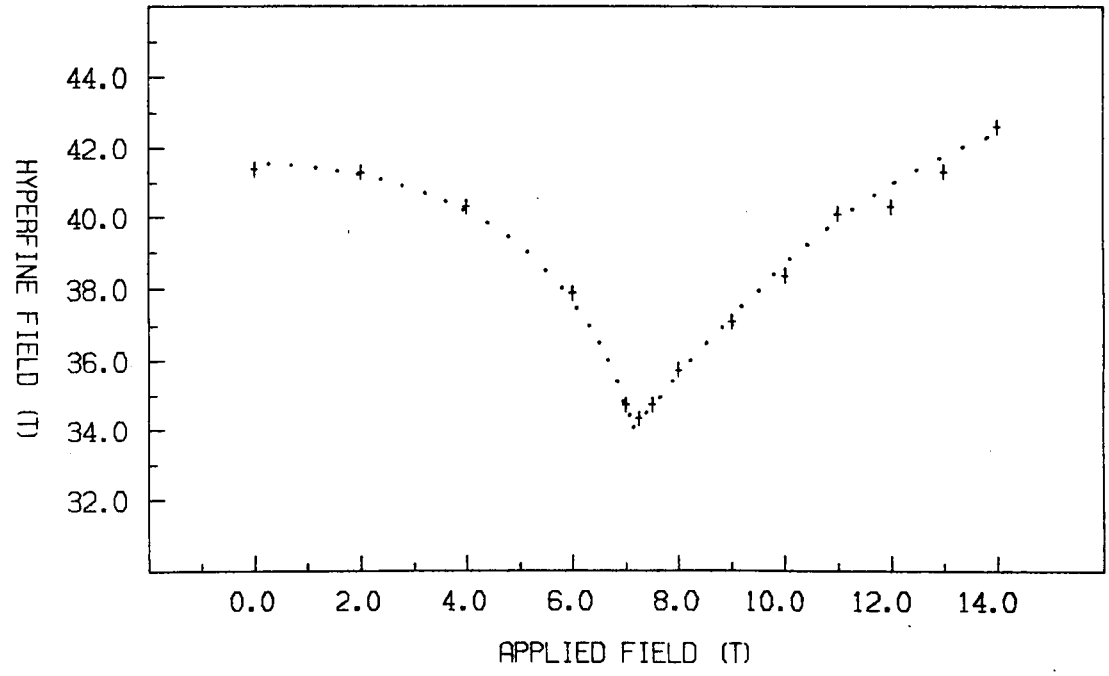

Figure 5.21 Observed field-dependence of the hyperfine field. The dotted curve is a guide to the eye.

quite sensible, with θ slowly changing from ~28° to ~90° as B is increased from zero to 14.0T. However, the fitted θ≈90° values for B≥11.0T must be regarded with some scepticism since in real terms a θ=90° configuration corresponds to the spin-flopped phase in which the hyperfine fields on each sublattice are identical and an unsplit six-line Mössbauer spectrum is observed. The fact that splitting is observed in the high field spectra indicates that the AFM axis of the spins is not perpendicular to $\underline{B}$ so that in fact θ<90°. A second misgiving about the fits is that the fitted canting angles are larger than theoretically expected, with e.g. α≈12° fitted in the B=14.0T spectrum, compared to a predicted canting of α≈6°. One other cause for concern is that the fitted differences between the two sublattice hyperfine fields (B_{hf1}-B_{hf2}) are surprisingly large. It is hard to imagine that direction-dependent spin reduction could account for such a large effect as the ΔB_{hf}≈2T fitted in the high field spectra. Taken together, these observations may lead us to conclude that although the 'canted rotation' model appears to be physically reasonable, the spectra which result when the relevant hyperfine parameters are allowed to freely vary are the subject of some doubts. On the other hand it should be recalled that the model provided quite close agreement between the experimental and theoretical spectra, and as such might at least be regarded as a good first approximation to the real situation in the crystal.

It may be noted that the fitting difficulties discussed above might perhaps be attributable to an inadvertent misalignment of the applied field with the b axis. However, if such a misalignment were significant it should have been observed in the low field spectra (B≤6.0T) as a superposition of two magnetically split spectra. Also, the similarity between the spectra recorded in this work and those reported by Gupta et al. (1978b) is sufficiently good to imply that the experiment is

repeatable and that misalignment is not a problem. Furthermore, we have no reason to expect the crystal ac-plane to contain a strong 'medium' anisotropy axis for the spins, and as such misalignment by a few degrees cannot explain the non-completion of the spin-flop that is apparent in the high field spectra.

In conclusion it is interesting to note that the observed spin-flop in Rb_2FeF_5, which appears to be a smooth second-order transition, has one or two features that are similar to those seen in the 'misaligned' K_2FeF_5 experiment. The variation of hyperfine field with applied field, shown in Figure 5.21, exhibits a minimum at ~7.25T. This again is presumably a result of field-induced spin reduction, and (as in the 'misaligned' K_2FeF_5 experiment) seems to be an incongruously 'sharp' feature in an otherwise 'smooth' transition. However, the B_{hf}-B curve provides a useful method of estimating the anisotropy field in Rb_2FeF_5. If we assume that the minimum in B_{hf} occurs when the component of applied field along the easy axis reaches the critical value, so that $B_{sf}(\psi)=B_{sf}\cos\psi$ where $\psi\simeq28^\circ$ is the misalignment angle, then $B_{sf}\simeq6.4T$ is obtained. Since $B_{sf}\simeq(2B_EB_A)^{\frac{1}{2}}$ and $B_E\simeq74T$ at 4.2K, we then obtain $B_A\simeq0.28T$. These parameters may then be used to compute the mean-field theory prediction for the field-dependence of the rotation angle θ, using equation (5.1). This curve is shown in Figure 5.20, where it is apparent that it is significantly broader than the observed curve, a feature that was also noted in the 'misaligned' K_2FeF_5 experiment. Thus it again appears that the mean-field theory does not provide very good quantitative predictions of the nature of the spin-flop.

5.4 DISCUSSION

It is useful to compare the spin-flop phase transitions that were observed in K_2FeF_5 and Rb_2FeF_5. In essence three experiments were performed : 'aligned' K_2FeF_5 in which the applied field was parallel to the easy axis; 'misaligned' K_2FeF_5 in which the field was at ~33° to the easy axis; and Rb_2FeF_5 in which the field was at ~28° to both easy axes. Representative spectra from each of these three experiments are shown in Figure 5.22. Comparing the transitions it appears that the character of the 'aligned' K_2FeF_5 spin-flop is significantly different to that observed in the 'misaligned' K_2FeF_5 and Rb_2FeF_5 experiments. This is in keeping with our earlier suggestions that the transition in the 'aligned' K_2FeF_5 experiment is of first-order, while in the other two cases the transition is of second-order.

In support of the conclusion that the 'aligned' K_2FeF_5 spin-flop is a first-order transition we should make one or two qualifying remarks. The transition was observed as a coexistence of unflopped and flopped phases over a range of applied fields $\Delta B \simeq 0.4T$, centered at $B_{sf} \simeq 3.65T$. This transition width is greater than the width that might be associated with either demagnetisation or hysteresis effects ($\Delta B \simeq 0.005T$ and $0.004T$ respectively), and so some other effect must be present. One simple explanation is that the degree of randomness in the crystal (due to impurities, defects, distortions etc.) is sufficiently large that a distribution of 'local critical field' values exists for the ferric ions. This could then account for the observation of a somewhat broadened transition, while the spin-flop for each individual ion was of first-order.

Another question which then arises is whether or not a first-order transition is a theoretically justifiable result of the 'aligned' K_2FeF_5 experiment. Mean-field theory predicts that in order to observe

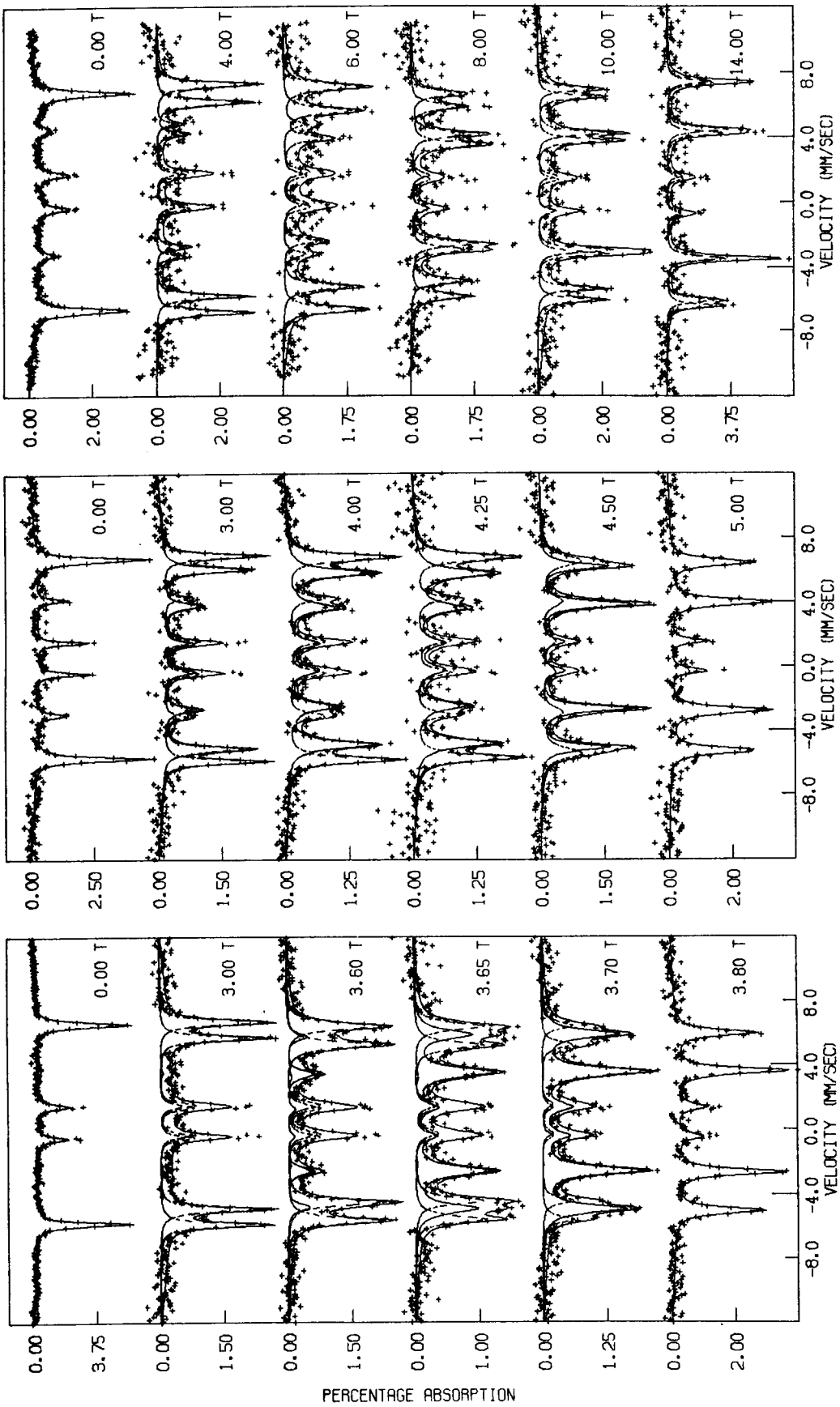

Figure 5.22 Representative spectra of the spin-flop transitions observed in the 'aligned' K_2FeF_5, 'misaligned' K_2FeF_5 and Rb_2FeF_5 experiments.

a first-order transition in a uniaxial antiferromagnet in which the exchange and anisotropy fields are the same as those in K_2FeF_5, the applied field must be aligned within ~0.03° of the easy axis. Since the estimated accuracy of alignment in the experiment was of the order of ±2°, it would therefore seem probable that a first-order transition would not occur. However, mean-field theory also predicts that the magnetic phase diagram of an orthorhombic antiferromagnet (such as K_2FeF_5) is quite different to the uniaxial case (see Chapter 2.2d). In an orthorhombic antiferromagnet the 'shelf' of first-order transitions extends to the paramagnetic phase boundary when the component of applied field perpendicular to the easy axis lies near the axis of hard anisotropy. In K_2FeF_5 there are two magnetically hard axes (corresponding to two sublattices of antiferromagnetically ordered spins) which lie in the crystal ac-plane at about ±40° to the a axis. It is therefore plausible that although we may not have had perfect alignment of the applied field and the easy axis, a first-order transition could have occurred at some of the ferric ions, resulting in a sharp transition as observed in the Mössbauer experiment.

In the case of the Rb_2FeF_5 and 'misaligned' K_2FeF_5 experiments there can be little doubt that second-order transitions were observed. Even so, the transitions exhibited some unexpected features. The observed field-dependence of the angle of rotation between the applied field and AFM axes was in both cases found to be less broad than the curve predicted by mean-field theory. A similar discrepancy was observed in a neutron diffraction study of $CuCl_2.2D_2O$ by Lynn et al. (1977), adding weight to the idea that the problem is something other than experimental error. It seems likely that the discrepancy is an indication of some inadequacies in the quantitative aspects of the mean-field description of the spin-flop. A second surprising feature of both experiments was the observation of a sharp minimum in the hyperfine

field as the applied field was increased. This minimum is presumably caused by the spin-wave induced spin reduction that is prevalent in magnetic systems with low Néel temperatures, and corresponds to a maximum in the spin-wave population at a given critical applied field. However, it is difficult to reconcile this 'sharp' feature in what otherwise are 'smooth' and second-order spin-flop transitions.

In conclusion it is clear that this Mössbauer study of the spin-flop in the quasi one-dimensional antiferromagnets K_2FeF_5 and Rb_2FeF_5 has provided some very interesting results relating to the mechanism of the spin-flop transition. In the following chapter we shall hope to find to what extent these results are dependent on the dimensionality of the systems, by looking at the nature of the spin-flop transition in the three-dimensional antiferromagnet α-Fe_2O_3.

CHAPTER SIX

α-Fe_2O_3

6.1 INTRODUCTION

The magnetic properties of hematite (α-Fe_2O_3) have interested researchers for many years, particularly after Morin (1950) reported a phase transition from a weakly ferromagnetic (WFM) to an antiferromagnetic (AFM) state on cooling below $T_M \simeq 260K$. A neutron diffraction study by Shull et al. (1951) showed that α-Fe_2O_3 is in essence an antiferromagnet below its Néel temperature $T_N \simeq 960K$, and that the WFM$\rightarrow$AFM transition that Morin had observed was in fact a temperature-driven spin-flop. Below T_M the ferric spins are antiferromagnetically aligned along the trigonal [111] axis, while above T_M the spins lie in the basal (111) plane but are not precisely antiparallel, being slightly canted to produce a WFM moment in the basal plane. Field-induced spin-flop transitions in the AFM state were subsequently observed by several investigators. Besser and Morrish (1964) and Foner (1965) applied magnetic fields parallel to the [111] direction at $T \leq 77K$ and observed a spin-flop at $B_{sf\parallel} \simeq 6.5T$. A more unusual transition induced by magnetic fields applied perpendicular to the [111] axis was observed by Kaczer and Shalnikova (1965) at temperatures just below T_M, and was also found to be a spin-flop between the AFM and WFM states.

The existence of these three distinct but complimentary phase transitions in α-Fe_2O_3 prompted the Mössbauer study undertaken in the present work. It was also thought that since hematite is a three-dimensional antiferromagnet the effect of spin-waves (either magnons or 'solitons') on the spin-flop would be small and the observed transitions would therefore provide a useful foil to the work done on K_2FeF_5 and Rb_2FeF_5. Other advantageous features were that reasonably large single crystal specimens were commercially available, and that the magnetic fields required for the field-induced transitions were

within the scope of the apparatus available in our laboratory. Also, despite the large number of reports in the literature on these transitions, there appears to have been relatively few Mossbauer experiments on the field-induced transitions. To the knowledge of the author only Blum et al. (1965) have published spectra of a field induced transition (the B$\|$[111] spin-flop), and as even those spectra were of minimal quality it was anticipated that a careful Mössbauer study would yield useful results.

In the remainder of this introductory section we will review the crystallographic, electric and magnetic structures of α-Fe_2O_3. In subsequent sections the experimental observations of the Morin transition, the 'parallel' (B$\|$[111]) spin-flop transition and the 'transverse' (B$^{\perp}$[111]) spin-flop transition will be presented and discussed.

6.1a Crystal Structure and Electric Field Gradient

The hematite crystal structure was first determined by Pauling and Hendricks (1925) and was later refined by Blake et al. (1966), in both cases using X-ray diffraction techniques. The unit cell was found to be rhombohedral (as illustrated in Figure 6.1) with edge length ~5.4A and rhombohedral angle ~55°, and contains two Fe_2O_3 molecules. Slightly distorted layers of oxygen anions normal to the trigonal [111] axis of the rhombohedral cell form a hexagonally close-packed lattice. The ferric ions fill two-thirds of the octahedral interstices within this lattice, following the stacking sequence ABCA where C corresponds to a vacant site. Interatomic distances of ~2.9A between nearest neighbour ferric ions were measured, while the distance between two ferric ions separated by a vacant site was found to be ~4.0A. This geometry is evident in Figure 6.1.

Since the iron in α-Fe_2O_3 is in the high-spin Fe^{3+} state the electric field gradient (EFG) at the ferric nuclei is dominated by the

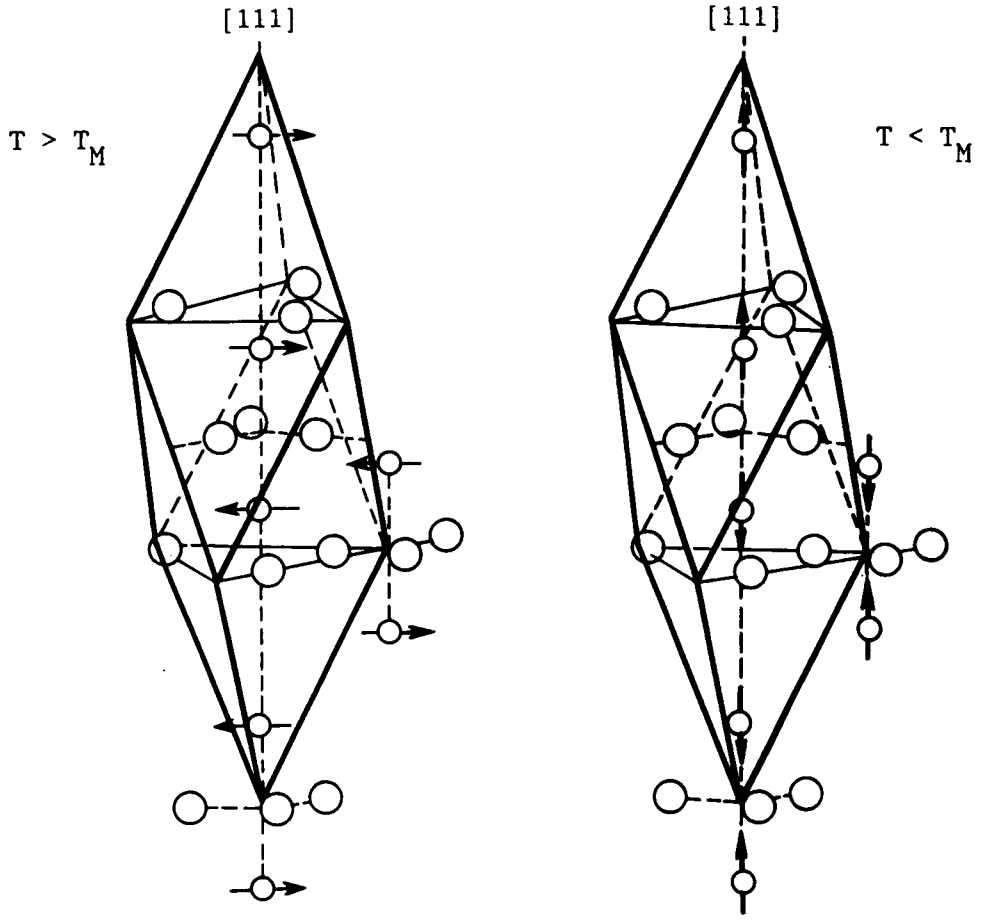

Figure 6.1 Crystallographic and magnetic structures of α-Fe_2O_3 above and below the Morin transition. Arrows represent the ferric spins.

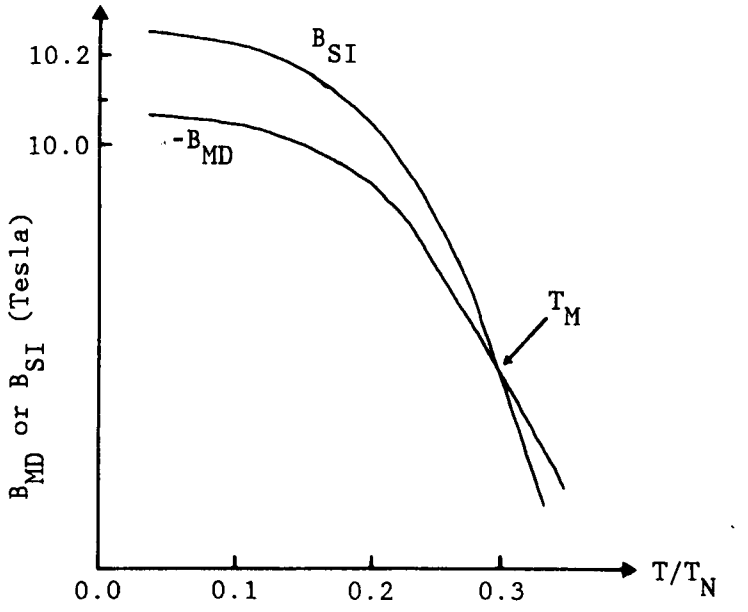

Figure 6.2 Temperature dependence of the magnetic dipole and single-ion anisotropy fields of α-Fe_2O_3 (Besser et al. 1967).

'lattice' contribution and may be directly related to the symmetry properties of the crystal structure. As discussed above hematite has a rhombohedral unit cell, the major axis of which passes through four ferric ions. This implies that the ferric ion environment possesses threefold rotational symmetry about the trigonal axis so that the crystal is invariant to a 120° rotation about the [111] axis. This symmetry is sufficient to establish that V_{zz} (the principal component of the EFG) will lie along the [111] axis and that V_{xx} will equal V_{yy} so that the asymmetry parameter η will be zero. This conclusion has been borne out by experimental observation. In a careful Mössbauer study of hematite single crystal and powder samples van der Woude (1966) confirmed that V_{zz} was directed along the trigonal axis, and measured an asymmetry of $\eta \leq 0.03$.

6.1b Magnetic Properties

In early studies of the magnetic behaviour of α-Fe_2O_3 a "strange" ferromagnetism with an ordering temperature of about 960K was discovered. An anomalously small spontaneous magnetisation of ~0.5emu/g was observed at room temperature, corresponding to about 2×10^{-4} of the nominal moment. Interest heightened in the 1950's when magnetic susceptibility measurements by Morin (1950) and Guillaud (1951) showed that the weak ferromagnetic moment disappeared on moderate cooling below room temperature in a narrow transition at about 260K. This transition has now come to be known as the 'Morin transition', although it is interesting to note that Honda and Sone (1914) and Charlesworth and Long (1939) had previously reported the effect but their work had been subsequently overlooked.

The nature of the Morin transition was revealed by a comprehensive neutron diffraction and scattering study over the temperature range 80K to 1000K by Shull, Strauser and Wollan in 1951. Below the 'Morin

temperature' $T_M \simeq 260K$ Shull et al. found that the ferric spins were directed along the crystallographic trigonal axis. They determined that the relative orientation of the spin directions at the four ferric sites within a given unit cell was --++, as depicted in Figure 6.1. Above T_M the spins were found to lie in the basal (111) plane, again with the --++ relative orientation. Thus the Morin transition was established as a temperature-driven spin-flop transition.

It is interesting to note that the overall magnetic lattice structure of hematite is somewhat similar to that found in simple cubic oxides. If one visualises additional unit cells to that shown in Figure 6.1 it is seen that both above and below T_M the magnetic structure consists of a series of 'puckered' basal plane sheets of ferric ions. The ferric spins within any given sheet are parallel, while those sheets that are separated by a single layer of oxygen ions are antiferromagnetically coupled. This alternating 'ferromagnetic' sheet structure with intermediate oxygen planes is reminiscent of the structure of simple cubic oxides such as MnO (Shull et al. 1951).

For much of the 1950's the origin of the weak ferromagnetism observed for $T_M<T<T_N$ was the subject of some controversy. Many possible explanations were proposed, such as ferrous ion impurities, rhombohedral magnetite imperfections and moment-bearing domain walls. However, these ideas were later discarded in favour of the explanation of Dzyaloshinsky (1958) who showed that the WFM moment in hematite was an intrinsic property of the symmetry of the crystal, arising from the effect of relativistic spin-lattice and the magnetic dipole interactions. By expanding the thermodynamic potential of the crystal as a function of spin density, Dzyaloshinsky found that a stable state exists in which the spins are slightly canted to produce a weak net ferromagnetism whose strength is from $\sim 10^{-2}$ to $\sim 10^{-5}$ of the nominal moment. This result compares favourably to the experimental value of

2×10^{-4}. In a later work Moriya (1960) developed a microscopic model of the magnetic behaviour of hematite (based on anisotropic super-exchange theory) and was able to express Dzyaloshinsky's spin canting term as an antisymmetric interaction $\underline{D}\cdot\underline{S}_1\times\underline{S}_2$ between neighbouring spins, where $\underline{D}$ is a constant vector directed along the [111] axis. Using this model Moriya obtained an estimate of the magnitude of the WFM moment which was in good agreement with the experimental value.

A theoretical interpretation of the Morin transition itself was subsequently proposed by Tasaki and Iida (1961) and later by Artman et al. (1965) on the basis of competing magnetocrystalline anisotropies. They showed that spin-orbit effects in hematite give rise to a fine structure (single ion) anisotropy energy constant K_{SI} which keeps the spins in the [111] direction. Magnetic dipole interactions give rise to a second anisotropy energy K_{MD} which gives the spins a preferred orientation in the (111) plane. The Morin transition may therefore be explained as a differing temperature dependence of the two anisotropies. Above T_M, $K_{SI}<K_{MD}$ and the spins lie in the basal plane, while below T_M, $K_{SI}>K_{MD}$ and the spins flop to the trigonal axis. Besser et al. (1967) calculated the temperature variations of the single ion and dipolar anisotropy fields B_{SI} and B_{MD} (via mean-field theory) from the measured field-induced spin-flop fields at low temperatures. The resultant curves (see Figure 6.2) show the anticipated crossover at T_M, confirming the applicability of the competing anisotropy model of the Morin transition.

6.2 EXPERIMENTAL RESULTS

In this section the results of a Mössbauer study of the Morin transition and of the 'parallel' and 'transverse' field-induced spin-flop transitions in α-Fe_2O_3 are presented.

For the most part the experiments were performed on two large single crystal specimens of hematite that had been synthetically grown at the Clarendon Laboratory, Oxford, via the 'flux growth' method (see Chapter 4.2a). The two crystals differed in the fluxes used during the growing process : PbO/PbF_2 for the so-called 'lead-flux' crystal, and $Na_2B_4O_7$ for the 'sodium-flux' crystal. Both crystals were received as platelets, and were of approximate dimensions 4×4×0.5 mm^3 and 2×1.5×0.2 mm^3 respectively. X-ray diffraction measurements established that both crystals were basal-plane platelets, with the trigonal [111] axis perpendicular to the plane of the platelet. The 0.5mm thickness of the lead-flux crystal was found to be too great to allow the passage of γ-rays through the sample, so it was set in a tablet of epoxy resin and abrasively thinned (using the technique described in Chapter 4.2b) to a thickness more suitable for Mössbauer experiments. Unfortunately the crystal was found to be very brittle and the thinning process had to be stopped before an ideal thickness had been obtained in order that total disintegration could be avoided. The sodium-flux crystal was sufficiently thin in its original state to allow the acquisition of Mössbauer spectra, although again it was rather thicker than what would normally be regarded as a 'thin' absorber. This excess thickness in both crystals is evident in all the spectra subsequently recorded (see later).

6.2a The Morin Transition

In the first of the experiments the Morin transition was investigated by recording the Mössbauer spectra of both crystals at a number of temperatures ranging between ~220K and room temperature. The samples were cooled in a variable temperature cryostat (described in Chapter 4.1b) which provided temperature control to better than ±0.1K over the period of time taken to accumulate the spectra (about one day each). Particular care was taken to ensure that the crystals were in good thermal contact with the sample holder so that the reading from the resistance thermometer mounted in the sample holder could be taken to be a true reflection of the sample temperature. Spectra were recorded with the γ-ray beam incident along the [111] axis of the crystals.

6.2a(i) Lead-flux Crystal

Over twenty spectra of the lead-flux crystal were recorded at temperatures ranging between 221K and 289K. From these spectra, seven representative spectra are given in Figure 6.3.

At room temperature (T≈289K) a six line hyperfine spectrum was recorded in which a line intensity ratio of about 1.8:2.0:1 in outer:middle:inner pairs of lines was evident. This intensity ratio is somewhat surprising since we expect that above the Morin transition at T_M~260K the ferric spins lie in the (111) plane, so that with the γ-rays directed along the [111] axis a spectrum with intensity ratio 3:4:1 should appear. The most probable explanation for this discrepancy is that substantial thickness-effect line broadening is present, with the larger intensity lines being broadened more than the weaker lines to give an apparent accentuation of the weaker lines in the observed spectrum. (This effect was discussed in Chapter 3.4.) If this were the case, and assuming that the thickness effect is not so great that the Lorentzian line-shape is lost, the 289K spectrum could still

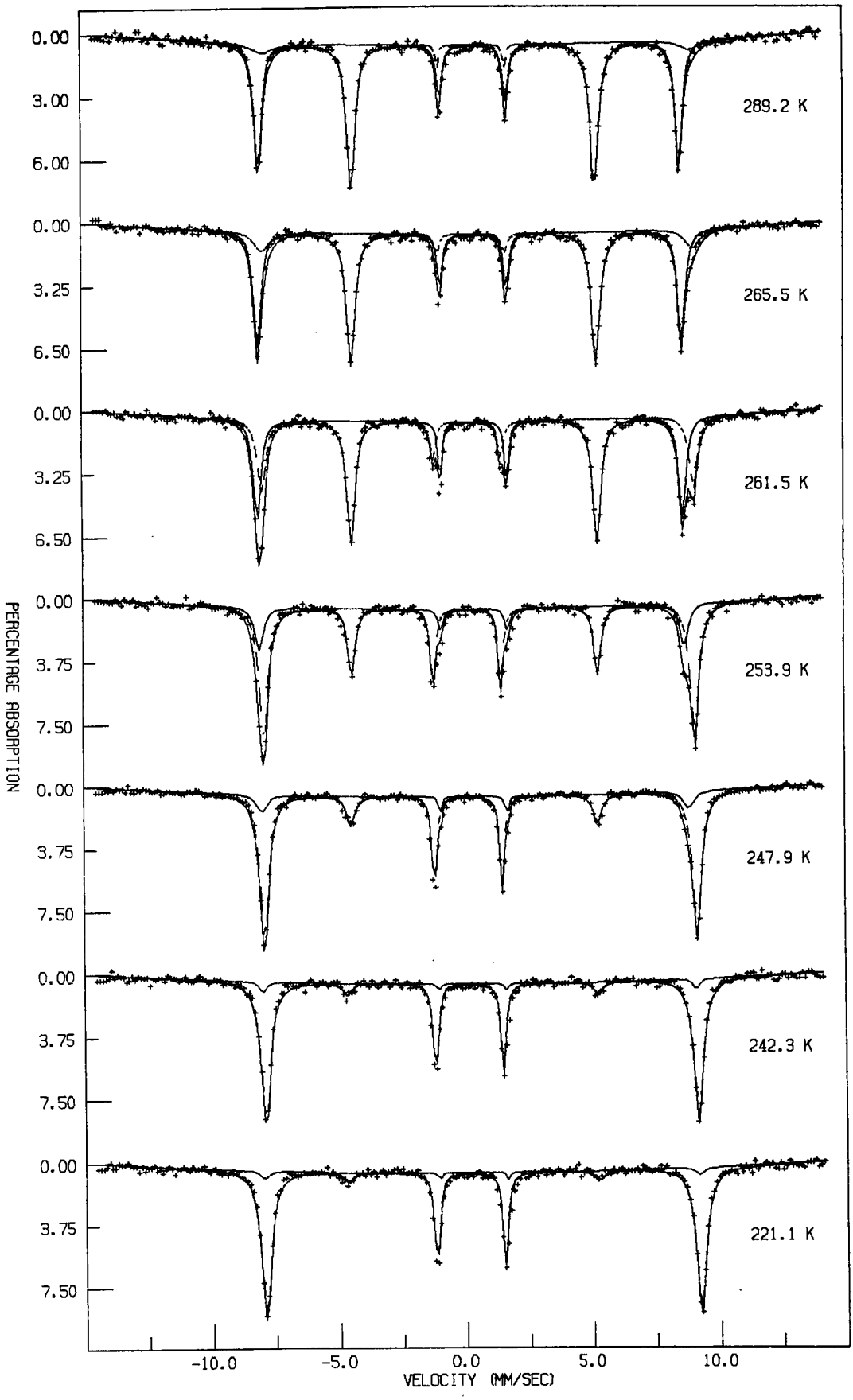

Figure 6.3 Spectra of the Morin transition in the lead-flux hematite crystal, with γ-rays directed along the [111] axis.

be interpreted as a 3:4:1 spectrum, with the provision that it has a 3:4:1 line area ratio, rather than a 3:4:1 line intensity ratio. Computer analysis of the spectrum (see later) shows this to be the case.

The spectrum recorded at 266K was quite similar to the 289K spectrum, with the intensity of the $\Delta m=0$ lines (lines two and five of the sextet) diminishing slightly. On lowering the temperature further major changes in the spectra became apparent. At 262K the innermost lines and the right-most line were visibly split, implying that the spectrum consisted of two component sextets with slightly different hyperfine parameters. At 254K and 248K this splitting was still apparent (although not so obvious) as an inequality in the intensities of the left-most and right-most lines. In addition, between 266K and 242K the $\Delta m=0$ lines (whilst remaining unsplit) decreased in their relative intensity until at 242K they were virtually absent, implying that at that temperature the ferric spins were almost parallel to the γ-ray beam. The spectrum recorded at 221K was not appreciably different from the 242K spectrum.

It is noticeable that although the intensity of the $\Delta m=0$ lines in the 221K spectrum was very small, they were still evident. Since we might have expected that the Morin transition would be complete at that temperature (which appears to be the case considering the similarity of the 242K and 221K spectra) and that the spins would therefore be aligned along the [111] axis, the presence of $\Delta m=0$ lines would appear to indicate that the γ-ray beam was not aligned with the [111] axis. This possibility was tested by repeating the experiment after re-positioning the crystal in the spectrometer. Rather surprisingly an almost identical spectrum was recorded, implying that misalignment might not be the cause of the non-zero $\Delta m=0$ lines. In the review article of Creer et al. (1975) it was noted that several experimenters have observed a small 'remanent' ferromagnetic moment in natural and

(less commonly) synthetic crystals of hematite which persists at temperatures well below T_M. This remanent WFM moment is thought to be a result of structural defects in these crystals, and as such is distinguished from the Dzyaloshinsky moment which is present only above T_M. Gallon (1968) has suggested that the remanence may be confined to small regions (domains) in the crystal which do not undergo the Morin transition. This model would explain our observations of small $\Delta m=0$ lines at 221K as a small admixture of a 3:4:1 component subspectrum due to domains of the high temperature WFM phase into a predominantly 3:0:1 spectrum corresponding to the low temperature AFM state.

In light of the above considerations the spectra shown in Figure 6.3 were computer analysed using Fit-A by assuming a superposition of two component subspectra corresponding to the WFM and AFM phases. Fit-A was used, despite the resultant loss of information and rigour that Fit-Q could have provided, because it is better suited to the analysis of thickness-broadened spectra. For example, using Fit-A the WFM subspectrum could be specified as having a line area ratio of 3:4:1, while allowing the spectral linewidths to vary independently. Similarly the AFM subspectrum was specified by a 3:0:1 area ratio. The fitted values of the isomer shift δ, quadrupole shift ε, linewidth Γ_{16} of the outermost lines, and hyperfine field B_{hf} of each component are given in Table 6.1.

The computer fits of the high temperature spectra (T≈289K and 266K) indicated that about 85% of the spins were in the WFM phase, although the unrealistically large linewidth fitted for the AFM component casts some doubt on this figure. It is likely that in fact nearly all of the spins are in the WFM state and that the 15% component of AFM-like spectrum is an artefact of the fit that is related to the thickness-effect problems known to be present. The low temperature spectra (T≈242K and 221K) both showed that about 10% of the spins re-

mained in the WFM state whilst the remaining spins had undergone the Morin transition. This estimate of the degree of completion of the transition is fairly reliable since the area of the WFM component in these spectra is largely determined by the intensity and linewidth of the $\Delta m=0$ lines, which are sufficiently weak that thickness-broadening should be negligible.

Table 6.1 Fitted hyperfine parameters of the spectra of the lead-flux α-Fe_2O_3 basal-plane crystal, as discussed in the text. δ, ε and Γ_{16} measured in mm/s; B_{hf} in Tesla.

T	δ	2ε	Γ_{16}	B_{hf}	Area
289.2 K	0.39	-0.18	0.33	51.4	85%
	0.51	0.19	1.86	52.2	15%
265.5 K	0.41	-0.17	0.34	51.8	84%
	0.51	0.23	0.75	52.6	16%
261.5 K	0.40	-0.18	0.35	52.0	71%
	0.42	0.38	0.39	52.8	29%
253.9 K	0.41	-0.12	0.40	52.0	41%
	0.41	0.46	0.41	52.7	59%
247.9 K	0.42	0.04	0.50	52.1	23%
	0.41	0.47	0.42	52.9	77%
242.3 K	0.43	0.25	0.34	52.9	10%
	0.41	0.48	0.45	52.8	90%
221.1 K	0.46	0.31	0.42	53.2	9%
	0.42	0.49	0.46	53.1	91%

The spectra at the intermediate temperatures T≈262K, 254K and 248K were sufficiently well resolved to allow a reasonably accurate measurement of the hyperfine parameters of both the AFM and the WFM subspectra. In all three spectra the hyperfine fields of the two phases were found to differ by about 0.8T. This figure compares very favourably with the prediction by van der Woude (1966) of a change in B_{hf} of ~0.6T at the Morin transition as a result of the different direction dependences of the orbital and dipolar components of the

hyperfine field. Another interesting feature evident from the fitted parameters is that the quadrupole shifts of the subspectra are quite different. As discussed in Chapter 3.3d, when $\eta=0$ the observed shift is related to the quadrupole splitting Δ by the expression $2\varepsilon=\frac{1}{2}(3\cos^2\theta-1)\Delta$, where θ is the angle between the EFG principal axis and the magnetic axis of the spins. Since V_{zz} is directed along the [111] axis both above and below the Morin transition we expect that this angle will change from $\theta=90°$ above T_M to $\theta=0$ below T_M as the spins flop from the (111) plane to the [111] axis. Thus we anticipate that the quadrupole shift will be $2\varepsilon=-\frac{1}{2}\Delta$ above T_M and $2\varepsilon'=\Delta$ below T_M. This prediction would appear to be confirmed at 262K where the measured shifts were $2\varepsilon\simeq-0.18$mm/s and $2\varepsilon'\simeq0.38$mm/s. At 254K and 248K the two component sextets were not so well defined and the agreement is less convincing.

The observation of two distinct sextets in the transition region spectra supports the idea that the Morin transition is a first-order spin-flop, as predicted by Artman et al. (1952) and Levinson et al. (1969). In addition the observed differences in hyperfine field and quadrupole shift in the two sextets are in agreement with those expected for a 90° spin reorientation. We may therefore envisage the transition as a growth of AFM domains at the expense of WFM domains in the crystal as the sample is cooled through T_M. The Morin transition for each individual ion would then be of first-order, with the observed transition width being a result of sample inhomogeneities or structural defects giving rise to a distribution of local environments for the ferric ions.

However, if the transition is of first-order then hysteresis should be a feature of the transition with the Morin temperature being dependent on whether it is approached from above (T_{M+}) or from below (T_{M-}). Previous workers, including van der Woude (1966) and Nininger

and Schroeer (1978), have observed such hysteresis in a number of samples, with values for T_{M-} - T_{M+} ranging from ~1K to as much as ~11K. To investigate the possibility of hysteresis in our lead-flux crystal two series of spectra were recorded for both ascending and descending temperatures. The fitted relative areas of the WFM and AFM components in each of these spectra are shown in Figure 6.4, where it is evident that there is no obvious indication of hysteresis being present. Although this is a somewhat surprising observation it is not unprecedented. There are several reports in the literature, including Blackman and Gustard (1962) and Gallon (1968), of a lack of hysteresis in what otherwise would be interpreted as a first-order transition. It is reasonable to suggest that this effect may again be a result of sample inhomogeneity and the general variability in the quality of the crystals studied by different researchers.

6.2a(ii) Sodium-flux Crystal

A total of six spectra of the sodium-flux hematite crystal were recorded at temperatures ranging between 246K and 258K. The spectra (shown in Figure 6.5) were very similar in character to those obtained from the lead-flux crystal and therefore will not be described further. The spectra were fitted using Fit-Q and gave the hyperfine parameters listed in Table 6.2.

The major difference between the Morin transitions in the lead-flux and sodium-flux crystal is clearly in the 'sharpness' of the transition. This is illustrated in Figure 6.6 by the temperature dependence of the WFM:AFM relative areas in the two samples. In the lead-flux crystal the transition occurred over a range of temperatures $\Delta T \simeq 25K$ centered at $T_M \simeq 255K$, whereas in the sodium-flux crystal $\Delta T \simeq 12K$ and $T_M \simeq 252K$. Such a difference is not very surprising as it is clearly evident in the literature that the width and mid-point of the Morin transition is highly dependent on the quality of the particular sample

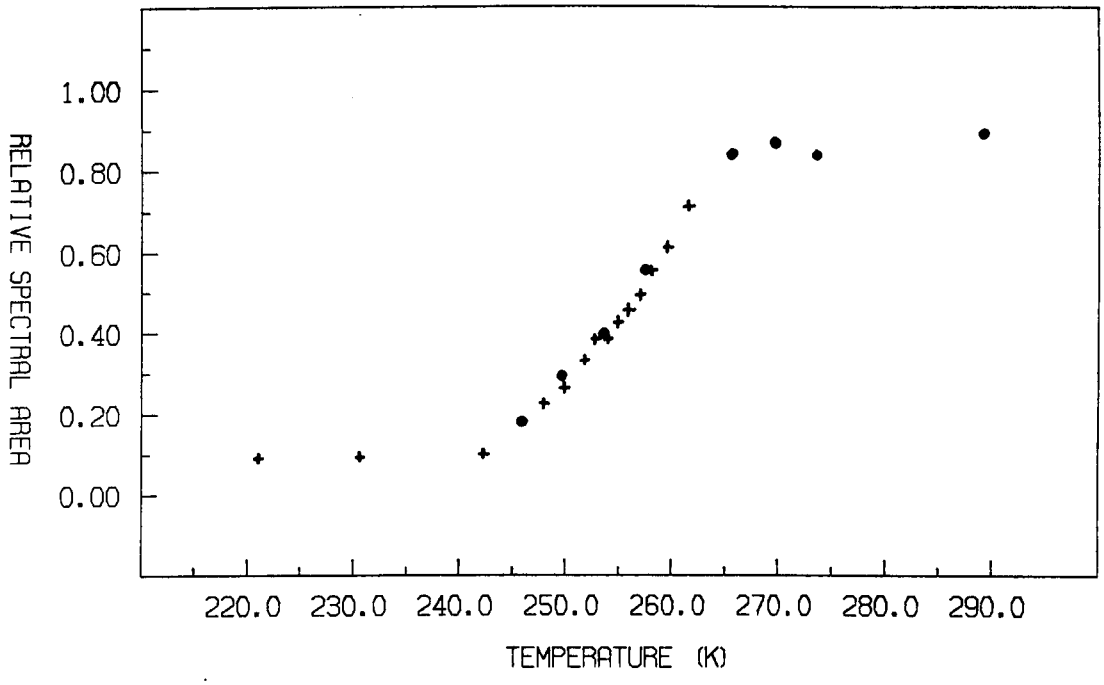

Figure 6.4 Observed temperature-dependence of the relative area of WFM to AFM components in the lead-flux hematite Morin transition spectra, as measured for ascending (•) and descending (+) temperatures.

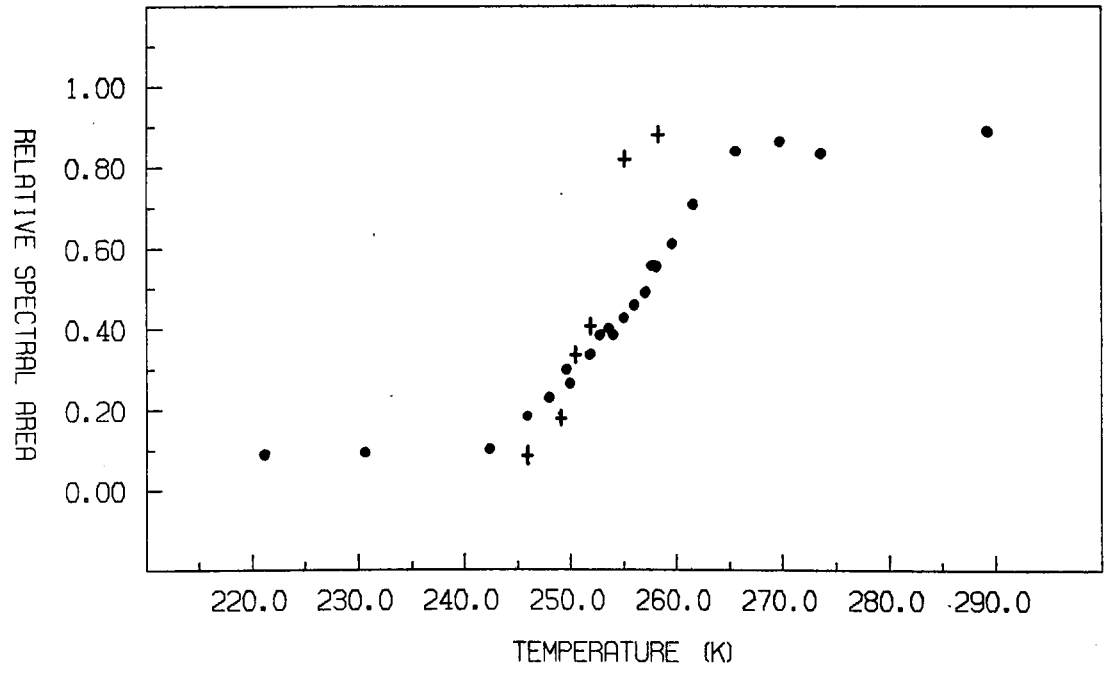

Figure 6.6 Observed temperature-dependence of the WFM:AFM relative areas in the lead-flux (•) and sodium-flux (+) hematite Morin transition spectra.

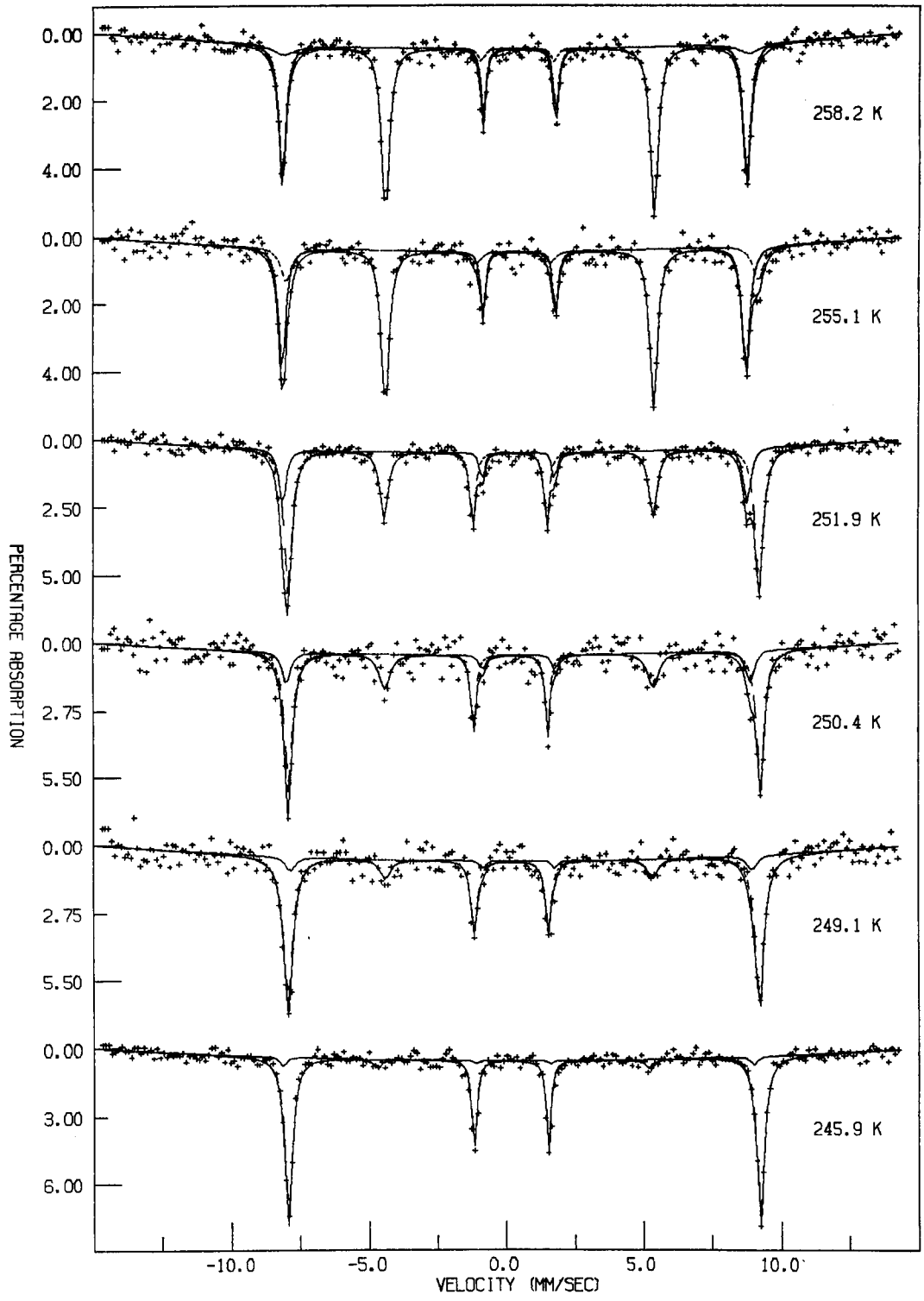

Figure 6.5 Spectra of the Morin transition in the sodium-flux hematite crystal, with γ-rays directed along the [111] axis.

being used. For example, widths as high as ~70K have been reported in some natural single crystals (Imbert and Gerard 1963), while Besser et al. (1967) observed $\Delta T<1K$ in a pure synthetic crystal. In general the transition in synthetically grown crystals is sharper than in natural crystals, although even with synthetic crystals the magnetic properties are sensitive to the exact method of preparation (Takada et al. 1965). The presence of foreign cations in hematite has also been shown to have a large effect on the transition, usually lowering the Morin temperature (Tasaki and Iida 1961, Curry et al. 1965, Besser et al. 1967). In particular Ti^{4+} has an enormous effect, with a doping of only 0.3% being sufficient to completely suppress the transition. Tin is also known to have a strong influence (Flanders and Remeika 1965).

Table 6.2 Fitted hyperfine parameters of the spectra of the sodium-flux α-Fe_2O_3 basal-plane crystal, as discussed in the text. δ, ε and Γ_{16} measured in mm/s; B_{hf} in Tesla.

T	δ	2ε	Γ_{16}	B_{hf}	Area
258.2 K	0.42	-0.21	0.31	52.2	88%
	0.41	-0.07	1.06	52.3	12%
255.1 K	0.42	-0.21	0.32	52.2	82%
	0.45	0.30	0.49	53.1	18%
251.9 K	0.42	-0.15	0.31	52.3	41%
	0.42	0.49	0.36	53.1	59%
250.4 K	0.47	-0.03	0.37	52.2	33%
	0.43	0.49	0.34	53.2	67%
249.1 K	0.51	0.08	0.44	52.0	18%
	0.42	0.45	0.40	53.1	82%
245.9 K	0.35	0.17	0.28	53.0	8%
	0.42	0.49	0.33	53.2	92%

It is therefore natural to conclude from our observation of the Morin transition in the two hematite crystals that the observed dif-

ferences in transition width indicates that the sodium-flux hematite is of a higher purity, or contains fewer structural defects, than the lead-flux hematite.

6.2b The 'Parallel' Field-Induced Spin-Flop

In the first of the two field-induced spin-flop experiments Mossbauer spectra of the lead-flux and sodium-flux crystals were recorded at 4.2K with both the incident γ-rays and applied fields of up to 10T directed parallel to the [111] axis.

6.2b(i) Lead-flux Crystal

The spectra obtained from the lead-flux crystal are shown in Figure 6.7. In zero applied field a four line spectrum was observed. The complete absence of the $\Delta m=0$ lines implies that the γ-ray beam was directed within one or two degrees of the magnetically easy axis (the [111] axis). It is also notable that the zero $\Delta m=0$ line intensity implies that at 4.2K the Morin transition has taken place for all of the spins in the crystal, and the residual magnetisation that had been apparent in the 221K spectrum is no longer present. In applied fields of up to 6.0T the spectral lines split into pairs and the intensity of the $\Delta m=0$ lines (which were also split) increased. This behaviour is in keeping with a gradual rotation (in unison) of the spins away from the field as it was increased. The spectra obtained for $6.0T<B<9.0T$ were rather complicated, with additional lines appearing at the $\Delta m=0$ line positions and the outer lines showing evidence of structure. With $B\geq 9.0T$ applied a single sextet pattern was observed, with a line intensity ratio of about 3:4:1, indicating that the spin-flop was complete and the spins were lying in the basal plane.

The spectra were computer analysed using Fit-Q. This program was used (despite being ill-equipped to simulate thickness-broadened spectra) because it was thought that more information could be ex-

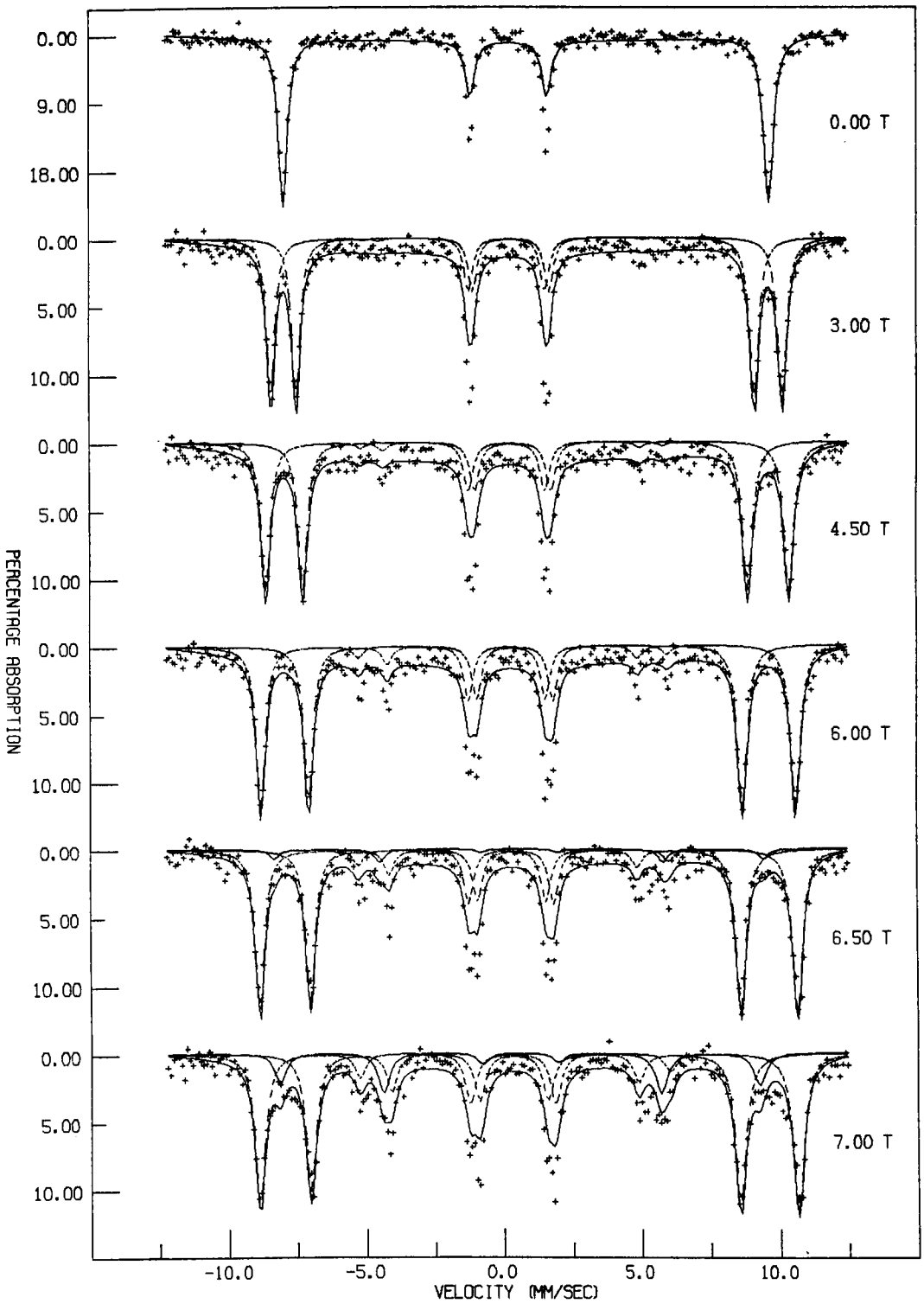

Figure 6.7 Spectra of the lead-flux hematite crystal, with applied fields and γ-rays directed along the [111] axis. Continued overleaf.

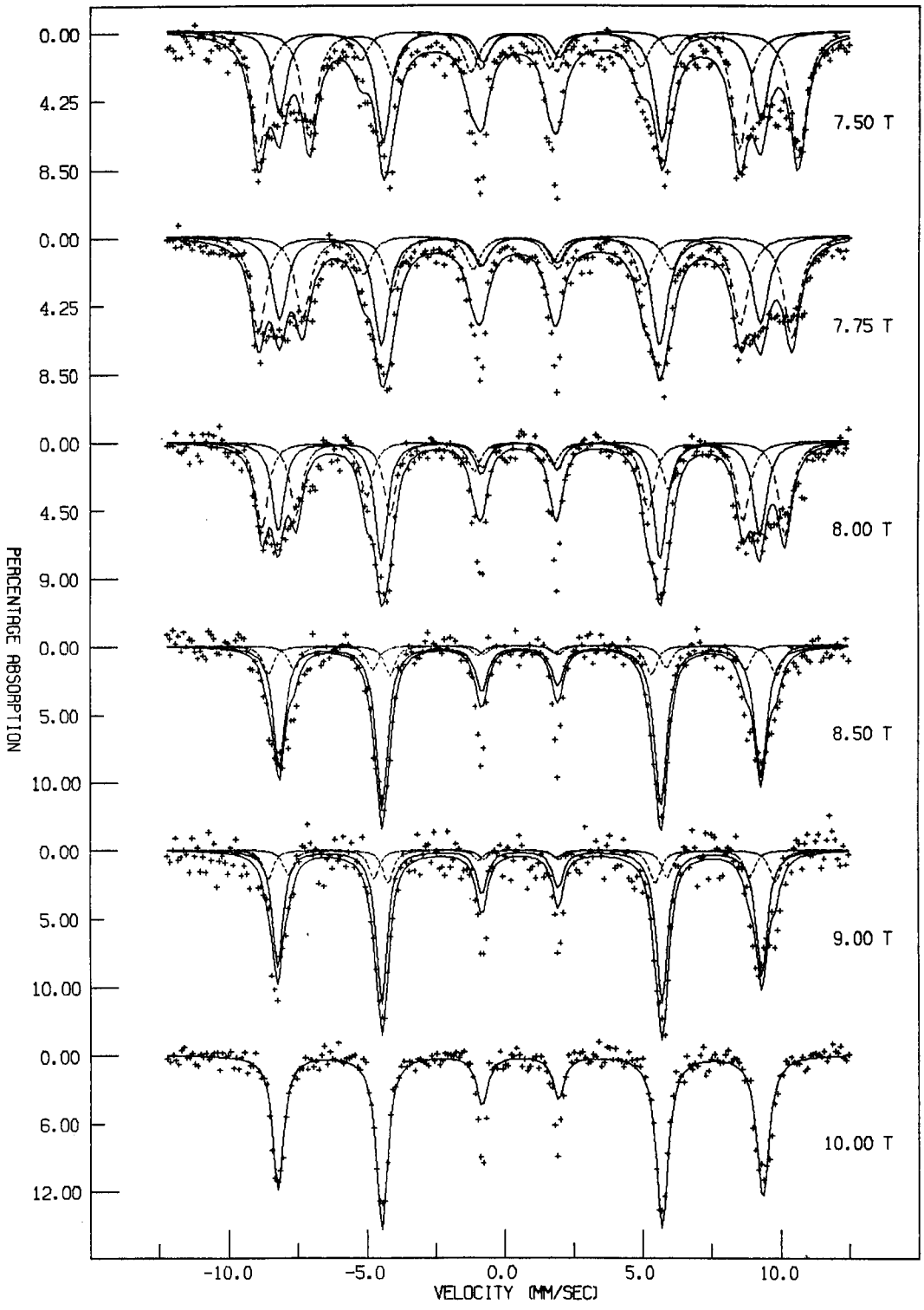

Figure 6.7 (continued) Spectra of the lead-flux hematite crystal, with applied fields and γ-rays directed along the [111] axis.

tracted from the spectra by fitting the observed line positions within the solid theoretical framework that Fit-Q provides. In other words, using Fit-Q the spectra could be fitted with a more physically justifiable model than could be obtained with the curve-fitting program Fit-A. The fitted hyperfine parameters determined with Fit-Q are given in Table 6.3. Since the EFG principal axis lies along the [111] axis and since η=0 the polar angles θ_g, ϕ_g, θ_H and ϕ_H of the γ-rays and applied field (in the crystallographic coordinate system) were all taken to be zero in these fits.

Table 6.3 Fitted hyperfine parameters of the spectra of the lead-flux hematite crystal subject to an applied field B parallel to its [111] axis, as discussed in the text. Δ and Γ measured in mm/s, B and B_{hf} in Tesla. * denotes parameters that were not allowed to vary.

B	Δ	Γ	B_{hf}	θ_B	Area
0.00	0.43	0.41	54.4	0°*	-
3.00	0.43	0.38	54.4	7°	-
4.50	0.43	0.42	54.4	12°	-
6.00	0.45	0.41	54.3	19°	-
6.50	0.47	0.42	54.3	22°	95%
		0.43	54.6	90°*	5%
7.00	0.47	0.47	54.2	29°	84%
		0.50	53.4	90°*	16%
7.50	0.47	0.67	54.1	35°	64%
		0.65	53.4	90°*	36%
7.75	0.42	0.68	54.1	47°	59%
		0.72	53.4	90°*	41%
8.00	0.42	0.57	54.0	58°	60%
		0.55	53.5	90°*	40%
8.50	0.42	0.45	53.4	67°	26%
		0.50	53.4	90°*	74%
9.00	0.43	0.47	53.6	73°	29%
		0.48	53.5	90°*	71%
10.00	0.41	0.50	53.5	90°*	-

The zero applied field spectrum was fitted with θ_B=0 assumed, confirming that the γ-ray beam was well aligned with the [111] axis. For moderate applied fields (B≤6.0T) it was assumed that the AFM axis of the spins had rotated by an angle θ_B away from the applied field direction (the [111] axis). The fits obtained using this model show an appreciable mis-fit in the intensities of the weak Δm=0 lines and the two innermost lines. This mis-fit arises from the 'thin absorber approximation' that is used in Fit-Q, whereby equal linewidths are assigned to all of the lines in a given spectrum. The fitted linewidth Γ is largely determined by the most intense (and therefore most thickness-broadened) lines, resulting in a misrepresentation of the intensities of the weaker lines. Fortunately this problem is not too significant as regards the validity of the fits. The rotation angle θ_B in the low-field spectra could be reliably determined from the observed splitting $\Delta B_{eff}=2B\cos\theta_B$ between the two effective fields resulting from the vector addition of the applied and hyperfine fields.

The spectra in the transition region (6.5T≤B≤9.0T) were modelled as a superposition of a 'rotated' spectrum with split lines and intermediate intensity Δm=0 lines, and a 'flopped' spectrum of unsplit lines in 3:4:1 intensity ratio. The effect of canting of the spins in the flopped phase by an angle $\alpha\approx\sin^{-1}(B/2B_E)$ was considered to be negligible since the exchange field in hematite is known to be large, $B_E\approx$450T (Ozhogin and Shapiro 1968). The relative spectral area of the flopped component was found to increase a B increased, until at B=10.0T it constituted the total spectrum. The quality of the fits in this transition region is moderate, but sufficiently high that the model may be regarded as an adequate description of the behaviour of the sample.

Thus it appears from the spectra and the fits that the spin-flop in the lead-flux hematite crystal has two parts : a gradual spin ro-

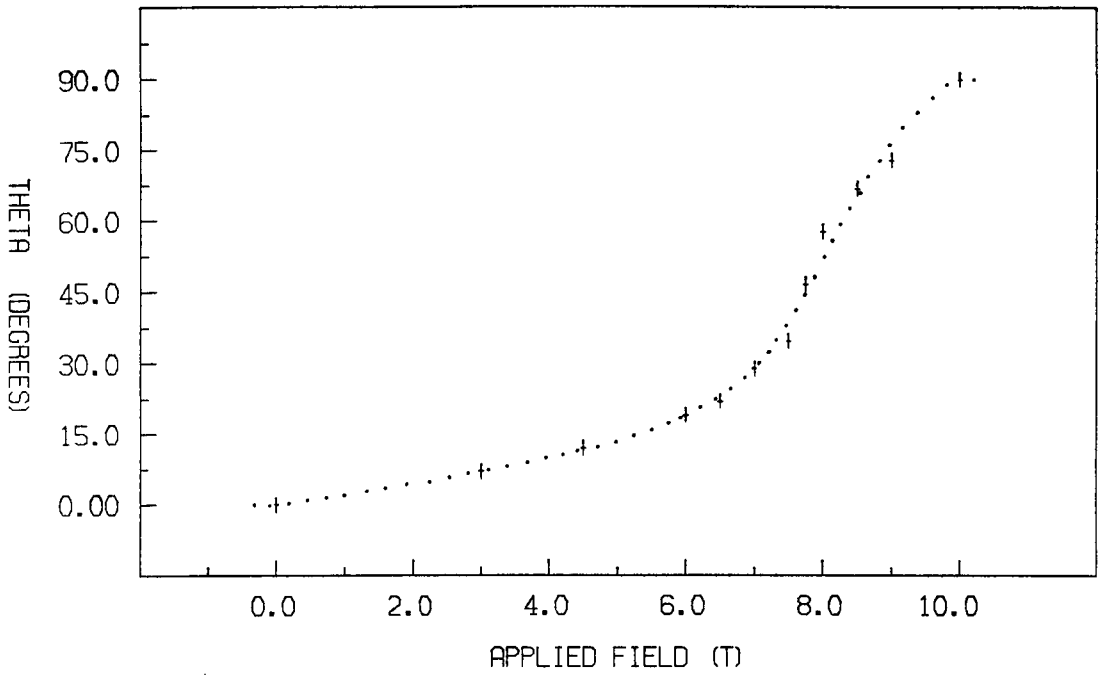

Figure 6.8 Observed field-dependence of the rotation angle θ between the AFM axis of the spins and the applied field in the lead-flux crystal. The dotted curve is a guide to the eye.

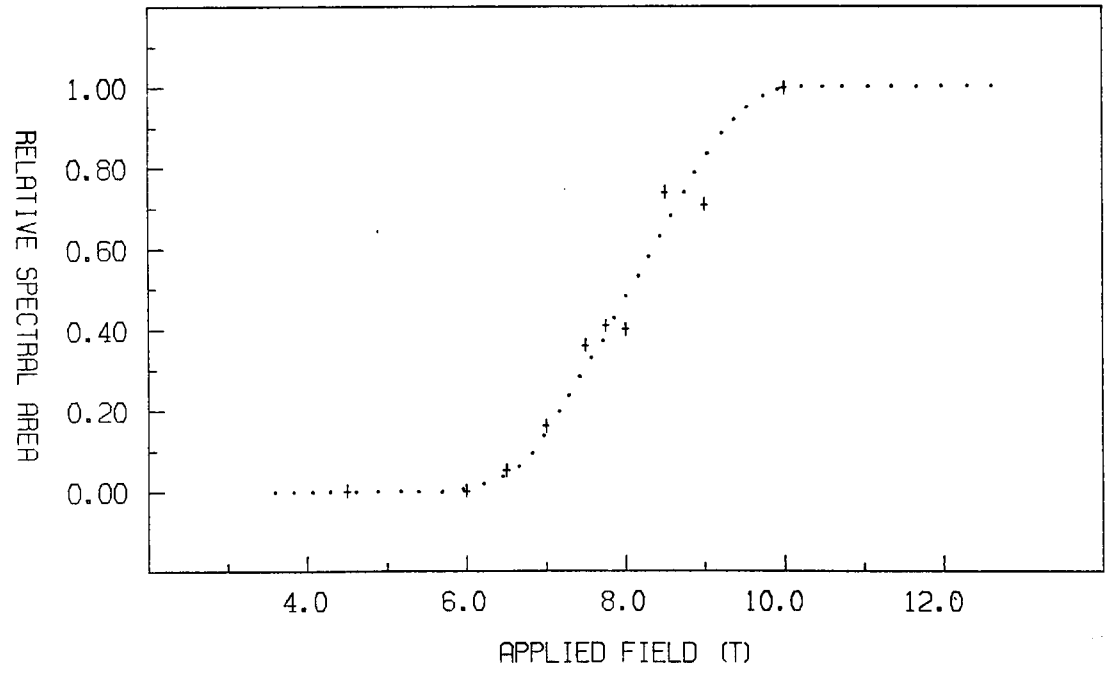

Figure 6.9 Observed field-dependence of the relative areas of spin-flopped to unflopped spectral components in the lead-flux crystal. The dotted curve is a guide to the eye.

tation from the [111] axis to the (111) plane in a broad transition (see Figure 6.8), superimposed on a sharp transition of first-order character beginning at B≈6.5T in which a spin-flopped component appears (see Figure 6.9). Both of these transitions merge together at B≈9.0T, so that by B=10.0T all the spins have flopped into the (111) plane and the spin-flop is complete.

This observation of a combined first-order and second-order transition is rather unusual. Previous workers, including Kaneko and Abe (1965), Besser et al. (1967) and Ozhogin and Shapiro (1968), have observed abrupt spin-flop transitions at critical fields in the range 6.3T to 6.8T. Although some of these experiments were conducted at 77K it is well established that B_{sf} varies only slightly below ~130K (Besser et al. 1967, Foner and Shapiro 1969), so the fact that our experiment was conducted at 4.2K should have no bearing on the transition. It would appear that once again the quality of the sample may be called into question, a possibility which we may investigate by looking at the spin-flop in the sodium-flux crystal.

6.2b(ii) Sodium-flux Crystal

The spectra obtained from the sodium-flux hematite crystal are shown in Figure 6.10, where it is evident that the transition was a good deal sharper and more clear-cut than that which was seen in the lead-flux crystal. The zero applied field spectrum showed no $\Delta m=0$ lines, confirming the alignment of the γ-rays with the trigonal axis. As B was increased to 6.0T the spectral lines split whilst the intensity of the $\Delta m=0$ lines remained zero, implying that the AFM axis of the spins had not moved away from the [111] axis. At B≈6.3T two unsplit $\Delta m=0$ lines appeared while the outer lines showed structure consistent with the spectrum being composed of an unsplit 3:4:1 component superimposed on a split 3:0:1 spectrum. As the field was increased the

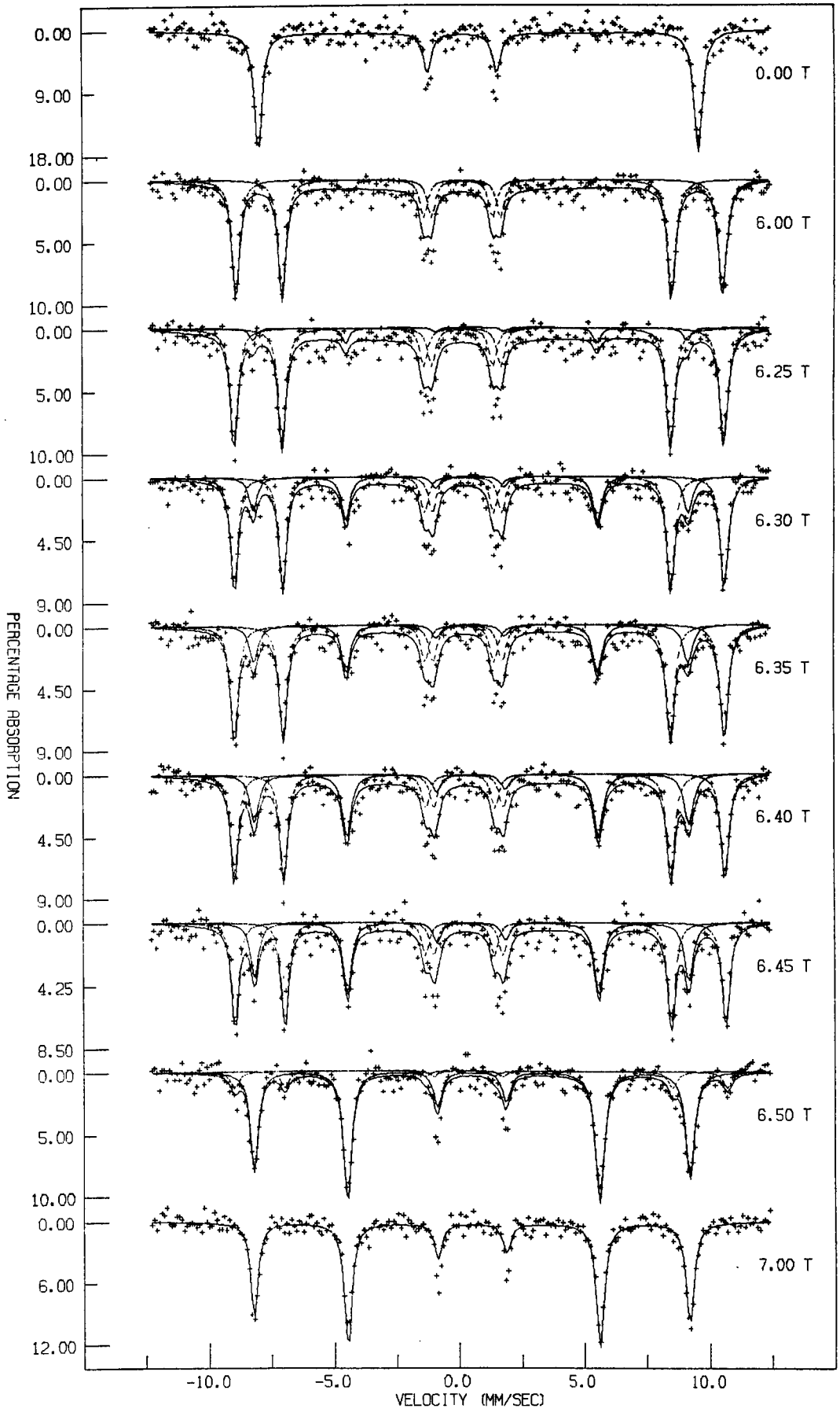

Figure 6.10 Spectra of the sodium-flux hematite crystal, with applied fields and γ-rays directed along the [111] axis.

relative area of the 'flopped' 3:4:1 component increased until for $B \geq 6.5T$ it accounted for the entire spectral area.

The spectra were analysed with Fit-Q, yielding the parameters given in Table 6.4. The transition spectra were fitted as a composite of a split 3:0:1 spectrum corresponding to unflopped spins aligned with the [111] axis ($\theta_B=0$), plus an unsplit 3:4:1 spectrum due to flopped spins in the (111) plane ($\theta_B=90°$). The field dependence of the relative spectral area of the flopped component is plotted in Figure 6.11, and shows that the spin-flop took place over a range of fields $\Delta B \approx 0.6T$ centered at $B_{sf} \approx 6.4T$. The fitted hyperfine fields were ~54.3T for the unflopped phase and ~53.5T for the flopped phase, a difference that is comparable to the drop that was observed at the Morin transition.

It would appear that the spin-flop in the sodium-flux hematite is an abrupt transition, with domains of flopped spins growing at the expense of unflopped spins as the applied field is increased. This behaviour is similar to that observed in the 'aligned' K_2FeF_5 experiment. The spin-flop at each individual ferric ion seems to be of first-order, with the 0.6T transition width being attributable to a distribution of critical field values within the crystal resulting from random impurities, defects and distortions. The observed 'mean' spin-flop field of $B_{sf} \approx 6.4T$ compares favourably with previously reported values for the critical field.

Given that the spin-flop observed in the sodium-flux crystal is in keeping with previous observations of the transition, it appears that the unusual transition that was found in the lead-flux crystal is not typical of hematite. The most likely reason for such atypical behaviour is that the lead-flux hematite is of inferior quality, either in terms of chemical purity or in terms of structural defects, to the sodium-flux hematite. To test the chemical purity of the crystals representative specimens from the lead-flux and sodium-flux hematite

Table 6.4 Fitted hyperfine parameters of the spectra of the sodium-flux hematite crystal subject to an applied field B parallel to its [111] axis, as discussed in the text. Δ and Γ measured in mm/s, B and B_{hf} in Tesla. θ_B was not allowed to vary.

B	Δ	Γ	B_{hf}	θ_B	Area
0.00	0.43	0.38	54.3	0°	-
6.00	0.42	0.37	54.1	0°	-
6.25	0.41	0.38	54.3	0°	92%
		0.33	53.3	90°	8%
6.30	0.38	0.37	54.3	0°	74%
		0.40	53.5	90°	26%
6.35	0.37	0.39	54.3	0°	73%
		0.43	53.5	90°	27%
6.40	0.37	0.37	54.4	0°	64%
		0.43	53.5	90°	36%
6.45	0.40	0.35	54.2	0°	61%
		0.40	53.3	90°	39%
6.50	0.41	0.40	54.4	0°	14%
		0.41	53.5	90°	86%
7.00	0.45	0.38	53.4	90°	-

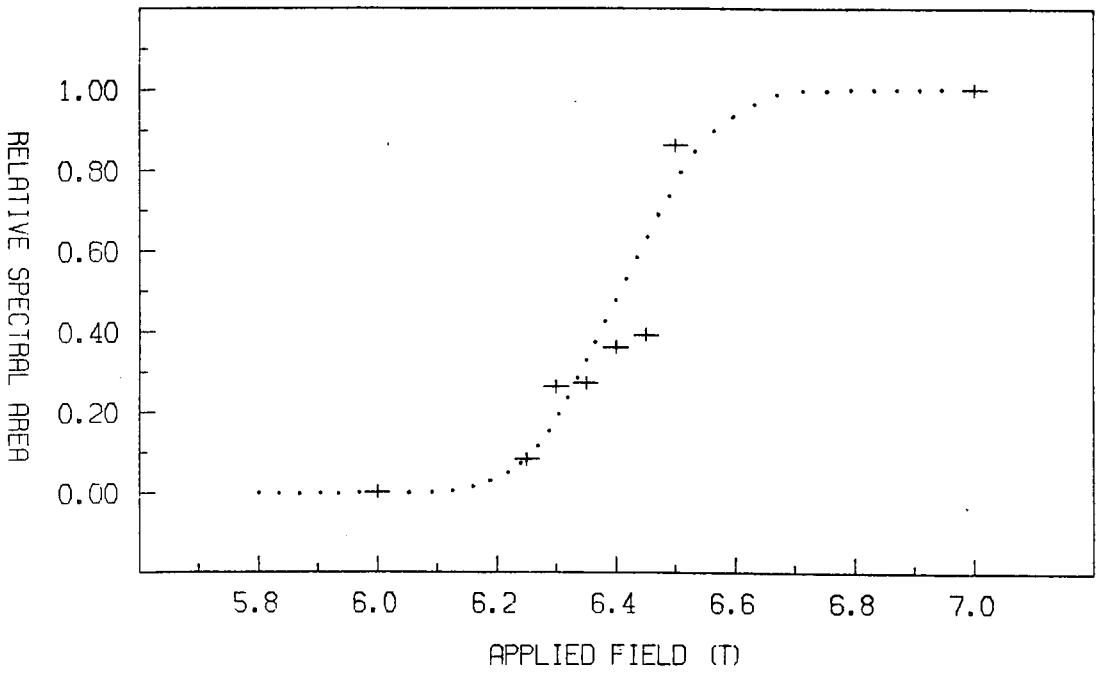

Figure 6.11 Observed field-dependence of the relative area of spin-flopped to unflopped spectral components in the sodium-flux crystal. The dotted curve is a guide to the eye.

batches were sent to the Universities Research Reactor, Risley, for neutron activation analysis. The γ-ray emission spectra recorded after the samples had been irradiated with neutrons showed that the major impurity nuclides in both samples were V, Rh and Ir. Minor impurities of Na and Sb were also found, and traces of Pt, Mn, Ti, Co and Ga were discernible. (We should note that although we might anticipate that Pb impurities would appear in the lead-flux crystal, Pb is one of the few nuclides that is not easily observed via neutron irradiation.) With the exception of Na and Sb the impurity concentrations were greater in the lead-flux sample than in the sodium-flux sample. Quantitative estimates of the concentrations of the major impurity elements (see Table 6.5) showed that in general the lead-flux hematite is about one hundred times more impure than the sodium-flux hematite.

Table 6.5 Concentrations in parts-per-million of the major impurity nuclides found to be present in the synthetic hematite crystals used in this work, as determined by neutron activation analyses.

	Vanadium	Rhodium	Iridium
Lead-flux hematite	2040 ± 20	57.7 ± 0.9	34.2 ± 0.4
Sodium-flux hematite	9.1 ± 0.2	0.46 ± 0.04	0.38 ± 0.02

The presence of relatively large amounts of vanadium and iridium in the lead-flux crystals might explain the broad Morin transition and unusual spin-flop transition that were observed, especially if these ions were in their 4+ valence state. Besser et al. (1967) explained the high sensitivity of the Morin transition to the substitution of titanium into hematite in terms of the lattice distortion produced by large Ti^{4+} ions on Fe^{3+} sites, as well as the associated presence of charge-compensating Fe^{2+} ions which exhibit strong spin-orbit coupling. Similarly large effects may well be observed if V^{4+} and Ir^{4+} ions

are substituted onto Fe^{3+} sites. The other major impurity detected in the lead-flux crystal, rhodium, is also known to alter the properties of hematite, and is unique in that doping Rh^{3+} ions into hematite raises T_M (Krens et al. 1965, Morrish and Eaton 1971), in contrast to most other cations (such as Ti^{4+}, Al^{3+}, Ga^{3+} and Sb^{4+}) which lower T_M.

A second effect which is known to influence the properties of hematite samples is the presence of structural defects and internal stresses and strains. Several workers have noted that T_M may be increased by the application of external pressures (Whorlton et al. 1966, Kawai and Ono 1966, Searle 1967), and Besser et al. (1967) found that basal-plane anisotropy could be induced in a single crystal specimen simply by subjecting it to the non-uniform stresses invoked by immersing the crystal in a tablet of slow-drying epoxy resin. This latter result is particularly interesting, bearing in mind that the lead-flux crystal used in this work was abrasively thinned and then encased in an epoxy resin tablet, while the sodium-flux crystal was kept in its original state. To further investigate this question a second platelet was selected from the lead-flux hematite batch and (of necessity) abrasively thinned, but instead of being fully immersed in epoxy resin it was supported on one side only by a thin slab of resin. Mossbauer spectra of the Morin transition were recorded with this sample, and showed that the transition occured over a range of temperatures $\Delta T \simeq 25K$ centered at $T_M \simeq 248K$. Comparison of these values with the $\Delta T \simeq 25K$ and $T_M \simeq 255K$ observed for the fully encased sample implies that while the transition width was unaffected, T_M was slightly smaller in the 'half-mounted' crystal. This is perhaps indicative of a greater pressure being transferred to the fully encased crystal via the surrounding epoxy resin.

From the above considerations it is apparent that several factors may be contributing to the unusual behaviour of the lead-flux crystal during the course of the 'parallel' field-induced spin-flop transition. However it is also clear that the response of the sodium-flux crystal to the applied field is consistent with previous observations of this spin-flop, and that it agrees with the predicted first-order character of the transition.

6.2c The 'Transverse' Field-Induced Spin-Flop

In the last of the α-Fe_2O_3 spin-flop experiments the rather unusual 'transverse' field-induced transition was investigated. As discussed in Chapter 2.2d(ii) mean-field theory predicts that this transition, which is a particular feature of 'Dzyaloshinsky' antiferromagnets, will occur in hematite when an applied field is directed perpendicular to the magnetically easy [111] axis. In essence the transition takes place because the Dzyaloshinsky exchange interaction establishes a preference for any weakly ferromagnetic spin arrangement (such as that which occurs naturally above the Morin transition) to be contained in the basal (111) plane. The application of an external field perpendicular to the [111] axis induces a canted spin state which has an associated WFM moment. Because of the Dzyaloshinsky interaction it is energetically preferable for this WFM spin configuration to be contained in the (111) plane, so that the AFM axis of the spins will move away from the [111] axis and into the (111) plane as the applied field passes through the critical value $B_{\perp c}$. The transition is generally thought to be abrupt, but there are also some conflicting theories which predict that the transition will be of second-order.

In the experiment Mössbauer spectra of the 'pure' sodium-flux crystal were recorded at 230K and 245K with applied fields of up to 10T perpendicular to the [111] axis and with the γ-ray beam parallel

to the [111] axis. The high sample temperatures were needed because previous observations of the 'transverse' spin-flop had shown that below ~100K the critical field $B_{\perp c} \simeq 16.2T$ (Foner and Shapira 1969, Jacobs et al. 1971), a value which is beyond the fields available in this laboratory. At temperatures approaching the Morin temperature the critical field is considerably smaller owing to the strong temperature dependence of the anisotropy field (see Chapter 2.2d(ii)). Foner and Shapira (1969) measured $B_{\perp c}(230K) \simeq 5.4T$ and $B_{\perp c}(245K) \simeq 2.5T$, both of which are fields that were readily available in this laboratory. The high sample temperatures were obtained using a variable temperature 'insert' (Cooper 1981) which in essence consists of a copper block (into which the crystal was mounted) inside an evacuated tube which was lowered into the centre of the superconducting magnet assembly. Sample temperature control to better than about ±0.2K could be obtained by controlling the current flowing through a coil mounted on the copper block.

The spectra obtained, five of which were recorded at 230K and one of which was recorded at 245K, are shown in Figure 6.12. At 230K and with zero applied field a four line pattern was observed, with the absence of the $\Delta m=0$ lines confirming that the γ-rays were well aligned with the [111] axis. In an applied field of 3.0T the spectral lines remained unsplit while two small $\Delta m=0$ lines appeared. As the field was increased to 10.0T the relative intensity of the $\Delta m=0$ lines increased until for B=10.0T an unsplit sextet of lines with an intensity ratio of about 3:2.6:1 was observed. This behaviour is in keeping with a gradual rotation of the AFM axis of the spins away from the [111] axis towards the (111) plane, although even with 10.0T applied it appears that the transition was not complete since a 3:4:1 spectrum was not observed. Increasing the sample temperature to 245K and applying a field of 10.0T resulted in another simple sextet pattern, but with

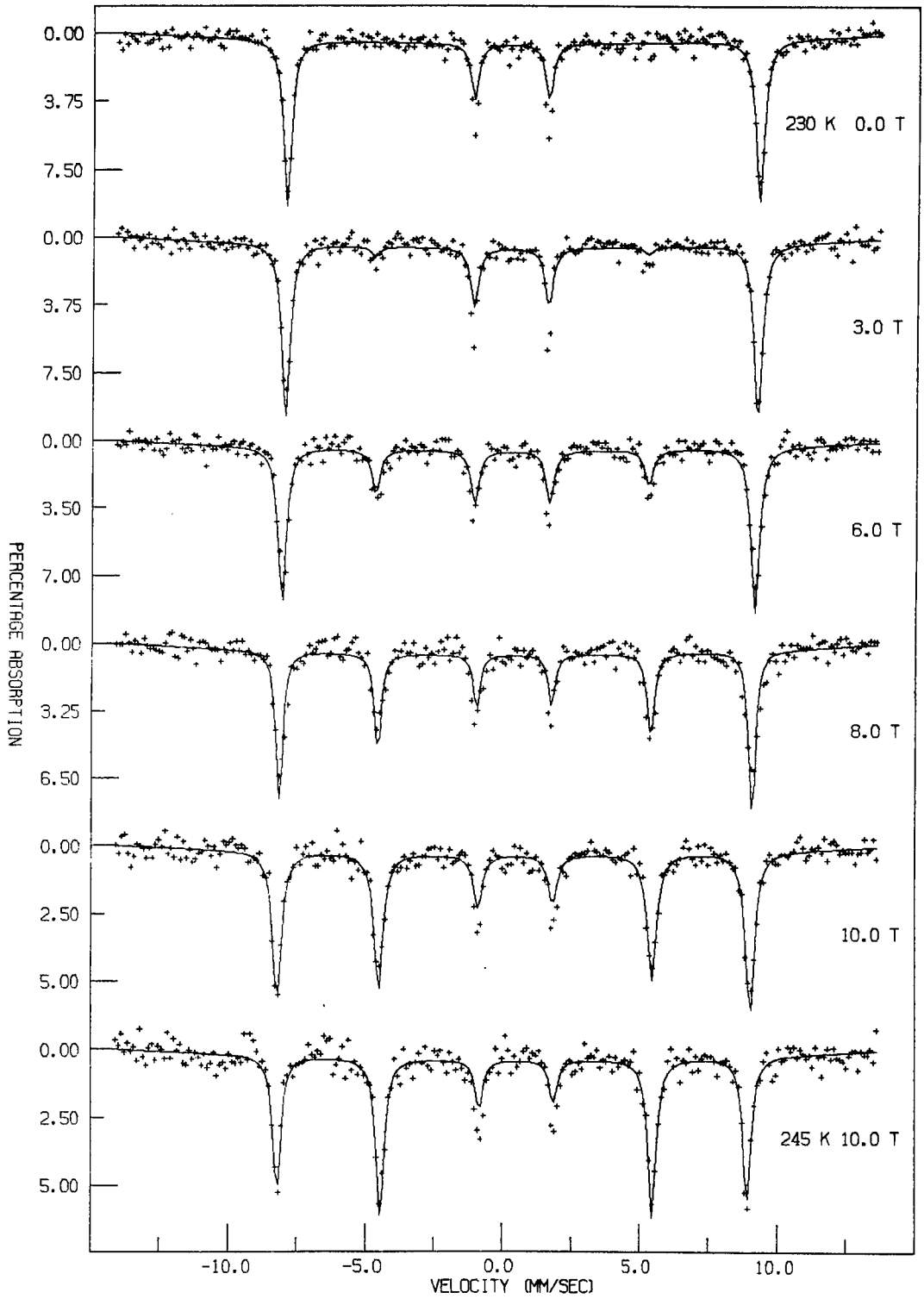

Figure 6.12 Spectra of the sodium-flux hematite crystal, with applied fields perpendicular to the [111] axis and γ-rays parallel to the [111] axis.

a slightly increased Δm=0 component and a line intensity ratio of about 3:3.6:1. This indicates that although at 245K a field of 10.0T brought the spins closer to the (111) plane than the same field at 230K, the transition was still not complete.

The spectra were computer analysed using Fit-Q, with $\eta=0$, $\theta_g=\phi_g=0$, $\theta_H=90°$ and $\phi_H=0$ assumed. The quadrupole splitting was fitted as $\Delta\simeq0.41$mm/s in the zero applied field spectrum, and constrained to this value for all the other fits. The fitted values of the linewidth and the magnitude and polar angles (in the EFG coordinate system) of the hyperfine field are given in Table 6.6. The isomer shift did not vary greatly between the spectra and is not included in Table 6.6.

The zero applied field 230K spectrum could be well fitted with $\theta_B=0$ assumed, confirming that the γ-rays were closely aligned with the trigonal axis. The fits of the non-zero applied field spectra showed that the polar angle θ_B of the hyperfine field increased smoothly as B was increased (see Figure 6.13), implying a gradual rotation of the AFM axis of the spins away from the [111] axis. The same fits also showed that the azimuthal angle ϕ_B of the hyperfine field did not move significantly away from ~90°, implying that the spins remained in the plane perpendicular to the applied field direction throughout the transition. The magnitude of the hyperfine field B_{hf} fell slowly as B was increased, an effect which is consistent with the known direction-dependence of its orbital and dipolar components (van der Woude 1966). With B=10.0T applied the AFM axis of the spins had rotated $\theta_B\simeq62°$ away from the trigonal axis, well short of the 90° motion normally associated with a complete spin-flop transition. At the higher temperature of 245K and with 10.0T applied the spins were closer to the basal plane ($\theta_B\simeq74°$), but again the transition was incomplete.

Judging by the spectra and their fits it is quite clear that our observation of the 'transverse' field-induced spin-flop in the

Table 6.6 Fitted hyperfine parameters of the spectra of the sodium-flux hematite crystal subject to an applied field B perpendicular to its [111] axis, as discussed in the text. Γ measured in mm/s, B and B_{hf} in Tesla. * denotes parameters that were not allowed to vary.

T	B	Γ	B_{hf}	θ_B	ϕ_B
230.0 K	0.0	0.35	53.3	0°*	90°*
	3.0	0.36	53.2	14°	91°
	6.0	0.37	53.0	33°	89°
	8.0	0.30	52.8	51°	90°
	10.0	0.39	52.9	62°	93°
245.0 K	10.0	0.35	52.1	74°	90°

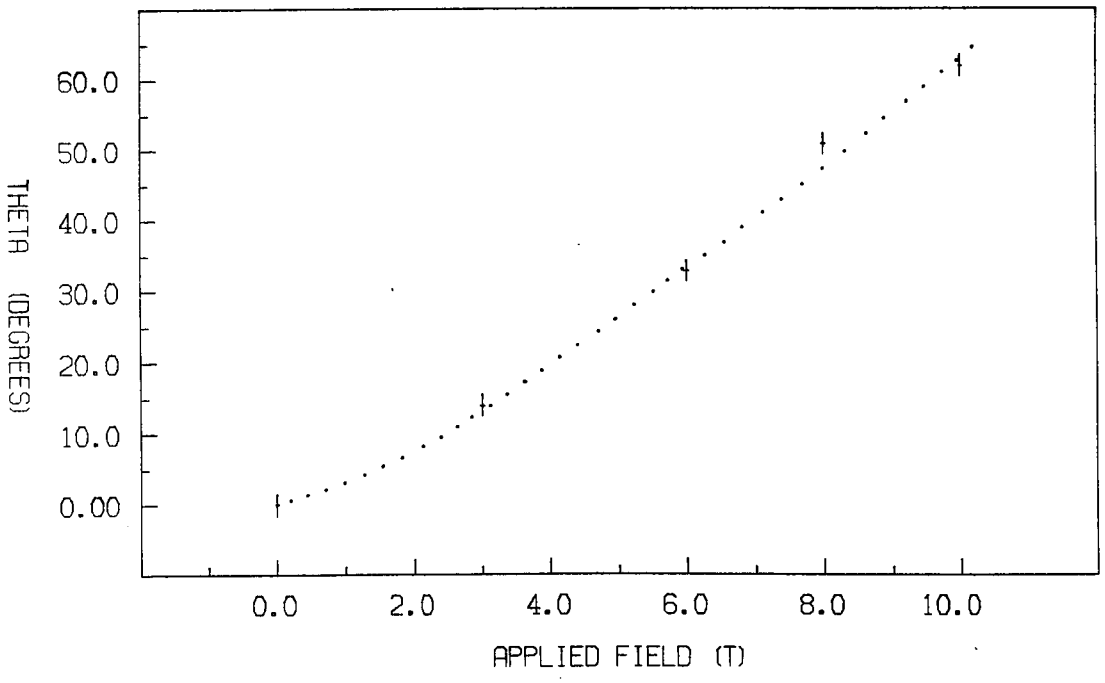

Figure 6.13 Observed field-dependence of the rotation angle θ_B between the AFM axis of the spins and the [111] axis in the sodium-flux crystal.

sodium-flux crystal shows the transition to be a very slow and gradual spin rotation in response to an increasing applied field. Even with 10.0T applied and T≈245K (a temperature just below the region of the Morin transition in the crystal) the transition was incomplete, with a 74° rotation having occurred rather than the anticipated 90° spin-flop. This result contradicts the reported observations of several previous experimenters. Voskanyan et al. (1968), Beyerlein and Jacobs (1969) and Foner and Shapira (1969) all noted a sharp upturn and 'step' in the perpendicular magnetic susceptibility $\chi_\perp$ at $B_{\perp c}$, separating two regions of different constant susceptibilities. Torque and magnetisation measurements on highly pure synthetic crystals by Kaczer and Shalnikova (1965) at temperatures just below T_M revealed abrupt and discontinuous transitions. Antiferromagnetic resonance experiments by Ozhogin and Shapiro (1968) showed a similar discontinuity in the net magnetisation parallel to the trigonal axis at $B_{\perp c}$. Also, Ozhogin and Shapiro (1967,1968) and Jacobs et al. (1971) noted that their measured values for $B_{\perp c}$ were about 30% higher than those predicted via conventional mean-field theory. As discussed in Chapter 2.2d(ii) this discrepancy could be resolved by introducing a fourth-order term $K'\cos^4\theta$ into the description of the anisotropy energy, a modification which had the added effect of changing the predicted character of the transition to that of fist-order.

However, second-order transitions have also been reported in the literature. Kaczer and Shalnikova found that while the spin-flop in some of their crystal samples was of first-order, in other samples it was gradual, an observation which they attributed to a 'smearing' of the transition due to inhomogeneities in composition and internal stresses in the latter samples. Cinader and Shtrikman (1966) searched without success for the transition and concluded that an anisotropy energy term of $K\cos^2\theta$ would account for the gradual rotation of the

AFM axis of the spins towards the basal plane. Mossbauer measurements by Blum and Frankel (1967) also indicated a gradual rotation of the spins rather than an abrupt spin-flop.

In light of the above considerations it would seem likely that our observation of a gradual spin rotation in the 'transverse' field induced spin-flop experiment is simply an indication that even the nominally 'pure' sodium-flux α-Fe_2O_3 crystal is not of sufficiently high quality that a first-order transition might take place.

6.3 DISCUSSION

In this chapter three separate experiments on spin-flop phase transitions in α-Fe_2O_3 have been described. The Morin transition and the 'parallel' field-induced spin-flop were studied in both the lead-flux and the sodium-flux hematite crystals, and the 'transverse' field-induced spin-flop was investigated in the sodium-flux crystal. Representative spectra from the three experiments conducted with the sodium-flux crystal are shown in Figure 6.14. Comparing the transitions it appears that while the 'transverse-field' transition is of second-order, the Morin and 'parallel-field' spin-flops are of first-order as evidenced by the coexistence of the initial and final states of the crystal over a finite transition region.

Before discussing the significance of these results, the question of sample purity should be considered. Throughout this chapter the possibility of sample inhomogeneity and structural imperfection has been called upon to explain any anomalous features in the observed transitions. This is not as much of an ad-hoc remedy as it might at first appear. Over the last thirty-five years a large number of papers have been published concerning the magnetic properties of α-Fe_2O_3, amongst which a great diversity of behaviour has been observed in

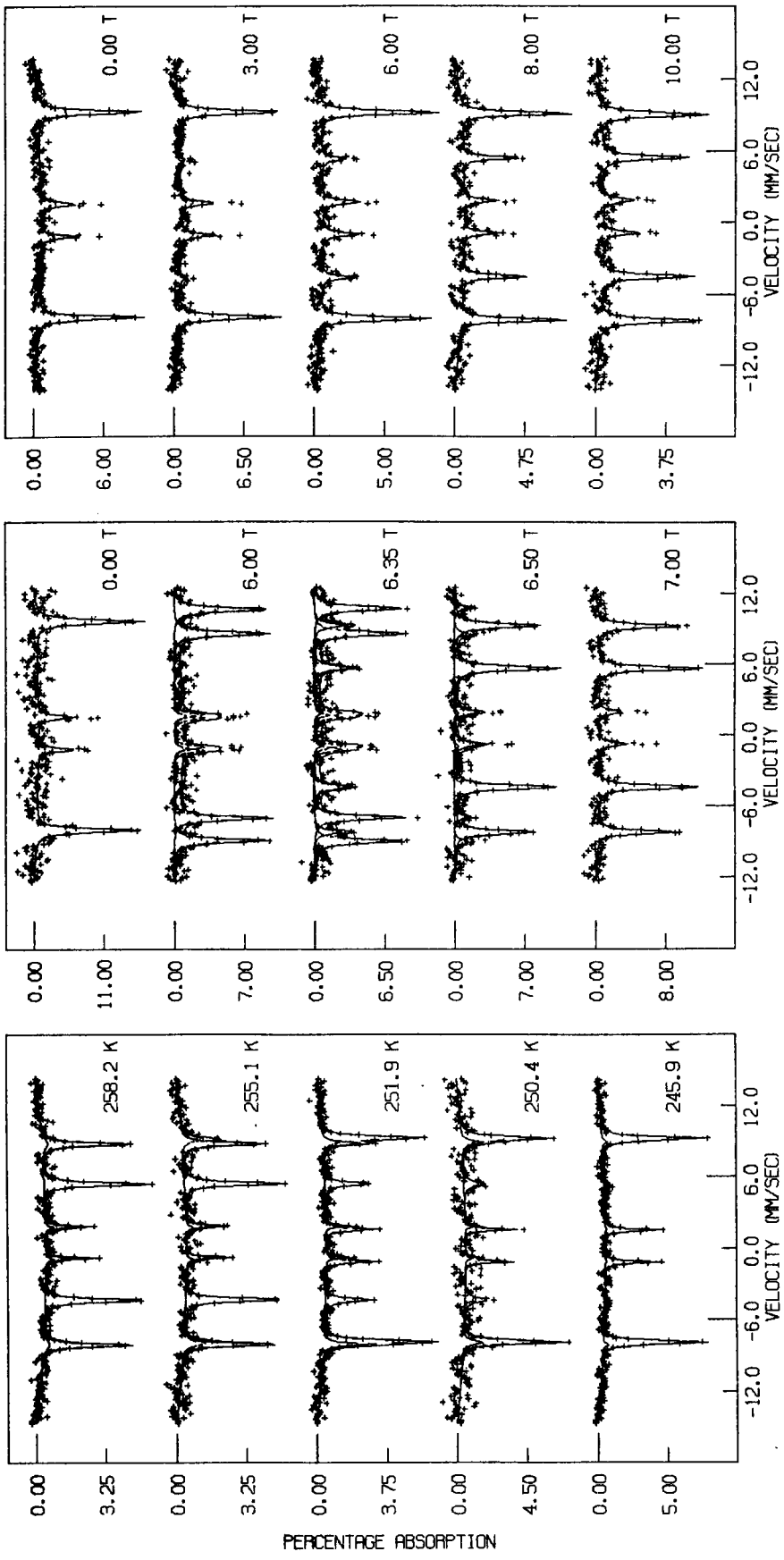

Figure 6.14 Representative spectra of the Morin transition and the 'parallel' and 'transverse' spin-flop transitions observed in the sodium-flux hematite crystal.

different natural and synthetic crystal samples. By about 1960 it was recognised that reproducible and reliable results could be obtained by conducting experiments with high purity synthetically grown crystals. The substitution of foreign cations into hematite also displayed the high sensitivity of the crystal's magnetic properties to any disturbing influences in the lattice. In this way it has become well established that the sample quality has a large and direct bearing on the character of the magnetic behaviour observed in hematite.

In the present work two different synthetically grown hematite crystals, both of which were nominally 'pure', were studied. However the broad Morin transition and unusual parallel-field spin-flop that were observed in the lead-flux crystal led to speculation as to its true quality. Subsequent neutron activation analysis revealed that significant quantities of vanadium, rhodium and iridium ions were present in the crystal, at a level of concentration that was about one hundred times greater than that found in the sodium-flux crystal. It therefore seems likely that a relatively high impurity content may indeed be the cause of the anomalous behaviour of the lead-flux crystal during the parallel-field transition.

In the case of the sodium-flux crystal the observed widths of the Morin and parallel-field spin-flops were sufficiently large to be indicative of some degree of sample inhomogeneity. Despite this, in both transitions the spin-flop at each individual ferric ion appeared to be of first-order, in agreement with theoretical predictions. The observed transition widths are attributable to the randomness in the crystal due to the chemical impurity and structural defects giving rise to a distribution of local Morin temperatures and spin-flop fields within the crystal.

In light of the first-order character observed in the Morin and parallel-field transitions, it is somewhat surprising that the

transverse-field spin-flop in the sodium-flux crystal was found to be a gradual, second-order spin rotation which did not reach completion even with 10.0T applied and a sample temperature of 245K. A possible explanation for this may be related to the current theory of the spin-flop in Dzyaloshinsky antiferromagnets. Theoretically the first-order character of the transverse-field spin-flop is established by the inclusion of a small fourth-order term in the expression of the anisotropy energy. This implies that only a small distortion of the basal-plane anisotropy in hematite would be required to overcome this subtle effect. Hence it is plausible that the small degree of randomness thought to be present in the sodium-flux crystal might well be large enough to destroy the first-order character of the transverse-field transition, while retaining the abrupt Morin and parallel-field transitions.

In conclusion it is evident that while the question of sample purity has a large bearing on the reliability of experimental observations of the spin-flop transitions in hematite, we have in this work found evidence to support the existence of first-order spin-flop phase transitions in three-dimensional antiferromagnetic crystals.

CHAPTER SEVEN : CONCLUSIONS

In this thesis the results of a Mössbauer study of the spin-flop phase transition in the antiferromagnetic materials K_2FeF_5, Rb_2FeF_5 and α-Fe_2O_3 have been presented. The character of the transitions observed in these crystals has provided information on the applicability of several different theoretical descriptions of the spin-flop phenomenon.

The first part of this work dealt with the quasi one-dimensional antiferromagnets K_2FeF_5 and Rb_2FeF_5. A spin-flop of first-order character was observed in K_2FeF_5 when an external field was applied in a direction parallel to the easy anisotropy axis of a single crystal sample. The transition width was found to be greater than the width anticipated from demagnetisation and hysteresis effects, and was attributed to some randomness in the crystal lattice (due to impurities, defects, distortions etc.) giving rise to a distribution of local critical fields throughout the crystal. In two subsequent experiments second-order transitions were observed when applied fields were directed at ~33° to the K_2FeF_5 easy axis, and at ~28° to the Rb_2FeF_5 easy axes. In both cases the measured field-dependence of the rotation of the AFM axis of the spins away from the applied field direction was found to be less broad than the curve predicted by mean-field theory, implying some inadequacies in that theory. A notable feature of all three experiments was the occurrence of a sharp dip in the observed hyperfine field as the applied field passed through the critical value. This minimum could be qualitatively explained on the basis of spin-wave theory as a field-dependent spin reduction, although it was surprising that the effect should be so prominent in the second-order transitions, as well as in the first-order transition.

The second half of this work was concerned with the three-dimensional antiferromagnet α-Fe_2O_3, a material which is well known for its 'Dzyaloshinsky' type of anisotropy and the presence of a temperature driven spin-flop known as the Morin transition. Sample purity was found to be a problem with this material, and of the two synthetically grown crystals studied only one (grown from the melt in a flux of $Na_2B_4O_7$) gave results that were consistent with previously reported work. Three spin-flop transitions were observed in that crystal, with both the Morin transition and the spin-flop induced by an applied field directed along the easy anisotropy axis exhibiting first-order character. The finite transition widths observed in both of these cases were attributed to a degree on inhomogeneity in the crystal giving rise to a distribution of local Morin temperatures and critical field values. In the third experiment an applied field was directed perpendicular to the easy anisotropy axis. As the field was increased the spins remained perpendicular to the field but gradually rotated away from the easy axis in a second-order transition. This transition confirmed the predictions of the mean-field theory of α-Fe_2O_3, although it was not as abrupt as some researchers have reported. In all three transitions the observed hyperfine field was constant both above and below the critical regions, in keeping with the expected negligible effect of spin-wave induced spin reduction in α-Fe_2O_3.

In conclusion it is evident from the similarity of the first-order spin-flop transitions induced by the application of a magnetic field parallel to the easy anisotropy axes of K_2FeF_5 and α-Fe_2O_3 that the dimensionality of the magnetic lattice of an antiferromagnet is not a major factor in the spin-flop transition. Also, it seems that although field-dependent spin reduction may be a very noticeable feature in some systems, it does not have a direct bearing on the character of the spin-flop. With regard to the various theoretical models of the

spin-flop it appears that soliton theory cannot explain the observation of first-order transitions while in its present form spin-wave theory cannot account for second-order transitions, and that despite its inadequacies the mean-field theory of the transition can at least qualitatively describe the characteristics of the spin-flop phenomenon.

REFERENCES

Anderson P.W., Phys. Rev. 86 694 (1952)

Anderson P.W., in 'Magnetism, Volume 1', eds. G.T. Rado and H. Suhl, Academic Press : New York, p25 (1963)

Artman J.O., Murphy J.C. and Foner S., Phys. Rev. 138 A912 (1965)

Basten J.A.J., de Jonge W.J.M. and Frikkee E., Phys. Rev. B 21 4090 (1980a)

Basten J.A.J., de Jonge W.J.M. and Frikkee E., Phys. Rev. B 22 1429 (1980b)

Besser P.J. and Morrish A.H., Phys. Lett. 13 289 (1964)

Besser P.J., Morrish A.H. and Searle C.W., Phys. Rev. 153 632 (1967)

Beyerlein R.A. and Jacobs I.S., Bull. Amer. Phys. Soc. Ser. II 14 349 (1969)

Blackman M. and Gustard B., Nature 193 360 (1962)

Blake R.L., Hessevick R.E., Zoltai T. and Finger L.W., Amer. Min. 51 123 (1966)

Blazey K.W., Ondris M., Rohrer H. and Thomas H., J. Physique 32 C1-1020 (1971a)

Blazey K.W., Rohrer H. and Webster R., Phys. Rev. B 4 2287 (1971b)

Bloch F., Z. Physik 61 206 (1930)

Blum N.A. and Frankel R.B., Bull. Amer. Phys. Soc. Ser. II 12 23 (1967)

Blum N.A., Freeman A.J., Shaner J.W. and Grodzins L., J. Appl. Phys. 36 1169 (1965)

Boersma F., Cooper D.M., de Jonge W.J.M., Dickson D.P.E., Johnson C.E. and Tinus A.M.C., J. Phys. C 15 4141 (1982)

Charlesworth G. and Long F.A., Proc. Leeds Phil. Lit. Soc. Sci. Sect. 3 315 (1939)

Chepurnykh G.K., Sov. Phys. Solid State 10 1517 (1968)

Cinader G., Phys. Rev. 155 453 (1967)

Cinader G., Flanders P.J. and Shtrikman S., Phys. Rev. 162 419 (1967)

Cinader G. and Shtrikman S., Sol. St. Commun. 4 459 (1966)

Cohen R.L. and Wertheim G.K., in 'Methods of Experimental Physics Volume 11 : Solid State Physics', ed. L. Marton, sub-ed. R.V. Coleman, Academic Press : New York, Chpt. 6 (1974)

Cohen E.U. and Shortley G.H., 'The Theory of Atomic Spectra', Cambridge Univ. Press (1935)

Cooper D.M., 'A Mössbauer Investigation of the Magnetic Properties of the Quasi One-Dimensional Antiferromagnet K_2FeF_5', Ph.D. Thesis, Liverpool (1981)

Cooper D.M., Gupta G.P., Dickson D.P.E. and Johnson C.E., J. Phys. C 15 3391 (1982)

Cranshaw T.E., Nucl. Instrum. Methods 30 101 (1964)

Creer K.M., Hedley I.G. and O'Reilly W., in 'Magnetic Oxides Part 2', ed. D.J. Craik, Wiley : London, Chpt. 11 (1975)

Curry N.A., Johnston G.B., Besser P.J. and Morrish A.H., Phil. Mag. 12 221 (1965)

Dance J.M., Soubeyroux J.L., Sabatier R., Fournes L., Tressaud A. and Hagenmuller P., J. Magn. Magn. Mater. 15-18 534 (1980)

DeBendetti S., Lang G. and Ingalls R., Phys. Rev. Lett. 6 60 (1961)

de Groot H.J.M. and de Jongh L.J., to appear in Phys. Stat. Sol. B (1986)

de Jongh L.J., J. Appl. Phys. 53 8018 (1982)

de Jongh L.J. and de Groot H.J.M., Sol. St. Commun. 53 731 (1985)

Dzyaloshinsky I., J. Phys. Chem. Solids 4 241 (1958)

Enz U., Helv. Phys. Acta 37 245 (1964)

Flanders P.J., J. Appl. Phys. 40 1247 (1969)

Flanders P.J. and Remeika J.P., Phil. Mag. 11 1271 (1965)

Foner S., in 'Proceedings of the International Conference on Magnetism, Nottingham 1964', I.O.P. and Phys. Soc. : London, p438 (1965)

Foner S. and Shapira Y., Phys. Lett. 29A 276 (1969)

Frauenfelder H., 'The Mössbauer Effect', Benjamin : New York (1962)

Gallon T.E., Proc. Roy. Soc. A303 511 (1968)

Goodenough J.B., 'Magnetism and the Chemical Bond', Interscience : New York (1963)

Gorter C.J., Revs. Mod. Phys. 25 277 (1953)

Gorter C.J. and Haantjes J., Physica 18 285 (1952)

Greenwood N.N. and Gibb T.C., 'Mössbauer Spectroscopy', Chapman and Hall : London (1971)

Guillaud C., J. Phys. Rad. 12 489 (1951)

Gupta G.P., 'Mössbauer Investigation of some One-Dimensional Antiferromagnets', Ph.D. Thesis, Liverpool (1978)

Gupta G.P., Dickson D.P.E. and Johnson C.E., J. Phys. C 11 215 (1978a)

Gupta G.P., Dickson D.P.E. and Johnson C.E., J. Phys. C 12 2419 (1979)

Gupta G.P., Dickson D.P.E., Johnson C.E. and Wanklyn B.M., J. Phys. C 10 L459 (1977)

Gupta G.P., Dickson D.P.E., Johnson C.E. and Wanklyn B.M., J. Phys. C 11 3889 (1978b)

Hanzel D., Tressaud A., Dance J.M. and Hagenmuller P., Sol. St. Commun. 22 215 (1977)

Heisenberg W., Z. Physik 49 619 (1928)

Honda K. and Sone T., Sci. Rept. Tohoku Imp. Univ. Ser. I 3 223 (1914)

Imbert P. and Gerard A., Compte Rendus Acad. Sci. Paris 257 1054 (1963)

Ito A., Torikai E., Kitazawa M., Tamaki T., Goto T., Sakakibara T., Todo S. and Oguru I., J. Magn. Magn. Mater. 54-57 39 (1986)

Jacoboni C., de Pape R., Poulain M., Le Marouille J.Y. and Grandjean D., Acta Cryst. B30 2688 (1974)

Jacobs I.S., Beyerlein R.A., Foner S. and Remeika J.P., Inter. J. Magn. 1 193 (1971)

Jabcobs I.S. and Silverstein S.D., Phys. Rev. Lett. 13 272 (1964)

Johnson J.A., 'Mossbauer Spectroscopic Studies of Linear and Non-Linear Magnetic Excitations in Crystals', Ph.D. Thesis, Liverpool (1985)

Kaczer J. and Shalnikova T., in 'Proceedings of the International Conference on Magnetism, Nottingham 1964', I.O.P. and Phys. Soc. : London, p589 (1965)

Kanamori J., in 'Magnetism, Volume 1', eds. G.T. Rado and H. Suhl, Academic Press : New York, Chpt. 4 (1963)

Kanamori J. and Yosida K., Prog. Theor. Phys. 14 423 (1955)

Kaneko T. and Abe S., J. Phys. Soc. Japan 20 2001 (1965)

Kawai N. and Ono F., Phys. Lett. 21 297 (1966)

Keffer F., in 'Handbuch der Physik Volume XVIII/2 : Ferromagnetism', ed. S. Flugge, sub-ed. H.P.J. Wijn, Springer-Verlag : Berlin, pp1-273 (1966)

King A.R. and Paquette D., Phys. Rev. Lett. 30 662 (1973)

King A.R. and Rohrer H., Phys. Rev. B 19 5864 (1979)

Kittel C., 'Quantum Theory of Solids', Wiley : New York (1963)

Kittel C., 'Introduction to Solid State Physics, Fifth Edition', Wiley : New York (1976)

Krens E., Szabo P. and Konczos G., Phys. Lett. 19 103 (1965)

Kuhn W., Phil. Mag. 8 625 (1929)

Kundig W., Nucl. Instrum. Methods 48 219 (1967)

Landau L.D. and Lifshitz E.M., 'Electrodynamics of Continuous Media', Pergamon : London, Sect. 37 (1960)

Lang G. and Dale B.W., 'Program for Least Squares Fitting of Mössbauer Spectra in Applied Fields', A.E.R.E. Harwell Report R7478 (1973)

Lang G. and Dale B.W., Nucl. Instrum. Methods 116 567 (1974)

Leung K.M., Hone D., Mills D.L., Riseborough P.S. and Trullinger S.E., Phys. Rev. B 21 4017 (1980)

Levinson L.M., Luban M. and Shtrikman S., Phys. Rev. 187 715 (1969)

Levitin R.Z. and Shchurov V.A., J.E.T.P. Lett. 7 110 (1968)

Lynn J.W., Heller P. and Lurie N.A., Phys. Rev. B 16 5032 (1977)

Margulies S. and Ehrman J.R., Nucl. Instrum. Methods 12 131 (1961)

Marshall W. and Johnson C.E., J. Phys. Rad. 23 733 (1962)

May L., editor of 'An Introduction to Mössbauer Spectroscopy', Hilger : London (1971)

Mikeska H.J., J. Phys. C 13 2913 (1980)

Mikeska H.J., J. Appl. Phys. 52 1950 (1981)

Morin F.J., Phys. Rev. 78 819 (1950)

Moriya T., Phys. Rev. 117 634 and 120 91 (1960)

Morrish A.H., 'The Physical Principles of Magnetism', Wiley : New York (1965)

Morrish A.H. and Eaton J.A., J. Appl. Phys. 42 1495 (1971)

Mössbauer R.L., Z. Physik 151 124 (1958a)

Mössbauer R.L., Naturwiss. 45 538 (1958b)

Nagamiya T., Prog. Theor. Phys. 11 309 (1954)

Nagamiya T., Yosida K. and Kubo R., Adv. Phys. 4 1 (1955)

NBS (National Bureau of Standards), 'Certificate of Calibration : Iron Foil Mossbauer Standard 1541', (1971)

Néel L., Ann. Physique 18 5 (1932)

Néel L., Ann. Physique 5 232 (1936)

Nininger R.C. and Schroeer D., Phys. Chem. Solids 39 137 (1978)

Oguchi T., Phys. Rev. 133 A1098 (1964)

Ozhogin V.I. and Shapiro V.G., J.E.T.P. Lett. 6 7 (1967)

Ozhogin V.I. and Shapiro V.G., Sov. Phys. J.E.T.P. 27 54 (1968)

Ozhogin V.I. and Shapiro V.G., Sov. Phys. J.E.T.P. 28 915 (1969)

Pankhurst Q.A., Johnson C.E. and Thomas M.F., J. Phys. C 18 3249 (1985)

Pankhurst Q.A., Johnson C.E. and Thomas M.F., Hyp. Int. 29 1361 (1986)

Pauling L. and Hendricks S.B., J. Amer. Chem. Soc. 47 781 (1925)

Portier J., Tressaud A., de Pape R. and Hagenmuller P., Mater. Res. Bull. 3 433 (1968)

Rohrer H., Phys. Rev. Lett. 34 1638 (1975)

Rohrer H., Derighetti B. and Gerber Ch., Physica 86-88 597 (1977)

Rohrer H. and Gerber Ch., Phys. Rev. Lett. 38 909 (1977)

Rohrer H. and Gerber Ch., J. Appl. Phys. 49 1341 (1978)

Rohrer H. and Thomas H., J. Appl. Phys. 40 1025 (1969)

Sabatier R., Soubeyroux J.L., Dance J.M., Tressaud A., Wintenberger M. and Fruchart D., Sol. St. Commun. 29 383 (1979)

Searle C.W., Phys. Lett. 25A 256 (1967)

Shull C.G., Strauser W.A. and Wollan E.O., Phys. Rev. 83 333 (1951)

Sternheimer R.M., Phys. Rev. 105 158 (1957)

Stevens J.G. and Preston R.S., in 'Mössbauer Effect Data Index : Covering the 1970 Literature', ed. J.G. Stevens and V.E. Stevens, I.F.I./Plenum : New York, p16 (1972)

Stevens J.G. and Stevens V.E., in 'Mössbauer Effect Data Index : Covering the 1975 Literature', ed. J.G. Stevens and V.E. Stevens, I.F.I./Plenum : New York, p56 (1975)

Takada T., Yamamoto N., Shinjo T., Kiyama M. and Bando Y., Bull. Inst. Chem. Res. Kyoto Univ. 43 406 (1965)

Tasaki A. and Iida S., J. Phys. Soc. Japan 2 167 (1961)

Thomas H., in 'Chania International Conference on Magnetism, Crete', unpublished lecture notes (1969a)

Thomas H., Phys. Rev. 187 630 (1969b)

Tressaud A., Ph.D. Thesis, Bordeaux (1969)

Tressaud A., Portier J., de Pape R. and Hagenmuller P., J. Sol. St. Chem. 2 269 (1970)

Tressaud A., Soubeyroux J.L., Dance J.M., Sabatier R., Hagenmuller P. and Wanklyn B.M., Sol. St. Commun. 37 479 (1981)

van der Woude F., Phys. Stat. Sol. 17 417 (1966)

Van Vleck J.H., J. Chem. Phys. 9 85 (1941)

Vlasse M., Matejka G., Tressaud A. and Wanklyn B.M., Acta Cryst. B33 3377 (1977)

Voskanyan R.A., Levitin R.Z. and Shchurov V.A., Sov. Phys. J.E.T.P. 26 302 (1968)

Walker L.R., Wertheim G.K. and Jaccarino V., Phys. Rev. Lett. 6 98 (1961)

Wang Y. and Callen M.B., J. Phys. Chem. Solids 25 1459 (1964)

Wanklyn B.M., J. Mater. Sci. 10 1487 (1975)

Wanklyn B.M., Wondre F.R., Maqsood A., Yanagisawa K. and Davison W., J. Mater. Sci. 14 1447 (1979)

Weiss P., J. Phys. 4 661 (1907)

Weng C.Y., Ph.D. Thesis, Carnegie Mellon Univ. Pittsburg (1968)

Wertheim G.K., 'Mössbauer Effect : Principles and Applications', Academic Press : New York (1964)

Whorlton T.G., Bennion R.B. and Brugger R.M., Phys. Lett. 24A 653 (1967)

APPENDIX

The following is a list of publications and conference contributions that the author has completed in the past three years, submitted as additional evidence in candidature for the degree of Doctor of Philosophy.

Publications

'The electric field gradient in the quasi one-dimensional disordered compound $FeMgBO_4$', Q.A. Pankhurst, M.F. Thomas and B.M. Wanklyn, J. Phys. C 18 (1985) 1255-1261

'A Mössbauer investigation of the spin-flop transition in the one-dimensional antiferromagnet K_2FeF_5', Q.A. Pankhurst, C.E. Johnson and M.F. Thomas, J. Phys. C 18 (1985) 3249-3253

'Mössbauer measurements of the spin-flop transition in some α-Fe_2O_3 crystals', Q.A. Pankhurst, C.E. Johnson and M.F. Thomas, J. Magn. Magn. Materials 54-57 (1986) 1163-1164

'Spin-flop phase transitions in the one-dimensional antiferromagnets K_2FeF_5 and Rb_2FeF_5', Q.A. Pankhurst, C.E. Johnson and M.F. Thomas, Hyperfine Interactions 29 (1986) 1361-1364

'A Mössbauer spectroscopic study of the magnetocrystalline anisotropy in α-FeOOH', A. Meagher, Q.A. Pankhurst and D.P.E. Dickson, Hyperfine Interactions 29 (1986) 533-536

Conference Contributions

'$FeMgBO_4$: A quasi one-dimensional spin glass?', Q.A. Pankhurst and M.F. Thomas, Mössbauer Spectroscopy Discussion Group 25th Meeting, Oxford, England, 2-4 July 1984 (Oral contribution)

'Spin-flop phase transitions in the one-dimensional antiferromagnets K_2FeF_5 and Rb_2FeF_5', Q.A. Pankhurst, C.E. Johnson and M.F. Thomas, Mössbauer Spectroscopy Discussion Group 26th Meeting, Norwich, England, 8-10 July 1985 (Oral contribution)

'Mössbauer measurements of spin reorientations in α-Fe_2O_3', Q.A. Pankhurst, C.E. Johnson and M.F. Thomas, International Conference on Magnetism, San Francisco, U.S.A., 26-30 August 1985 (Poster)

'Spin-flop phase transitions in the one-dimensional antiferromagnets K_2FeF_5 and Rb_2FeF_5', Q.A. Pankhurst, C.E. Johnson and M.F. Thomas, International Conference on the Applications of the Mössbauer Effect, Leuven, Belgium, 16-20 September 1985 (Poster)

'A Mössbauer spectroscopic study of the magnetocrystalline anisotropy in α-FeOOH', A. Meagher, Q.A. Pankhurst and D.P.E. Dickson, International Conference on the Applications of the Mössbauer Effect, Leuven, Belgium, 16-20 September 1985 (Poster)

Journal of Magnetism and Magnetic Materials 54–57 (1986) 1163–1164

MÖSSBAUER MEASUREMENTS OF THE SPIN-FLOP TRANSITION IN SOME α-Fe_2O_3 CRYSTALS

Q.A. PANKHURST, C.E. JOHNSON and M.F. THOMAS

Department of Physics, University of Liverpool, Liverpool L69 3BX, UK

Large differences are found in the Mössbauer spectra of the spin-flop transition in two synthetically grown crystals of α-Fe_2O_3. A sharp first-order transition is seen at $B_{sf} \approx 6.4$ T for one relatively pure sample, while the other undergoes a complicated transition thought to result from Pb impurities in the crystal.

The magnetic properties of hematite (α-Fe_2O_3) have been studied extensively [1]. Below the Morin transition at $T_M \approx 260$ K the ferric spins are antiferromagnetically aligned along the crystallographic [111] (trigonal) axis. The spins can be reoriented to the basal plane by applying a sufficiently strong magnetic field along the trigonal axis. Several investigators [2–6] have observed this 'spin-flop transition' and found that the critical field B_{sf} is in the range 6.3–6.8 T at 77 K. However, the details of the transition process are not well understood. Mössbauer spectroscopy provides a useful tool for studying the spin-flop, as readily measurable changes occur in the observed positions, splittings and intensities of the spectral lines.

Single crystals of α-Fe_2O_3 were grown from the melt using a flux of either PbO/PbF_2 or $Na_2B_4O_7$. Measurements were made on basal-plane platelets of approximate dimensions $2 \times 3 \times 0.2$ mm^3.

^{57}Fe Mössbauer spectra were recorded at 4.2 K with both incident γ-rays and applied field parallel to the trigonal axis. These are shown in fig. 1 for the sodium-flux crystal, and in fig. 2 for the lead-flux crystal.

In zero applied field the Mössbauer spectrum of the sodium-flux crystal (fig. 1) consists of four lines. The complete absence of the $\Delta M_I = 0$ lines (lines two and five of a magnetic sextet) shows that the field and γ-ray beam was aligned within a few degrees of the antiferromagnetic axis of the spins. With $B_{app} = 6$ T the spectral lines are split, corresponding to different effective fields on each sublattice of the antiferromagnet. At $B_{app} = 7$ T a sextet with intensity ratios 3 : 4 : 1 in outer : middle : inner pairs of lines is observed, characteristic of a perpendicular orientation of the spins to the γ-ray beam. The intermediate spectra, $6\ \text{T} < B_{app} < 7$ T, show a coexistence of the two phases: unflopped spins with split lines in 3 : 0 : 1 intensity ratio, and flopped spins with unsplit lines in 3 : 4 : 1 ratio.

Computer analysis of the spectra showed that the apparent quadrupole splitting changed from $\epsilon \approx 0.43$ mm/s for the unflopped phase to $\epsilon' \approx -0.21$ mm/s in the flopped phase. This compares favourably with the expected ratio $\epsilon = -2\epsilon'$ for a complete spin reorientation [7]. The relative area of the flopped component was found to vary smoothly through the transition region (see fig. 3).

The spectra of the lead-flux crystal (Figure 2) show a similar trend from a low field 3 : 0 : 1 unflopped spectrum to a high field 3 : 4 : 1 flopped pattern. However the intermediate spectra are more complicated than in the sodium-flux case. At $B_{app} = 6$ T the splitting in the outer lines is less than $2B_{app}$ and split $\Delta M_I = 0$ lines are present, indicating a rotation of the antiferromagnetic axis of the spins away from the trigonal axis. At higher fields the rotation angle and intensity of the $\Delta M_I = 0$ lines increase, but also an unsplit 3 : 4 : 1 component appears. This flopped component increases in relative area until at $B_{app} = 10$ T it constitutes the total spectrum (see fig. 3).

The spin-flop transition has been observed in two synthetic single crystals of α-Fe_2O_3. In the sodium-flux crystal the transition was seen as a coexistence of the flopped and unflopped phases over a range of fields $\Delta B_{app} \approx 0.8$ T centered at $B_{sf} \approx 6.4$ T. This coexistence may most easily be interpreted as a distribution of critical field values within the crystal as a result of random impurities, defects and distortions affecting the local environment of each ferric ion. The spin-flop transition for each individual ion appears to be of first-order, since no evidence of a gradual spin rotation was found in the spectra.

In contrast, the transition in the lead-flux crystal showed a rotation of the spins away from the applied field in addition to the growth of a spin-flopped phase over $\Delta B_{app} \approx 3.0$ T centered at $B_{sf} \approx 7.5$ T. The magnetic properties of hematite are known to be highly sensitive to impurities [5,8], and so the presence of Pb ion impurities in the lead-flux crystal may account for its complicated spin-flop transition.

The authors are indebted to Mrs. B.M. Wanklyn of the Clarendon Laboratory, Oxford, for the crystal samples used in this work. Q.A. Pankhurst wishes to thank the Commonwealth Scholarship Commission UK for their support.

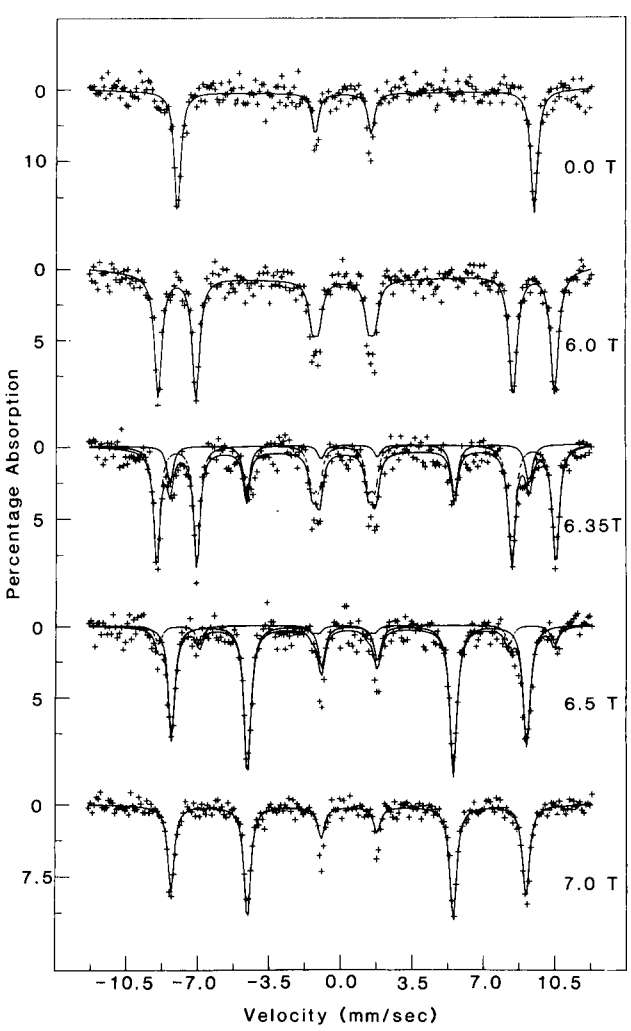

Fig. 1. Mössbauer spectra at 4.2 K of hematite grown in a $Na_2B_4O_7$ flux. The γ-rays and applied field were parallel to the trigonal axis. Full curves represent computer fits.

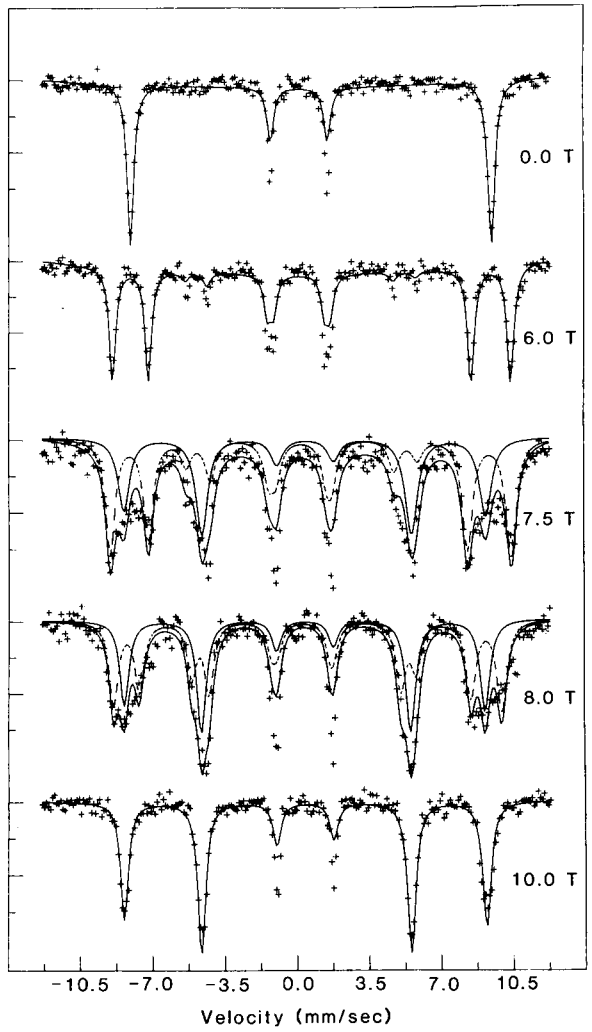

Fig. 2. Mössbauer spectra at 4.2 K of hematite grown in a PbO/PbF_2 flux. Conditions as in fig. 1.

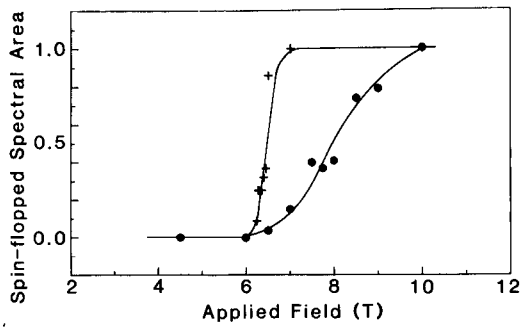

Fig. 3. Applied field dependence of the relative spectral area of spin-flopped to antiferromagnetic components in the Mössbauer spectra of the sodium-flux (+) and lead-flux (●) hematite crystals. Full curves are a guide to the eye.

[1] For a review article see K.M. Creer, I.G. Hedley and W. O'Reilly, in: Magnetic Oxides Part 2, ed. D.J. Craik (Wiley, London, 1975) chap. 11.
[2] S. Foner, Proc. Intern. Conf. Magnetism, Nottingham, 1964 (Institute of Physics and the Physical Society, London, 1964) p. 438.
[3] N. Blum, A.J. Freeman, J.W. Shaner and L. Grodzins, J. Appl. Phys. 36 (1965) 1169.
[4] T. Kaneko and S. Abe, J. Phys. Soc. Japan 20 (1965) 2001.
[5] P.J. Besser, A.H. Morrish and C.W. Searle, Phys. Rev. 153 (1967) 632.
[6] V.I. Ozhogin and V.G. Shapiro, Sov. Phys. JETP 27 (1968) 54.
[7] F. van der Woude, Phys. Stat. Sol. 17 (1966) 417.
[8] P.J. Flanders and J.P. Remeika, Phil. Mag. 11 (1965) 1271.

Hyperfine Interactions 29 (1986) 1361-1364

SPIN-FLOP PHASE TRANSITIONS IN THE ONE-DIMENSIONAL ANTIFERROMAGNETS K_2FeF_5 AND Rb_2FeF_5

Q.A. PANKHURST, C.E. JOHNSON and M.F. THOMAS

Oliver Lodge Laboratory, University of Liverpool, Liverpool, L69 3BX, U.K.

The characteristics of the spin-flop transition in K_2FeF_5 and Rb_2FeF_5 are found by Mössbauer spectroscopy to be very different, and are discussed in relation to the ordered magnetic structures of the two systems.

1. INTRODUCTION

The spin-flop phase transition occurs when a magnetic field B is applied along the easy anisotropy axis of a weakly anisotropic antiferromagnet. At the critical field B_{sf} the antiferromagnetic (AFM) axis of the spins reorients ('flops') to a direction perpendicular to the easy axis. The transition will be abrupt provided B is perfectly aligned with the easy axis. However, if there is significant misalignment the transition may be smooth, with the AFM axis gradually rotating away from the easy axis as the applied field is increased.

Mössbauer spectroscopy provides a useful tool for studying the spin-flop transition. The unflopped, flopped and rotated phases are readily distinguishable in the observed positions, splittings and intensities of the spectral lines.

2. EXPERIMENTAL RESULTS

Although K_2FeF_5 and Rb_2FeF_5 display similar quasi one-dimensional behaviour /1,2/ they have different lattice dimensions and low temperature magnetic structures. K_2FeF_5 has an orthorhombic lattice with unit cell dimensions a=2.039nm, b=1.284nm and c=0.740nm, in which the Fe^{3+} ions form zig-zag chains along the a-axis /3/. Below T_N = 6.95K it shows AFM order with the spins aligned collinearly along the b-axis. Rb_2FeF_5 is also orthorhombic with cell dimensions a=0.579nm, b=1.198nm and c=0.754nm (adopting the convention b>c, a an extremum), and with the Fe^{3+} ions in zig-zag chains along the a-axis /4/. Below T_N = 9.3K it forms a four-sublattice magnetic structure in which the spins are confined to the bc-plane and are canted at an angle $\phi=25^\circ$ to the b-axis /2,4/.

In this work ^{57}Fe Mössbauer spectra were recorded at 4.2K from single crystal samples of K_2FeF_5 and Rb_2FeF_5 in applied fields of up to 7T and 14T respectively (Figure 1). In the case of K_2FeF_5 an ac-plane crystal was used, and both the incident γ-rays and the applied field were parallel to the crystal b-axis (the magnetic easy axis). In zero applied field the spectrum consisted of four lines. The complete absence of the $\Delta M_I=0$ lines (lines two and five of a magnetic sextet) implies that the γ-ray beam was aligned within a few degrees of the b-axis. With B=3.0T applied the spectral lines

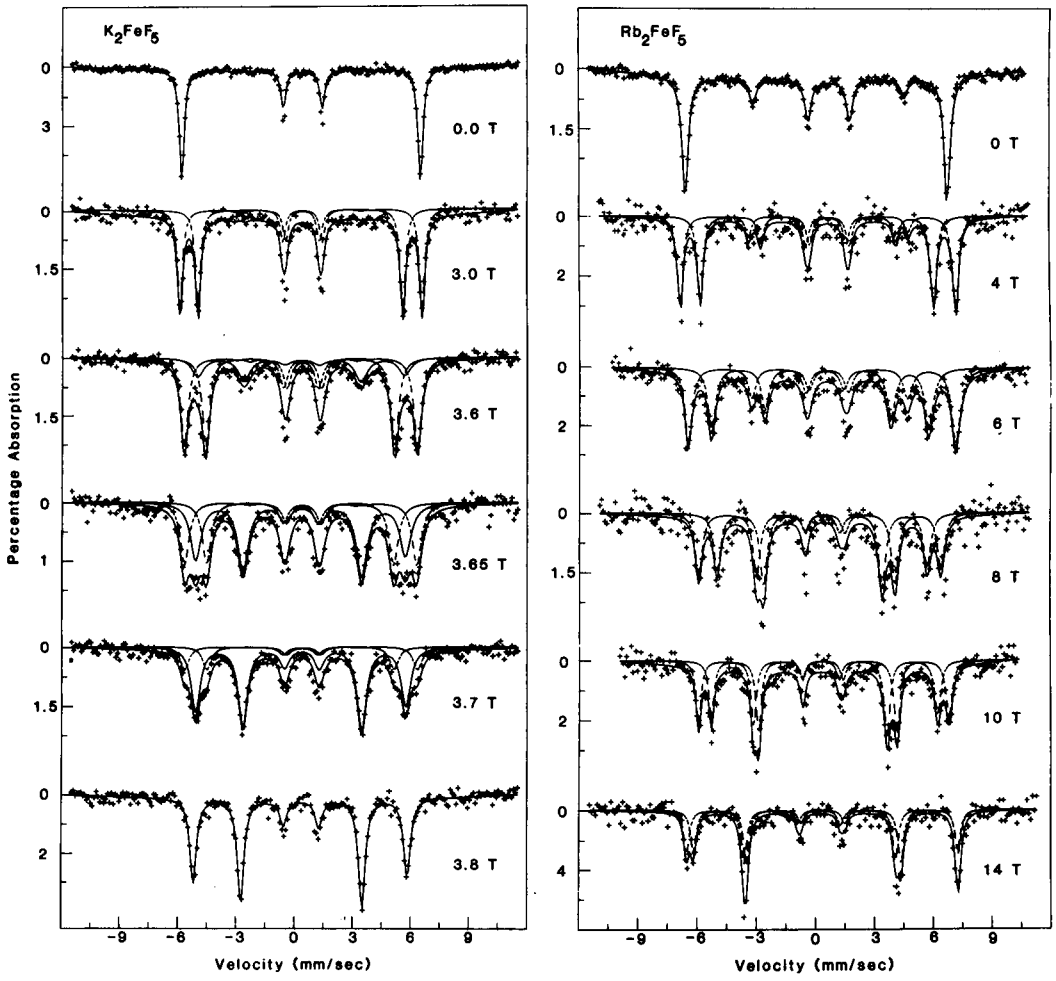

Figure 1. Mössbauer spectra of ac-plane single crystals of K_2FeF_5 and Rb_2FeF_5 at 4.2K. γ-rays and applied field were parallel to the b-axes. Full curves represent computer fits.

were split, corresponding to different effective fields on each AFM sublattice. At $B \gtrsim 3.8T$ a sextet with intensity ratios 3:4:1 in outer:middle:inner pairs of lines was observed, characterising a perpendicular orientation of the spins to the γ-ray beam. The intermediate spectra, $3.0T < B < 3.8T$, showed a coexistence of two phases : unflopped spins with split lines in 3:0:1 intensity ratio, and flopped spins with unsplit lines in 3:4:1 ratio. Computer analysis of the spectra /5/ showed that the relative area of the flopped component underwent a sharp transition near B=3.65T (Figure 2).

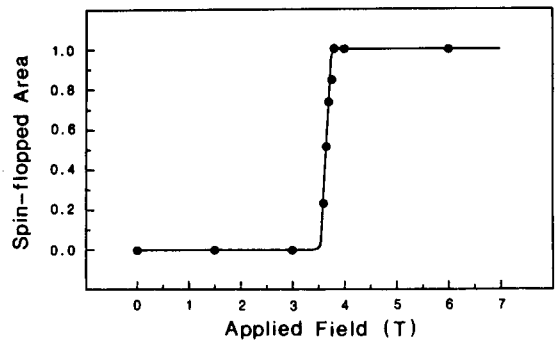

Figure 2. Applied field dependence of the relative spectral area of flopped to unflopped components in the Mössbauer spectra of K_2FeF_5.

In the case of Rb_2FeF_5 an ac-plane crystal was again used, with the applied field and γ-ray beam directed along the b-axis. However, this meant that B was not parallel to the easy anisotropy axis in the crystal, but was in effect misaligned by about 25° to both easy axes. The zero applied field spectrum (Figure 1) reflected this situation, with non-zero $\Delta M_I=0$ line intensities. Computer analysis indicated that the spins were canted at about 30° to the γ-ray beam. As the external field was applied all the spectral lines were seen to split, and the intensity of the $\Delta M_I=0$ lines increased. This implies that the spins were rotating in unison away from the applied field. Even with B=14T the lines showed splitting and the intensity ratio had not reached 3:4:1. Computer fitting the spectra indicated that the AFM axis of the spins had slowly rotated from ϕ=30° to the applied field to ϕ=87° as B had increased from zero to 14T (Figure 3).

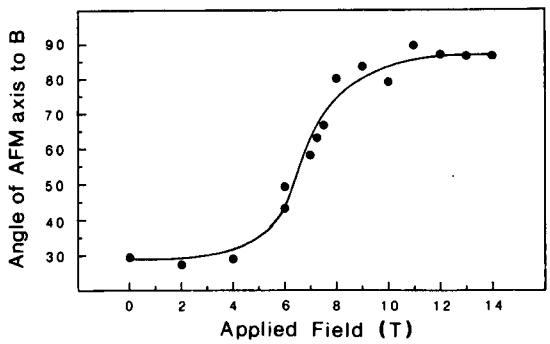

Figure 3. Applied field dependence of the angle ϕ between the AFM axis of the spins and the applied field B in Rb_2FeF_5.

3. DISCUSSION

The spin-flop transition in K_2FeF_5 was seen as a coexistence of unflopped and flopped phases over a range of fields $\Delta B=0.4T$ centered at $B_{sf}=3.65T$. Demagnetisation effects are too small in this case to account for the width of the transition ($B_{dm}<0.01T$). The simplest explanation of the coexistence might be a distribution of critical field values within the crystal due to random impurities, defects and distortions affecting the local environments of the ferric ions. The spin-flop for each individual ion appears to be of first-order, since no evidence of a rotated phase was found in the spectra.

In contrast, the spectra of the spin-flop in Rb_2FeF_5 consisted entirely of the rotated phase. This different behaviour may be related to the magnetic structure of the system, which is such that a magnetic field applied along the crystal b-axis is effectively misaligned by about 30° to the easy anisotropy axes. It is known that if the misalignment angle ψ exceeds a critical angle $\psi_c(T)$, a first-order transition will not occur /6/. This critical angle is often small in a uniaxial antiferromagnet, being of the order of the anisotropy to exchange field ratio, but may be larger in an antiferromagnet with orthorhombic anisotropy when the component of B perpendicular to the easy axis lies near the axis of hard anisotropy /7/. In Rb_2FeF_5 it appears that ψ exceeds ψ_c so that a sharp transition is not present, and a gradual rotation takes place. This is consistent with the observation that even in large fields (B=14T) a spin-flopped phase is not present. We would expect that as B was increased to very large values the spins would continue to rotate until they became uncoupled at the paramagnetic phase transition.

ACKNOWLEDGEMENTS

The authors are indebted to Mrs. B.M. Wanklyn of the Clarendon Laboratory, Oxford, for the single crystal samples used in this work. Q.A. Pankhurst wishes to thank the Commonwealth Scholarship Commission, UK, for their support.

References

/1/ G.P. Gupta, D.P.E. Dickson and C.E. Johnson, J. Phys. C 11(1978)215.
/2/ G.P. Gupta, D.P.E. Dickson, C.E. Johnson and B.M. Wanklyn, J. Phys. C 11(1978)3889.
/3/ M. Vlasse, G. Matejka and A. Tressaud, Acta Crystallogr. B 33(1977)3377.
/4/ A. Tressaud, J.L. Soubeyroux, J.M. Dance, R. Sabatier, P. Hagenmuller and B. Wanklyn, Solid State Commun. 37(1981)479.
/5/ Q.A. Pankhurst, C.E. Johnson and M.F. Thomas, J. Phys. C 18(1985)3249.
/6/ H. Rohrer and H. Thomas, J. Appl. Phys. 40(1969)1025.
/7/ H. Rohrer and Ch. Gerber, J. Appl. Phys. 49(1978)1341.

Hyperfine Interactions 28 (1986) 533-536

A MÖSSBAUER SPECTROSCOPIC STUDY OF THE MAGNETOCRYSTALLINE ANISOTROPY IN α-FeOOH

A. MEAGHER*, Q.A. PANKHURST and D.P.E. DICKSON

Department of Physics, University of Liverpool, Liverpool L69 3BX, England

Mössbauer spectra are obtained for a single crystal of α-FeOOH, with a magnetic field of up to 10T applied along the c axis. No spin reorientation is observed, indicating a lower limit of 6×10^4 J/m^3 for the anisotropy constant K. A theoretical estimate gives $K > 1.1 \times 10^6$ J/m^3.

1. INTRODUCTION

Mössbauer spectroscopy may be used to obtain information on the magnetic anisotropy of small single-domain particles via the observation of superparamagnetism /1/. For iron oxyhydroxide materials quoted values of the anisotropy constant K range from 1×10^3 J/m^3 for α-FeOOH (goethite) /2/ to 6.7×10^3 J/m^3 for the iron core of ferritin /3/ to $4\text{-}5\times10^4$ J/m^3 for amorphous iron hydroxide gels /4,5/.

An estimate of the magnetic anisotropy of bulk materials may be obtained by observing spin reorientation in single crystals when a magnetic field is applied along the easy axis. When the applied field reaches a value given by

$$B = (2K/ \chi_{\perp} - \chi_{\parallel})^{1/2} \qquad (1)$$

(where $\chi_{\perp}$ and $\chi_{\parallel}$ are the perpendicular and parallel susceptibilities), then the spins will abruptly reorientate into a direction perpendicular to the original easy axis /6/. Our aim here is to apply this method to α-FeOOH, using Mössbauer spectroscopy to detect the spin reorientation.

2. EXPERIMENTAL

α-FeOOH is antiferromagnetic below its Néel temperature of 403 ± 2K with the collinear spins lying parallel to the c axis /7/. Natural crystals cleave perfectly normal to the b-axis and moderately normal to the a axis /8/. Our single crystal was mounted in our superconducting 10T magnet with its c axis vertical, parallel to the field direction. A ^{57}Co(Rh) source, external to the magnet assembly, was used to transmit γ-rays through the sample parallel to its b axis. The sample temperature was 4.2 K.

*present address : Physics Department, Emory University, Atlanta, GA 30322 , USA

3. RESULTS

Figure 1 shows the spectra obtained in zero field, at 6 T and at 10 T. Corresponding fit parameters are given in table 1. In zero field the sextet observed has parameters close to those previously observed for α-FeOOH at 4.2 K /7/. The 3:4:1 line intensity ratio indicates that the spins are oriented perpendicular to the γ-ray direction. For applied fields of 6 and 10 T we observe <u>two</u> sextets with fields given by

$$B_{hf}(B_{app}) = B_{hf}(0) \pm B_{app}$$

This shows that spin reorientation does not take place at fields of 10 T or less. Putting B = 10 T and $\chi_{\parallel} - \chi_{\perp}$ (4.2K) = 0.28 $JT^{-2}kg^{-1}$ (a value obtained from the data presented in /9/,10/) into equation (1), it is found that the lack of spin reorientation up to 10 T corresponds to a minimum value for K of 6×10^4 J/m^3, larger than any of those previously mentioned for oxyhydroxide materials. We therefore try to estimate K, the anisotropy constant for α-FeOOH from first principles.

4. CALCULATIONS

For Fe^{3+} ions the major sources of magnetic anisotropy are (i) dipole-dipole anisotropy and (ii) single-ion anisotropy /11/.

4.1. dipole-dipole contribution

To estimate this contribution we have performed a classical calculation using eq. 5.46 of /12/ for a sphere of α-FeOOH of radius 1.4 nm. The iron atom positional parameters are taken from /7/ and the size of the unit cell from /13/. Each iron ion is assumed to possess a moment of $5\mu_B$. We find that c is the easiest axis, that a is intermediate at 5.4×10^5 J/m^3 above c and that the b axis is hardest at 3.1×10^5 J/m^3 above a. Although this value by itself is large enough to explain the absence of spin reorientation up to 10 T, we need to also calculate the single-ion anisotropy since it may possibly cancel with the dipole anisotropy just as it does in α-Fe_2O_3 at low temperature /14/.

4.2. single-ion contribution

It is notoriously difficult to calculate this contribution for S-like ions from first principles. We resort to using the effective-spin Hamiltonian parameters for Fe^{3+} doped into α-AlOOH, which is isomorphous to α-FeOOH. These parameters were obtained using EPR by Gavrilov et al /15/. Their values are: D = -0.53 K and E = -0.25 K. Using these values in the equation

$$\mathcal{H} = D\,[S_z^2 - 1/3\ S(S+1)] + E\,(S_x^2 - S_y^2)$$

where S = 5/2 is the effective spin and knowing the ionic volume in goethite we calculate that z is easiest, x is at 5.55×10^5 J/m^3 above z and y is hardest at 9.9×10^5 above x. But z is coincident with c, while x,y are rotated relative to a,b by 34° /15/. Thus in goethite the single-ion and dipole-dipole anisotropies reinforce each other.

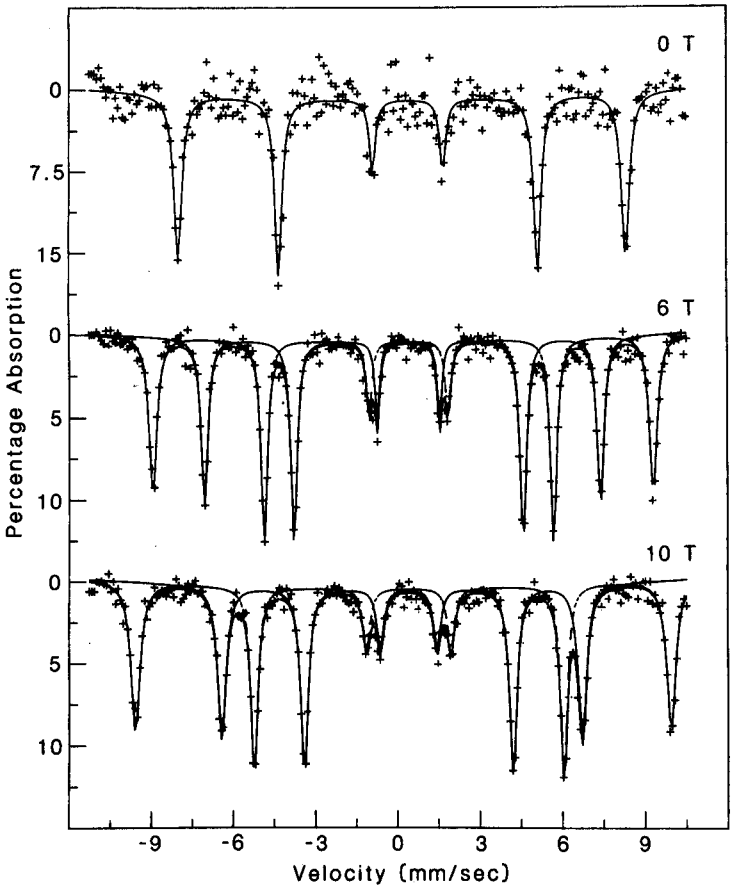

Fig.1. Mössbauer spectra at 4.2K of a single crystal of α-FeOOH, with the γ-rays directed along the b axis. Spectra are shown in zero field and with 6 and 10 Tesla applied parallel to the c axis.

Table 1
Fit parameters for the spectra of figure 1.

B_{app}(T)	B_{hf}(T)	2ε(mm/s)	IS(mm/s)[a]
0	50.7	-0.24	0.48
6	44.8,56.6	-0.23	0.50
10	40.8,60.5	-0.23	0.49

[a] relative to iron foil at room temperature.

5. DISCUSSION

Our calculations indicate that goethite does not have uniaxial anisotropy. We may note that Mørup et al /16/ have observed for small particles of goethite a superparamagnetic Mössbauer behavior different from that expected for uniaxially anisotropic particles. Measurement of all three values of the magnetic susceptibility of goethite is needed.

Our calculated and experimental values for the magnetic anisotropy of bulk goethite are far larger than that reported for small particles /2/, a trend opposite to that noted for Fe_3O_4 and α-Fe_2O_3 /17/. The reason for this remains to be elucidated.

REFERENCES

/1/ S. Mørup, J.A. Dumesic and H. Topsoe, in Applications of Mössbauer Spectroscopy, ed. R.L. Cohen, Vol.II (Academic, New York, 1980) pp.1-53.
/2/ T. Shinjo, J. Phys. Soc. Japan 21(1966)917.
/3/ J.M. Williams, D.P. Danson and C. Janot, Phys. Med. Biol. 23(1978)835.
/4/ Z. Mathalone, M. Ron and A. Biran, Solid State Comm. 8(1970)333.
/5/ J.M.D. Coey and P.N. Readman, Earth Planet. Sci. Lett. 21(1973)45.
/6/ L. Néel, in Low-temperature Physics, eds. C. DeWitt, B. Dreyfus and P.G. de Gennes (Gordon and Breach, New York, 1981) p.417.
/7/ J.B. Forsyth, I.G. Hedley and C.E. Johnson, J. Phys. C 2(1968)179.
/8/ W.A. Deer, R.A. Howie and J. Zussman, Rock-forming Minerals, vol. 5 (non-silicates), (Longmans, London, 1962) p.118.
/9/ G.W. Van Oosterhout, Proc. Int. Conf. Magnetism, Nottingham, (Institute of Physics, London, 1965) p.529.
/10/ I.G. Hedley, Z. Geophysik 37(1971)409.
/11/ G.T, Rado, J. Appl. Phys. 50(1979)7285.
/12/ S. Krupipka and K. Zaveta in Magnetic Oxides, ed. D.J. Craik, Vol.1 (Wiley, London, 1975).
/13/ C.F. Sampson, Acta Cryst. B25(1969)1683.
/14/ J.O. Artman, J.C. Murphy and S. Foner, Phys. Rev. 138(1965)A912.
/15/ I.A. Gavrilov, L.P. Litovkina and M.L. Meil'man, Fiz. Tverd. Tela 10(1968)2705. (Soviet Physics Solid State 10(1969)2177)
/16/ S. Mørup, M.B. Madsen, J. Franck, J. Villadsen and C.J.W. Koch, J. Magn. Magn. Mat. 40(1983)163.
/17/ S. Mørup and H. Topsoe, Appl. Phys. 11(1976)63.

J. Phys. C: Solid State Phys. 18 (1985) 3249–3253. Printed in Great Britain

A Mössbauer investigation of the spin-flop transition in the one-dimensional antiferromagnet K_2FeF_5

Q A Pankhurst, C E Johnson and M F Thomas
Oliver Lodge Laboratory, University of Liverpool, Liverpool L69 3BX, UK

Received 15 October 1984, in final form 20 December 1984

Abstract. Mössbauer spectra of K_2FeF_5 near the spin-flop phase transition indicate that domains of antiferromagnetic and spin-flopped spins coexist over a range of applied fields $\Delta B_{app} = 0.4\,T$ centred at $B_{sf} = 3.65\,T$. This is discussed with reference to the first-order character of the spin-flop transition.

1. Introduction

The spin-flop magnetic phase transition occurs when a magnetic field B_{app} is applied along the easy axis of a weakly anisotropic antiferromagnet. At the critical field B_{sf} the antiferromagnetic axis of the spins reorients (flops) to a direction perpendicular to the easy axis.

Investigations of the spin-flop transition in a number of antiferromagnets have shown that the reorientation takes place over a finite range of applied fields (Holmes *et al* 1969, Basten *et al* 1980). Such broadened transitions are often attributed to a misalignment of B_{app} and the easy axis. If the misalignment angle ψ exceeds a critical angle $\psi_c(T)$, corresponding to the edge of the first-order spin-flop shelf (Rohrer and Thomas 1969), one will observe a gradual rotation of the antiferromagnetic axis away from the magnetic easy axis as the applied field is increased.

However, even with near-perfect alignment one will not see a sharp transition if the demagnetisation factor N of the sample is non-zero. In such a case an intermediate state consisting of domains of antiferromagnetic and spin-flopped material may occur, over the field range $\Delta B = \chi_\perp N B_{sf}$ where $\chi_\perp$ is the susceptibility perpendicular to the easy axis (King and Paquette 1973).

In the present work the Mössbauer spectra of the one-dimensional antiferromagnet K_2FeF_5 have been studied in detail close to the spin-flop transition. The Mössbauer hyperfine spectrum is a powerful tool for studying the transition as both unflopped and flopped spin configurations may be directly observed via different features, namely the line splitting by an external field and the intensities of the $\Delta M_I = 0$ lines.

2. Experimental results

K_2FeF_5 crystallises in an orthorhombic lattice with unit-cell dimensions $a = 2.039$ nm, $b = 1.284$ nm and $c = 0.7399$ nm, and with the Fe^{3+} ions forming zigzag chains along

0022-3719/85/163249 + 05 $02.25

the *a* axis. This structure leads to quasi-one-dimensional behaviour and a low Néel temperature of 6.95 K below which the spins align antiferromagnetically along the magnetic easy axis which is the crystal *b* axis. A large single crystal was grown in the form of an *a–c* plane and ^{57}Fe Mössbauer spectra were recorded at 4.2 K with incident gamma rays and applied field parallel to the *b* axis. These spectra are shown in figure 1.

In zero applied field a four-line hyperfine spectrum was observed. The complete absence of the $\Delta M_I = 0$ lines (lines two and five of a magnetic sextet) implies that the *b* axis was aligned within a few degrees of the γ-ray direction. In small applied fields ($B_{app} \leqslant 3.5$ T) the spectral lines are seen to split, corresponding to different effective fields on each of the two sublattices of the antiferromagnet. For $B_{app} \simeq 3.7$ T additional lines appear at the $\Delta M_I = 0$ positions, and the outer lines show evidence of structure. For $B_{app} \geqslant 3.8$ T a sextet with intensity ratios 3:4:1 in outer:middle:inner lines is observed,

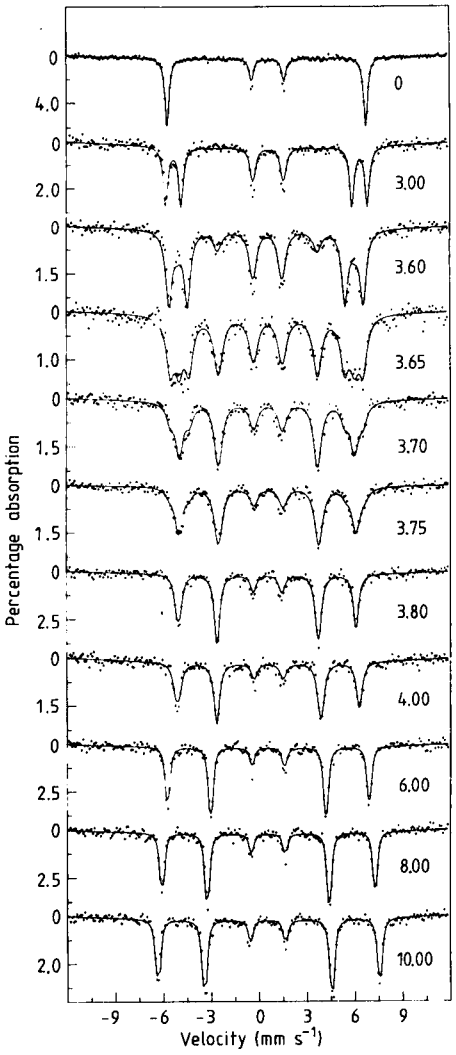

Figure 1. Mössbauer spectra of an *a–c* plane single crystal of K_2FeK_5 with gamma rays and applied field parallel to the *b* axis. Full traces represent computer fits as discussed in the text. Values by traces are of applied field in teslas.

characteristic of a perpendicular orientation of spins to the γ-ray beam. Increasing B_{app} to a maximum of 10 T did not alter the relative line intensities and therefore did not appreciably cant the spins out of the *a–c* plane.

The spectra were computer analysed with a modified form of the program of Lang and Dale (1974), using a quadrupole splitting of $-0.68\,\mathrm{mm\,s^{-1}}$ and the asymmetry parameter $\eta = 0.57$ found for polycrystalline samples (Gupta *et al* 1977). The electric field gradient principal axis was taken to be at 42° to the crystal *b* axis, lying in the *a–b* plane (Gupta *et al* 1979). Computer fits of the spectra obtained with $B_{app} < 3.5\,\mathrm{T}$ confirmed that the applied field was aligned within two or three degrees of the *b* axis. The $B_{app} > 3.8\,\mathrm{T}$ fits showed that the spins had flopped into the *a–c* plane.

Spectra in the transition region ($B_{app} \simeq 3.7\,\mathrm{T}$) could not be adequately fitted as the superposition of two component sextets resulting from spins canted at some intermediate

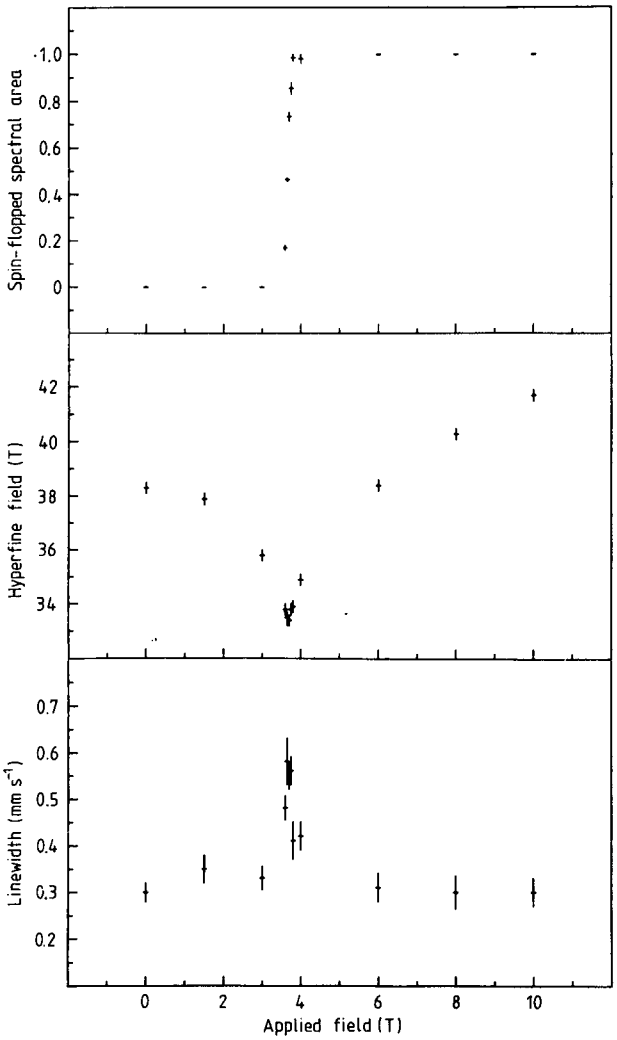

Figure 2. Applied field dependence of (*a*) the relative spectral area of spin-flopped to antiferromagnetic components, (*b*) the hyperfine field and (*c*) the linewidth of the Mössbauer spectra.

angle to the b axis, as suggested for a misaligned antiferromagnet. Good fits were obtained using a superposition of components corresponding to unflopped (antiferromagnetic) and flopped phases. The antiferromagnetic phase is characterised by intensity ratios 3:0:1 and splitting of the lines by the applied field; the flopped component has intensity ratios 3:4:1 and is not split by the applied field. The relative area of the flopped component increased smoothly through the transition region from zero to one (figure 2(a)).

In principle one should be able to observe hysteresis in a first-order spin-flop (Keffer 1966), but K_2FeF_5 has a very small anisotropy to exchange field ratio ($B_A/B_E \sim 10^{-3}$) resulting in a predicted hysteresis of less than 0.005 T in B_{sf}. This is too small to be detected in the present experiment.

The variation of hyperfine field B_{hf} is shown in figure 2(b) and is characteristic of the applied field dependence of spin reduction in antiferromagnets with low T_N (Gupta *et al* 1978). An applied field $B_{app} < B_{sf}$ parallel to the easy axis promotes the thermal excitation of spin waves (magnons) in the antiferromagnetic chains, and the increased spin fluctuation is observed as a decreased B_{hf}. The fluctuations are maximal at $B_{app} = B_{sf}$ and B_{hf} is at a minimum. For $B_{app} > B_{sf}$ the field is perpendicular to the spin axis and the spin waves are inhibited so B_{hf} increases, approaching saturation for large B_{app}.

A peak in the linewidth of the Mössbauer spectral lines is observed at the spin-flop (figure 2(c)). This is consistent with the presence of finite-width domain walls separating flopped and unflopped regions, although the possibility of dynamic effects has not been discounted.

3. Conclusions

Direct evidence for the simultaneous existence of antiferromagnetic and spin-flopped states has been observed in the Mössbauer spectra of K_2FeF_5. The mechanism of the spin-flop is thought to involve the growth of domains of flopped spins at the expense of unflopped spins over a finite range of applied fields near B_{sf}.

This result is somewhat surprising when one considers that the estimated misalignment angle between B_{app} and the easy anisotropy axis was $\psi = 0 \pm 3°$, compared with the critical angle $\psi_c \leqslant 0.3°$ predicted for a uniaxial antiferromagnet with $B_A \ll B_E$ (Rohrer and Thomas 1969). However the phase diagram of an antiferromagnet with orthorhombic anisotropy (as in K_2FeF_5) is quite different, with the 'shelf' of first-order transitions extending to the paramagnetic phase boundary when the component of B_{app} perpendicular to the easy axis lies near the axis of hard anisotropy (Rohrer and Gerber 1978). These two cases are illustrated in figure 3. In the spin-flopped phase of K_2FeF_5 there are four distinct magnetic sublattices corresponding to different orientations of the constituent $(FeF_6)^{3-}$ octahedra (Vlasse *et al* 1977), and therefore two different axes of hard anisotropy. Cooper (1981) established that each hard axis lies in the crystal a–c plane at about 50° to the c axis. Thus it is possible that although we may not have perfect alignment of B_{app} and the easy axis we could still cross the first-order spin-flop shelf (seeing a sharp transition in the Mössbauer spectra) at some of the ferric ions as B_{app} is increased.

The domain structure is reminiscent of that seen in MnF_2 (King and Paquette 1973) and K_2MnF_4 (de Jongh *et al* 1982). In MnF_2 the domain state is established by demagnetising fields, but in K_2MnF_4 such effects do not account for the width of the observed transition region and an explanation in terms of soliton excitations is suggested

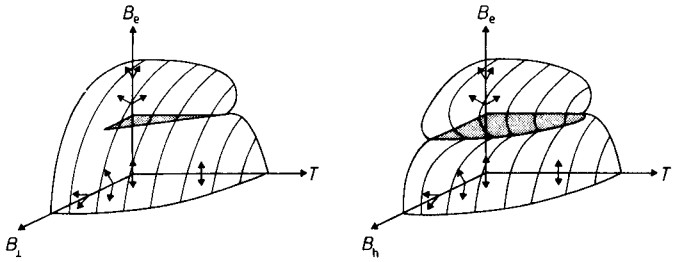

Figure 3. Schematic phase diagrams of antiferromagnets with (*a*) uniaxial and (*b*) orthorhombic anisotropy. In (*a*) B_e and $B_\perp$ are magnetic fields applied parallel and perpendicular to the axis of easy anisotropy, while in (*b*) the fields B_e and B_h are along the easy and hard anisotropy axes. The pairs of arrows represent sublattice spin directions, and the shaded areas indicate surfaces of first-order spin-flop transitions.

(de Jongh 1982). For K_2FeF_5 the maximum possible width of a demagnetisation-broadened transition is $\Delta B_{max} \leqslant 0.01$ T when the demagnetisation factor $N = 1$, and where $\chi_\perp$ is estimated from the susceptibility measurements on powder samples of Dance *et al* (1980). Thus the width of the observed spin-flop transition in K_2FeF_5 of $\Delta B_{app} = 0.4$ T cannot be attributed entirely to demagnetising fields and some other effects, of which solitons are an intriguing possibility, must be present.

Acknowledgments

The authors are indebted to Mrs B M Wanklyn of the Clarendon Laboratory, Oxford, for the single-crystal sample used in this work. Q A Pankhurst wishes to thank the Commonwealth Scholarship Commission, UK, for their support.

References

Basten J A J, Frikkee E and de Jonge W J M 1980 *Phys. Rev. B* **22** 1429
Cooper D M 1981 *PhD Thesis* University of Liverpool
Dance J M, Soubeyroux J.L, Sabatier R, Fournes L, Tressaud A and Hagenmuller P 1980 *J. Magn. Magn. Mater.* **15–18** 534
Gupta G P, Dickson D P E and Johnson C E 1978 *J. Phys. C: Solid State Phys.* **11** 215
—— 1979 *J. Phys. C: Solid State Phys.* **12** 2419
Gupta G P, Dickson D P E, Johnson C E and Wanklyn B M 1977 *J. Phys. C: Solid State Phys.* **10** L459
Holmes L, Eibschütz M and Guggenheim H J 1969 *Solid State Commun.* **7** 973
de Jongh L J 1982 *J. Appl. Phys.* **53** 8018
de Jongh L J, Regnault L P, Rossat-Mignod J and Henry J Y 1982 *J. Appl. Phys.* **53** 7963
Keffer F 1966 *Handbuch der Physik* vol 18 *Ferromagnetism* part 2, ed. S Flugge (Berlin:Springer)
King A R and Paquette D 1973 *Phys. Rev. Lett.* **30** 662
Lang G and Dale B W 1974 *Nucl. Instrum. Methods* **116** 567
Rohrer H and Gerber Ch 1978 *J. Appl. Phys.* **49** 1341
Rohrer H and Thomas H 1969 *J. Appl. Phys.* **40** 1025
Vlasse M, Matejka G and Tressaud A 1977 *Acta Crystallogr.* B **33** 3377

J. Phys. C: Solid State Phys., 18 (1985) 1255–1261. Printed in Great Britain

The electric field gradient in the quasi-one-dimensional disordered compound $FeMgBO_4$

Q A Pankhurst†, M F Thomas† and B M Wanklyn‡

† Oliver Lodge Laboratory, University of Liverpool, Liverpool L69 3BX, UK

‡ Clarendon Laboratory, Oxford OX1 3PU, UK

Received 25 July 1984

Abstract. Mössbauer spectra obtained from powder and single-crystal samples of the insulating compound $FeMgBO_4$ show distributions in the nuclear quadrupole parameters. The sign of the quadrupole splitting Δ is found to be positive, and a probability distribution $P(\Delta)$ is determined, with the mean value $\bar{\Delta} = 0.83$ mm s^{-1} at 30 K. The mean electric field gradient has asymmetry $\bar{\eta} = 0.58 \pm 0.05$, and its principal axis lies preferentially in the crystallographic a–b plane.

1. Introduction

Low-dimensional magnetic systems and disordered crystals have aroused a great deal of interest in recent years. The boroferrite insulator $FeMgBO_4$ has been reported as falling into both categories.

$FeMgBO_4$ is an orthorhombic compound with the Warwickite space group (V_h^{16}-$Pnam$) and unit-cell dimensions $a_0 = 9.258$ Å, $b_0 = 9.427$ Å and $c_0 = 3.104$ Å (Wyckoff 1964). Initially it may be thought to have the crystal structure represented in figure 1: a pure system in which Fe^{3+} ions in the centres of O^{2-} octahedra form zigzag chains in the c direction, well separated by linear Mg^{2+} and B^{3+} chains. Magnetic susceptibility measurements by Wiedenmann and Burlet (1978) have established that strong antiferromagnetic interactions are present in the magnetic chains, with $J_1/k = -16$ K between nearest-neighbour and $J_2/k = -8$ K between next-nearest-neighbour Fe^{3+} ions. Interchain coupling is weak with $J'/J_1 < 10^{-2}$ giving $FeMgBO_4$ its quasi-one-dimensional nature. An interesting consequence of the competition between J_1 and J_2 in the chain is that a ground state of helical spin order is predicted (Selke 1977), a magnetic structure never before reported in a one-dimensional system.

However, x-ray and neutron diffraction studies (Wiedenmann and Burlet 1978) have revealed a degree of crystallographic site inversion between some Fe^{3+} and Mg^{2+} ions. Strictly, the compound should be described as $(Fe_{1-x}Mg_x).(Mg_{1-x}Fe_x).BO_4$, where $x \simeq 0.15$. At temperatures below ~13 K, susceptibility, magnetisation and neutron diffraction measurements all show properties characteristic of a disordered material or a spin glass. It is thought that the substituted Mg^{2+} ions sufficiently modify the one-dimensional spin correlations in the Fe^{3+} chain that instead of complete three-dimensional ordering at low temperatures, a highly frustrated spin glass state is established.

0022-3719/85/061255 + 07 $02.25

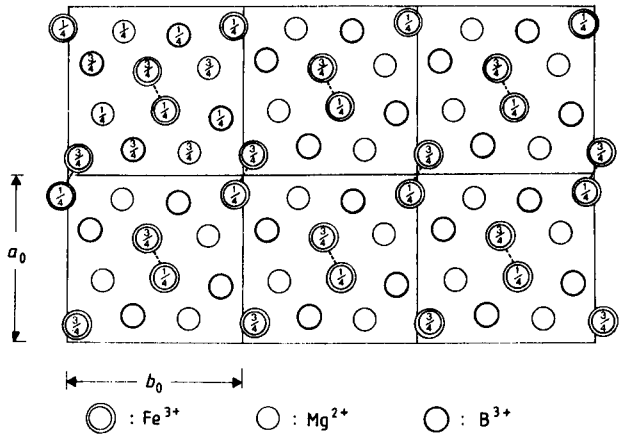

Figure 1. Projection onto the (001) plane of the idealised crystal structure of $FeMgBO_4$. Oxygen ions have been omitted for clarity.

In this paper we report on a determination of the sign and direction of the electric field gradient in $FeMgBO_4$, an essential prerequisite to the detailed study of the magnetic properties of the compound by Mössbauer spectroscopy.

2. Experimental results

2.1. Crystal preparation

Crystalline platelets of $FeMgBO_4$ were prepared by melting stoichiometric quantities of Fe_2O_3, MgO and B_2O_3 in a flux of PbO, PbF_2, $PbCl_2$ and MoO_3 at 1250 °C followed by slow cooling. The largest platelets obtained were generally of the morphology shown in figure 2, and were typically of dimensions $4 \times 1 \times 0.2\ mm^3$. The orientation of the crystallographic axes within the platelets was established using back-reflection Laue x-ray diffraction.

^{57}Fe Mössbauer spectra of both powder and single-crystal absorbers were recorded on a conventional constant-acceleration spectrometer, at temperatures between 1.3 K and room temperature.

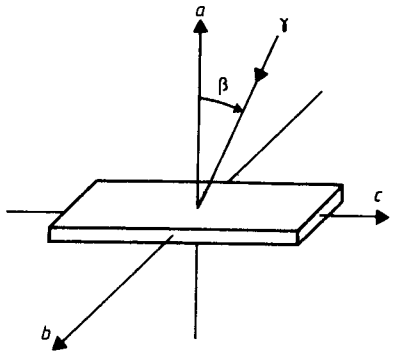

Figure 2. Platelet morphology, indicating the orientation of the incident γ-ray beam described in § 2.3.

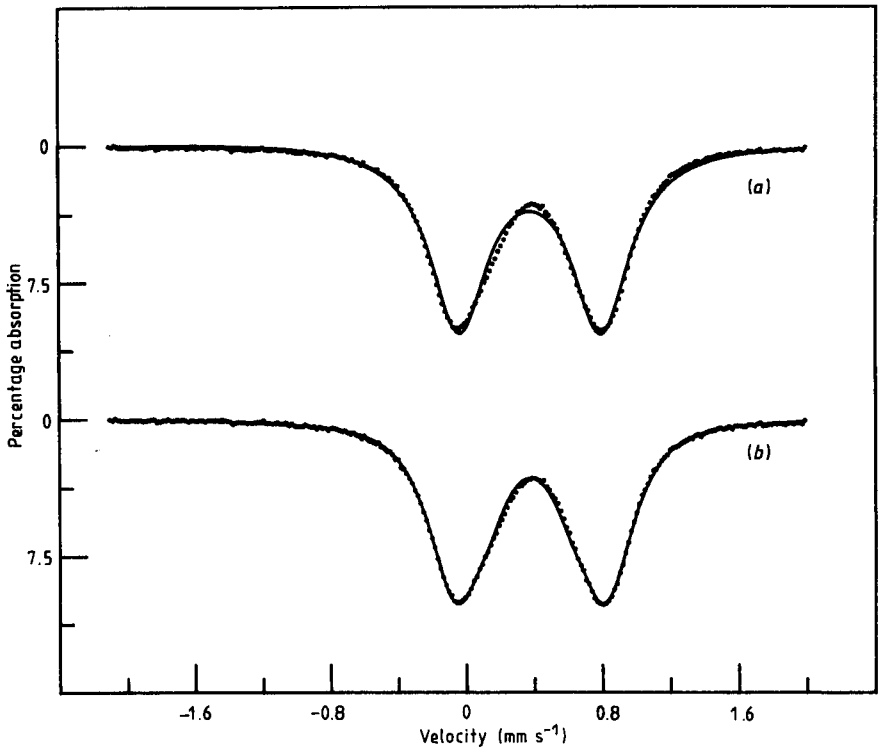

Figure 3. Mössbauer powder spectrum at 30 K. Full curves represent (*a*) Lorentzian and (*b*) $P(\Delta)$ fits.

2.2 Powder spectra

Above $T \simeq 14$ K the spectrum consists of a single quadrupole-split doublet, shown in figure 3 for a powder sample at 30 K. The absorption lines are very broad, with linewidth $\Gamma = 0.41$ mm s^{-1}, compared with the experimental natural linewidth $\Gamma_0 = 0.25$ mm s^{-1} of the innermost lines of a thin natural iron foil. This broadening is due to the disordered nature of the compound, where each Fe^{3+} ion experiences one of a variety of possible nuclear environments. The Mössbauer effect nuclear parameters isomer shift (δ) and quadrupole splitting (Δ) are therefore not unique, but are distributed about mean values $\bar{\delta}$ and $\bar{\Delta}$ corresponding to Fe^{3+} sites in relatively undisturbed parts of the crystal.

The mean parameters may be estimated by fitting the spectrum as a pair of Lorentzian lines, as in figure 3(*a*), giving $\bar{\delta} = 0.51 \pm 0.02$ mm s^{-1} relative to metallic iron, and $\bar{\Delta} = 0.83 \pm 0.02$ mm s^{-1}. Here the quadrupole splitting is defined as $\Delta = \frac{1}{2}eQ|V_{zz}|(1 + \eta^2/3)^{1/2}$ where Q is the nuclear quadrupole moment of the excited state of ^{57}Fe and V_{zz} is the principal axis of the electric field gradient (EFG). The asymmetry parameter η is defined as $\eta = (V_{xx} - V_{yy})/V_{zz}$ following the convention $|V_{zz}| \geqslant |V_{yy}| \geqslant |V_{xx}|$.

Since the Fe^{3+} ions are in sites of octahedral coordination and the diversity of local environments is at most a second-nearest-neighbour effect, we may as a first approximation treat the spectrum as a pure quadrupole distribution. That is, we assume no correlation between δ and Δ. The observed symmetry of the absorption lines in the powder spectrum is consistent with this assumption. We therefore fit the spectrum as a

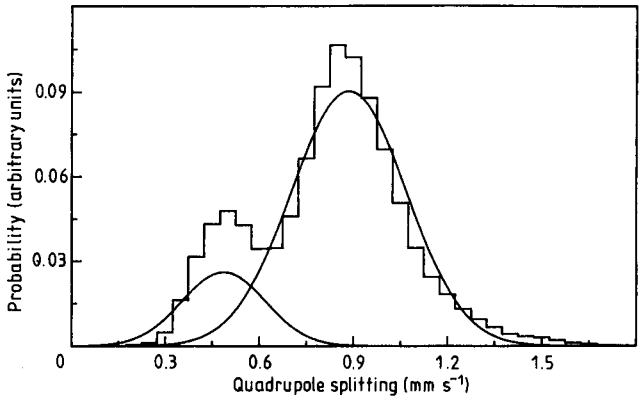

Figure 4. Fitted quadrupole distributions for powder at 30 K, using discrete (histogram) and two-component Gaussian (full curves) models.

superposition of doublets with identical isomer shift, $\delta = 0.51$ mm s^{-1}, and natural linewidth Γ_0 (figure 3(*b*)), and extract a probability distribution $P(\Delta)$ shown in figure 4. The distribution was smoothed using the law $P_i' = \frac{1}{4}(P_{i-1} + 2P_i + P_{i+1})$. Two peaks are seen in the $P(\Delta)$ which we believe correspond to the majority of Fe^{3+} ions in largely undisturbed environments at $\Delta \simeq 0.85$ mm s^{-1}, and to those Fe^{3+} ions substituted into Mg^{2+} sites at $\Delta \simeq 0.50$ mm s^{-1} which have a more nearly cubic arrangement of surrounding O^{2-} ions.

The analysis was extended by assuming a probability distribution

$$P(\Delta) = xP_1(\Delta) + (1 - x)P_2(\Delta) \tag{1}$$

where the $P_i(\Delta)$ are normalised Gaussian distributions of the form

$$P_i(\Delta) = \exp[-(\Delta - \bar{\Delta}_i)^2/2\sigma_i^2]/\sigma_i \tag{2}$$

centred about isomer shifts δ_i. The $\bar{\Delta}_i$ and σ_i are the mean quadrupole splittings and standard deviations for Fe^{3+} ions either in the linear Mg^{2+} chains ($i = 1$) or in the zigzag Fe^{3+} chains ($i = 2$). Using this $P(\Delta)$ a fit of similar quality to that found with the discrete $P(\Delta)$ was obtained, with parameters $\delta_1 = 0.52$ mm s^{-1}, $\bar{\Delta}_1 = 0.49$ mm s^{-1}, $\sigma_1 = 0.12$, $\delta_2 = 0.51$ mm s^{-1}, $\bar{\Delta}_2 = 0.89$ mm s^{-1} and $\sigma_2 = 0.18$. The Gaussian distributions $P_i(\Delta)$ are shown in figure 4. Site inversion was estimated as $x = 0.18 \pm 0.02$, which compares favourably with the value $x \simeq 0.15$ determined by Wiedenmann and Burlet (1981) from diffraction experiments.

2.3 Single-crystal spectra

Crystalline absorbers were made by forming a mosaic of three or four platelets, either laid side by side or stacked on top of one another, and then set in an epoxy resin mount. The absorber was then thinned by abrasion until a good transmission spectrum was obtained. In this way both *b–c* plane and *a–b* plane absorbers were prepared.

Room-temperature spectra (figure 5) were taken with the absorber's *a* axis oriented at a series of angles β to a γ-ray beam incident in the *a–c* plane (figure 2), and showed line asymmetry. Although four separate Fe^{3+} sites exist within the zigzag chains in the

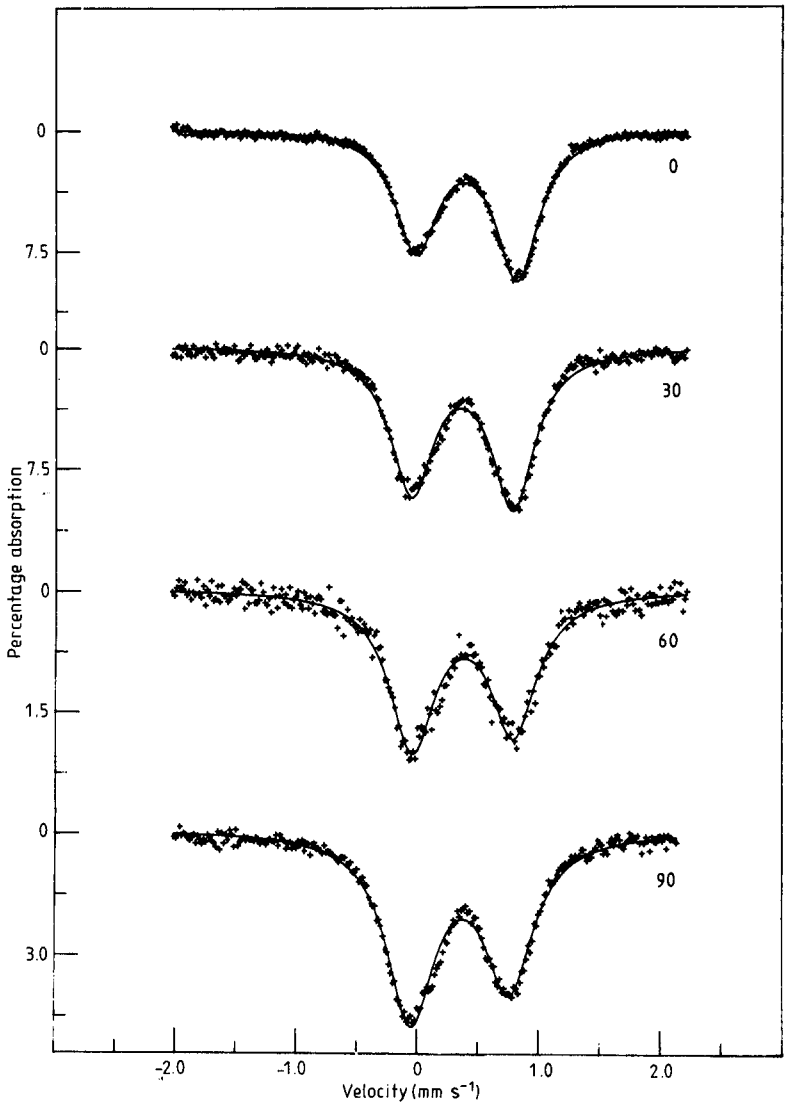

Figure 5. Single-crystal spectra at room temperature, with γ-rays incident at angle β (given by the spectra in degrees) to the a axis. Full curves represent Lorentzian fits.

Warwickite structure, all are equivalent with respect to the quadrupole interaction with a γ-ray beam incident in the a–c plane. Therefore the observed line asymmetry was indicative of a well defined preferred direction of the EFG principal axis within the crystal.

In a quadrupole-split ^{57}Fe Mössbauer spectrum the absorption lines result from nuclear transitions between the $M_I = \pm\frac{3}{2}$ and $\pm\frac{1}{2}$ excited states, and the $M_I = \pm\frac{1}{2}$ ground state. The relative probabilities (and hence intensities) of these transitions (Zory 1965) are

$$\frac{P(\frac{3}{2}\rightarrow\frac{1}{2})}{P(\frac{1}{2}\rightarrow\frac{1}{2})} = \frac{4(1+\eta^2/3)^{1/2} + (3\cos^2\theta - 1 + \eta\sin^2\theta\cos 2\varphi)}{4(1+\eta^2/3)^{1/2} - (3\cos^2\theta - 1 + \eta\sin^2\theta\cos 2\varphi)} \tag{3}$$

where θ and φ are the polar angles of the incident γ-ray beam relative to the EFG principal axes.

The ratio of line intensities of the single-crystal spectra as a function of orientation angle β was estimated by fitting as Lorentzian doublets, and is shown in figure 6.

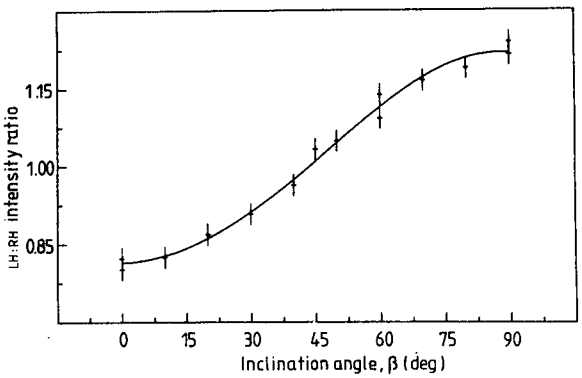

Figure 6. Ratio of intensity of left-hand to right-hand lines of single-crystal spectra, as a function of inclination angle β. The full curve is a fit made using equation (3).

Thickness effects were considered to be unimportant since the spectra observed at $\beta \leqslant 60°$ for the b–c plane absorber showed a crossover of line intensities for $\beta > 45°$, and were consistent with the spectra taken with $\beta \geqslant 60°$ on the a–c plane absorber. Least-squares fitting the expression in equation (3) to the data yielded a unique solution, with a positive quadrupole interaction, mean asymmetry $\bar{\eta} = 0.58 \pm 0.05$ and EFG principal axes in the crystallographic coordinate system given by

$$V_{xx} = (0.00 \pm 0.05, 0.01 \pm 0.05, 1.00 \pm 0.05)$$

$$V_{yy} = (0.66 \pm 0.05, -0.75 \pm 0.05, 0.01 \pm 0.05)$$

$$V_{zz} = (0.75 \pm 0.05, 0.66 \pm 0.05, -0.01 \pm 0.05).$$

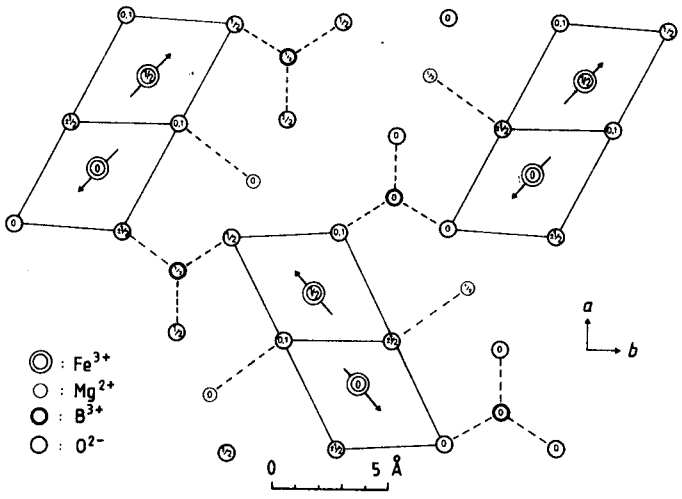

Figure 7. Projection onto the (001) plane of the local environment of Fe^{3+} ions in undisturbed regions of the crystal. The arrows represent the direction of the EFG principal axis.

This solution is represented in figure 7. The result that V_{zz} is confined to the a–b plane is physically reasonable, since (disregarding the disorder in second and further neighbours) the a–b plane is a mirror symmetry plane for the Fe^{3+} ions and the EFG tensor should also have that symmetry.

The spectra were also fitted using the two-component Gaussian $P(\Delta)$ distribution described in § 2.2. The relative line intensities of the component doublets were not well defined, and the parameters resulting from a fit using equation (3) had large uncertainties. Asymmetry parameters were estimated as $\bar{\eta}_1 = 0.40 \pm 0.20$ for the ~18% of Fe^{3+} ions substituted into Mg^{2+} chains, and $\bar{\eta}_2 = 0.58 \pm 0.10$ for the remaining Fe^{3+} ions in undisturbed sites. The EFG principal axes were close to those previously determined using the Lorentzian fitted line intensities.

3. Conclusion

The sign and mean directions of the EFG principal components in $FeMgBO_4$ have been determined. A detailed Mössbauer study of the magnetic properties of this compound at low temperatures is now possible, and is currently being undertaken.

Acknowledgments

We would like to thank Professor C E Johnson for clarifying discussions, and one of us (QAP) wishes to acknowledge the support of the Commonwealth Scholarship Commission UK.

References

Selke W 1977 *Z. Phys.* B **27** 81
Wiedenmann A and Burlet P 1978 *J. Physique* **39** C6 720
—— 1981 *Solid State Commun.* **38** 129
Wyckoff R W G 1964 *Crystal Structures* vol 2 (New York: Interscience) p 521
Zory P 1965 *Phys. Rev.* **140** A1401